# Droplet freezing in clouds induced by mineral dust particles: Sensitivities of precipitation and radiation

Zur Erlangung des akademischen Grades eines
DOKTORS DER NATURWISSENSCHAFTEN

von der Fakultät für Physik des
Karlsruher Instituts für Technologie (KIT)
genehmigte
DISSERTATION
von

Dipl.-Met. Marco Paukert
aus Regensburg

| | |
|---|---|
| Tag der mündlichen Prüfung: | 15. Juli 2016 |
| Referentin: | Prof. Dr. C. Hoose |
| Korreferent: | Prof. Dr. T. Leisner |

# Abstract

This thesis aims to enhance our understanding of cloud microphysical processes under conditions of varying droplet freezing efficiencies. The amount of ice particles present in clouds influences a multitude of cloud particle interactions in the mixed-phase regime. Consequently, the growth of large precipitating particles and dissipation of small ones depends on the efficiency of droplet freezing, thus modulating the evolution of clouds, surface precipitation and radiative properties.

Predicting the freezing probabilities of droplets in the atmosphere involves a number of uncertainties, owing to the presence of aerosols as a prerequisite to trigger the freezing mechanism in a wide range of temperatures. These uncertainties involve a) the identification of relevant types of aerosols (ice nuclei, IN) in lab or field studies, b) the theoretical or empirical description of IN efficiencies depending on the type of IN and thermodynamic conditions, c) the knowledge of atmospheric concentrations including the variability in time and space, and d) appropriate numerical models as a basis to incorporate the corresponding microphysical parameterizations.

Owing to these aspects, we want to quantify the potential sensitivities of clouds to a number of assumptions. These assumptions can comprise the type of IN, their atmospheric concentration, various freezing mechanisms as well as the complexity of parameterizations used to describe the freezing process in models. Here we investigate two cloud types: Arctic mixed-phase stratocumulus and isolated deep convective cells. Assuming that mineral dust particles constitute the dominant type of atmospheric IN, the sensitivity of cloud properties is investigated in a wide range of atmospherically-relevant particle concentrations.

A novel framework of immersion freezing is implemented in the model in order to compare different degrees of parameterization complexity. While often in models each potential ice nucleating particle is attributed to one cloud droplet, here we consider the collisions of droplets and subsequent accumulation of IN in rain-sized drops. This enables the simulation of the direct influence of IN on precipitation formation. We show that particularly in deep convection, the aerosol-dependent freezing of rain-sized drops makes important contributions to the simulated aerosol effects. Extensive analysis of microphysical process budgets yields a comprehensive characterization of the sensitivities of precipitation and radiation to ice nuclei perturbations.

Furthermore, a new modeling method is implemented (“perturbed microphysics”) to extract microphysical sensitivities while suppressing the feedback on the atmospheric circulation. Based on this, we conclude that microphysics-dynamics feedbacks do have a modulating character, but the primary effects of IN perturbations in clouds can be well-described by the sole action of microphysical feedbacks. While here we focus on idealized simulations of isolated clouds, it may be interesting whether this holds for cloud systems on larger scales.

For both precipitation and radiative sensitivities of deep convective clouds to IN perturbations, we find both positive and negative signs, depending on environmental conditions as well as IN background concentrations. Although this implies the need for a case-specific consideration of single-cloud sensitivities to IN perturbations, the improved understanding of cloud microphysics on the process level may ultimately lead to more accurate predictions of cloud properties and precipitation forecasts by paying attention to the relevant mechanisms in large-scale models.

# Contents

# 1. Introduction

Predictions of "sun or rain" – equivalent to cloud occurrence and cloud properties – concern both civil life and scientific research: Daily weather forecasts, global climate projections, and safety-related predictions of severe weather and conditions relevant to aviation. Therefore, we want to be capable of carrying out numerical simulations with a high reliability of the simulated cloud properties.

Along with the atmospheric environment which provides the thermodynamic conditions for clouds to form, integral cloud properties – geometric extent, altitude, integrated amounts of condensate or cloud reflectivity – are largely determined by cloud microphysical properties such as mass, number, phase, particle sizes and shapes of the cloud condensate (Lamb and Verlinde, 2011). These characteristics influence the further evolution in time by determining the efficiencies of several microphysical processes: growth and evaporation of liquid and frozen particles, particle collisions, and gravitational settling. Furthermore, radiative properties result from cloud particle number and size attributes, but also particle habit and surface characteristics (Yi et al., 2013). Depending on the type of cloud, the dominant hydrometeors to determine the radiative fluxes can be both cloud droplets and cloud ice.

## 1.1. Clouds and aerosols

A basic role to affect cloud microphysical properties is attributed to aerosols as ubiquitous particulate constituents of the atmosphere. In liquid-containing clouds, by acting as cloud condensation nuclei (CCN), these particles promote the process of initial condensation and cloud droplet formation. Hence, the droplet size distribution is a result of aerosol number concentration, particle sizes, and chemical composition (Petters and Kreidenweis, 2007).

Figure 1.1 illustrates the influence of aerosols at sub-zero temperatures: Supercooled droplets freeze without the influence of aerosol particles only in a narrow temperature range around $-36\,^{\circ}\mathrm{C}$ (homogeneous freezing). In contrast, heterogeneous freezing of droplets at warmer sub-zero temperatures is mediated by a subset of aerosol particles (ice nuclei, IN). With IN being immersed within droplets, the process of immersion freezing may trigger the droplet to freeze. When exposed to air which is supersaturated with respect to ice, dry aerosol particles may form ice from the vapor phase (deposition nucleation). The latter is expected to occur predominantly in the colder, ice-only containing cirrus regime. Depending on the abundance of deposition IN and the dynamical situation in the cirrus regime (Barahona and Nenes, 2011), either heterogeneous ice formation or homogeneous freezing of aqueous solution droplets is dominant, the latter being active only above a critical supersaturation (Koop et al., 2000, black dashed line in Fig. 1.1). Both mechanisms promote the formation of in-situ origin cirrus clouds (Luebke et al., 2016). Further pathways of heterogeneous ice formation include a potentially important recycling of IN including pre-activation to enhance the ability of IN to form ice (Wagner et al., 2016). Also contact freezing may influence clouds by causing droplets to freeze upon collision with dry (interstitial) aerosols,

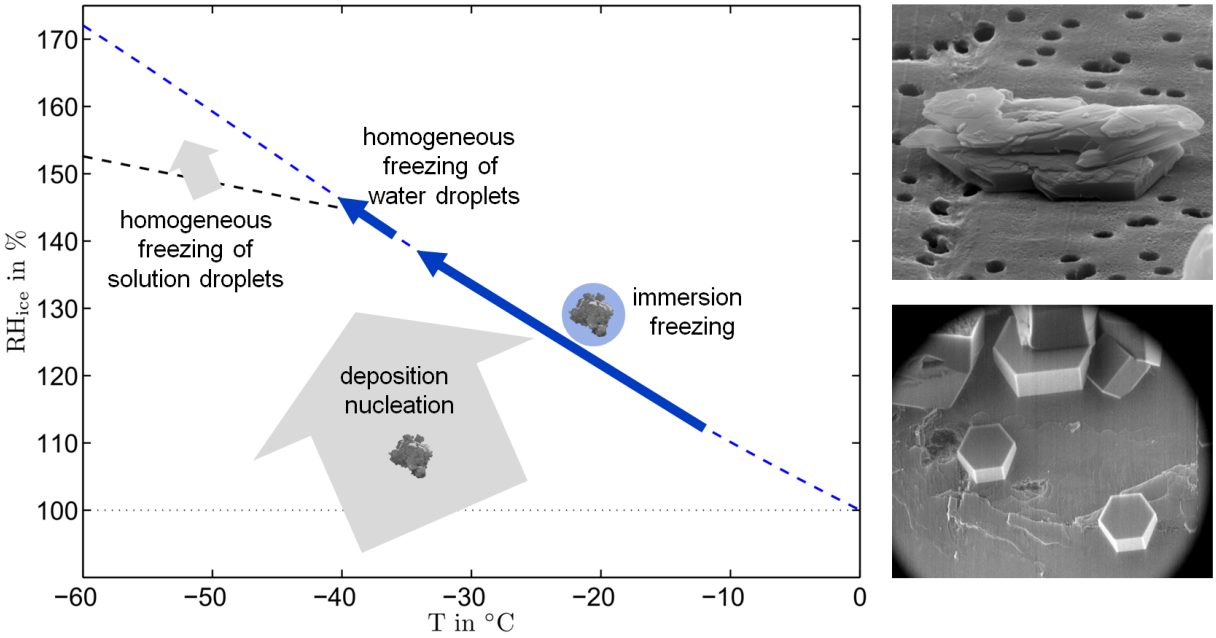


Fig. 1.1.: Left: Sketch of atmospheric ice nucleation processes, illustrated in the space of temperature and saturation with respect to ice ($RH_{ice}$). The blue dashed line indicates water saturation, and arrows indicate the thermodynamical trajectories associated with ice formation (see text for details). Mechanisms not contained in our model simulations (section 2.2) are excluded from the figure. Right: Pictures of a mineral dust particle (Kaolinite; top) with a size on the order of 1 µm, and ice crystals formed by deposition nucleation on a mineral surface with crystal sizes on the order of 100 µm (bottom), obtained from environmental scanning electron microscopy (courtesy of A. Kiselev).

but the description of aerosol-dependence has proven challenging (Ladino Moreno et al., 2013), and was enabled only recently (Hoffmann et al., 2013).

The particles relevant to act as ice nuclei have manifold origins and physicochemical properties, and a comprehensive description is among the today's scientific effort (Hoose and Möhler, 2012; Knopf et al., 2014). The current knowledge leads us to the conclusion that mineral dust – e.g., originating from deserts and lifted into the cloud regimes – is among the most important particle species to contribute to heterogeneous ice formation (e.g., Boose et al., 2016; Cziczo et al., 2013; Klein et al., 2010), relevant to both immersion freezing and deposition nucleation (Ullrich et al., 2016; Diehl and Mitra, 2015).

## 1.2. Ice nucleation in atmospheric models

The relations between aerosol particles and resulting cloud properties pose challenges to the representation in atmospheric models, since the relevant mechanisms occur on the scales of molecules (nucleation) to millimeters (cloud condensate), while the resolved processes in numerical models range from tens of meters (large-eddy simulations) to tens of kilometers (global simulations). Therefore, appropriate parameterizations are necessary to calculate the influence of subgrid-scale processes on grid-scale properties such as bulk ice contents within clouds. Bauer et al. (2015) summarize that the improved representation of physics was among the key features to enhance the skill of numerical weather prediction, and will

remain a key in future. In their evaluation of microphysical uncertainties in simulations of convective clouds, Johnson et al. (2015) point out the specific role of drop freezing. In climate simulations, substantial uncertainty arises from the model representation of aerosol-cloud-interactions, and from the effects of ice nucleation in particular (Boucher et al., 2013), while both radiative budgets and global precipitation patterns are quantities of high interest in future climate scenarios. Operational weather forecasts slowly move towards explicit cloud microphysical representation (Chosson et al., 2014), and potential benefits due to the representation of ice nucleation are among the primary motivations (Hong and Dudhia, 2012). Therefore, not only the quality of daily weather forecasts will depend on the assumptions incorporated in the cloud parameterization schemes. Also industries such as agriculture rely on the predicted precipitation for the sake of process optimization. Furthermore, warnings of severe weather conditions profit from improved predictions of liquid and ice precipitation, and the presence of large supercooled drops in clouds is relevant to aviation security because of potential aircraft icing (Thompson et al., 1997; Politovich, 2015). Obviously, the latter is directly influenced by the simulated behavior of freezing drops, and rain-sized drops in particular.

During past decades, attempts have been made to understand heterogeneous ice nucleation as such. A basic question is whether to interpret the immersion freezing mechanism analogous to the homogeneous freezing (stochastic hypothesis), appreciating the fact that nucleation is an inherently stochastic phenomenon. Alternatively, to capture the variability of ice nucleating particles in an approximated way, we may attribute the freezing event to the properties of specific features located on the aerosol which would induce the freezing instantaneously (i.e., non-stochastically), given the appropriate thermodynamical conditions, i.e., temperature (singular hypothesis; Vali and Stansbury, 1966). Although the stochastic component is usually found to be measurable, it is concluded to be of secondary importance, with the sole dependence on temperature yielding an appropriate reproducibility of measured freezing rates in models (Vali, 1994; Welti et al., 2012; Vali, 2014). A quantitative description of particle-specific ice nucleation efficiencies has been established only during the last years (Hoose and Möhler, 2012; Vali, 2014), providing the possibility to estimate the relative importances of different mechanisms and particle species.

The combined efforts of lab studies, theoretical considerations and application in numerical cloud models will show how to describe primary ice formation by parameterizations in a convenient way. An important question is therefore about the minimum model complexity needed for the appropriate process description, depending on whether or not the simulated cloud properties are sensitive to the specific parameterization approaches. In this work, an important aspect is the handling of freezing rain drops in models: Often in studies of aerosol-dependent immersion freezing, the total amount of potential ice nuclei is attributed to cloud droplets, while larger drops ("rain") may still freeze independent of aerosol particles – a treatment which has the potential to underestimate the effect of ice nuclei substantially (Khain et al., 2015). Here we drop this simplification by accounting for the redistribution of aerosol particles between small and large drops during droplet collisions.

The computational costs which arise from a detailed handling of cloud microphysics including the aerosol-dependent effect of ice nucleation become increasingly affordable, enabling three-dimensional high-resolution simulations on the scale of single clouds (Khain et al., 2015). This allows us to test basic expectations of microphysical consequences which result from the presence of ice nucleating particles in the atmosphere. Climatologically, the amounts and types of ice nuclei present in the atmosphere are

rather uncertain (Hande et al., 2015), and can be highly variable in time and space (Mason et al., 2016), e.g., during events of Saharan dust outbreaks (Seifert et al., 2010). Since the physical mechanisms involved in aerosol effects on clouds are often poorly understood (Boucher et al., 2013), the need for an enhanced process level understanding leads us to the question:

**What are the consequences of perturbed ice nuclei concentrations in the atmosphere?**

"Perturbation" refers to an enhanced particle content relative to some base state background concentration. In this work, we will focus on the effect of mineral dust particles as ice nuclei in the immersion and deposition mode. Any "consequences" will result from perturbations on the microphysical scale, will thus modify integral cloud properties, and are also expected to influence the atmospheric dynamics both within the clouds and on larger scales (Grabowski and Petch, 2009).

## 1.3. Expected cloud responses to ice nuclei perturbations

### 1.3.1. Microphysical effects

A widely-accepted expectation as a result of enhanced ice nuclei content is the enhanced efficiency of cloud glaciation (e.g., Lohmann and Feichter, 2005; Pinsky et al., 2014), i.e., supercooled liquid water in the mixed-phase regime is converted to ice on a shorter time scale in scenarios of perturbed IN concentrations (Korolev and Isaac, 2003). Based on microphysical considerations, there are several reasons:

1. A larger amount of potential IN present in the droplets will increase the overall droplet freezing probability, resulting in the enhanced depletion of liquid water. The freezing process itself may be interpreted as a trigger for a number of further consequences:
2. The increased amount of primarily formed ice is expected to deplete more liquid mass via the vapor phase, known as the Wegener-Bergeron-Findeisen (WBF) process (Korolev, 2007, and references therein). When coexistent in the same environment, both liquid water and ice will influence the adjacent vapor pressure according to their individual saturation vapor pressures, that of ice being smaller than that of liquid water (Pruppacher and Klett, 1997). The resulting gradient of water vapor concentration will therefore promote a continuous diffusion flux of vapor from liquid to ice.
3. Collisions among liquid and ice particles (riming) convert liquid mass to ice mass. In fact, it is ambiguous whether or not this type of conversion will be enhanced because a) the higher abundance of primarily formed ice may tend to increase the rates of riming, and b) enhanced liquid depletion during the freezing process tends to decrease the probability of liquid-ice-collisions. Since we have multiple types of liquid and solid particles with different properties, it is likely to find both increased and decreased collision rates for different particle classes and in different regimes of the cloud.

To sum up our expectations of cloud glaciation, both the freezing process and WBF process would act to glaciate the cloud more efficiently. For the riming growth of several types of ice particles, the tendencies may be case-specific.

These interdependencies have some implications for the precipitation formation in clouds. For mixed-phase clouds, we expect the majority of surface rain to originate from the ice phase (Lamb and Verlinde, 2011), the latter being converted to rain by melting during sedimentation. Therefore, we need to identify a) the dominant particle types responsible for surface rain, and b) the dominant growth mechanism of these particles, either through vapor depositional growth, or by accretion of mass during collisions. Such relations strongly depend the specific cloud regime:

For example, we can think of a mixed-phase stratocumulus layer, with a low efficiency of particle collisions, and a small number of ice particles whose growth is dominated by vapor deposition only (Ovchinnikov et al., 2011). With perturbed IN concentrations, it seems very likely to find enhanced ice growth and liquid depletion as a result of the WBF mechanism (Paukert and Hoose, 2014a), resulting in enhanced ice precipitation.

A more complex scenario is found in deep convective clouds, where all types of particles and associated growth mechanisms may coexist. In addition to a small amount of rain drops formed by collision-coalescence, the downward-flux of rain drops is dominated by the melting of graupel and hail particles (Lamb and Verlinde, 2011). Although it may be expected that in the presence of large particles riming is the most pronounced source for further growth (Lamb and Verlinde, 2011), the sign of surface rain change in a perturbed IN scenario remains dubious. It is also unclear whether the tendencies of both graupel and hail would act in the same direction, or counteract each other. Besides the riming of pre-existing graupel and hail particles, further effects such as conversion of cloud ice and snow to graupel or hail particles, will modulate the amount of melting particles in a perturbed IN scenario.

Early numerical studies of precipitation enhancement indicate the existence optimal ice crystal concentrations to form precipitation most efficiently (Rokicki and Young, 1978): By overseeding the cloud with ice nuclei, liquid water depletion was found too efficient, thus decreasing the efficiency of particle growth and leaving behind numerous but non-precipitating particles. The cloud regimes with the highest sensitivity to ice nuclei perturbations were characterized in terms of both cloud base temperature and convective strength.

In summary, our ability to specify a-priory expectations of surface rain changes as a result of IN perturbations is limited whenever riming is the dominant mechanism to form rain. Therefore, case-specific investigations with a detailed microphysical representation are necessary to analyze the underlying chain of processes.

### 1.3.2. Radiative effects

On a global average, the presence of clouds acts to cool the earth system compared to a non-cloudy state because the energy loss due to reflection of solar radiation is compensated only in part by the trapping of longwave radiation emitted from the surface (Lohmann and Feichter, 2005).

Low-level clouds with a sensitivity to ice nuclei are often found in the Arctic (Morrison et al., 2012). At high latitudes, an important effect on the local climate is the longwave forcing at the surface which is sensitive to the vertically integrated liquid water content (Shupe and Intrieri, 2004). In a perturbed scenario with the dominating WBF mechanism, cloud ice mass and number increases, while liquid mass is lost (Paukert and Hoose, 2014a). The overall expectation is therefore to find optically thinner clouds in

environments of more IN, with larger sensitivities in cases of thin clouds (Garrett and Zhao, 2006; Shupe and Intrieri, 2004).

High clouds make more pronounced contributions to the trapping of longwave radiation because their cold cloud tops emit less efficiently into space. The shortwave contribution depends on the cloud thickness, and similar to the Twomey effect of liquid clouds (Twomey, 1977), more numerous ice particles with smaller effective radii (Hansen and Travis, 1974) would result in an enhanced reflectivity (Lohmann and Feichter, 2005). In case of deep convection, cloud radiative properties are determined by the properties of small cloud ice particles in the convective outflow. Therefore, we are interested the primary mechanism of anvil ice formation, and its response to a perturbed concentration of IN.

In deep convective systems we expect the ice crystals contained within the convective outflow to originate from freezing droplets (Krämer et al., 2016; Järvinen et al., 2016). With a high background concentration of IN, we can think of a dominant immersion freezing in the mixed-phase regime of the convective core. With less IN present the homogeneous freezing in upper levels can be dominant. The latter case adds additional complexity because there is only an indirect link between homogeneous droplet freezing and IN perturbations: On the one hand, we can think of enhanced droplet depletion by enhanced riming, resulting from a more efficient immersion freezing. On the other hand, within the levels of homogeneous freezing, there is a strong interaction through the vapor phase between recently formed ice and the remaining droplets (Phillips et al., 2007). Because of the strict dependence of homogeneous freezing probabilities on droplet volumes (Pruppacher and Klett, 1997), the larger droplets freeze first, and the smaller ones lag behind. Thus, within a short interval of time, the remaining (smallest) droplets tend to evaporate as a result of the WBF process. Although the droplet evaporation can be suppresed in high-speed updrafts (Korolev, 2007), the suddenly strongly increased amount of homogeneously frozen larger droplet can outperform the effect of vertical velocities under these conditions, in addition to the low-speed updraft regions which favor the ice-induced droplet evaporation. Finally, a subset of the smallest droplets is able to evaporate before freezing can take place, which provides an efficient mechanism to reduce the cloud ice number densities in the convective outflow (Phillips et al., 2007). With enhanced IN contents, the question is then whether WBF-based droplet depletion in the homogeneous freezing regime would be more or less efficient.

The above discussion included the effect of anvil ice number only. The second contributor to perturbed radiative fluxes is the mass concentration of anvil ice, for which we can expect an enhanced relative contribution by larger drops, while numbers are likely dominated by the smaller cloud droplets. Therefore, we may ask for the relative contributions of cloud and small rain drops to anvil ice mass densities, and their corresponding determinants in the mixed-phase updraft regime. From these considerations, the roles of vapor depositional growth, riming, and droplets remaining in the homogeneous freezing regime are a-priori unknown.

### 1.3.3. Cloud-dynamical effects

The release of latent heat during phase transitions provides a direct link between cloud microphysics and the atmospheric circulation. E.g., condensation and freezing within a convective updraft will further destabilize the atmospheric stratification, and thus enhance the updraft speed. Also the evaporation of cloud condensate within downdrafts and corresponding cooling will tend to strengthen the vertical

dynamics. Since the cloud itself critically depends on the structure of vertical motions, these relations provide a feedback which is modulated by the atmospheric aerosol content.

A prominent example of aerosol effects on cloud dynamics (Khain et al., 2005) is the invigoration hypothesis, with deeper convective clouds resulting from increased amounts of CCN (Rosenfeld et al., 2008; Altaratz et al., 2014). Assuming that more numerous but smaller cloud droplets would form precipitation via drop-drop-collisions less efficiently at warm temperatures, more liquid mass would reach the mixed-phase regime to release latent heat by freezing, thus increase updraft speeds compared to a clean environment. Another pathway to increase buoyancy is given by an enhanced total droplet surface in a polluted environment, depleting the supersaturation more efficiently within convective updrafts, thus yielding enhanced updraft speeds by increased condensation rates (e.g., Dagan et al., 2015). Invigoration may not occur in all situations – for example, Fan et al. (2009) find both enhancement or suppression of convective strength with perturbed aerosol concentrations, depending on the vertical wind shear as a regulator of entrainment and supersaturation.

While the above-named mechanisms are related to the enhanced concentrations of CCN, we can think of similar interdependencies under conditions of perturbed IN concentrations to induce perturbed cloud dynamics (e.g., van den Heever et al., 2006).

1. A simple relation might result from the enhanced glaciation in the mixed-phase regime of the convective core, yielding enhanced updraft speeds driven by the mid-levels. However, with all remaining liquid mass freezing homogeneously at latest, the enhanced glaciation corresponds to a vertical shift of the heating distribution, rather than enhanced overall heating.
2. A larger/smaller ice crystal total surface in the ice-only regime of the convective updraft may remove supersaturation more/less efficiently, thereby modulating the latent heat release.
3. We can expect perturbed properties of precipitating ice particles, modified evaporation efficiencies and corresponding water vapor perturbations in the sedimentation regimes, which have the potential to feed back on the convective core and buoyancy production by entrainment. As shown by Fan et al. (2009), such effects may be much dependent on the vertical wind shear and relative humidity profiles.

In addition to the release of latent heat, radiative cooling or heating couples cloud dynamics to microphysics. Dominant contributions are primarily made by cloud-top radiative cooling, i.e., the emission of longwave radiation, which is higher in magnitude than radiative heating by shortwave radiation (Stephens, 1978). This is particularly important for the vertical dynamics induced in stratocumulus cloud layers, in which the cloud-top is destabilized and turbulence is induced. The strength of vertical motions created by cloud-top radiative cooling depends mainly on the liquid water content and its vertical distribution (e.g., Stephens, 1978).

To address the question of cloud-dynamical feedbacks, a novel approach was implemented in the model, called “perturbed microphysics”. It enables us to separate cloud microphysical feedbacks from cloud-dynamical feedbacks, which we will regard as two distinct contributions.

## 1.4. Case studies and research questions

Two types of clouds will be the subject of investigation in this work: The stratiform boundary layer cloud deck as observed in the Arctic, and the idealized setup of deep convection are introduced in the following.

### 1.4.1. Arctic stratocumulus

Only two decades ago, the Arctic region received increasing scientific attention, attributed to the outstanding role in the climate system (e.g., Curry et al., 1996). The underlying processes between the surface properties (sea or land), atmosphere and radiation are distinct from lower latitudes. In particular, the high surface albedo, originating from the cover ob sea ice or snow, offers the possibility for strong radiative feedbacks between surface properties and overlying clouds. A further link between surface and clouds is given by the fluxes of heat and moisture, which are in turn sensitive to the coverage by ice and snow. These mechanisms, in addition to cloud-related uncertainties and the dependencies on the mechanisms of droplet freezing (e.g., de Boer et al., 2010) render the representation of Arctic climate in models challenging. The reduction of uncertainties related to Arctic cloud glaciation in climate models was shown to make significant improvements (Klaus et al., 2016).

A number of field campaigns have been carried out to characterize the role of Arctic clouds. During the Indirect and Semi-Direct Aerosol Campaign (ISDAC), ground-based and in-situ measurements were taken in the vicinity of Barrow, Alaska in April 2008 (McFarquhar et al., 2011) to characterize aerosol-cloud-interactions. The transition between winter and summer time provides particularly high chances to find single-layer mixed-phase cloud decks on top of the stable boundary layer (Curry et al., 1996). In the presence of single-layer clouds, the clear-structured atmosphere is beneficial for the investigation of basic dependencies (Klein et al., 2009), while multi-layered clouds are often found during summer, resulting in a higher degree of complexity (Morrison et al., 2009).

Here we focus on Flight 31 of the ISDAC campaign (Fan et al., 2011; Ovchinnikov et al., 2011, 2014; Yang et al., 2013; Paukert and Hoose, 2014a) in order to quantify the feedback between cloud microphysics perturbations and cloud dynamics: With perturbed IN concentrations, we expect weakened vertical motions (i.e., boundary layer turbulence) as a result of enhanced liquid water depletion and decreased cloud-top radiative cooling, while the turbulent motions will feed back on cloud processes such as condensation, ice depositional growth and the vertical transport of potential ice nuclei into the cloud layer. Because these feedbacks are expected to be particularly strong for this type of cloud (Morrison et al., 2012), we seek to answer the questions:

1. **What is the sole microphysical contribution of IN perturbations to the resulting liquid water depletion?**
2. **How much is the microphysical effect enhanced by the coupling to cloud dynamics?**

### 1.4.2. Deep convection

On a global annual average, Cumulonimbus clouds cover the sky to an extent of 4% over land and 6% over sea (Warren et al., 2007). Isolated convective cells can be classified according to their dynamical structure and lifetime, largely determined by vertical wind shear properties and static stability of the environment. The three major categories are summarized in the following, based on the descriptions of Houze (1993):

Single cells are the most common type of convective clouds, with life times on the order of one hour. With a weak environmental vertical wind shear, large precipitating particles fall into the convective core, thus counteracting the vertical dynamics. Furthermore, evaporating precipitation in the lower atmosphere creates a pool of cold air, disrupting the continuous transport of warm, moist air into the convective updraft at cloud base, thus shutting off the primary source of potential energy.

Multicells consist of a group of single cells – either as aggregates of cells in various stages of development at the same time, or as a sequence of multiple single cells that develop one after another. Follow-up cells are initiated by the lifting associated with precipitation-induced cold pools. These may be regarded as gravity currents (Simpson, 1997), slipping under the warmer boundary layer air mass.

Supercells are long-lasting systems with quasi-stationary updrafts. The lifetime of several hours is enabled by the presence of a pronounced vertical wind shear whose rotational energy contributes to the rotating cloud dynamics, and to the vertical acceleration via the associated pressure fields: The vertical shear of the environmental wind corresponds to horizontal vorticity. The lifting associated with the convective updraft converts horizontal vorticity into vertical vorticity. The two resulting vertical vortices create dynamically induced pressure perturbations within each of the vortices, and the initial storm splitting is triggered by the two pressure minima located within the vortices, coinciding with the outer boundaries of the updraft. The vertical gradients of the pressure minima contribute to drive the convective acceleration, and the updraft cores detach from each other with time. A symmetric splitting is expected in the presence of unidirectional wind shear. With directional shear – e.g., a clockwise-turning hodograph with increasing altitude – asymmetric behavior becomes evident, and the right-moving part is often observed to be dominant (e.g., Noppel et al., 2010). Although the supercell-type of convection is less common, the potential damage to humans is particularly high due to the risk of tornadoes and hail precipitation.

Further convective phenomena in the atmosphere involve the spatial organization of multiple cells on larger scales. Lines of convective cells (squall line) can consist of ordinary convective cells or – less commonly – supercells. These lines represent one type of mesoscale convective systems (MCS), the latter defined as “a cloud system that occurs in connection with an ensemble of thunderstorms and produces a contiguous precipitation area $\approx$100 km or more in horizontal scale in at least one direction”. MCS are not part of this work, although larger cloud fields including multiple types of clouds may be particularly interesting from the cloud-dynamical (Grabowski and Petch, 2009) and climatological point of view.

Here we focus on a well-known and widely-used (e.g., Morrison and Milbrandt, 2011) idealized test case, originally introduced by Weisman and Klemp (1982) to investigate the dynamics of isolated thunderstorms. In a conditionally unstable atmosphere, convection is triggered by a warm bubble with a radius of 10 km and temperature excess of 2 K. The cloud properties result from the combination of

boundary layer water vapor content and the magnitude of the unidirectional wind shear. The setups used in this study correspond to supercells as well as short-lived cells (chapter 4).

Deep convection involves all types of cloud particle classes and corresponding microphysical interactions. This is reflected in many previous studies of aerosol-cloud-interactions which report a case-specific behavior, partly seeming to contradict each other, as reviewed by Khain (2009) for simulated effects of CCN on precipitation. A similar behavior of case-specific sensitivities to ice nuclei perturbations may be expected. Therefore, it should be kept in mind that any results emerging from this study may not be directly applicable to different types of convection found in the atmosphere – however, it will be shown that some general interdependencies of microphysical processes are relatively robust under varying environmental conditions. An important aspect is therefore to understand the underlying mechanisms, before we may be able to establish a generalized picture of cloud-type-dependent sensitivities to aerosol perturbations – both CCN and IN.

Here, we will aim to answer the following questions for the case of deep convection:

1. **What is the sign and magnitude of the sensitivities of precipitation and radiation to perturbations of mineral dust-induced ice nucleation in deep convective clouds?**
2. **How robust are the cloud sensitivities in different meteorological environments, and with varying amounts of aerosol background concentrations?**
3. **Which microphysical interdependencies dominate the sensitivities?**
4. **What is the role of rain drop immersion freezing and its aerosol-dependent model representation?**

## 1.5. Organization of subsequent chapters

Chapter 2 will introduce the model, the mechanisms represented in the microphysics scheme, and model extensions made in the frame of this work: Aerosol-dependent rain drop freezing with consideration of the drop microphysical history, deposition nucleation and the "perturbed microphysics" approach.

Chapter 3 will analyze the consequences of IN perturbations in Arctic stratocumulus clouds, with a focus on the distinct contributions of microphysical and cloud-dynamical sensitivities.

Subsequent chapters will be based on deep convection, introduced by an overview of the simulated cells (chapter 4). The impact of aerosol-dependent rain freezing – as compared to the default implementation – is presented in chapter 5. Finally, the sensitivities of precipitation and radiation to IN perturbations in different environments are analyzed (chapter 6). Some model-related uncertainty discussions are included in Appendix B.

# 2. Methods

This chapter gives an overview of the atmospheric model used in this work. In sections 2.1 and 2.2, we will introduce the COSMO model, basic numerical methods and physical parameterizations, as well as the cloud microphysical processes represented in the code. Sections 2.3 and 2.4 give a detailed description of new model implementations related to aerosol-dependent primary ice formation by immersion freezing and deposition nucleation. Section 2.5 presents the "Perturbed Microphysics" (PM) method for the analysis of aerosol effects on cloud properties.

## 2.1. COSMO model

Our model is based on the non-hydrostatic COSMO model (Baldauf et al., 2011) which is the operational weather forecast model of the German weather service (DWD). The approximated Navier-Stokes equations are solved on an Arakawa C-grid with a terrain-following vertical coordinate. In the setup used in this work, time integration is based on a third-order Runge-Kutta scheme. The third-order accuracy horizontal advection scheme is combined with implicit vertical advection. Moisture variables and any additional tracers relevant for cloud microphysics are advected using a Bott second-order finite volume scheme (Bott, 1989).

In the convection-permitting setup, the spatial and temporal resolution in combination with the compressible model formulation allows vertical dynamics to develop based on the atmospheric stratification. To resolve in-cloud motions and turbulent mixing of aerosols and cloud particles directly, the model is used with sub-kilometer resolutions, i.e., 100 m for Arctic stratocumulus clouds (chapter 3) and 500 m for deep convection (chapter 4). The model time steps for the two cases are 2 s and 3 s, respectively.

The model can be applied in two basic modes. In real case-based simulations on a limited-area domain (e.g., operational weather forecasts), the initial conditions are given by three-dimensional fields of the atmospheric state and lateral boundary conditions vary in time and space. In this work, we use idealized simulations, initialized with horizontally homogeneous fields of temperature, wind vectors and humidity as a function of altitude. The lateral boundary conditions are periodic in both directions, i.e., northern/southern and western/eastern boundaries interact with each other. For the case of Arctic stratocumulus (chapter 3), weak nudging towards a reference state is applied (Paukert and Hoose, 2014a).

The aerosol physics module ART is available for COSMO in order to explicitly account for the emission, transport, and chemical processing of several aerosol species (Vogel et al., 2009). Although not used used for the calculation of aerosol physics in the frame of this work, we rely on parts of the technical infrastructure of the existing implementation for use in our extended cloud microphysical calculations (chapter 2).

With the sub-kilometer resolutions used here, a prognostic three-dimensional turbulence scheme is applied to parameterize subgrid turbulent diffusion of heat, mass and momentum. Different from the coarser resolution setups (Baldauf et al., 2011; Raschendorfer, 2001), we make use of a Prandtl-Kolmogorov

approach and an extension of the Smagorinsky (1963) model to calculate the diffusion coefficients (Herzog et al., 2002a,b).

Radiative calculations are based on the two-stream radiative transfer model of (Ritter and Geleyn, 1992). The radiative fluxes are calculated columnwise in two directions, i.e., upward and downward. With the plane-parallel approximation, the problem of three-dimensional radiances is reduced to one-dimensional columns, meaning that no radiative interaction between neighboring columns is present. The wavelength spectrum is divided into 8 bands, and the "fast exponential sum fitting technique" according to (Ritter and Geleyn, 1992) ensures high accuracy in spite of the limited number of spectral bands. A final roundup yields the net fluxes (positive downward) of both shortwave and longwave radiation, and the vertical flux divergences result in the local heating rates to provide the link between radiation and atmospheric stability and dynamics.

The interaction of clouds and radiation depends on the grid-scale properties of vapor, cloud droplets and cloud ice. By default, no explicit dependence on cloud particle number concentrations is given. Instead, we use a recent implementation of Dr. Uli Blahak to account for the effective radii of cloud droplets and cloud ice as a function of both mass and number concentrations. Cloud droplet radiative properties are based on Hu and Stamnes (1993), and cloud ice properties are based on Fu (1996) and Fu et al. (1998). These parameterizations yield the wavelength- and cloud particle size-dependent extinction coefficients for the subsequent determination of grid box optical depths and radiative fluxes in the vertical column.

Simulated cloud properties are based on the two-moment cloud microphysics module of Seifert and Beheng (2006, SB06 hereafter) which predicts number and mass densities of six cloud particle classes (section 2.2). Parameterizations of shallow and deep convection are not used in this work.

## 2.2. Cloud microphysics

The two-moment cloud microphysics scheme based on SB06 is used to represent both mass and number densities of six cloud particle classes, i.e., cloud droplets ($D < 80\,\mu$m), rain ($D > 80\,\mu$m), cloud ice, snow, graupel and hail. Besides transport by grid-scale advection and turbulent diffusion, the time evolution of simulated cloud properties is given by the microphysical budgeting summarized below. With the particle size dependencies of any microphysical processes, the rates of mass and number changes result from the integration over the particle size distributions, defined by generalized gamma distributions with respect to particle mass x.

The basic process groups of microphysical mechanisms are summarized in the following. Any details can be found in Seifert and Beheng (2006), Seifert (2002) and the references cited in the following.

### Droplet activation

Activation of cloud droplets is based on lookup-tables following Segal and Khain (2006). Given a grid-scale relative humidity higher than 100%, the vertical velocity in combination with pre-defined aerosol properties (number, mode diameter, standard deviation, soluble fraction) yield the total number of activated CCN. The rate of activation results from the difference of parameterized CCN and pre-existing activated aerosols, the latter being identified with the local number of cloud droplets.

Another option for cloud droplet activation is given by the Twomey approach as described in SB06. Instead of the vertical velocity dependence, the number of activated CCN results from a power law which is a function of grid-scale supersaturation. The differences resulting from the choice of CCN parameterization are summarized in section B.2.

### Ice nucleation

Primary ice formation is represented by a number of different mechanisms: In liquid-containing regimes, cloud ice may be initiated by freezing cloud droplets (homogeneous and heterogeneous freezing) and freezing rain drops ($D < 500\,\mu$m, homogeneous and heterogeneous). In the cirrus regime, cloud ice can result from deposition nucleation (Ullrich et al., 2016, section 2.4) and homogeneous freezing of solution droplets (Kärcher et al., 2006).

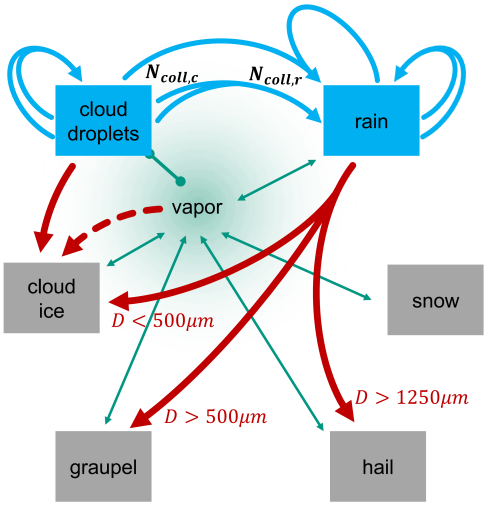


Fig. 2.1.: Sketch of primary ice formation (red arrows) by droplet freezing and from the vapor phase. For heterogeneous droplet freezing, we consider the redistribution of potential ice nuclei between cloud droplets and rain drops ($N_{coll,c/r}$, section 2.3). The concentration of water vapor is coupled to saturation adjustment in the presence of cloud droplets, while the exchange of vapor with larger particles is calculated explicitly (green arrows).

Homogeneous droplet freezing is based on the nucleation rates of Jeffery and Austin (1997) with a fit based on Cotton and Field (2002). By default, only cloud droplets are considered explicitly, while rain drops freeze very efficiently by the heterogeneous rain freezing implementation following Bigg (1953) and Barklie and Gokhale (1959). In this work, we replace the Bigg-based rain freezing with a new approach and explicit homogeneous freezing is also calculated for rain (sections 2.3, 5.2).

Heterogeneous droplet freezing by immersion freezing is the specific topic of this work. The aerosol-dependence of cloud droplet freezing including ice nuclei depletion is implemented as described in Paukert and Hoose (2014a). In this work, further extensions were implemented to account for the redistribution of aerosol particles between cloud droplets and rain during droplet collisions, as described in section 2.3. The aerosol-dependent parameterization relies on the singular hypothesis (section 1.2) to calculate the number of "activated sites" per aerosol surface area as a function of temperature, with the "active surface site density" of mineral dust according to Niemand et al. (2012). Freezing rain drops not

only contributes to cloud ice formation ($D < 500\,\mu m$), but also to the initiation of graupel ($D > 500\,\mu m$) and hail ($D > 1250\,\mu m$) according to Blahak (2008).

#### Growth from the vapor phase and evaporation

Condensational growth and evaporation of cloud droplets is given by saturation adjustment. The adjustment of relative humidity to 100% in the presence of cloud droplets is performed in the very end of a time step. This means that any remaining supersaturation (with respect to water) after all microphysical calculations is converted to cloud water mass, and subsaturation results in a loss of cloud water mass.

Evaporating droplet mass does not affect the number density in the majority of situations, corresponding to the assumption of homogeneous mixing (e.g., Korolev et al., 2015). Only in case that the droplet mean diameter (i.e., the diameter corresponding to the mean droplet mass) becomes smaller than 2 µm, the droplet number is adjusted in order to retain a mean size of 2 µm. As will be shown in section 6.2, this implicit influence on the number concentrations during evaporation of cloud droplets has some important implications for the number concentrations of anvil ice and radiative fluxes.

Rain drop evaporation is calculated explicitly. According to the implementation following Seifert (2008), the shape of the drop size distribution is a function of bulk properties, and the loss of drop number is calculated to better capture the evaporation efficiency below cloud base, and resulting surface precipitation.

Cloud ice, snow, graupel and hail growth by vapor deposition is calculated depending on the grid-scale supersaturation in the microphysical code. Ventilation as an effect of sedimentation is taken into account, which enhances the fluxes of water vapor. When large frozen particles fall into the melting regime ($T > 0\,^\circ C$), they are covered by a liquid shell which modifies the vapor fluxes according to the saturation vapor pressure over liquid water rather than ice. The size-dependent mass-diameter-relationships are approximated by power laws.

#### Cloud particle collisions

The collisions as parameterized in the model are manifold (Fig. 2.2) and make large contributions to the microphysical budgets (chapter 6). Any of the six classes may interact with each other, and different types of conversion may occur ($x + y \rightarrow z$), as well as ice multiplication upon riming.

Warm rain formation is parameterized following Seifert and Beheng (2001) and with extensions described in SB06, taking into account the selfcollection of cloud droplets ($c + c \rightarrow c$), autoconversion of cloud droplets ($c + c \rightarrow r$) and accretion of cloud droplets on rain ($r + c \rightarrow r$). The selfcollection of rain ($r + r \rightarrow r$) may lead to further drop growth, while breakup of large drops accounts for the instability of large drops to prevent rain from growing infinitely. Collision efficiencies are based on Pinsky et al. (2001) and coalescence efficiencies are based on Low and List (1982) and Beard and Ochs (1995).

During collisions of frozen particles (cloud ice, snow, graupel and hail), the masses of smaller particles are attributed to the class of the larger, collecting particle. Snow – which basically represents aggregates of "pristine" crystals – is initialized by aggregation of cloud ice ($i + i \rightarrow s$). The budgets of collisions involving ice particles are based on a generalized approach for "arbitrary particles" (SB06), with temperature-dependent sticking efficiencies according to Lin et al. (1983) and Cotton et al. (1986).

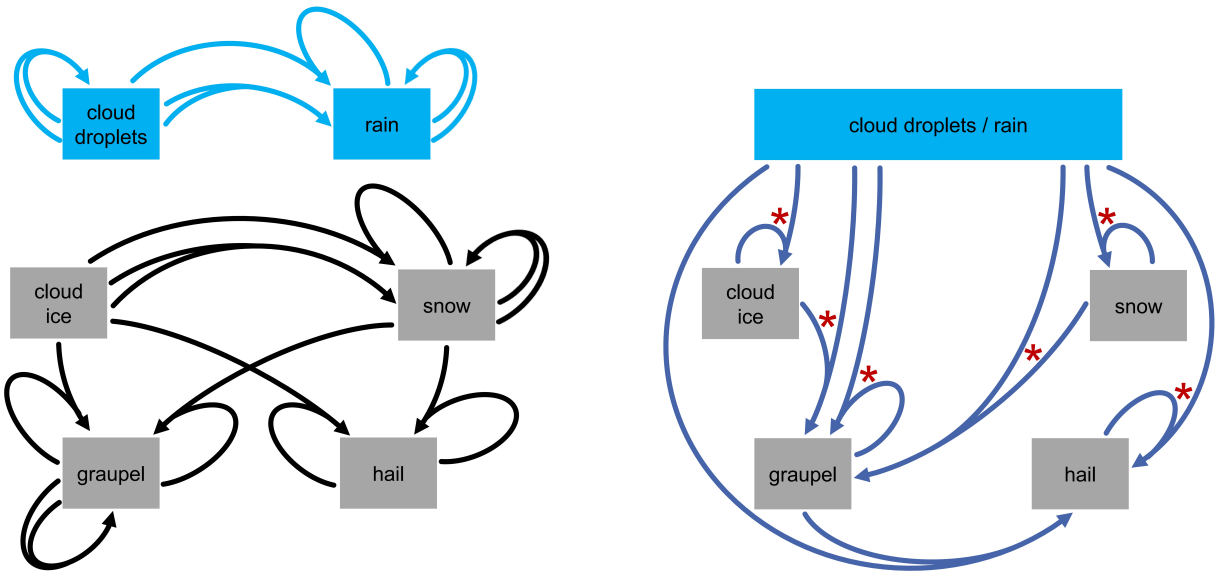


Fig. 2.2.: Sketch of particle collisions. Left: Liquid-liquid collisions (blue arrows) involve selfcollection, autoconversion and accretion. Ice-ice collisions (black arrows) involve aggregation of cloud ice to form snow, collection of cloud ice by snow, selfcollection of snow and graupel, and collection of cloud ice and snow by graupel and hail. Right: Riming of ice particles with liquid mass (blue arrows) and secondary cloud ice formation by rime splintering (red asterisks). For simplicity, cloud and rain drops are merged in the figure, while considered separately in the model calculations.

In the notation used throughout this work, "riming" indicates any kinds of collisions between liquid and frozen cloud particles (c/r + i/s/g/h). Not all possible interactions are mentioned in the following, but the dominant ones based on the analysis of chapter 6. In the simulations analyzed in this work, snow generally makes minor contributions.

Most important for the formation of surface precipitation is the riming growth of graupel and hail, i.e., the collision of pre-existing large ice particles with large supercooled drops. Besides graupel formation by freezing rain, graupel may originate from the conversion of cloud ice (and snow) during riming. This occurs when the rimed mass acts to reshape the ice particle from aspherical to spherical (Beheng, 1981). The wet growth of graupel yields hail embryos (in additon to freezing rain), i.e., under conditions of heavy graupel riming.

Low-level cloud ice numbers ($T \approx -5\,°\mathrm{C}$) can be enhanced greatly by ice multiplication following Hallett and Mossop (1974). Given the appropriate conditions, it may occur during riming of any particle classes.

### Melting

The instantaneous melting of cloud ice at $T > 0\,°\mathrm{C}$ may result in both cloud and rain drops, depending on the sizes. In contrast, snow, graupel and hail may penetrate the warm layer to some extent, depending on their melting efficiencies as a result of their local properties. In the cases analyzed in section 6.1, only hail and minor amounts of graupel sediment fast enough to reach the ground. Enhanced melting of graupel and hail may occur due to the concurrent accretion of cloud and rain water mass in the melting

regime. In this version of the code, there is no possibility to distinguish between ice-only and partly liquid particles.

#### Sedimentation

The explicit representation of sedimenting particles provides the link between in-cloud microphysics and surface precipitation formation. It is calculated for all particles except cloud droplets, owing to their small sizes. Gravitational size sorting of sedimenting particles is considered implicitly by calculating both mass and number fluxes. The size-dependent mass-speed-relationships are approximated by power laws, with consideration of the local air density.

#### Implementation

For the interpretation of the results, it may be advantageous to note the sequential order of the microphysical implementation in the model: After advection (which can be interpreted as a source or sink for supersaturation), the activation of cloud droplets and ice crystals is calculated. Subsequently, any kinds of particle-particle and particle-vapor interactions (except saturation adjustment) as well as melting are computed. Finally in the presence of cloud droplets, saturation adjustment imposes a relative humidity of $RH_w = 100\%$ on the local vapor concentration to mimic cloud droplet growth or shrinking. Subsequently, after sedimentation, the next cycle of the model time stepping begins.

### 2.3. Immersion freezing

In this work, a new approach to account for the aerosol-dependent freezing of rain drops is derived and implemented in the COSMO model. After describing the motivation, the implementation is presented in greater detail.

#### 2.3.1. Motivation

In bulk models without explicit representation of aerosol, common parameterizations of immersion freezing are based on Bigg (1953). Even with cloud droplet freezing being aerosol-dependent, this approach is the basis to account for the freezing of rain drops (see below). Based on droplet freezing experiments, the theoretical considerations of Bigg (1953) yield the possibility to calculate droplet freezing probabilities as a function of droplet volume. The rate of ice particle numbers originating from freezing rain is then

$$\frac{\partial N_{ice,r}}{\partial t} = Q_r \, b \left( e^{-a T_c} - 1 \right) \rho_w^{-1} \quad [\mathrm{m^{-3}\,s^{-1}}] \qquad [2.1]$$

with the drop mass density $Q_r$ in $\mathrm{kg\,m^{-3}}$, temperature $T_c$ in °C, $\rho_w = 1000\,\mathrm{kg\,m^{-3}}$. The parameters $a$ and $b$ are usually based on freezing experiments of collected rain water (Barklie and Gokhale, 1959; Wisner et al., 1972).

Concerning the quantification of ice nucleation activity of collected rain water, a potential problem may arise a) when significant amounts of rain mass evaporate below cloud base (i.e., with a partly evaporation of drops, the relation between water mass and aerosol mass is not conserved) and b) when the drops scavenge significant amounts of aerosol below cloud base, i.e., when falling through a polluted,

IN-containing atmospheric boundary layer ("washout", e.g., Garrett et al., 2006; Beheng and Herbert, 1986). Both effects would tend to increase the aerosol content per liquid mass in the measured rain water, although these enhancements are not related to the in-cloud conditions relevant for the parameterizations. Thus, the drops within their cloudy environment may be less polluted than measured.

Furthermore, we may ask whether to follow the "stochastic" or the "singular hypothesis" (Vali and Stansbury, 1966). With the formulation of eq. 2.1 as commonly applied in models, a drop ensemble which resides in a constant-temperature environment would be subject to constant freezing rates (and freezing may occur even during warming). Given enough time under these conditions (e.g., when low-speed updrafts balance the drop sedimentation velocity), this would result in a frozen fraction of droplets close to 1. This behavior basically represents the stochastic hypothesis which applies to homogeneous freezing, but which was shown to be incompatible with the aerosol-dependent mechanism of immersion freezing (Vali and Stansbury, 1966; Vali, 1994). In contrast, the singular hypothesis was shown to be a good approximation for heterogeneous freezing, with the stochastic component being a secondary effect (Vali, 1994; Welti et al., 2012; Vali, 2014). From the latter point of view, the freezing rate is close to zero in a constant-temperature drop environment, since the aerosol is activated in the moment of reaching its "characteristic freezing temperature" for the first time during its thermodynamical history. Consequently, with larger cooling rates (but identical local temperature), we would expect enhanced freezing rates, as more aerosols reach their characteristic freezing temperature per time interval, as confirmed by Vali and Stansbury (1966). The new method includes these dependencies explicitly (section 2.3.2).

In atmospheric models, we want to know the number and mass of freezing droplets rather than activated particles. When model studies aim to investigate ice nucleation effects with explicit aerosol dependence, often the number of activated aerosol particles is directly translated into the number of freezing cloud droplets (Khain et al., 2015). Thus, with none of the particles being attributed to rain drops, immersion freezing of rain is still parameterized as an aerosol-independent process (eq. 2.1). In clouds with low droplet collision activities and no significant warm rain formation, this is may be no caveat, but it is not clear how this very basic assumption influences the simulated aerosol effects on clouds in cases with non-negligible rain formation. Early evidence for the role of large freezing drops to initiate large ice particles, followed by riming and precipitation formation was found by Koenig (1963) and Braham (1964). Phillips et al. (2001) find a paramount influence on cloud glaciation, and Taylor et al. (2016) report significant contribtuions of drizzle and rain drop freezing to the formation of large ice.

It can be speculated whether the overall simulated ice formation is overestimated when all available aerosols are attributed to small droplets, but large drops are allowed to freeze in addition to, and independent of the aerosol-dependent parameterizations. This would imply an overestimated cloud glaciation, also because the Barklie and Gokhale (1959)-based parameters for use in eq. 2.1 yield relatively efficient drop freezing rates (see Fig. 5.6; section 5.2.1).

To date, only some spectral microphysical schemes account for the redistribution of aerosol among the cloud particle classes (e.g., Diehl and Mitra, 2015). However, these are computationally demanding, and become applicable to large three-dimensional domains only slowly, particularly when sensitivity studies involve numerous simulations.

To account for aerosol-dependent rain freezing, we need to know the aerosol content immersed in the drops which yields the surface area of immersed aerosols. A first order assumption could be that a specific rain drop consists of the mean properties of cloud droplets which have been collected, yielding

the number of CCN per liquid mass, with a certain fraction of potential ice nuclei (IN) among the CCN. Hence, a representative cloud droplet size needs to be estimated in order to calculate the number of small droplets (and corresponding CCN) contained in a rain drop. It can be expected that the representative droplet sizes are strongly dependent on the specific atmospheric situation as well as the initial droplet spectra determined by the CCN properties. Furthermore, in case of partly rain drop evaporation, the decreased mass of rain drops yields a higher concentration of CCN per drop volume (or mass), making the estimated properties of "mean collected droplets" no longer representative.

In this work, we want to overcome any a-priori assumptions. The two-moment microphysical model (SB06) is extended to track the microphysical history of rain drops explicitly. A suggestion similar to the basic ideas of this work was made by Phillips et al. (2008), but to our knowledge, no model implementation exists to date. In the following, an overview of the implementations is presented (section 2.3.2). The tracking of droplet collisions will be presented in section 2.3.3, and the freezing parameterization specifically derived for rain drops is described in section 2.3.5. Chapter 5 will present the resulting redistribution of dust between cloud and rain drops, as well as freezing rates and resulting cloud properties.

### 2.3.2. Extended immersion freezing framework

In this work, a new approach is derived and implemented in the COSMO model to overcome the potential deficiencies when rain drops ($D > 80\,\mu m$) are expected to contribute to primary ice formation significantly. An overview of the involved processes and notation is given in Fig. 2.3.

After CCN activation at cloud base, each cloud droplet contains exactly one aerosol particle. To consider the rain drop microphysical history, the collected CCN by drop-drop-collisions contained in cloud droplets ($N_{coll,c}$) and rain ($N_{coll,r}$) are tracked by accounting for selfcollection and autoconversion of cloud droplets as well as accretion on rain drops. Therefore, no a-priori assumption about the number of cloud droplets contained per rain drop is necessary. The collection rates are based on the existing implementation following Seifert and Beheng (2001) and extensions presented in later work (SB06). $N_{coll,c}$ may accumulate due to the selfcollection of cloud droplets. Conversion of cloud-immersed CCN to rain-immersed CCN is given by autoconversion and accretion. Depletion of immersed aerosols results from droplet removal mechanisms during riming, freezing and complete drop evaporation. For $N_{coll,r}$, the sedimentation of rain is considered. Both $N_{coll,c}$ and $N_{coll,r}$ are represented by tracers in the model, i.e., they are subject to grid-scale advection and turbulent diffusion.

Combining the information of CCN per drop with the fraction of ice nuclei during CCN activation at cloud base ($f_{dust,cb}$) yields the number of potential IN immersed in cloud droplets ($N_{dust,c}$) and rain droplets ($N_{dust,r}$) relevant for freezing. In contrast to cloud droplet freezing, rain may also form large precipitating ice particles, i.e., graupel ($D > 500\,\mu m$) and hail ($D > 1250\,\mu m$). The cloud droplet branch is implemented with explicit ice nuclei depletion as presented in earlier work (Paukert and Hoose, 2014a), and the rain drop branch is further discussed below.

### 2.3.3. Particle accumulation in cloud and rain drops

$N_{coll}$ can be interpreted as the number concentration of CCN incorporated into a droplet by collisions. $N_{coll}$ is defined such that it accounts only for collected CCN. Therefore, in a population of cloud droplets

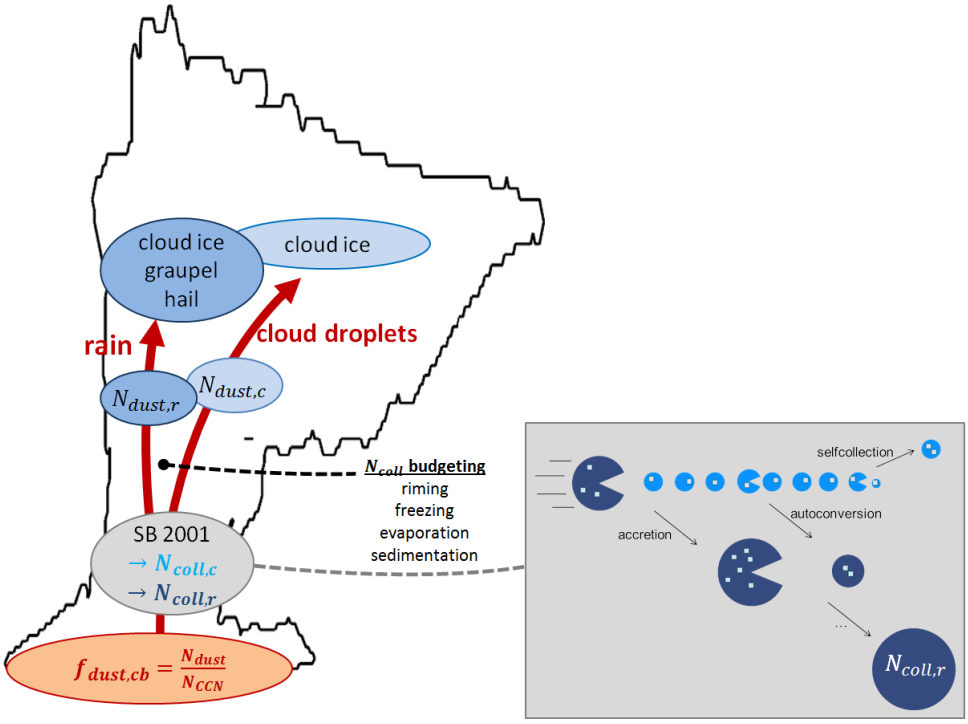


Fig. 2.3.: Sketch of the processes involved in the extended immersion freezing approach as implemented in this work. Combined with the mineral dust fraction at cloud base ($f_{dust,cb}$), the number of collected total CCN in cloud and rain drops ($N_{coll,c/r}$) yield an estimate for the dust particles immersed in both drop classes, $N_{dust,c/r}$. These are used to calculate the freezing rates of both cloud and rain drops. Consistent with the implementation of Blahak (2008), frozen rain results in cloud ice, graupel and hail particles. Droplet collisions are parameterized following Seifert and Beheng (2001, SB2001), and the number of cloud droplets at cloud base ($N_{CCN}$) results from Segal and Khain (2006).

without the presence of selfcollection $N_{coll,c} = 0$, while the presence of rain is always linked to $N_{coll,r} > 0$, i.e., $N_{coll,r} \geq 2N_r$.

$N_{coll,c}$ and $N_{coll,r}$ provide the time-integrated total number of collected drops. Thus, particularly for rain, an assumption for the distribution of $N_{coll,r}$ among the rain drop spectrum needs to be made. Since rain drops consist of the cloud droplets that were collected during collisions, the number of collected particles per single rain drop is proportional to the drop liquid mass. This assumption is taken as a basis in the following, and will be tested and largely confirmed in section 2.3.6 by analysis of detailed bin microphysical simulations with the SPECS model. Here, the proportionality of particle number to drop mass is expressed as $r_{CCN}$, defined as $\frac{N_{coll,r}}{Q_r}$ and assumed to be independent of the rain drop size. Note that with the notation used below, $r_{CCN} = \frac{1}{x_{coll,r}}$.

In the following, the budgeting of $N_{coll}$ by single processes is described. These are given by liquid-liquid collisions on the one hand, and by liquid-depleting mechanisms on the other hand.

### Selfcollection, autoconversion, accretion

With the cloud droplet number $N_c$, we define the mean number of collected particles in cloud droplets as

$$\lambda_c = \frac{N_{coll,c}}{N_c} \geq 0 \quad [2.2]$$

which is typically smaller than 0.1 in our simulations (see below). As indicated above, the cloud droplet population consists of two types of droplets, a) "pristine droplets" with one CCN per droplet, and b) a small subset of "non-pristine" droplets with more than one CCN per droplet due to selfcollection.

During selfcollection, the collision of two cloud droplets results in one cloud droplet. The accumulation of $N_{coll,c}$ is the result of collisions between both pristine and non- pristine droplets. The total number of collected CCN per time step is therefore given by

$$\mathrm{d}N_{coll,c} = -\,\mathrm{d}N_{c,sc}(\lambda_c + 1) \quad [2.3]$$

where $\mathrm{d}N_{c,sc}$ is the parameterized selfcollection rate of cloud droplets (Seifert and Beheng, 2001, eq. A.9). The sum on the right hand side corresponds to the mean number of total CCN per cloud droplet. By definition, rain properties are not affected in this case.

During autoconversion, two cloud droplets form one rain drop. To account for the collision of both pristine and non-pristine cloud droplets, the budget equations for collected CCN in cloud and rain drops are

$$\mathrm{d}N_{coll,r} = -2\ \mathrm{d}N_{c,au}(\lambda_c + 1) \quad [2.4]$$

$$\mathrm{d}N_{coll,c} = 2\ \mathrm{d}N_{c,au}(\lambda_c) \quad [2.5]$$

with the number change rate of cloud droplets due to autoconversion $\mathrm{d}N_{c,au}$ (Seifert and Beheng, 2001, eq. A.5). The rates of accretion are tracked analogously, with

$$\mathrm{d}N_{coll,r} = -\,\mathrm{d}N_{c,acc}(\lambda_c + 1) \quad [2.6]$$

$$\mathrm{d}N_{coll,c} = \mathrm{d}N_{c,acc}(\lambda_c) \quad [2.7]$$

and $\mathrm{d}N_{c,acc}$ being the number change rate of cloud droplets due to accretion (Seifert and Beheng, 2001, eq. A.6).

### Budgeting of sinks other than drop-drop collisions

Sinks for both $N_{coll,c}$ and $N_{coll,r}$ are given by processes which consume liquid droplets completely at a time, such as droplet freezing and collisions with ice particles. Again, it is necessary to make assumptions about the scaling of $N_{coll}$ depletion with the depleted drop number and mass (section 2.3.6).

Because of the different nature of the growth mechanisms of cloud and rain drops $N_{coll,c}$ and $N_{coll,r}$ are treated differently. The dominant condensational growth of cloud droplets implies that nearly all droplets contain only one particle, independent of the droplet mass. Thus, during cloud droplet removal ($dN_c$), the depletion of $N_{coll,c}$ by scales with the mean number of CCN per droplet rather than droplet mass, i.e.,

$$\mathrm{d}N_{coll,c} = (1 + \lambda_c)\ \mathrm{d}N_c \quad [2.8]$$

In contrast, rain drop growth is dominated by drop-drop-collisions, with each of the original cloud droplets corresponding to one CCN. Thus, it is assumed that the bulk content of collected particles in rain, $N_{coll,r}$, is distributed homogeneously among the rain drop mass, and the number of CCN for each drop is proportional to the drop mass, independent of the drop sizes throughout the size distribution. Therefore the assumption is that during rain drop removal, the depletion of $N_{coll,r}$ is proportional to the depleted rain mass $dQ_r$ during freezing and riming of rain drops. Thus, the CCN number density per liquid mass, $x_{coll,r}$, is conserved. We define $x_{coll,r}$ to be the mean rain mass attributed to exactly one CCN, therefore

$$x_{coll,r} = \frac{Q_r}{N_{coll,r}} \qquad [2.9]$$

The sink of $N_{coll}$ during homogeneous freezing and riming with mass changes $dQ_r$ are then

$$\mathrm{d}N_{coll,r} = \frac{\mathrm{d}Q_r}{x_{coll,r}} \qquad [2.10]$$

Heterogeneous freezing is not a sink for $N_{coll}$ because the number of IN as parameterized by eq(below) is a function of all dust particles within both unfrozen and heterogeneously frozen drops. Therefore, a strict interpretation as CCN per liquid mass is not valid any longer when heterogeneous freezing begins to influence the budget.

For evaporating rain drops, changes of drop number concentrations are explicitly parameterized (Seifert, 2008). The budget of $N_{coll,r}$ is only influenced by those drops which evaporate completely. Since the rate of evaporating rain mass contains also the incomplete evaporation of larger drops, it cannot be used here. Instead, because the change of rain drop number is defined by the number of drops becoming smaller than 80 µm (Seifert, 2008), we use the simple assumption of

$$\mathrm{d}N_{coll,r} = \frac{\mathrm{d}N_{r,eva} \cdot x_{80}}{x_{coll,r}} \qquad [2.11]$$

where $x_{80}$ is the mass corresponding to drops of $D = 80\,\mu\mathrm{m}$.

Furthermore, the budgeting of $N_{coll,r}$ accounts for the sedimentation of rain drops, where again the number change rate of $N_{coll,r}$ is a function of rain mass change rate. Sedimentation fluxes result in a transport of rain mass into the grid box at its upper boundary ( $\mathrm{d}Q_{r,in}$), and transport out of the box at its lower boundary ( $\mathrm{d}Q_{r,out}$), while $\mathrm{d}Q_{r,in}$ has the properties of $x_{coll,r}$ of the above grid box. Analogously to the rain mass change as a result of the sedimentation flux divergence, the budget of collected particles is determined by the difference of incoming and outgoing collected particles, each of which is calculated from $\mathrm{d}Q_{r,in}$ and $\mathrm{d}Q_{r,out}$.

$$\mathrm{d}N_{coll,r,in/out} = \frac{\mathrm{d}Q_{r,in/out}}{x_{coll,r,in/out}} \qquad [2.12]$$

In cloud-free regions, both $N_{coll,c}$ and $N_{coll,r}$ are reset to zero.

### 2.3.4. Cloud base fraction of potential ice nuclei

Since we are interested in the composition of aerosols immersed in the droplets, the goal is to determine the fraction of potential ice nuclei (here: mineral dust) relative to the total CCN concentration, $f_{dust,cb}$. Ideally, this fraction is determined during CCN activation, whenever activation occurs in the model

in different locations. Depending on the specific model settings, this may be also within the cloud and at different altitudes. Because in general, the droplet activation occurs at different locations than the events of immersion freezing, $f_{dust,cb}$ is represented by a tracer which is subject to advection and turbulent diffusion. However, a simplified approach is used throughout this study, assuming a constant $f_{dust,cb}$ within the cloud, representative for the boundary layer concentrations of aerosols available for droplet activation, and the mineral dust concentration. This simplification is used because of several sources of uncertainty for calculating $f_{dust,cb}$ in the current model setup, such as independence of CCN of specific aerosol compositions, a temporally constant spatial distribution of background aerosol available for droplet activation, and a high sensitivity of $f_{dust,cb}$ to the vertical decay of this aerosol background. The assumption of constant $f_{dust,cb}$ means that the coarse mode mineral dust fraction relative to the total aerosol does not vary throughout the atmosphere.

In future, the aerosol module ART (Vogel et al., 2009) could be used to determine dust fraction among the total CCN in a more sophisticated way. Note that a constant $f_{dust,cb}$ does not confine the re-distribution of dust between cloud and rain drops which is determined from the freely evolving $N_{coll,c}$ and $N_{coll,r}$ tracers.

In spite of the difficulties described here, the basic ideas for a simple first approach are summarized in the following. The local fraction of potential IN during CCN activation is

$$f_{dust,loc} = \frac{N_{dust}}{N_{CCN}} \qquad [2.13]$$

where $N_{dust}$ is the number concentration of dust immersed in droplets. Since the corresponding parcel may contain activated particles, the contribution of the pre-existing $f_{dust,cb}$ is weighted by the fraction of pre-existing activated CCN ($N_{act}$) and newly activated CCN ($N_{CCN}$),

$$W = \frac{N_{act}}{N_{CCN}} \qquad [2.14]$$

Since we track the number of collected CCN as described in section 2.3.3, we can use this information for the representation of $N_{act}$:

$$N_{act} = N_c^{t-1} + N_{coll,c}^{t-1} + N_{coll,r}^{t-1} \qquad [2.15]$$

A more exact but computationally more expensive method would be a specific tracer for activated aerosol (e.g., Cohard and Pinty, 2000) because $N_{coll}$ is subject to budgeting by microphysical processes, and $N_{coll,r}$ is subject to sedimentation (section 2.3.3). A brief discussion of activated CCN is also included in section B.2. Finally, the updated fraction of dust at time step t is

$$f_{dust,cb}^{t} = f_{dust,cb}^{t-1} W + f_{dust,loc}\,(W-1) \qquad [2.16]$$

### 2.3.5. Rain drop freezing

Droplet freezing probabilities depend on the number of mineral dust particles immersed in the rain drops, the fraction of these particles which are activated as ice nuclei (IN), and their distribution among the drops. With knowledge of the bulk number concentration of collected CCN ($N_{coll,r}$) and the fraction of mineral dust among the total CCN content ($f_{dust,cb}$), the mean number of dust particles contained in the rain drop ensemble is given by,

$$N_{dust,r} = N_{coll,r}\, f_{dust,cb} \quad \left[\mathrm{m}^{-3}\right] \qquad [2.17]$$

A temperature-dependent fraction of this dust population contained in rain drops will be activated as IN. By integration over the mineral dust size distribution (dust diameter D), the total number of activated IN at a specific temperature is

$$N_{IN,r} = \int n_{dust,r}(D) \left(1 - e^{-n_s \pi D^2}\right) \mathrm{d}D \qquad [2.18]$$

with the temperature dependence parameterized according to (Niemand et al., 2012, N12 hereafter), where the surface site density $n_s$ is

$$n_s(T) = e^{-a_{N12} T_c + b_{N12}} \quad \left[\mathrm{m}^{-2}\right] \qquad [2.19]$$

with temperature $T_c$ in °C and fit parameters $a_{N12}$ and $b_{N12}$. Rain drops can contain multiple activated particles at a time (Fig. 5.2 in section 5.1) which is more likely to occur for larger drops since we assume the particle content to be proportional to the drop mass. In the following, we consider a monodisperse sample of rain drops with known $N_{IN,r}$ as result of eq. 2.18. For this equal-sized drop ensemble, we can assume the particles to be Poisson-distributed among the drops to estimate the freezing probabilities (Vali, 1971; Hartmann et al., 2013). With the mean number of activated particles per drop

$$\lambda_{IN} = \frac{N_{IN,r}}{N_r} \qquad [2.20]$$

the probability of finding k IN immersed in one drop is

$$P(X = k) = \frac{\lambda_{IN}^k}{k!} e^{-\lambda_{IN}} \qquad [2.21]$$

Freezing of a drop is triggered with at least one activated IN being immersed in it. No freezing will occur with $k = 0$, therefore the probability for the freezing of a drop is $P(X > 0) = 1 - P(X = 0) = 1 - e^{-\lambda_{IN}}$. For an ensemble of drops, this is equal to the freezing fraction, therefore the number of frozen rain drops is

$$N_{ice,r} = N_r \left(1 - e^{-\lambda_{IN}}\right) \qquad [2.22]$$

The functional form of the frozen fraction is similar to the calculations of N12. The difference is that here we calculate the freezing fraction of the drops, while in N12 the freezing fraction is related to the number of mineral dust particles.

Equation 2.22 is not directly applicable in models because during the model time integration the rate of freezing is required in each time step. In case of cloud droplet freezing, the rate can be reconstructed by making assumptions about previously activated aerosol particles, most easily by assuming that pre-existing cloud ice and snow number densities correspond to activated aerosol particles (SB06), or by introducing specific tracers for activated IN in the model (Paukert and Hoose, 2014a). Such methods are particularly problematic for rain drops because of non-negligible sedimentation effects not only of rain, but also of sedimenting large ice particles. Also explicit tracking activated IN may result in inconsistencies because of sedimentation. For these reasons, we want to avoid the use eq. 2.22 in the model, but derive a rate equation instead ("cooling rate approach" in the following).

In the cooling rate approach, the freezing rate is derived by calculating the time derivative of eq. 2.22, where $\lambda_{IN}$ is a function of $n_s(T)$. With knowledge of the vertical velocities and temperature gradients, the freezing rate depends on the steepness of $n_s(T)$ and the cooling rate of the parcel. More exactly, it

depends on the effective cooling rate of the rain drops which is modified by their sedimentation velocity. This effect can be considered easily in the cooling rate approach, resulting in a decreased effective cooling rate for sedimenting drops and a reduced freezing rate. The treatment implies that heterogeneous freezing occurs only for drops which move upwards, i.e., where $(w - v_{sed}) > 0$ with $v_{sed}$ being positive downwards. This is consistent with the singular hypothesis (Vali and Stansbury, 1966; Vali, 1994). Thus, none of the droplets falling from colder into warmer regions would be able to freeze by immersion freezing which is a basic difference to the Bigg-based model implementation (eq. 2.1). By performing the time derivative of eq. 2.22 we get

$$\frac{\partial N_{ice,r}}{\partial t} = N_r \, e^{-\lambda_{IN}} \frac{d}{dt} \lambda_{IN} \tag{2.23}$$

$$= e^{-\lambda_{IN}} \frac{d}{dt} \int n_{dust,r}(D) \left(1 - e^{-n_s \pi D^2}\right) \mathrm{d}D \tag{2.24}$$

$$\frac{\partial N_{ice,r}}{\partial t} = -e^{-\lambda_{IN}} \, n_s \, a_{N12} \, (w - v_{sed}) \, \frac{\partial T}{\partial z} \int \pi D^2 n_{dust,r}(D) \, e^{-n_s \pi D^2} \, \mathrm{d}D \tag{2.25}$$

where $a_{N12}$ is the fit parameter belonging to the parameterization of $n_s(T)$ (eq. 2.19). $\frac{\partial T}{\partial z}$ is the moist adiabatic temperature gradient, and $D$ is the diameter of dust particles. Note that at this point we are still considering a monodisperse drop ensemble, with $v_{sed}$ being the individual drop sedimentation velocity. In the model, eq. 2.25 is applied to multiple drop sizes, as described below in this section. Integration over the dust size distribution becomes important particularly at high freezing fractions, i.e., low temperatures. The integral is applied to a bin-resolved, prescribed dust size distribution in the model.

A higher degree of approximation (eq. 2.27) is shown in Fig. 2.4 for comparison. Also here we start from eq. 2.22 to calculate the time derivative, using the mean dust surface area ($\overline{S}_{dust,r} = \frac{S_{dust,r}}{N_{dust,r}}$) to calculate the total number of activated dust particles,

$$\lambda_{IN} = \frac{N_{IN}}{N_r} = \frac{N_{dust,r} \left(1 - e^{-n_s \overline{S}_{dust,r}}\right)}{N_r} \tag{2.26}$$

$$\frac{\partial N_{ice,r}}{\partial t} = -e^{-\lambda_{IN}} \, n_s \, a_{N12} \, (w - v_{sed}) \, \frac{\partial T}{\partial z} N_{dust,r} \, \overline{S}_{dust,r} \, e^{-n_s \overline{S}_{dust,r}} \tag{2.27}$$

For comparison, also the simplest approximation is shown in Fig. 2.4, without consideration of multiple particles per drop. We start from the linear approximation (N12 eq. 4) using the total rain-immersed dust surface area $S_{dust,r}$ to arrive at the corresponding freezing rate:

$$N_{ice,r} = n_s \, S_{dust,r} \tag{2.28}$$

$$\frac{\partial N_{ice,r}}{\partial t} = -a_{N12} \, n_s \, S_{dust,r} \, (w - v_{sed}) \, \frac{\partial T}{\partial z} \tag{2.29}$$

It will be shown that this equation is not appropriate for use in a cooling rate approach, as it cannot account for the leveling off of the freezing rates when all dust particles have been activated at cold temperatures.

#### Consideration of the drop size spectrum

In the preceding calculations, we assumed a monodisperse sample of rain drops in order to derive the number freezing rate under consideration of multiple activated IN per drop. In a bulk microphysical

scheme, we want to know the rates of number and mass as an integrated effect of the whole drop size distribution. In a drop size dependent calculation, $\lambda_{IN}$ is a function of drop mass (or volume), i.e., larger rain drops will have higher freezing probabilities than small rain drops. A numerical approach is used to solve eq. 2.25 in the model for several rain drop sizes, i.e., the spectrum resulting from the bulk rain properties is sub-divided into 8 drop size intervals ("PSD splitting" hereafter).

The drop spectrum is given by the two moments $N_r$ and $Q_r$, and the size distribution $f(x) = A\,x^{\nu}\,e^{-Bx^{\mu}}$. $\nu$ and $\mu$ specify the shape of $f(x)$, $A$ and $B$ can be calculated as function of the two moments and shape parameters (Seifert, 2002).

In the PSD splitting method, we divide the rain spectrum into a number of 8 size categories. The edges of these intervals are defined at masses ($x_{ubd}$) corresponding to the diameters of 60, 125, 250, 500, 600, 1250 and 1500 µm. In order to calculate $q_r$ and $n_r$ contained in each one of the size intervals, we integrate from 0 to each one of the upper boundaries ($x_{ubd}$),

$$n_r = \frac{A}{\mu\, B^{\frac{\nu+1}{\mu}}}\,\gamma\left(\frac{\nu+1}{\mu}, B\,x_{ubd}^{\mu}\right) \qquad [2.30]$$

$$q_r = \frac{A}{\mu\, B^{\frac{\nu+2}{\mu}}}\,\gamma\left(\frac{\nu+2}{\mu}, B\,x_{ubd}^{\mu}\right) \qquad [2.31]$$

$$B = \left[\frac{\Gamma(\frac{\nu+1}{\mu})}{\Gamma(\frac{\nu+2}{\mu})}\,\frac{Q_r}{N_r}\right]^{-\mu} \qquad [2.32]$$

$$A = \frac{\mu\, n_r\, B^{\frac{\nu+1}{\mu}}}{\Gamma(\frac{\nu+1}{\mu})} \qquad [2.33]$$

Small letters indicate the number and mass fractions of rain contained per interval, and capital letters indicate bulk properties. Subtraction of smaller categories from larger ones yields the concentrations within a single interval. The concentration of dust particles per interval results from

$$n_{dust,r} = \frac{q_r}{x_{liq,dust}} \qquad [2.34]$$

where the denominator represents the liquid mass per dust particle. With $r_{CCN} = const.$ (section 2.3.3), it can be inferred from the bulk properties of rain,

$$x_{liq,dust} = \frac{Q_r}{N_{dust,r}}. \qquad [2.35]$$

Applying these properties in eq. 2.25 yields the number of frozen drops per size interval. The corresponding mass rate results from multiplication by the mean drop mass of the corresponding interval.

In the reference calculation, a fine grid is involved to represent the size distribution with respect to drop mass x. Here we calculate the amount of rain mass ($q_r$) and numbers ($n_r$) contained in each of the size intervals as

$$n_r = f(x)\,\mathrm{d}x \qquad [2.36]$$

$$q_r = x\,f(x)\,\mathrm{d}x \qquad [2.37]$$

with d$x$ being the mass increment of the size distribution. The agreement between the reference solution and the PSD splitting method is described below in this section. In the following, we will compare the reference solution for parameterized freezing rates (eq. 2.25) with the linear approximation (eq. 2.29), and the existing model implementation for freezing rain (eq. 2.1) according to Bigg (1953).

A sanity test of the freezing rate approach as compared to explicit IN depletion will be described in chapter 5, where we adopt the method for cloud droplet freezing.

### Freezing rates resulting from the cooling rate approach and B53

In this section, a comparison is shown for different methods to calculate the total number of freezing drops and the corresponding rates. The calculations are based on $10^3\,\mathrm{m}^{-3}$ (panel a) and $10^5\,\mathrm{m}^{-3}$ (panel b) dust particles contained in the rain drop spectrum, consisting of $10^4\,\mathrm{m}^{-3}$ drops which are lifted with a vertical velocity of $1\,\mathrm{m\,s}^{-1}$, and a rain mass density of $1\,\mathrm{mg\,m}^{-3}$. The drop spectrum is defined consistent with the COSMO model.

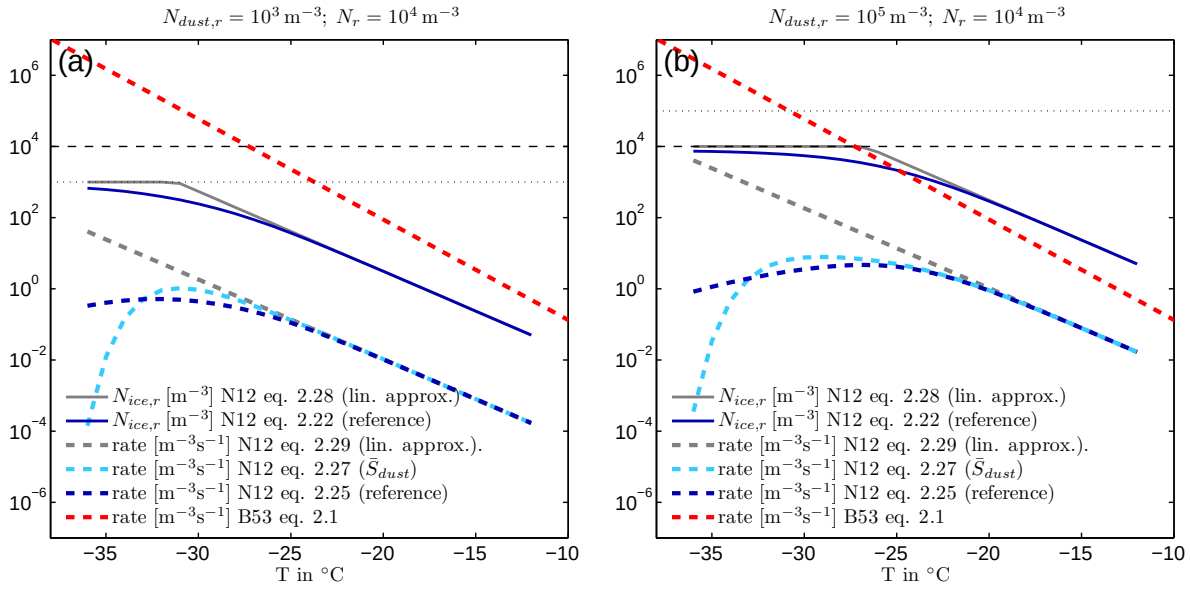


Fig. 2.4.: Total ice number densities (full lines) and freezing rates (dashed lines) resulting from different approaches, with (a) $N_{dust,r} = 10^3\,\mathrm{m}^{-3}$ and (b) $N_{dust,r} = 10^5\,\mathrm{m}^{-3}$. Horizontal dashed lines indicate $N_r = 10^4\,\mathrm{m}^{-3}$ in both cases, and horizontal dotted lines indicate $N_{dust,r}$. The examples are based on $w = 1\,\mathrm{m\,s}^{-1}$ and $Q_r = 1\,\mathrm{mg\,m}^{-3}$. The COSMO model makes use of the eq. 2.25 (dark blue), while the linear approximation (grey, eq. 2.29) diverges strongly at medium and cold temperatures. The default model implementation (B53, red dashed) yields rates which are higher by several orders of magnitude.

In Fig. 2.4, the total ice numbers ($N_{ice,r}$) are shown by thick full lines as a function of temperature. The plotted lines can be interpreted as a convective updraft in which a parcel would start in the warmer temperature regime and move from right to left with time. With decreasing temperature, the activated fraction of dust particles approaches 1, and depending on the specific approach, most of the drops freeze. N12 show that for activated fractions smaller than 0.1, the calculation can be done by a linear approximation (eq. 2.29), shown in grey for comparison. With larger freezing fractions, the linear approximation

overestimates ice numbers, and a hard limit needs to be introduced to prevent the ice number from becoming larger than the drop or dust number.

As indicated above, we need to parameterize the rates of freezing rather than the total ice number. This is a problem with the linear approximation, since there is no way to specify a reasonable hard limit for the local ice formation rate. Depending on the local properties of drops and dust, the deviation from the reference solution (dark blue dashed) can be considerable even at intermediate temperatures.

The exact calculation (eq. 2.22) avoids hard-limiting as the freezing fraction of drops approaches 1 by construction (full dark blue line). In the plateau region with quasi-constant frozen drop numbers, the parameterized rate decreases accordingly (dashed dark blue line). Although it may be counterintuitive to find decreasing freezing rates at colder temperatures, this is reasonable for two reasons, as shown in panels (a) and (b). On the one hand, $N_{ice,r}$ approaches the limit given by $N_{dust,r}$ (horizontal dotted line, panel a). Even with homogeneously-distributed dust particles in the drops, $N_{ice,r}$ cannot exceed $N_{dust,r}$ when considering immersion freezing only. On the other hand, with $N_{dust,r} > N_r$ (panel b), it is clear that $N_{ice,r}$ is limited by $N_r$. In both cases (a) and (b), the rates must decrease necessarily in order not to exceed the limits given by $N_{dust,r}$ and $N_r$. It is also evident in Fig. 2.4 that even with an activated dust fraction close to 1 at the coldest temperatures, $N_{ice,r}$ is smaller than $N_{dust,r}$ because the calculation allows for multiple IN being immersed in large drops.

For comparison, the rate B53-based rate is indicated by the grey dashed line. It is independent of the vertical velocity, i.e., with higher cooling rates, N12-based rates would become more similar to B53. In section 5.2.1 it will be shown that also with $N_{dust} = 10^6\,\mathrm{m}^{-3}$ and in strong convection, N12 immersion freezing is less efficient than B53.

#### Justification of the PSD splitting method

As described above, the bulk rain spectrum is divided into 8 size intervals in order to apply eq. 2.25 to each one of the intervals separately. By doing so, we can account for the higher freezing probability of large drops due to their higher particle contents. The PSD splitting approach is applied as an alternative to the analytical integration of eq. 2.22 over the drop size distribution.

Freezing rain drops contributes to the formation of cloud ice, graupel and hail particles Blahak (2008). By default, the drop distribution is divided into three size ranges, up to 500 µm for cloud ice, from 500 µm to 1250 µm for graupel, and from 1250 µm onwards for hail. PSD splitting avoids the need for piecewise analytical integration over the rain PSD by applying eq. 2.25 to a small number of size intervals. The subsequent attribution of frozen particles to the three ice particle classes is straight-forward. In the current implementation, the size spectrum corresponding to cloud ice is sub-divided into 4 intervals, and graupel and hail-forming drops are sub-divided into 2 intervals each.

Hail-forming drops have smaller effective cooling rates than cloud ice-forming drops. Size-specific sedimentation is calculated consistent with the model assumptions depending on the drop mass and a correction factor for air density. In a comparison of bulk rates of the reference solution and the results of PSD-splitting, we find an agreement within 20% in the relevant space of mean drop sizes and $\lambda_{IN}$ (not shown). Remembering the long way of any potential ice nuclei, starting from droplet activation at cloud base and droplet collision budgeting to the freezing event, the magnitude of this deviation appears acceptable.

For the sake of simplification, we could think of disregarding the PSD splitting, i.e., treating the whole rain size distribution a time. When doing so, the parameterization approach follows the default implementation, i.e., first calculating the freezing rates of the whole spectrum, and subsequent splitting of the rates into the three particle classes of cloud ice, graupel and hail. In sensitivity tests with intermediate dust concentrations (section 5.2.1), the effect of PSD splitting as compared to a disregard of the splitting will be discussed. It will be shown that accounting for the drop size dependencies have the largest impact on hail formation, while cloud ice and graupel are influenced to a minor extent.

### 2.3.6. SPECS parcel model simulations

The data analyzed in this section were provided by model simulations of Dr. Martin Simmel from TROPOS Leipzig. This contribution enables us to validate the assumptions described in sections 2.3.3 and 2.3.5.

Consistent with the bulk microphysical assumptions in the COSMO model, "cloud droplets" identify droplets with diameters smaller than 80 µm, while "rain drops" indicate sizes larger than 80 µm (Seifert, 2008), and x is the single-droplet mass in kg. The process names are used in accordance with Seifert and Beheng (2001), where the selfcollection of cloud droplets is collision-coalescence of two cloud droplets which results in another droplet small enough to remain a cloud droplet, while during autoconversion, two cloud droplets yield one rain drop. Accretion is the collection of cloud droplets by pre-existing rain drops.

#### Motivation

For the budgeting of collected aerosol particles in rain drops as well as for rain drop immersion freezing, it was assumed that the number of CCN per drop mass ($r_{CCN}$) is constant throughout the rain drop spectrum (sections 2.3.3 and 2.3.5), i.e., for drops with $D > 80\,\mu m$:

$$\frac{N_{CCN}(x)}{x} = r_{CCN} = const. \qquad [2.38]$$

This approximation is expected to be valid in case that a) the rain drop growth is dominated by autoconversion and accretion rather than by condensation, and b) the cloud droplets converted to rain have a narrow range of $r_{CCN}$. Otherwise, if a broader range of $r_{CCN}$ is involved, the assumption will still be valid if the stochastic behavior of the collisions acts to mask the variability, i.e., the distribution of multiple $r_{CCN}$ of cloud droplets contained within one rain drop would yield the same average $r_{CCN}$ for all rain drops.

Cloud droplets are expected to grow mainly from condensation because the selfcollection of cloud droplets is relatively inefficient (see Fig. 5.1, 5.3). Thus, with the average aerosol particle number per cloud droplet being close to 1, $r_{CCN} \approx x^{-1}$, and condition b) corresponds to the requirement that only a narrow size range of cloud droplets is favored for the conversion to rain. The condition is not fulfilled if different rain drop sizes prefer to collect cloud droplets of considerably different sizes.

Given the fulfilled conditions a) and b) as defined above, subsequent collisions among rain drops increase the number of CCN per drop, with $r_{CCN}$ being conserved throughout the rain spectrum.

In order to validate the assumption of $r_{CCN}$ being independent of the rain drop size (or mass), parcel simulations were carried out by Dr. Martin Simmel. In the two-dimensional bin microphysics version of the SPECS (spectral cloud microphysics) model (Simmel et al., 2002) as used here, the drop spectrum is divided into 132 bins (first dimension), while every drop size interval is binned into 180 aerosol mass categories (second dimension). By solving the stochastic collection equation numerically, the SPECS model yields the evolution of drop spectra as well as CCN mass contents within the droplets. Furthermore, supersaturation and and condensational growth is predicted.

#### Model setup

The box model is driven by a constant ascent of $2\,\mathrm{m\,s^{-1}}$, with an initial temperature of 263 K and 99% relative humidity with respect to water. The slow updraft (compared to the deep convection analyzed in chapter 6) provides enough time for the narrow spectrum to yield large rain drops in the end of the simulations (3000 s, corresponding to 8 km altitude).

In a sensitivity simulation, the effect of entrainment and detrainment of aerosol particles and drops is considered by parameterizing the mixing between the parcel and its environment depending on the vertical velocity and parcel size (Simmel et al., 2005). Aerosol particles are mixed in both directions, and droplets are detrained. Overall, this modifies the supersaturation within the parcel and enables CCN activation above the cloud base due to the continuous flux of freshly entrained aerosol.

The initial aerosol size distribution is unimodal and very narrow: Our primary interest is the number of CCN per drop depending on drop size, while the model tracks the mass of CCN. During time integration, the drop collisions act to redistribute the masses of liquid and aerosols in the two-dimensional spectrum, thereby losing any information about the underlying particle spectrum associated with the accumulated mass per bin. Since we want to relate aerosol mass to aerosol number concentrations, the initial aerosol spectrum is quasi-monodisperse in our simulations, with a concentration of $283\,\mathrm{cm^{-3}}$, a mode diameter of 50nm and a standard deviation of 1.01. Therefore, we can infer the aerosol number from the simulated aerosol mass per bin which is directly available from the model output, using the constant mean aerosol mass during initialization.

In order to focus on the effect of droplet collisions, freezing and ice microphysics are excluded. Unactivated, interstitial aerosol particles are enabled to interact with droplets, and may be incorporated in the droplets as a result of scavenging. By disabling scavenging, it was confirmed that its effect on $r_{CCN}$ is negligible for this study (not shown).

Breakup of large drops is disregarded for the simulations which are analyzed in the following, although the effect is rather inefficient with the narrow initial spectrum and limited time for growth. The default model assumption during breakup is to redistribute the aerosol masses contained in the fragmenting drop proportional to the resulting masses of the small drops. This is basically equivalent to the assumption of conserved $r_{CCN}$, shifting the mean $r_{CCN}$ towards constant values in the size range of 50 µm to 500 µm (not shown). Since our primary interest is the effect of collisions on $r_{CCN}$, breakup is neglected here.

#### SPECS Results

Figure 2.5 shows the temporal evolution of the parcel-integrated number concentrations and supersaturation. Upper panels without entrainment, and lower panels include entrainment.

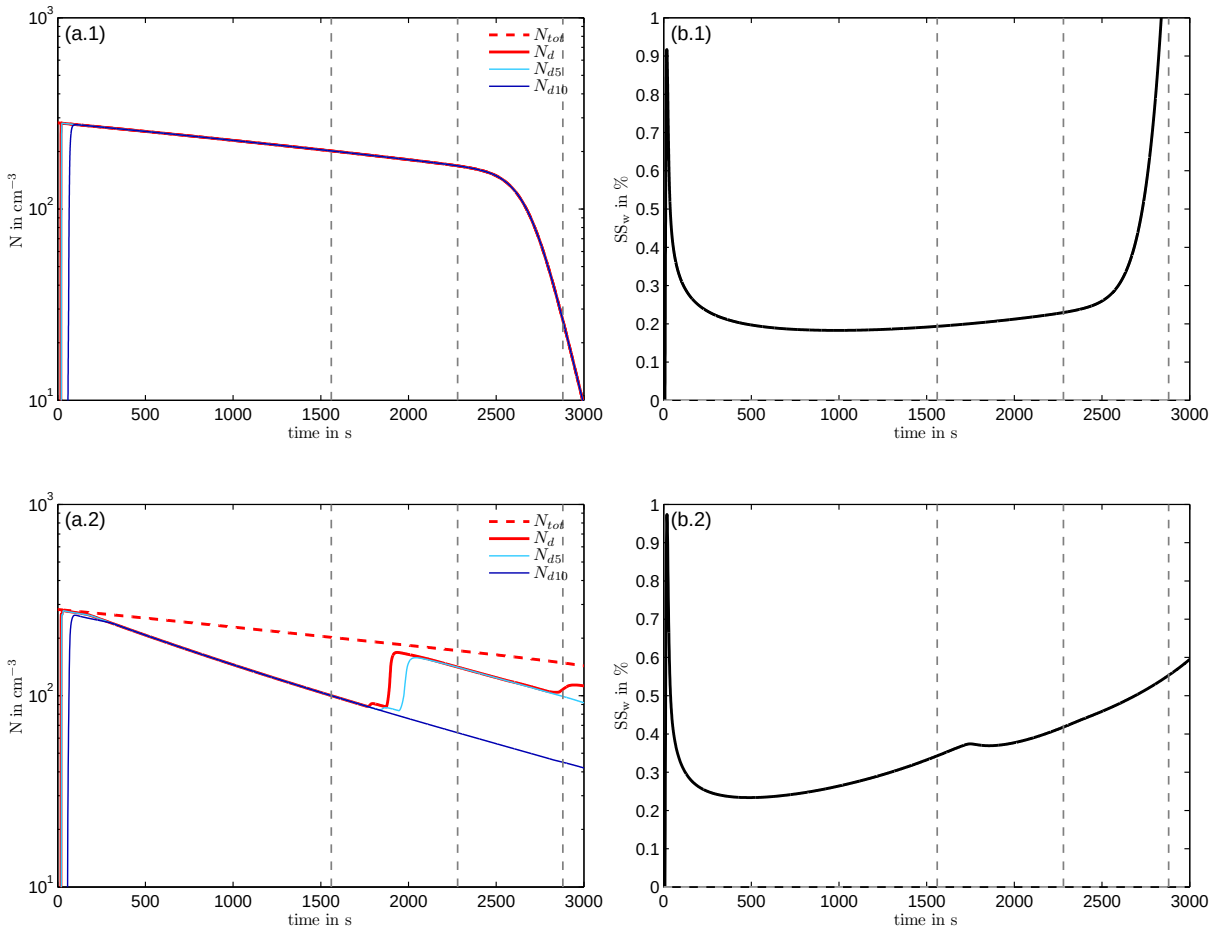


Fig. 2.5.: Time evolution of the number concentrations (left panels) of total particles (unactivated aerosol and droplets; $N_{tot}$), total droplets ($N_d$), droplets larger than 5 µm ($N_{d5}$) and droplets larger than 10 µm in diameter($N_{d10}$). The parcel supersaturation with respect to water is shown in the right panels. Upper panels are simulated without entrainment, lower panels with entrainment included. Vertical dashed lines indicate the time steps shown in Fig. 2.6.

In panel a.1, the time evolution of total particles is given by the sum of unactivated aerosol ($D < 1$ µm) and droplets ($D > 1$ µm). It is basically equal to the droplet concentrations, except that droplets larger than 10 µm need some time to grow by condensation initially. The primary reduction of particle concentrations is attributed to the expanding parcel size with height. After 2500 s, the majority of small droplets is converted to rain, and the rapidly-decreasing total droplet number (including smaller rain-sized drops) enables the supersaturation (b.1) to rise quickly.

With entrainment included (a.2), the total number concentration (red dashed) and the droplet number concentrations diverge because of the continuous entrainment of aerosol on the one hand, and detrainment of droplets on the other hand. Because of smaller droplet numbers, the supersaturation (b.2) is higher and increases faster when entrainment is included. At 1800 s, this enables the activation of new CCN (full red line in panel b.1). These "secondary" droplets grow beyond 5 µm within 100 seconds (light blue line), but the condensational growth is not efficient enough to yield sizes larger than 10 µm (dark

blue line). Another smaller amount of CCN is activated after 2900 s when the supersaturation exceeds 0.5%. Overall, the activation events above cloud base result in a bimodal size distribution of droplets, with a slowly-growing mode diameter of the smaller mode with time ($D < 10\,\mu m$; not shown).

Figure 2.6 shows the simulated distribution of $r_{CCN}$ for three distinct time steps (1560 s, 2280 s, 2880 s), the latter being indicated by vertical dashed lines in Fig. 2.5. Left Panels show the results without entrainment, and right panels include entrainment. In the first line, $r_{CCN}$ is calculated as a mean value of equal-sized drops as a function of drop diameter, each graph corresponding to one time step. In lines 2-4, the colors illustrate the frequencies of occurrence of $r_{CCN}$ on a logarithmic scale, each "count" corresponding an individual droplet.

From the first line, we can clearly distinguish the regimes of condensational growth and collisional growth: As expected, in the condensation regime $r_{CCN}$ decreases with increasing drop size because the aerosol mass within a drop is not affected by condensation.

In the simulation without entrainment, the mean value of rain-sized drops fulfills the expectation very well in all time steps, although the variability of $r_{CCN}$ for a given drop size comprises about one order of magnitude from minimum to maximum values, owing to the stochastic nature of droplet collisions.

A more complicated behavior is evident when entrainment is included (panels on the right hand side). We have seen above that an event of in-cloud CCN activation occurs at 1800 s. Prior to this event, the mean value of $r_{CCN}$ (dark line in the top right panel) is rather flat for droplets larger than 30 µm. Afterwards, rain drops larger than 100 µm tend to have increased values relative to the smaller drops, and the increase tends to continue in time. Larger $r_{CCN}$ corresponds to the collection of smaller cloud droplets, i.e., the secondary activation event provides the droplets which cause the enhancements of $r_{CCN}$ of larger drops at later times. The drop size-dependent variability of the average $r_{CCN}$ appears to be within a factor of 2 for drops between 30 µm and 3 mm which is still small compared to the variability of $r_{CCN}$ for equally-sized drops. Nevertheless, the assumption of constant $r_{CCN}$ during the freezing process would tend to overestimate the freezing rates of small droplets (say, $D < 200\,\mu m$ which make the major contribution to the bulk rain drop number concentration), and underestimate the freezing probabilities of larger drops.

In convective clouds, we expect the entrainment effects to be more relevant close to the cloud edges than within the convective core. Based on the SPECS simulations discussed here, this means that the assumption of $r_{CCN} = const.$ holds very well within the convective core. In case of CCN activation associated with entrainment, smaller drops might be favored to freeze.

For our simulations of deep convection it will be shown (section 5.2.1) that the explicit consideration of rain drop sizes is most relevant to the freezing rates of drops associated with hail formation ($D > 1250\,\mu m$). Because of the dependencies on vertical velocity, we expect these freezing events to occur mainly in the convective core rather than at cloud edges, so we may be confident that a potential bias introduced by a drop size-dependent $r_{CCN}$ is of minor importance in our simulations.

For simplicity, entrainment concerns only solid and liquid particles, while the exchange of water vapor between the simulated parcel and its environment is disregarded. In nature, in cloud environments which are clearly subsaturated with respect to water, the entrainment of dry air reduces the supersaturation (Korolev and Mazin, 2003), and may be able to suppress the CCN activation as simulated here. Nevertheless, activation as a result of lateral entrainment is cannot be excluded (Khain et al., 2000), and in-cloud activation may also occur in case of very efficient droplet depletion by collisions and subse-

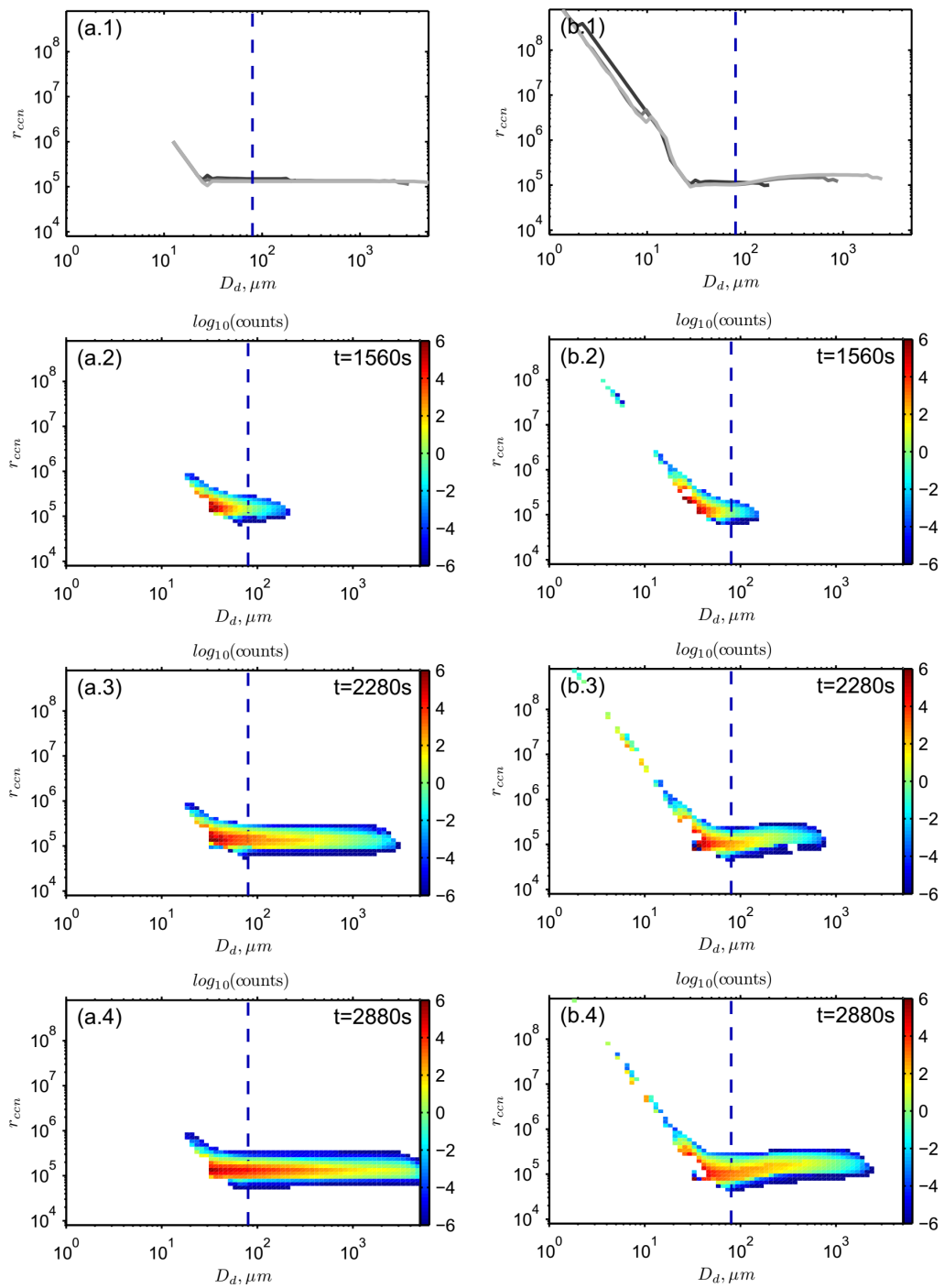


Fig. 2.6.: Simulated results of $r_{CCN}$ without (a.*) and with entrainment (b.*), shown for three distinct time steps. Top panels illustrate the mean value for equal-sized drops as a function of drop size (dark/medium/light grey: 1560 s/2280 s/2880 s). Lower panels indicate the variability of $r_{CCN}$ for each drop size, with one "count" of the frequency of occurrence corresponding to a single droplet. Vertical dashed lines indicate the separation size between cloud and rain drops at 80 µm.

quent increase of supersaturation (Pinsky and Khain, 2002). From the bulk-microphysical point of view,

in-cloud activation is not allowed by design because of the simplified representation of droplet growth and supersaturation (section B.2).

We conclude that the simple assumptions made for the budgeting and freezing of rain-immersed aerosol particles are appropriate for use in bulk microphysical schemes. Nevertheless, the exact quantification of the impact of the $r_{CCN}$ variability on freezing rates remains for future work. In such calculations, in-cloud CCN activation might be regarded as a scenario with a potential maximum variability of $r_{CCN}$.

Another conclusion from these simulations concerns the calculation of droplet volume-dependent freezing rates, which implicitly assumes that the aerosol content is proportional to the drop masses (e.g., Bigg, 1953). Our results suggest that the volume-dependent immersion freezing rates may be problematic for those droplets which have grown from the vapor phase, since condensation decouples drop mass and aerosol content, the latter being ultimately responsible for heterogeneous droplet freezing.

## 2.4. Deposition Nucleation

In addition to triggering immersion freezing, mineral dust has the potential to form ice crystals from the vapor phase via the pathway of deposition nucleation. The recently developed parameterization of Ullrich et al. (2016) was implemented in the model and is included in all simulations presented in this work. Although in most of the simulations this mechanism does not contribute significantly to the resulting cloud properties, anvil ice number concentrations can be sensitive in case of relatively high atmospheric dust concentrations (section 6.2).

The active surface site density $n_s$ is a function of both temperature (T in K) and ice supersaturation ratio ($s_i = \frac{RH_i}{100\%} - 1$),

$$n_s(T, s_i) = \exp\left\{ a\, s_i^{\frac{1}{4}} \cos\left[b\,(T-c)\right]^2 \left[\frac{\pi}{2} - \arctan\left[d\,(T-e)\right]\right] \frac{1}{\pi} \right\} \quad \left[\mathrm{m}^{-2}\right] \qquad [2.39]$$

with fit parameters a to e. With known $n_s$, the number of activated particles results from eq. 2.19, analogously.

In the model, deposition nucleation may occur in water-subsaturated but ice-supersaturated regions as a precondition. Therefore, the method to determine the aerosol concentrations relevant for deposition nucleation is different from immersion freezing (section 2.3). A passive tracer is used for mineral dust number concentrations in order to resolve grid-scale advection and subgrid turbulent diffusion. The explicit depletion of activated IN is implemented consistent with the method for immersion freezing of cloud droplets by tracking the maximum $n_s$ reached during previous time steps ($n_{s,act}$, green arrows in Fig. 2.7).

Technically, the same $n_{s,act}$ represents both immersion freezing and deposition nucleation IN, based on the idea that the same type of ice-forming particles would induce both mechanisms – depending on the local thermodynamic environment. While no explicit IN depletion is considered for rain (section 2.3.5), this is relevant for cloud droplets. The dust particles contained in the updraft and activated as cloud droplets are prevented from forming ice by deposition nucleation as a result of $n_{s,act}$ transported from the liquid-containing convective core into anvil regions. With this implementation, deposition nucleation in the convective outflow occurs predominantly close to anvil edges. The supersaturation is created by grid-scale turbulent eddies or wave structures, and the dust available for deposition nucleation originates from

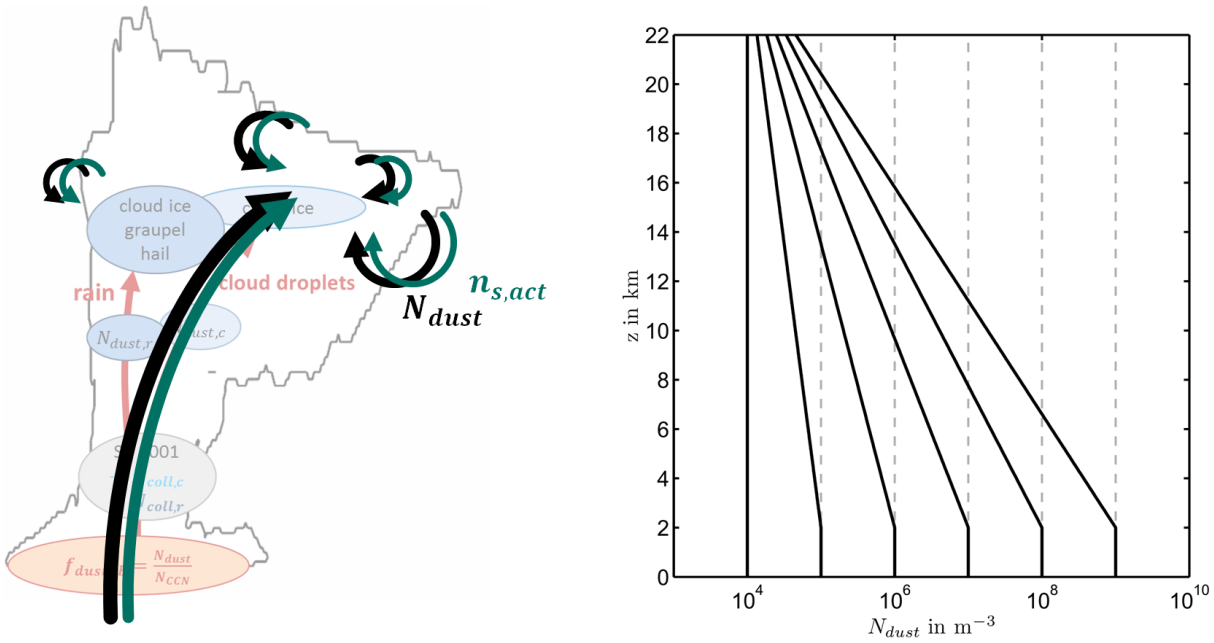


Fig. 2.7.: Left: Sketch of the model tracers relevant for deposition nucleation as implemented in this work. Together with the information of ice nuclei activation in previous time steps ($n_{s,act}$), a tracer for the mineral dust concentration ($N_{dust}$) is used to calculate deposition nucleation rates as a function of temperature and relative humidity at locations of ice supersaturation. Right: Vertical profiles of initialized dust concentrations, with boundary layer values ranging from $10^4\,\mathrm{m}^{-3}$ to $10^9\,\mathrm{m}^{-3}$.

the three-dimensional spatial distribution of mineral dust in upper levels, initialized in the beginning of the simulation and subsequent small-scale transport (Fig. 2.7).

Mineral dust concentrations are initialized with a vertical decay depending on the boundary layer concentration ($N_{dust,0}$), while homogeneously distributed in horizontal directions. Above a vertically constant profile up to an altitude of $z_0 = 2000\,\mathrm{m}$, the vertical dependence is given by

$$N_{dust}(z) = N_{dust,0}\, e^{-\frac{z-z_0}{z_e}} \qquad [2.40]$$

with $z_e$ summarized in Tab. 2.1. The profiles are loosely based on the climatology of mineral dust over Europe according to Hande et al. (2015). With increasing $N_{dust,0}$, the vertical decay becomes steeper, and no vertical decay is defined for the lowest concentration. Note that these are the concentrations at the time of model initialization, and three-dimensional transport is enabled during time integration.

## 2.5. "Perturbed Microphysics" and ensemble simulations

The majority of aerosol effects on cloud properties will be analyzed based on the "perturbed microphysics" (PM) method, as implemented in this work. With this approach, we distinguish between a) the pure microphysical effect of the aerosol perturbation, i.e., cloud property changes as a result of modified cloud microphysical interactions, and b) the cloud sensitivity including cloud-dynamical feedbacks, i.e.,

Tab. 2.1.: Exponential decay rates of initialized dust concentrations relevant to deposition nucleation.

| $N_{dust,0}\,[\mathrm{m}^{-3}]$ | $z_e\,[\mathrm{m}]$ |
|---|---|
| $10^4$ | 999999 |
| $10^5$ | 10000 |
| $10^6$ | 5000 |
| $10^7$ | 3333 |
| $10^8$ | 2500 |
| $10^9$ | 2000 |

by consideration of modified circulation patterns or strength. The basic ideas of the approach and the concept of model implementation are described in the following.

### 2.5.1. Idea

Cloud properties are tightly coupled to the atmospheric flow patters, and to the location and strength of vertical motions in particular. In “perturbed” simulations, any modifications of physical processes usually feed back on the atmospheric circulation. In a comparison of two independent model simulations – differing in a single parameter only – and with the non-linear response of the Navier-Stokes system to any perturbations, the resulting spread of simulation results can complicate the analysis considerably, or mask the desired signal completely when the dynamics-induced spread is more dominant than the process-based trigger of dynamics perturbations. This is owing to the nonlinearity of the equations of motion, i.e., minor differences in the initial conditions of the model may propagate and increase during the integration of the model time steps (e.g., Lorenz, 1963; Hohenegger et al., 2006). From their ensemble simulations, Hohenegger et al. (2006) conclude that the primary source of the ensemble spread in convective simulations is related to the diabatic forcing by condensation and evaporation.

In order to pinpoint the roles, magnitudes and interactions of perturbed cloud microphysical processes, the idea is to exclude the dynamical effect, i.e., suppression of the feedback of microphysical perturbations on the model dynamics. Once these microphysical effects are known, a comparison to perturbed ensemble simulations can be performed, the latter including both microphysical and dynamical feedbacks. This will lead us to an ensemble-mean dynamical effect.

### 2.5.2. Implementation

To extract the microphysical part of the total cloud sensitivity, the model was extended to compute the cloud microphysics scheme three times during a single time step (Fig. 2.8). The basic difference between the three calls is the aerosol concentration $N_{dust}$, resulting in differently strong primary ice formation. Therefore we use three sets of water vapor and cloud particle tracers in the model, each of which consists of number and mass density of cloud and rain droplets, cloud ice, snow, graupel and hail stones. In addition, the tracers implemented for ice nuclei depletion (Paukert and Hoose, 2014a) and aerosol particles contained in cloud and rain drops ($N_{coll,c/r}$) are specific to each of the microphysical calculations. At the time of initialization, the three sets of tracers are identical, and may evolve microphysically independent

of each other during the further simulation, while being based on the same wind flow and temperature fields.

As a result, the distribution of the available humidity among the cloud particle classes varies between the three clouds which are simulated in parallel within a single simulation. The number of three calls of the microphysics is based on the idea of centered differences: Two perturbed cloud states are compared to each other, both based on the same atmospheric flow which is driven by the "driving" microphysics scheme (DM) with an unperturbed base concentration ($N_{dust,0}$), the latter being in between the perturbed concentrations.

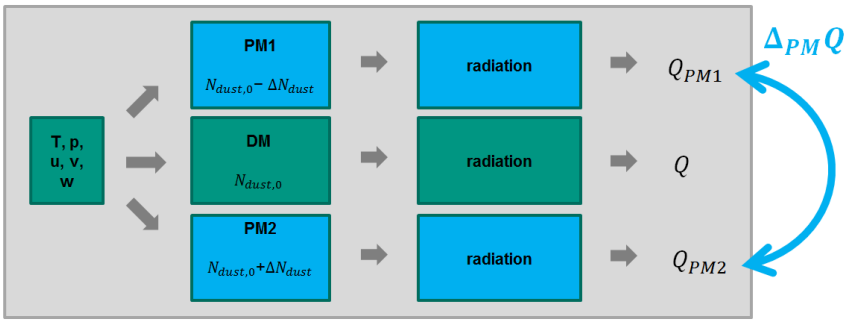


Fig. 2.8.: Illustration of the "Perturbed Microphysics" model implementation to analyze the effect of perturbed mineral dust concentrations ($N_{dust,0} \pm \Delta N$) on cloud properties and radiation. "Driving Microphysics" (DM) and radiation (green boxes) are fully coupled to the model dynamical core via latent heat, air density and radiative heating. "Perturbed Microphysics" (PM) and subsequent radiative calculations experience an identical atmospheric environment (T,p,u,v,w), but may not perturb the temperature field and circulation. Comparison of the perturbed states yields the sensitivity of any cloud property $Q$ to the dust perturbation, with $\Delta_{PM} Q = Q_{PM2} - Q_{PM1}$.

PM schemes may not interact with the model dynamics, which is subject to the DM scheme only. This is achieved by suppressing three possible pathways of interactions, which is 1) the latent heat perturbation due to the modified ice formation and subsequent microphysical processes, 2) the heating rate perturbation due to modified radiative fluxes, and 3) the air parcel's total density perturbation due to a modified cloud particle content.

An extension of the perturbed microphysics scheme was implemented to further investigate the effect of specific mechanisms in a greater detail. For the process to be investigated, the process rates are unperturbed by definition, i.e., the PM-based rates of this mechanism are equal to the corresponding DM-calculated rates. By intercomparison of the approaches, it is possible to extract the sensitivity of the cloud properties to the perturbed mechanism, with process perturbations still being induced by aerosol perturbations. For example, in section 6.2.7 the perturbed anvil ice number concentration will be shown to be highly dependent on effect of cloud ice vapor depositional growth, which is difficult to identify based on a pure analysis of PM-based process rates.

Each of the microphysics schemes is coupled to the delta-two-stream radiative transfer parameterization after Ritter and Geleyn (1992), allowing for the diagnosis of radiative impacts. An extension of the radiative code ensures the sensitivity of radiative fluxes to mass and number concentrations of cloud droplets and cloud ice (Fu, 1996; Fu et al., 1998).

### 2.5.3. Notation

The figures presented in chapter 6 will show the microphysical "base states" as well as "absolute and relative changes resulting from ice nuclei perturbations". In this notation, base state refers to the DM-calculated microphysical or radiative properties, absolute changes of a quantity Q ($\Delta_{PM}Q$) refer to the subtraction of $Q_{PM2} - Q_{PM1}$, and a relative change ($\Delta^{rel}_{PM}Q$) means a subtraction normalized by the magnitude of PM1-based properties, $\frac{Q_{PM2}-Q_{PM1}}{|Q_{PM1}|}$.

In PM2, $N_{dust} = N_{dust,0} + \Delta N$ and in PM1, $N_{dust} = N_{dust,0} - \Delta N$, with $\Delta N$ being x% of $N_{dust,0}$. x typically varies between 10 and 90 in the different simulations, as described in the case-specific sections.

In principle, we want to set x as small as possible in order keep potential cloud-dynamical differences small between the two states, while still being able to extract any $\Delta_{PM}Q$. However, a minimum magnitude of perturbations is needed for the reasons described next.

### 2.5.4. Ensemble simulations

For the quantification of cloud-dynamical feedbacks, PM-based sensitivities are compared to the sensitivities which result from multiple model simulations based on the DM scheme only, i.e., with feedbacks of microphysics on cloud dynamics being included. Here, the microphysics schemes are used with the two "perturbed" concentrations, i.e., $N_{dust,0} \pm \Delta N$.

Because of the chaotic nature of a perturbed circulation, usually we find that a single pair of DM simulations $N_{dust,0} \pm \Delta N$ is not sufficient to obtain unambiguous results of the sensitivity. This means that the "noise" arising from the chaotic behavior of the perturbed atmospheric flow dominates over the microphysical signal. Two ways exist to amplify the desired signal. On the one hand, we can increase aerosol-induced changes by specifying a larger $\Delta N$. On the other hand, the signal-to-noise ratio can be improved by simulating ensembles for each of the perturbed scenarios and comparing the ensemble mean properties. Therefore, a balance between $\Delta N$ and a reasonable number of ensemble members is to be found. For reasons of computational costs, here we want to limit the number of ensemble members to a maximum of 30, corresponding to 60 simulations for the comparison of two aerosol backgrounds.

Ensemble members are initialized with slightly different initial conditions, with the initial fields of temperature and vertical velocity within the boundary layer being perturbed by a combination of random fluctuations d$T$ and d$w$. The range of fluctuations is $0.01\,K \leq \mathrm{d}T \leq 0.3\,K$ and $0\,\mathrm{m\,s^{-1}} \leq \mathrm{d}w \leq 0.3\,\mathrm{m\,s^{-1}}$, respectively. Model initialization with randomly-distributed fluctuations of the atmospheric fields are commonly used in idealized simulations (e.g., Siebesma et al., 2003; Ovchinnikov et al., 2014), and also for the creation of ensemble variability (Grabowski, 2014, 2015).

### 2.5.5. Validity

When analyzing PM-based aerosol-cloud-interactions, we may speculate about the validity of the simulated sensitivities, since some basic physical feedbacks are neglected – strictly speaking, PM simulations are physically inconsistent.

In our simulations we find that the sensitivities originating from the "physically consistent" ensemble simulations are very similar to PM-based properties in many ways. Therefore, a preliminary conclusion is that aerosol effects on clouds can be well-captured by PM-based simulations, while the additional

interactions with the atmospheric dynamics may be interpreted as a secondary effect. A justification is given in sections 3 in more detail for Arctic stratocumuls, and in section 7.3 for deep convection.

A first introduction to the distinction between microphysical and cloud-dynamical senstivities was presented by Grabowski (2014, “Piggybacking method”), referring to the initial suggestion by Bjorn Stevens. As a development independent of that (Paukert and Hoose, 2014b), the technical implementation as described here is slightly different in some details, while the basic intentions are quite similar. Further application of the method showed the benefits for cases of shallow convection (Grabowski and Jarecka, 2015) and deep convection as simulated by a single-moment microphysical scheme (Grabowski, 2015). In general circulation models, similar methods were used to assess lifetime effects of warm clouds as a result of aerosol perturbations (Kristjánsson, 2002).

# 3. Coupling of microphysics and dynamics in Arctic mixed-phase clouds

As outlined in section 1.4, Arctic mixed-phase stratocumulus clouds (AMPC) are expected to be particularly sensitive to the interactions of microphysics and the boundary layer circulation, since the cloud itself is a major driver of turbulence via cloud-top radiative cooling. The basic influence of perturbed IN concentrations on AMPC (Paukert and Hoose, 2014a) is a reduction of liquid water path ($LWP$) and decreased cloud-top cooling rates, which in turn promotes enhanced cloud glaciation via the pathway of weakened vertical dynamics.

In this section, we apply the perturbed microphysics implementation (PM, section 2.5) in order to split the overall cloud sensitivity into two distinct contributions, 1) the pure cloud microphysical contribution $S^*$, triggering cloud property changes due to enhanced primary ice formation and 2) the cloud-dynamical contribution which may either act as enhancement or as suppression of the microphysical interactions. By definition, $S^*$ involves no feedbacks on cloud dynamics (section 2.5). Therefore we define the enhancement factor $e$ as the difference between the total sensitivity $S$ and $S^*$ relative to the magnitude of $S^*$:

$$e = \frac{S - S^*}{S^*} \qquad [3.1]$$

According to this definition, $e = 0$ corresponds to a negligible effect of cloud dynamics. In case of positive feedbacks among circulation and microphysical properties being present, cloud circulation contributes with $e > 0$. $e = 1$ corresponds to a 100% enhancement of the pure microphysical effect, and with $e = -1$, the feedbacks suppress the microphysical contribution, resulting in $S = 0$. In the following, $S$ is measured in terms of ensemble-based $\Delta LWP$, and $S^*$ is identified with $\Delta_{PM} LWP$ (section 2.5).

The dust perturbations are summarized in Tab. 3. In the case presented here, the thinner clouds ($LWP \leq 20\,\mathrm{g\,m^{-2}}$) are perturbed with $N_{dust,0} \pm 10\%$, while $N_{dust,0} \pm 90\%$ is specified for the thicker clouds. Here we present four ensemble sets, consisting of a total of 168 simulations. These are divided into two base states with higher and lower $N_{dust,0}$ ("HighIce"/ "LowIce"), corresponding to a thinner and thicker stratocumulus cloud layer, respectively. The two base ensembles consist of 30 ensemble members each, where one "member" consists of a pair of two single simulations ($N_{dust,0} \pm x\%$). Two more ensemble sets are discussed, each consisting of 12 members which are characterized by nudging of the horizontal wind in the lower boundary layer in order to examine the influence on turbulence production.

## 3.1. Case description

The simulated Arctic mixed-phase stratocumulus scenario and initialization procedures follow Paukert and Hoose (2014a) and Ovchinnikov et al. (2014), where idealized simulations of Flight 31 of the Indirect and Semi-Direct Aerosol Campaign (ISDAC) were conducted. The single-layer cloud is located below a

Tab. 3.1.: Summary of sensitivity ensemble simulations. "Default" nudging coefficients are defined according to Ovchinnikov et al. (2014).

| | HighIce | HighIceUV | LowIce | LowIceUV |
|---|---|---|---|---|
| ensemble members | 30 | 12 | 30 | 12 |
| $N_{dust,0}$ | $1.25 \times 10^8\,\mathrm{m}^{-3}$ | $1.25 \times 10^8\,\mathrm{m}^{-3}$ | $2.5 \times 10^5\,\mathrm{m}^{-3}$ | $2.5 \times 10^5\,\mathrm{m}^{-3}$ |
| perturbation | 10% | 10% | 90% | 90% |
| $c_{u/v}$ | default | $\frac{1}{7200}\,s^{-1}$ | default | $\frac{1}{7200}\,s^{-1}$ |
| $LWP$ after 12 hours | $20\ \mathrm{g\,m}^{-2}$ | $14\ \mathrm{g\,m}^{-2}$ | $63\ \mathrm{g\,m}^{-2}$ | $63\ \mathrm{g\,m}^{-2}$ |

temperature inversion and boundary layer turbulence is primarily driven by cloud top radiative cooling, with a mixed-layer that is decoupled from the ground. As single eddies penetrate into the statically stable lower boundary layer with time, these levels serve as a humidity reservoir to sustain the cloud layer, which would otherwise be dissipated by humidity loss due to ice precipitation and the evaporation of cloud droplets due to the Wegener-Bergeron-Findeisen process. We note that this situation is in contrast to the ISDAC case presented by Solomon et al. (2011), where humidity inversion above the cloud layer was the main source of humidity.

The evaluation period begins after two hours of spin-up, before which no ice is present in the model. Primary ice formation is represented by immersion freezing of mineral dust and bacteria as presented in Paukert and Hoose (2014a). Here we keep the contribution of bacteria small ($N_{bac} = 10^{-3}\,\mathrm{cm}^{-3}$), thus concentrating on varying mineral dust concentrations. However, for the results presented here, no dependence on specific ice nuclei species is expected. This means that our primary interest is the presence of more or less cloud ice, regardless of the specific source. Ice particle size distributions follow the default model settings, corresponding to "Hi-WBF" specifications in Paukert and Hoose (2014a). Following the model intercomparison of Ovchinnikov et al. (2014), large scale subsidence is superimposed, and altitude-dependent nudging of temperature, humidity and wind components is used in our simulations. Nudging coefficients are prescribed such that the mixed-layer is influenced only to a small extent. In sensitivity tests, stronger nudging of the horizontal wind components is applied: In our simulations we see that the turbulence characteristics vary considerably with time, and it becomes apparent that in specific periods the change of horizontal wind components and the resulting shear influence the vertical turbulent fluxes. While the default coefficients for the horizontal winds are defined as cosine-shaped vertical profiles, we use a vertically constant coefficient in our HighIceUV and LowIceUV sensitivity runs with a relaxation time scale of 2 hours (Tab. 3). Also following the ISDAC model intercomparison, the physical parameterization of longwave radiation is based on the vertical profile of the liquid water path, resulting in a strong cooling of the cloud top, and a slight warming in the lower levels of the liquid cloud volume.

## 3.2. Results

Figure 3.1 illustrates the changes of $LWP$ in PM simulations (blue line), ensemble simulations (gray shadings) and the resulting enhancements (red shadings). Light gray shading corresponds to total minima and maxima of the ensemble spread, and the dark shading represents the ensemble mean value and

uncertainty. The latter is calculated as the standard error of the mean value, i.e., the standard deviation divided by the square root of the number of ensemble members. Accordingly, the spread of $e$ is a result of the uncertainty of the mean value. Vertical dashed lines highlight the time period between 300 minutes and 400 minutes. In the HighIce simulation, this corresponds to the period of decaying $e$, and in the LowIce ensemble the main peak occurs within this interval as described below.

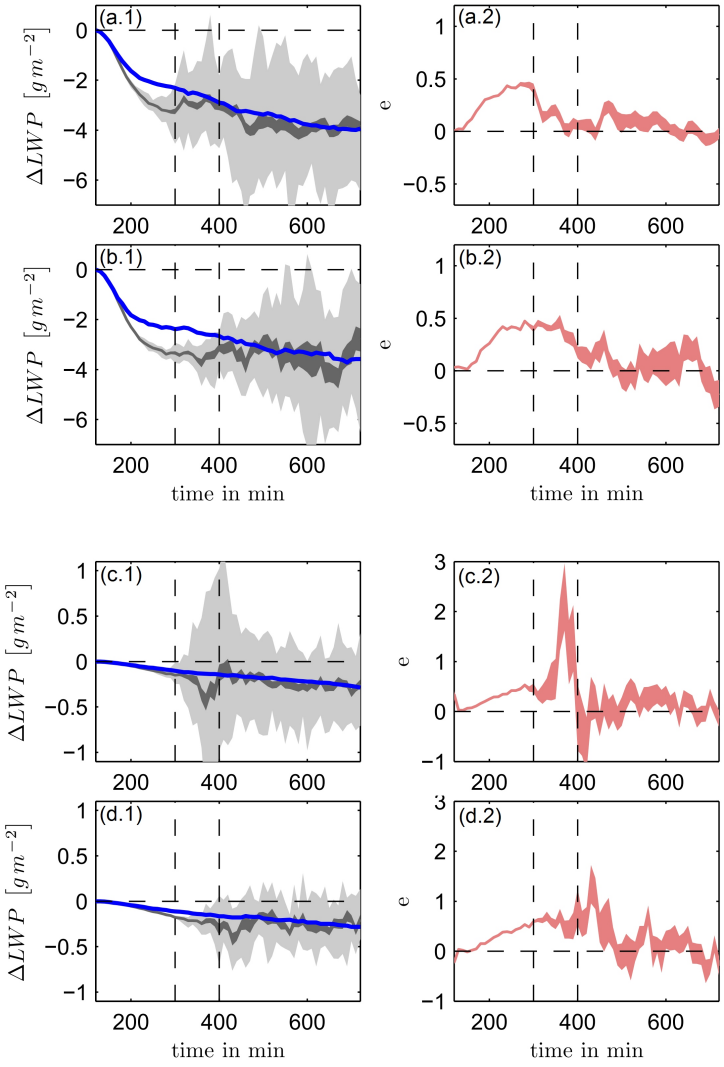


Fig. 3.1.: Left: Time series of liquid water path changes in perturbed simulations, originating from the sole microphysical contributions ($\Delta_{PM}LWP$, blue), and from ensemble simulations (grey). Right: "enhancement" of the microphysical sensitivity by the coupling to cloud dynamics as defined by eq. 3.1. Scenarios (a) to (d) illustrate HighIce, HighIceUV, LowIce and LowIceUV simulations.

After ice initialization (120 min), $e$ increases up to 0.5 ($t \approx 300$ min) as the feedbacks of microphysics, radiation and turbulence make their contribution to the ensemble results. After this period, the evolution of $e$ differs among the four ensembles (panels a-d), but in any case tends to be decayed after some more time. Thus, cloud-dynamical enhancements of $LWP$-sensitivities appear to become negligible in the quasi steady state periods. Differences between the scenarios are further described in the following.

Panels (a.*) and (b.*) show the HighIce and HighIceUV simulations with $LWP < 20\,\mathrm{g\,m^{-2}}$ and $14\,\mathrm{g\,m^{-2}}$, respectively. The main differences appear in the ensemble simulations. On the one hand, the total ensemble spread increases more gradually with time in HighIceUV. On the other hand, the enhancement factor $e \approx 0.5$ is sustained for a longer time, i.e., the adjusted boundary layer dynamics make the cloud thinner for a longer time than in HighIce simulations.

Panels (c.*) and (d.*) illustrate the LowIce situation with increasing cloud thickness with time and $LWP$ up to $63\,\mathrm{g\,m^{-2}}$. Until $t \approx 350\,\mathrm{min}$, the enhancement of $\Delta_{PM}LWP$ is similar to the HighIce simulations. A peak of $e \approx 3$ appears prior to 400 min in the LowIce runs, corresponding to an enhancement of $S^*$ by 300%. This behavior coincides with a sudden increase of the ensemble spread and indicates a high degree of turbulence-induced chaotic perturbations of the boundary layer circulation. In LowIceUV simulations, the peak is less pronounced and is shifted in time, again (like HighIceUV) with a more gradual increase of the ensemble spread with time. After the peaking periods, $e$ decays and tends to oscillate around zero. The ensemble spread is considerably smaller in the peaking period.

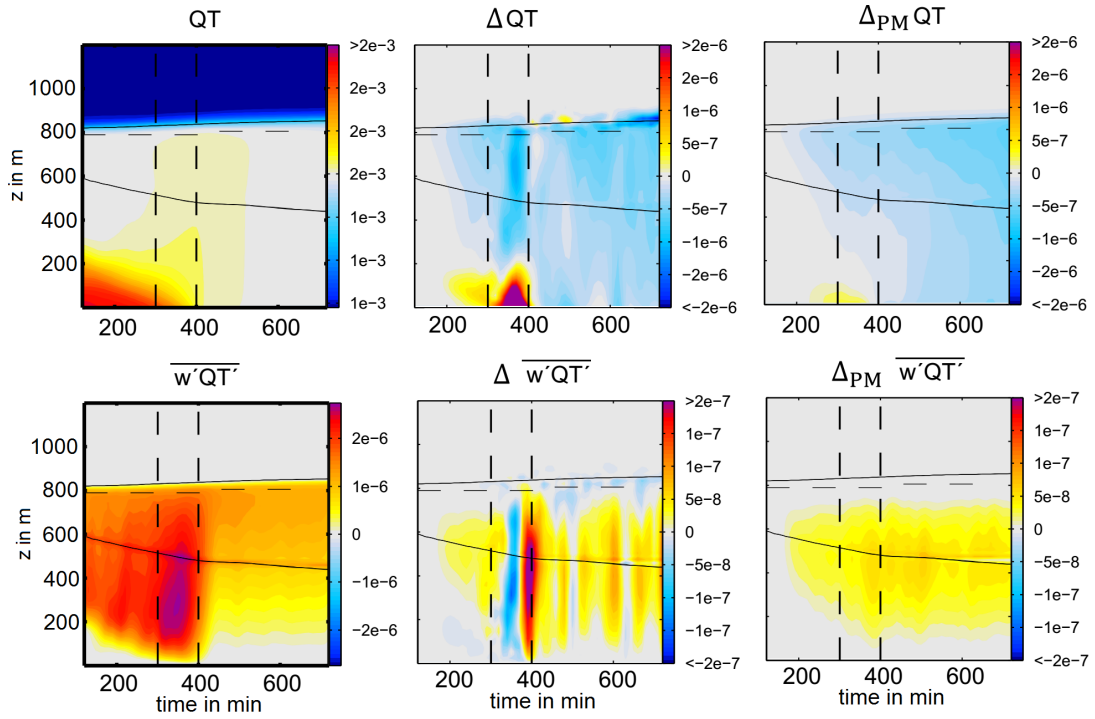


Fig. 3.2.: Vertically-resolved time series of total humidity (in $\mathrm{kg\,m^{-3}}$, upper panels) and turbulent vertical transport of total humidity (in $\mathrm{kg\,m^{-2}\,s^{-1}}$, lower panels). Left panels show the base states, mid panels the ensemble mean difference between perturbed states, and right panels the PM difference between perturbed states. The data illustrate the LowIce scenario, and horizontal black lines indicate the horizontal mean cloud-top and cloud-base ($Q_c = 10^{-7}\,\mathrm{kg\,m^{-3}}$).

The peaking period coincides with the situation when the initially ground-decoupled boundary layer turbulence penetrates deep enough to reach the surface, i.e., when the lower statically stable layer has been consumed. In Fig. 3.2, this is associated with the depletion of the lower-level reservoir of total humidity, i.e., water vapor (upper left panel prior to 400 min). The shift from one turbulence regime to another seems to be particularly sensitive to the perturbed microphysical state: In ensemble simulations,

this results a short period of considerably weakened vertical transport with more IN present (lower mid panel), therefore, the reduction of $LWP$ is particularly strong, reflected in the peaking $e$. Subsequently a short period of enhanced transport causes the peak to be reduced, i.e., the ensemble mean change of LWP adjusts to the PM state (lower panels in Fig. 3.2). As visible from the comparison of Fig. 3.1 (c) vs. (d), the vertical transport in perturbed states is sensitive to the horizontal components of turbulence. With vertically constant nudging of horizontal winds, the peak is damped in the LowIceUV case.

## 3.3. Summary and conclusions

In this chapter we presented the initial application of the perturbed microphysics scheme (PM) in the COSMO model in order to quantify cloud-dynamical feedbacks on cloud properties. We introduced the enhancement factor $e$ based on the sensitivity of $LWP$ to perturbed ice nuclei concentrations, defined as the relative difference between $LWP$ changes of the PM scheme and ensemble simulations. The test case is based on a mixed-phase Arctic stratocumulus cloud layer which was observed during Flight 31 of the Indirect and Semi-Direct Aerosol Campaign (ISDAC), a cloud type expected to be particularly sensitive to the presence feedback cycles (Morrison et al., 2012).

For $LWP$ we see a 50% increase of the microphysical sensitivity by the presence of cloud-dynamical feedbacks. This behavior is similar in the first few hours in all of our four ensembles which represent thinner and thicker clouds. When transitioning from decoupled to a ground-coupled regime, particularly thicker-cloud cases appear to go through a short period of more pronounced dynamics-cloud-interactions. After the transition, the dynamics-induced enhancement of the LWP change decays in the quasi-equilibrium state of the simulation.

Despite the peaking transition behavior between the two turbulence regimes, it seems remarkable that in the quasi equilibrium stage (t>500 min), both $S$ and $S^*$ are essentially the same. With $\Delta_{PM}w$=0 by definition in PM simulations, the stronger vertical velocity relative to the perturbed ensemble simulations can have several implications: Enhanced freezing is induced by increased vertical advection of IN, while increased vertical velocity also promotes more condensation. More complexity is added by the increased amount of sedimenting ice which acts as a source of water vapor in the lower boundary layer by evaporation. Therefore, we may argue that the single components in the cycle of humidity fluxes (upward advection, in-cloud phase changes, downward advection and sedimentation, below-cloud evaporation) is enhanced in the PM state, but at the same time, the budget of cloud water mass appears to be hardly affected.

Overall we conclude that in spite of the expected high contribution of cloud-dynamical feedbacks in this type of cloud, the initial 50% may be regarded as a modulating factor. In consideration of other uncertainties inherent to the challenge of quantifying aerosol cloud interactions, this may be even of secondary importance. Therefore in the following, we stick to the analysis of the PM-based cloud sensitivities to IN perturbations while profiting from the benefits:

1) Perturbed clouds simulated in the PM scheme can be compared one-to-one because spatial distributions of clouds – being primarily determined by atmospheric circulation patterns – are essentially the same. It is thus an easy way to analyze sensitivities which might otherwise appear noisy and scattering due to a spatial shift of clouds between independent simulations, based on independently-evolving cir-

culation patterns. Such a shift can complicate the inference of the effect of changing cloud properties which we are interested in.

2) We showed that ensembles are necessary to be able to interpret the effects of the aerosol perturbations, while a single PM simulation is sufficient to determine a non-ambiguous result of the microphyisical sensitivity.

3) We showed that the comparison of PM-based and ensemble-based sensitivities can highlight mechanisms and the corresponding tendencies, e.g., whether the blackbox of cloud-dynamical feedbacks tends to act in the same or opposing direction as the blackbox of microphysics.

# 4. Overview of simulated convective cells

This chapter will give an overview of the properties of convective cells which will be analyzed in subsequent chapters. The clouds are simulated on a domain of 300×250 grid points in horizontal directions, and 100 vertically-stretched levels which extend up to 22 km. The model time step is set to 3 s to enable horizontal resolution of 500 m.

The type of data processing, i.e., horizontal averaging methods used throughout this work, will be depend on the particular interest. The notation is summarized in Tab. A.1 in appendix A, and will be used in subsequent chapters. Time-averaging of vertical profiles includes data from 00:20 - 02:00 hours, unless stated otherwise.

After short introduction of the cloud dynamics, the typical microphysical properties and relevant processes will be described summarized.

## 4.1. Cloud evolution

Our simulations of deep convection are based on the idealized setup of Weisman and Klemp (1982, WK82 hereafter), with different environments with respect to vertical wind shear and boundary layer humidity. Our "standard case" of this work is based on a shear of $25\,\mathrm{m\,s^{-1}}$ and a vapor concentration of $14\,\mathrm{g\,kg^{-1}}$. Following WK82, the wind shear is unidirectional, yielding a quasi-symmetric cloud evolution after the initial cell splitting. In our base setup, the concentration of boundary layer condensation nuclei is defined as $1.7 \times 10^9\,\mathrm{m^{-3}}$, representative for continental aerosol environments.

The idealized atmospheric initial state results in a low cloud base at 1 km, and the freezing level is located at 4 km. According to the properties of mineral dust, immersion freezing begins at altitudes around 5 km ($T \leq -12\,^{\circ}\mathrm{C}$), and the levels of homogeneous freezing are found around 9 km. The largest amounts of anvil ice are located around 12 km in the convective outflow.

Figure 4.1 illustrates the evolution of the cloud structure with time, shown in terms of th vertical velocities in the main updraft regions. From left to right, the time steps of 00:30, 01:00, 02:00 and 03:30 hours are shown from the "front view" (panels a) and "side view" (panels b). Depending on the specific combination of shear and humidity, the cell splits into two main updrafts which detach from each other and move towards the outer boundaries of the model domain in y-direction ( (a.1 to a.4). In the later stage of the simulation, the convective activity becomes weaker and unorganized. These later stages are excluded from the analysis because the cloud dynamics may be disturbed due to interaction with the model boundaries. Because of computational efficiency, the model domain is limited to 300×250 grid points in x and y directions. Therefore, only the simulation data prior to 02:00 hours are considered throughout this work. Up to this stage, the main updrafts invigorate with time, and vertical velocities as high as $50\,\mathrm{m\,s^{-1}}$ are reached.

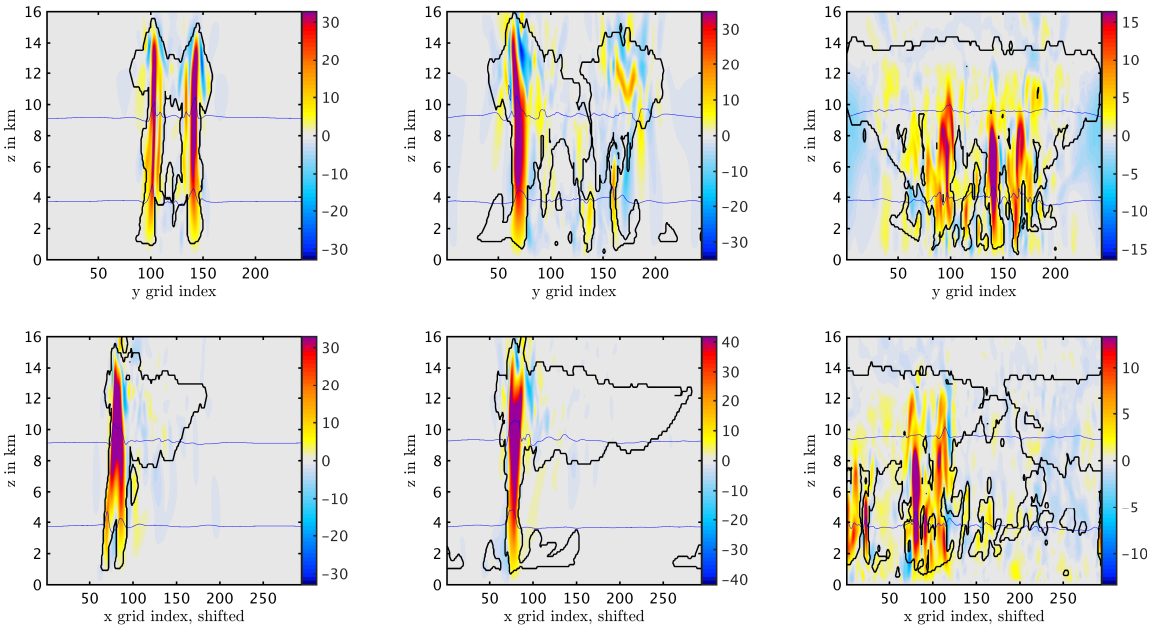


Fig. 4.1.: Slices of vertical velocities in the y-z-plane (upper panels) and x-z-plane (lower panels). Time increases from left to right (01:00, 02:00 and 03:30 hours after initialization). Black contours indicate "cloudy" regions (Tab. A.1). Blue horizontal lines indicate the levels of 0 °C and −36 °C. Color scale maxima correspond to the 99th percentiles of the data contained in the figure.

## 4.2. Convective environments

This section will summarize the different convective environments (Tab. 4.2), and the influence on cloud structure.

Tab. 4.1.: Summary of the convective environments as simulated in this work. "u*X*q*Y*" denotes a vertical wind shear of $X\,\mathrm{m\,s^{-1}}$ and a boundary layer humidity of $Y\,\mathrm{g\,kg^{-1}}$.

| | | |
|---|---|---|
| u10q11 ("weak") | u25q11 | |
| u10q14 | u25q14("standard case") | u40q14 |
| | u25q16 | u40q16 |

In general, we expect the wind shear to determine the supercell character and longevity (section 1.4). According to the concept of convective available potential energy (Houze, 1993), the vapor content of the lower atmosphere is an important component to determine the convective strength. Accordingly, our "standard case" (u25q14) yields a long-lived supercell.

In Fig. 4.2, side views of the clouds in different environments are shown (panels *.1/3), as well as slices in the x-y-plane (panels *.2/4) at the time steps of 01:00 hour (left columns) and 02:00 hours (right columns). Colors indicate the vertical velocities, W. In the side view panels, the maximum W of the columns perpendicular to the paper plane are shown ($W_{max,\#}$), while in the horizontal planes the local values ate the 8 km levels are illustrated.

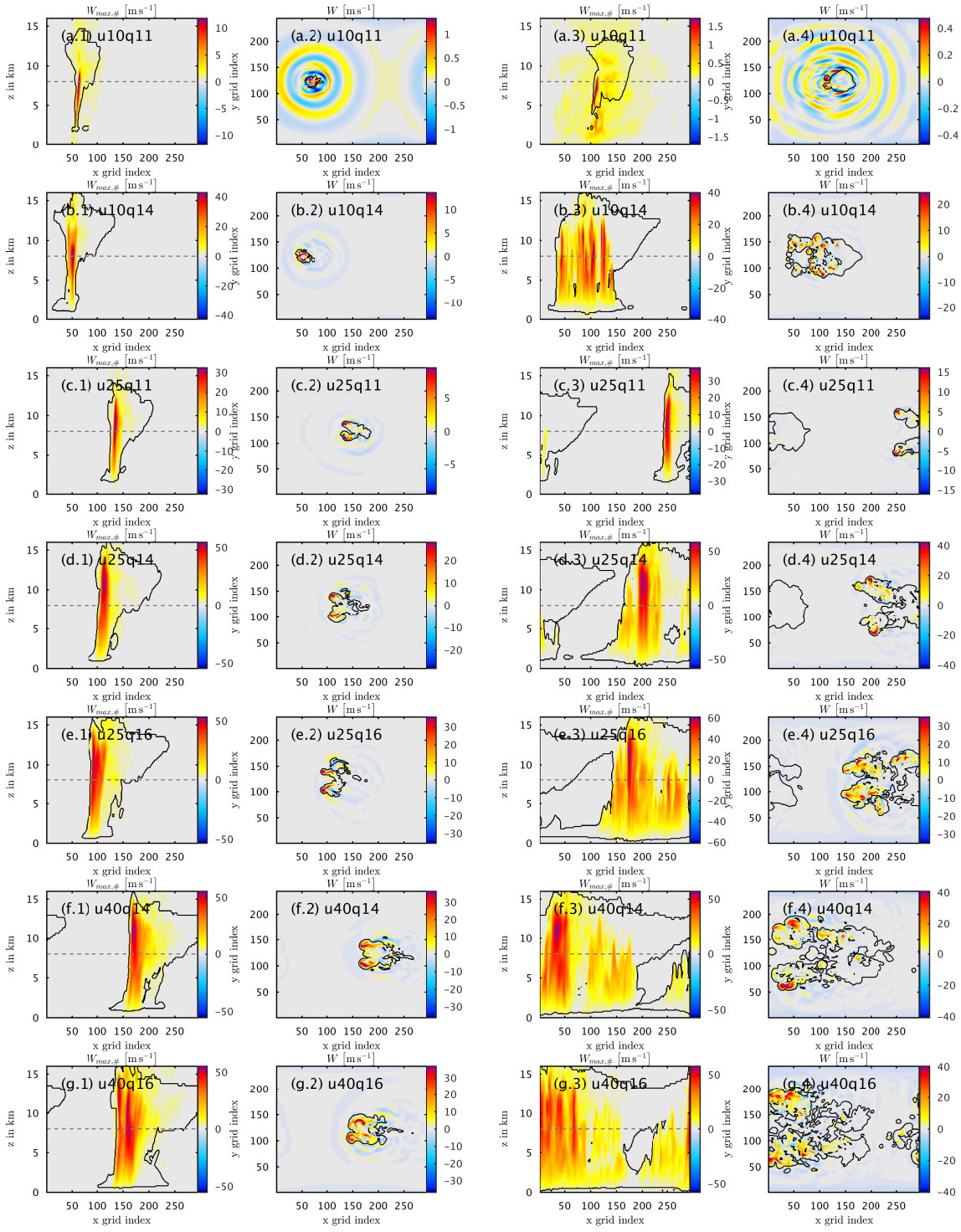


Fig. 4.2.: Vertical velocities in different atmospheric environments (a-g), shown at 01:00 hour ( *.1/2) and 02:00 hours (*.3/4) after initialization. Black contours indicate “cloudy” regions (Tab. A.1) integrated in y-direction. Horizontal dashed lines in the side views (*.1/3) indicate the altitudes of horizontal slices (*.2/4).

The cloud in our case of "weak convection" (u10q11) dissipates after 90 minutes, and may thus be interpreted as a single cell. The initially strong updraft ($w > 40\,\mathrm{m\,s^{-1}}$) cannot be sustained for a longer time. Medium-strength updrafts of 10-15 $\mathrm{m\,s^{-1}}$ are present until the beginning of the dissipating stage.

With higher wind shear, the cell moves faster from left to right, and tends to split into two parts more clearly (e.g., panels a/c; b/d/f). With increasing boundary layer humidity and constant wind shear, the horizontal extent of the strongest updraft regions is increased, with updrafts becoming heterogeneously-distributed (e.g., panels c/d/e). Particularly in case of the strongest convection (u40q16), the problem of a large horizontal cloud extent at later stages is evident. Therefore, simulated cloud stages later than 02:00 hours are not considered for the data interpretation.

## 4.3. Cloud condensate

Next, the spatial distributions of mass and number densities of each cloud particle species are illustrated (Fig. 4.3) on a logarithmic scale after 1.5 hours simulation time, with $< \mathrm{cld}_{\#} >$ averaging according to Tab. A.1.

- Cloud droplets ($Q_c$, $N_c$, panels a)
  In the continental scenario, cloud base droplet concentrations are around $10^9\,\mathrm{m^{-3}}$ and decrease with height continuously. In the strongest updraft regions, there are 2-3 orders of magnitude less droplets than at cloud base before reaching the homogeneous freezing levels. This depletion with height is much dependent on the details of the activation parameterization, as discussed in section B.2. Maximum mass concentrations are found around the 0 °C level (z=4 km).
- Rain drops ($Q_r$, $N_r$, panels b)
  Above 4 km altitude, rain mass becomes larger than cloud droplet mass. In the continental scenario, rain drop numbers are generally 2-3 orders of magnitude lower than cloud droplet numbers. In contrast to cloud droplets, they may also exist in water sub-saturated regions. The horizontally wide-spread areas at positive temperatures originate from melting graupel and hail particles.
- Cloud ice ($Q_i$, $N_i$, panels c)
  Compared to the anvil region ($z > 9\,km$), cloud ice mass and number densities at $T > -36\,^{\circ}\mathrm{C}$ are relatively small because the heterogeneous freezing ($N_{dust} = 10^5\,\mathrm{m^{-3}}$) is quite inefficient. At altitudes below 6 km, secondary ice formation rates are several orders of magnitude larger than those of dust immersion freezing (see also Fig. 5.7. Convective outflow ice properties are mostly dominated by homogeneous droplet freezing.
- Snow ($Q_s$, $N_s$, panels d)
  The snow class represents aggregates of crystals. They sediment more efficiently than cloud ice, but hardly contribute to precipitation in this case, as most of the snow amounts evaporates below the anvil.
- Graupel ($Q_g$, $N_g$, panels e)
  With larger mean masses and densities compared to snow, graupel sediments efficiently from anvil regions down to the melting level. Although only small amounts reach the surface, graupel makes large contributions to the surface precipitation by being converted to rain during sedimentation.

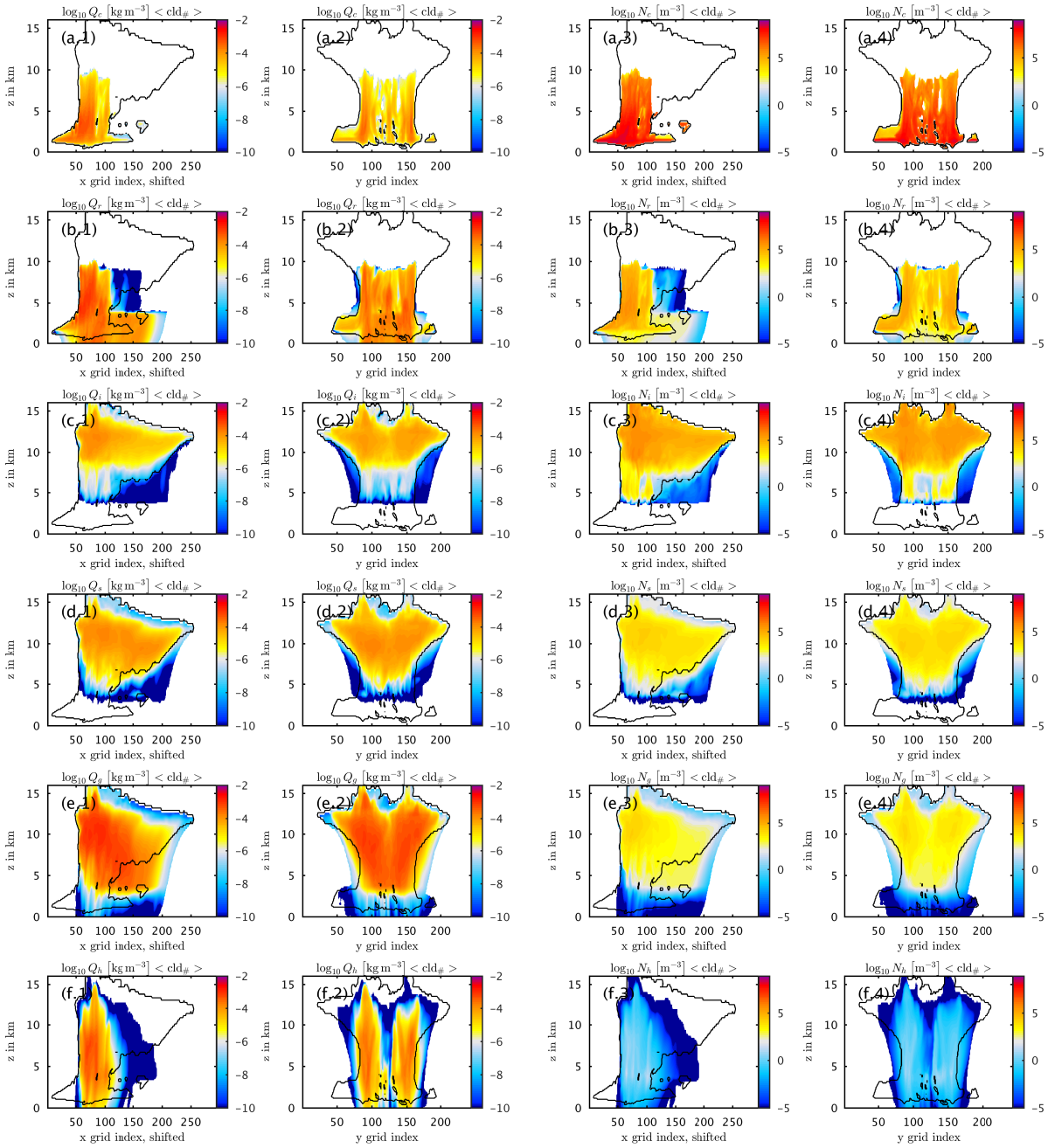


Fig. 4.3.: Cloud particle mass densities (*.1/2) and number densities (*.3/4) of cloud droplets (a), rain (b), cloud ice (c), snow (d), graupel (e) and hail (f) after 01:30 hours of simulation time. Black contours indicate "cloudy" regions (Tab. A.1) integrated in y-direction.

An important initiation mechanism is the freezing of large rain in the convective updraft, while further growth is dominated by riming.

- Hail ($Q_h$, $N_h$, panels f)
  The hail class has the largest mean masses. Due to the very efficient gravitational settling, large masses occur only in the direct vicinity of the main updrafts. Furthermore, significant amounts of

the hail particles survive the lowest 4 km of the atmosphere, while also an important contribution to rain formation is made by melting. In contrast to the smaller ice particles, the primary formation is most efficient well below the homogeneous freezing levels because the existence of large rain drops is a prerequisite.

## 4.4. Microphysical budgets

Here we give an overview of the microphysical process contributions to the mass change rates of total liquid and total mass. In Fig. 4.4, each process group is represented by two lines with the same color, owing to the different properties of lifting regimes and sedimentation regimes (Tab. A.1). If both were combined, e.g., updraft condensation rates would mask evaporation. For the liquid rates (panel a), the lifting and sedimentation regimes of rain drops are used to distinguish the regions – these are also the basis for the averaging of cloud droplet rates. For the ice phase, the graupel lifting regime is chosen to identify the updraft region – although hail stones may still fall down in these regions. Full lines represent lifting regimes, while dashed lines indicate sedimentation regimes. In addition to microphysical conversion and sedimentation flux divergences, advective tendencies are included for completeness.

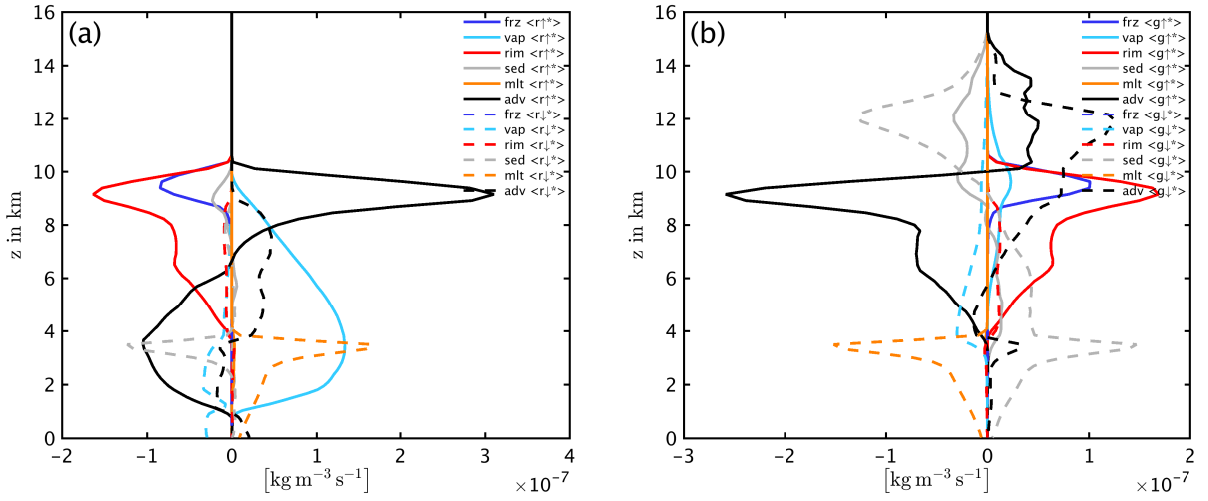


Fig. 4.4.: Microphysical process rates and tendencies of liquid mass (a) and ice mass (b) in lifting and sedimentation regimes. The rates are grouped into freezing (frz), exchange with the vapor phase (vap), riming (rim), sedimentation flux divergences (sed), melting (mlt), and three-dimensional advective tendencies (adv).

Liquid mass depletion and growth rates are shown in panel (a). During ascent, the only microphysical source of liquid mass is condensation which has its maximum around 0 °C. The most important liquid depletion mechanism is the riming, when cloud and rain drops collide with cloud ice, snow, graupel and hail. In turn, this is the largest growth factor of ice mass. In simulations without above-average mineral dust concentrations, significant liquid to ice conversion by freezing is restricted to the uppermost levels in which homogeneous freezing dominates. Sedimentation flux divergences of liquid are generally small except in the sedimentation regime of rain on top of the melting layer. After the initial growth period, the supercell as a whole may be regarded as a quasi steady state system which grows relatively slowly.

Therefore, the advective tendencies compensate the microphysical sources and sinks to a large extent. For example, the anvil region ($z > 10$ km, panel b), has a balance of sedimentation (gray) and advection (black), while the positive contribution of advection in the graupel sedimentation regime (dashed black, $z > 10$ km) is mainly horizontal from core regions into the convective outflow. Sedimentation fluxes and their divergence are generally much more important for the ice phase than for the liquid. Above 9 km, on average they deplete ice mass (negative sign), and tend to accumulate ice mass below (positive sign). For the sedimenting ice particles, mass loss by evaporation (dashed light blue) makes an important contribution to the amount of ice which finally reaches the melting levels ($z < 4$ km). Here the loss by melting is compensated by the sedimentation flux from above. Both sedimentation efficiency and evaporation efficiency depend on the mean masses of ice particles. For the changing precipitation fluxes with different ice nuclei concentrations it will be crucial how the sedimentation efficiencies of the two largest ice classes, graupel and hail, will be modified. These dependencies are the subject of section 6.1.

# 5. Freezing associated with cloud- and rain drop-immersed aerosol particles

As outlined in section 2.3, we expect the freezing properties of rain drops to depend on the number of collected cloud droplets (Fig. 2.3). This section will show the collection rates and simulated droplet properties as a result of the parameterizations presented in section 2.3. The simulation is based on the continental CCN scenario with $10^5\,\mathrm{m}^{-3}$ mineral dust particles and the u25q14 environment (Tab. 4.2).

## 5.1. Properties of droplets and immersed aerosols

In Fig. 5.1, panel (a) shows the contributions of cloud selfcollection, cloud autoconversion and accretion by rain which result in the conversion of cloud droplet-immersed CCN to rain droplet-immersed CCN. Values are averaged over updrafts ($< \mathrm{w}_5 >$, Tab. A.1). Accretion makes the highest contribution in all levels, with a maximum from 4 to 5 km corresponding to slight supercooling. The peak of the selfcollection contribution is below 4 km, when $N_c$ is larger than above. This rate describes the collision of two cloud droplets which are small enough to remain one cloud droplet ($D < 80\,\mu\mathrm{m}$), rather than being converted to rain ($D > 80\,\mu\mathrm{m}$). Although the mean rate is around $10^6\,\mathrm{m}^{-3}\,\mathrm{s}^{-1}$, this is rather small compared to the large $N_c$, therefore $\lambda_c$ is generally very small (see below), i.e., the number of CCN immersed in cloud droplets (given by $N_c + N_{coll,c}$) is not much larger than $N_c$. Finally, the autoconversion contribution to the accumulation of CCN in rain is very small compared to accretion.

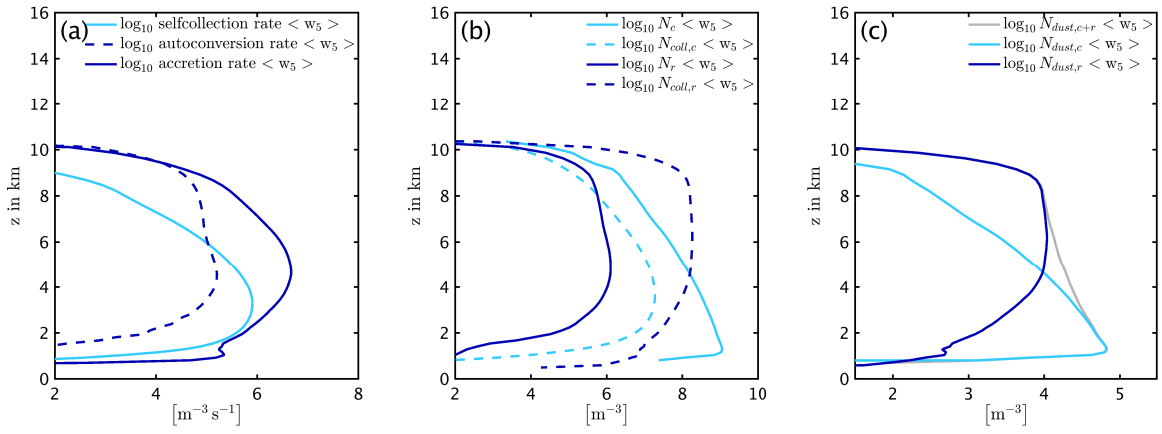


Fig. 5.1.: Collision rates of cloud and rain drops (a), number concentrations of cloud droplets, rain drops and collected particles (b) and number concentrations of cloud-immersed dust, rain-immersed dust and the sum of both (c). Shown are the vertical profiles averaged over updraft regimes $< \mathrm{w}_5 >$, and from 00:20 - 02:00 hours in time

The concentrations of collected CCN in cloud and rain drops are depicted in panel (b). In the convective core region, $N_{coll,r}$ is on average at least two orders of magnitude larger than $N_r$, i.e., rain drops contain on average more than 100 particles. This is different for cloud droplets which contain on average less than one collected CCN. Note that according to section 2.3.3, $N_{coll,c}$ here does not contain those CCN which activated the droplet at cloud base, therefore it can be smaller than $N_c$. The resulting mineral dust concentrations immersed in cloud and rain drops are shown in panel (c). It is calculated by multiplying the fraction of dust at the cloud base ($f_{dust,cb}$) with the total numbers of CCN:

$$N_{dust,c} = (N_c + N_{coll,c})\, f_{dust,cb} \quad [5.1]$$

$$N_{dust,r} = N_{coll,r}\, f_{dust,cb} \quad [5.2]$$

As expected, potential IN particles are slowly shifted from cloud to rain drops within the updraft. Here, they are equally-distributed ($N_{dust,c} \approx N_{dust,r}$) around the melting level, but this will depend on on several cloud properties like cloud base height, conversion efficiency and therefore the initial cloud droplet number, and updraft speed because in slower updrafts there is more time for conversion. At altitudes of the highest mineral dust immersion freezing activities, $N_{dust,c}$ is one to two orders of magnitude smaller than $N_{dust,r}$.

While horizontal averages representative for the core regions were shown above, a more detailed analysis is given in Figures 5.2 (a-c). The joint histograms a) and b) show the frequencies of occurrence of $\lambda_r$, which is the number of CCN per rain drop. The counts of occurrences are scaled by grid box volume such that each cubic meter corresponds to one count. In other words, each "event" within a grid box yields a number of counts which is equal to the grid box volume, on the order of $10^8\,\mathrm{m}^{-3}$. In panel (a), $\lambda_r$ as a function of temperature shows a high variability with values up to $10^6\,\mathrm{m}^{-3}$ CCN per drop, and even $10^8\,\mathrm{m}^{-3}$ in some exceptions. For a better interpretation, $\lambda_r$ is shown as a function of updraft velocity w in panel (b). Accordingly, these relatively high accumulations appear in updrafts with $w < 5\,\mathrm{m\,s}^{-1}$, i.e. when the drops are balanced within an updraft for a longer time in a quasi steady state. In stronger updrafts, mean CCN numbers per droplet are around $10^2\,\mathrm{m}^{-3}$ to $10^3\,\mathrm{m}^{-3}$. In panel (c), the concentrations of CCN per drop mass is expressed as mean diameters of collected droplets, i.e., the diameter corresponding to the the mean mass of collected droplets given by $x_{coll,r} = \frac{Q_r}{N_{coll,r}}$. It appears that this diameter peaks around 25-30 $\mu m$ in the core regions.

In Fig. 5.3, we show the number of collected CCN within cloud droplets as a result of selfcollection. Note that $\lambda_c = 0$ corresponds to exactly one particle per droplet. The majority of data indicates values smaller than 0.1, i.e., a weak contribution of selfcollection to $N_{coll,c}$, and therefore a minor contribution to $N_{coll,r}$ via autoconversion and accretion.

For an efficient freezing parameterization, it would be desirable not to track collection rates explicitly and not to use one or even two additional tracers for $N_{coll,r}$ and $N_{coll,c}$. Therefore the sharp peak of the mean diameter of collected droplets might be promising to parameterize $N_{coll,r}$ without explicit tracking. However, it is likely that these mean $D_{coll,r}$ are highly dependent on the cloud properties, such as initial $N_c$ and updraft velocity. Furthermore, in regions of evaporating rain drops, partly-evaporation of drop mass will lead to decreased $D_{coll,r}$. An example of a maritime simulation (CCN content of $100\,\mathrm{cm}^{-3}$) is given for comparison in Fig. 5.4. The different cloud and rain drop properties (panel a) are reflected in the resulting $D_{coll,r}$ (panel b) which is shifted to around 50 µm in the updraft regions. Cloud drops are rapidly depleted in the updraft, and above 5 km $N_r$ becomes larger than $N_c$.

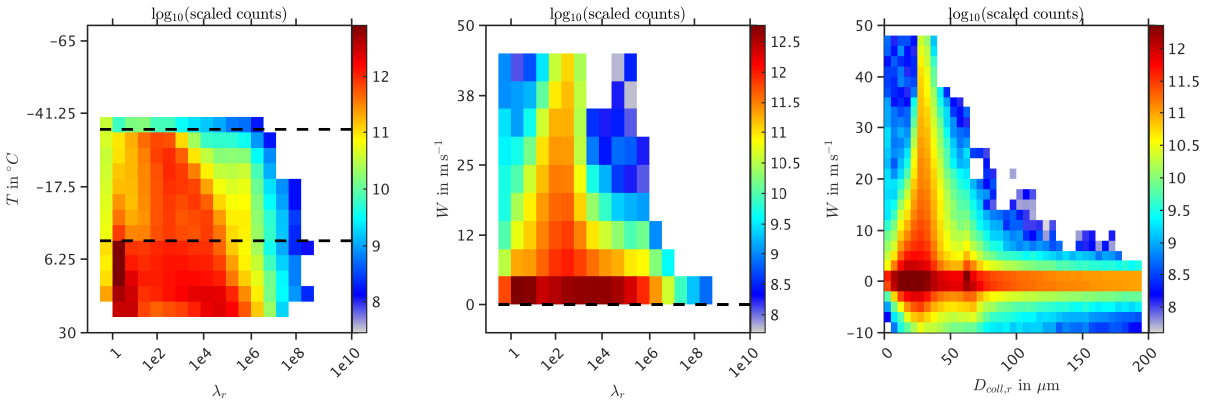


Fig. 5.2.: Mean number of collected CCN per rain drop ($\lambda_r$) shown as joint histograms as a function of temperature (a) and vertical velocity (b). In (c), the mean diameter of collected droplets ($D_{coll,r}$) contained within one rain drop is shown as a function of vertical velocity. The data contain all liquid-containing grid points from 00:20 - 02:00 hours, with 1 "count" corresponding to $1\,\mathrm{m}^{-3}$. Horizontal dashed lines indicate the levels of $0\,^{\circ}\mathrm{C}$ and $-36\,^{\circ}\mathrm{C}$.

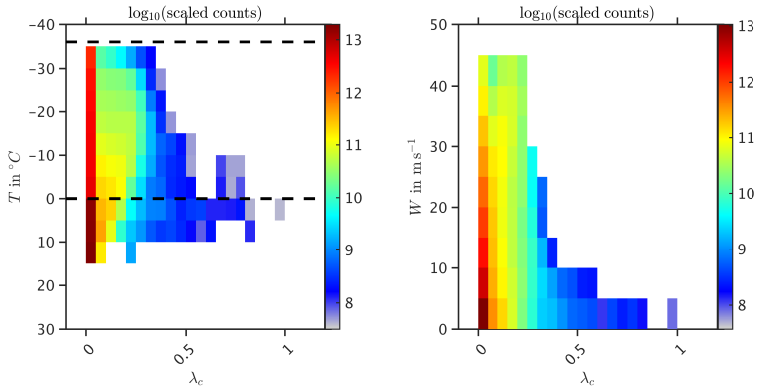


Fig. 5.3.: Mean number of collected CCN per cloud droplet ($\lambda_c$) shown as joint histograms as a function of temperature (a) and vertical velocity (b). The data contain all liquid-containing grid points from 00:20 - 02:00 hours, with 1 "count" corresponding to $1\,\mathrm{m}^{-3}$. Horizontal dashed lines indicate the levels of $0\,^{\circ}\mathrm{C}$ and $-36\,^{\circ}\mathrm{C}$.

Next, a sensitivity simulation is shown with a simplified treatment, neglecting sinks for both $N_{coll,c}$ and $N_{coll,r}$, the sedimentation of $N_{coll,r}$, and the effect of cloud selfcollection (i.e., $N_{coll,c} = 0$). Thus, only autoconversion and accretion influences the budget of $N_{coll,r}$, while assuming exactly one CCN per cloud droplet. Figure 5.5 compares the immersed dust concentrations of the sensitivity runs (full lines) to the reference run (dashed line). The overall differences are small between reference and simplified runs. The largest differences appear above 8 km where the disregarded sinks of $N_{coll,r}$ due to homogeneous freezing leave behind more dust immersed in rain drops. However, we can expect that these differences within the homogeneous freezing levels would hardly affect the results, since the homogeneous freezing rates increase very steeply with temperature and dominate over the heterogeneous contribution very quickly, thereby reducing the importance of any dust properties. $N_{dust,c}$ is slightly reduced because of $N_{coll,c} = 0$

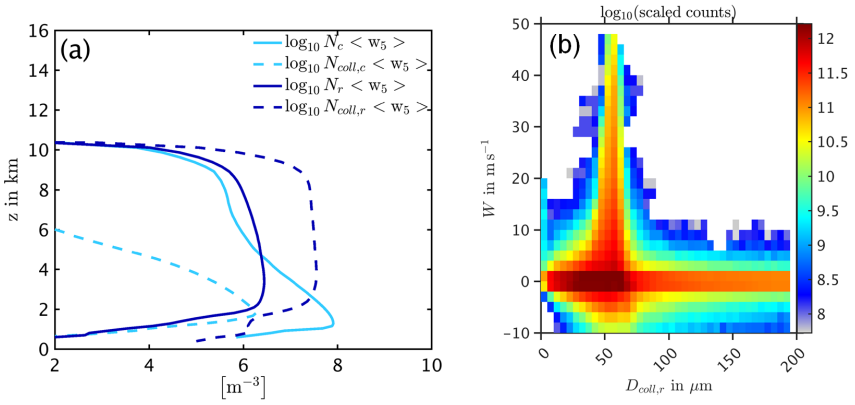


Fig. 5.4.: Maritime CCN conditions for comparison to the continental CCN conditions shown in Fig. 5.1 b) and Fig. 5.2: Number concentrations of cloud droplets, rain drops and collected CCN (a) and joint histogram of $D_{coll,r}$ as a function of vertical velocity (b).

by definition. Influences on the freezing rates are discussed below, underlining the conclusion that a simplified budgeting of $N_{coll,r}$ may be appropriate at least in strong updrafts when $w >> v_{sed}$. Note that for simplicity, the mean values shown in this section correspond to core regions ($< w_5 >$, Tab. A.1).

In cases of clouds with weaker vertical dynamics, where rain drops are approximately balanced by updrafts for a longer time, we can expect a more pronounced particle accumulation in these drops, and potentially higher sensitivity to simplified budgets.

As described in section 2.3.4, $f_{dust,cb}$ is assumed to be constant throughout the cloud due to the independence of the activation scheme on specific aerosol types. In case of prognostic $f_{dust,cb}$, the diagnosed concentrations of immersed IN are very sensitive to the calculation of $f_{dust,cb}$ during CCN activation, which seems to be the largest factor of uncertainty in these calculations.

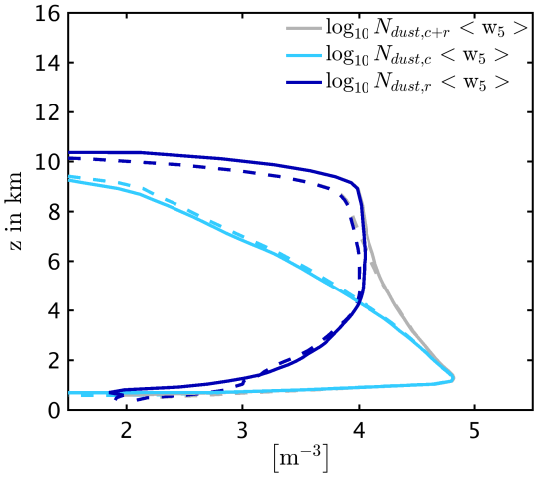


Fig. 5.5.: Cloud- and rain-immersed mineral dust concentrations in sensitivity simulations with simplified budgeting of collected particles. Dashed lines correspond to those shown in Fig. 5.1 c).

## 5.2. Cloud properties resulting from aerosol-dependent rain freezing (B53 vs. N12)

In this section, the simulated dust properties attributed to cloud and rain drops are used to determine the immersion freezing rates and subsequent microphysical processes. This will yield a comparison of simulated precipitation resulting from the aerosol-independent B53-based approach and the mineral dust-dependent N12-based parameterization, as introduced in section 2.3.2.

### 5.2.1. Freezing rates

Although in section 2.3.5 the PSD splitting method was identified as our default method to parameterize rain drop freezing rates, here we begin without the consideration of PSD splitting, treating the bulk rain spectrum as a whole. The effect of PSD splitting and further sensitivity studies is shown below in this section (Fig. 5.8). At this point, we note that the primary effect is found for the formation rates of hail particles which is modified by a factor of 2.

#### Rain drop freezing rates

Figure 5.6 compares the freezing rates of rain from the updated IN-dependent parameterization (N12, full lines) with the volume-dependent default parameterization (B53, dashed lines). Panels (a-c) are the results for different ice nuclei concentrations, with $N_{dust}$ ranging from $10^4\,\mathrm{m}^{-3}$ to $10^6\,\mathrm{m}^{-3}$.

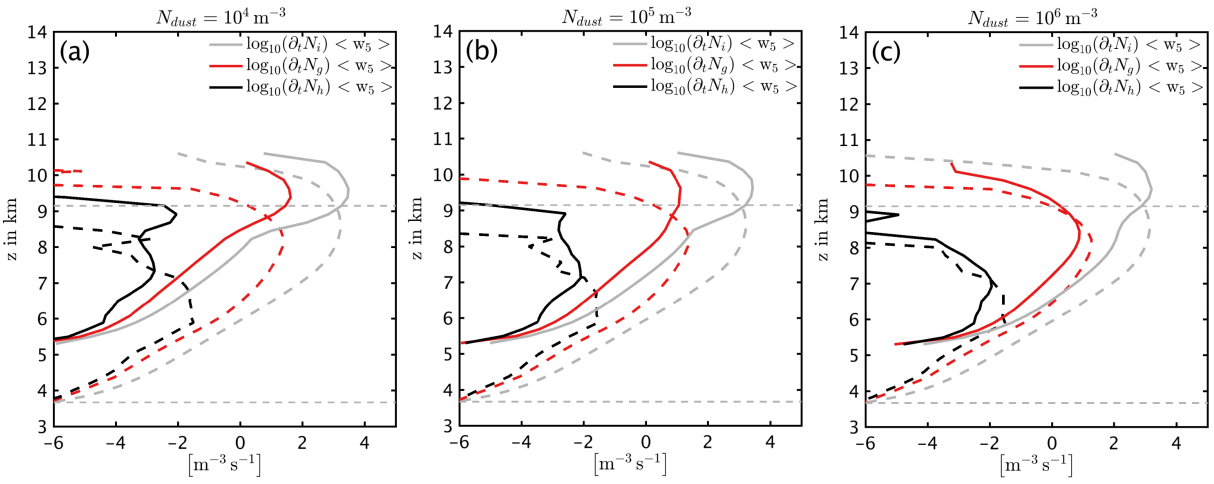


Fig. 5.6.: Formation rates of cloud ice, graupel and hail by freezing rain with $N_{dust} = 10^4\,\mathrm{m}^{-3}$ (a), $N_{dust} = 10^5\,\mathrm{m}^{-3}$ (b) and $N_{dust} = 10^6\,\mathrm{m}^{-3}$ (c). Dashed lines result from B53, and full lines from the new N12-based implementation. Horizontal dashed lines indicate the levels of 0 °C and −36 °C.

A general property of the B53 freezing is that it starts to form ice at 0 °C, while ice nucleation on mineral dust particles is parameterized for temperatures lower than −12 °C. With increasing dust, the ice formation rates with N12 tend to become more similar to the B53 approach, but are smaller even with $10^6\,\mathrm{m}^{-3}$ dust particles. With $10^6\,\mathrm{m}^{-3}$, the cloud ice formation rates by homogeneous freezing of rain (z > 9 km) compared to the mineral dust contribution (z < 9 km). The magnitude of the homogeneous freezing peak is nearly independent of the dust concentration, indicating that even with the highest con-

centration the number of small drops cannot be reduced significantly by freezing. A higher dependence of upper-level freezing rates on the immersion freezing efficiency is found for graupel, and particularly hail formation. With less dust, more ice is formed in these upper levels because of a less efficient depletion of large rain drops. Except for the lowest dust concentrations (a), hail is most efficiently formed in the heterogeneous freezing region.

### Cloud droplet freezing rates

Without the model extensions implemented in the course of this work, the default assumption is that every activated ice nucleating particle corresponds to one freezing cloud droplet. In Fig. 5.1 it was shown that in upper levels, the dust concentration within cloud droplets is reduced by one to two orders of magnitude, implying that the default assumption would overestimate the cloud droplet freezing rates by the same factor. Panel (a) compares the difference between cloud droplet freezing rates with and without accounting for the redistribution of IN from cloud to rain drops. Consistent with Fig. 5.1, the heterogeneous cloud droplet freezing rates are reduced by roughly two orders of magnitude compared to the default assumption (dashed light blue line). At the warmest freezing temperatures around $-12\,^{\circ}$C, cloud and rain drops contribute equally to small ice formation, but rain becomes more important in upper levels (dark blue). Only above 8 km, the cloud droplet contribution becomes larger than the rain contribution because in the homogeneous freezing regime, the pure number concentration dominates (see also Fig. 4.3 for drop concentrations). For comparison, also the production of secondary ice according to Hallett and Mossop (1974) at levels around 5 km is shown for comparison. This narrow peak is is also reflected in the ice concentrations (see Fig. 5.9, section 5.2.2).

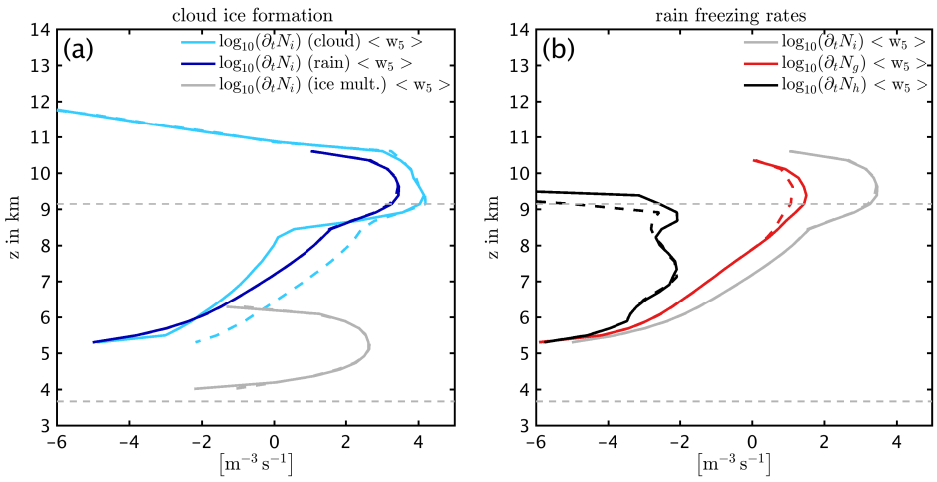


Fig. 5.7.: Comparison of freezing rates when accounting for reduced cloud-immersed dust (full lines) and with all dust particles attributed to cloud droplets (dashed lines). Both simulations are based on N12 with $N_{dust} = 10^5\,m^{-3}$. Panel (a) summarizes the rates of cloud droplet freezing, rain drop freezing and secondary ice formation, while in (b) the freezing rates of rain are split into the three resulting particle classes. Horizontal dashed lines indicate the levels of $0\,^{\circ}$C and $-36\,^{\circ}$C.

In panel (b), the effect of reduced cloud droplet freezing on the rain freezing rates is shown. When less cloud droplets freeze below 8 km, it appears that the graupel and hail formation is enhanced (full lines).

Although not shown, a possible reason for this behavior may be the enhanced growth of rain drops by accretion of more cloud drops.

Although the cloud droplet freezing rate in the heterogeneous freezing regime and upper-level graupel formation is modified, the influence on, e.g., sedimentation fluxes of graupel and hail in N12-based simulations are relatively small whether or not the reduced number of cloud-immersed dust due to conversion is considered (not shown). Therefore, the most important difference between B53 and N12 arises from the sensitivity of rain freezing, rather than from the cloud drop freezing.

### Sensitivity simulations

Based on this version of the freezing parameterization, further simulations have been conducted to estimate the sensitivity to

- a simplified budgeting with $N_{coll,c} = 0$, no sinks and no sedimentation for $N_{coll,r}$ (section 2.3.3)
- the disregard of the sedimentation velocity during the freezing process (eq. 2.25)
- rain PSD splitting for the freezing parameterization (eqs. 2.30 - 2.35).

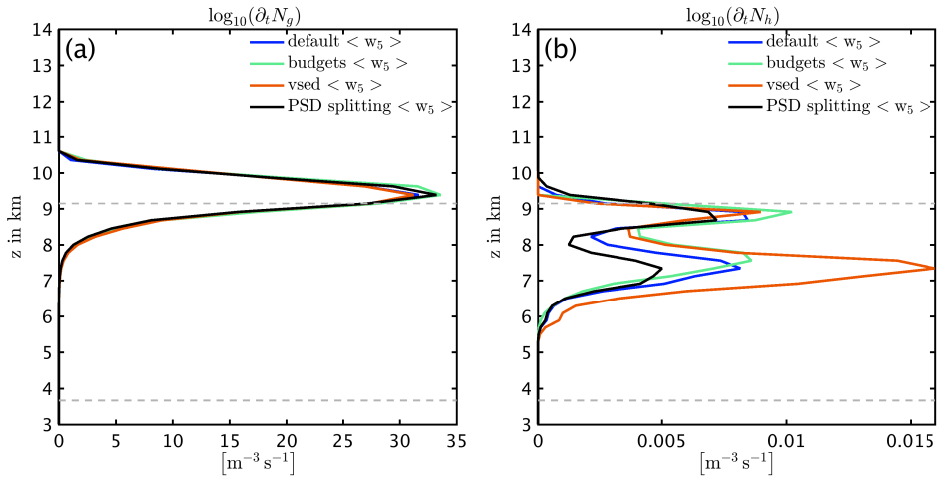


Fig. 5.8.: Graupel (a) and hail (b) formation rates by freezing rain, shown for the default version, simplified budgeting, negleted sedimentation velocities, and additional PSD splitting. The "default" corresponds to the simulation as presented above in this section. Horizontal dashed lines indicate the levels of 0 °C and −36 °C.

Figure 5.8 illustrates the sensitivities of graupel and hail formation rates, while cloud ice rates are hardly affected by the different treatments (not shown). Hail formation – which involves the largest drops – is generally most sensitive to the different versions. The "default" version (blue line) shows the profiles which have been analyzed above in this section. As expected from Fig. 5.5, the simplified budgeting of $N_{coll,c/r}$ makes only minor differences (green line). However, accounting for the drop sedimentation of large drops appears to be important: With $v_{sed} = 0$ by definition, the cooling rates of large drops are overestimated, and therefore hail formation in mid levels (panel b, orange line) is twice as large as the reference. By including PSD splitting, the rates are further reduced (black). On the one hand, for a given dust concentration, multiple IN per drop reduce the number of freezing drops. On the other hand, with

PSD splitting the effect of smaller cooling rates of larger drops becomes more pronounced. Note that the simulations shown here are based on $N_{dust} = 10^5\,\mathrm{m}^{-3}$, while the effect of multiple IN per drop will be more pronounced with higher concentrations. This will be relevant in chapter 6.

#### Comparison with explicit IN depletion

A brief sanity check of the new freezing parameterization is summarized in the following. This test may be interpreted as a comparison of the explicit ice nuclei depletion approach as presented in earlier work (Paukert and Hoose, 2014a) and the "cooling rate approach" presented in this work. For this purpose, eq. 2.25 is adopted for cloud droplets, while consideration of PSD splitting and sedimentation is not necessary here.

The cloud droplet freezing rates resulting from the two different methods show good agreement. Eq. 2.25 yields slightly smaller rates (on the order of 10%) in most of the mixed-phase regimes. This is associated with the difference between the moist adiabatic temperature gradient and the actual grid-scale temperature gradient in the model (relevant to the explicit IN depletion approach). Only in in the regions of the coldest mixed-phase temperatures, eq. 2.25 yields larger freezing rates up to a factor of 10 in some extreme cases, compared to the explicit depletion. However this occurs only in regions of dominant homogeneous droplet freezing, i.e., where the contribution of immersion freezing is rather irrelevant.

Although the differences appear to be of minor importance for this convective case, the explicit representation of IN depletion is still justified in cases when a liquid-containing parcel oscillates vertically, such as Arctic stratocumulus clouds or orographically induced waves. Furthermore, entrainment of unactivated particles at cloud edges cannot be mimicked without IN depletion, which may also contribute to the small difference described here.

### 5.2.2. Ice particle concentrations and sedimentation fluxes

An overview of the resulting differences in the number concentrations of small ice, graupel and hail is given in Fig. 5.9, representative for updraft regions (Tab. A.1).

The concentration of cloud ice shows a local maximum at 5 km which arises from the contribution of ice multiplication (see also Fig. 5.7), based on Hallett and Mossop (1974). This maximum is not very sensitive to the changes introduced by the different immersion freezing treatments, therefore the cloud ice concentration reduction in the immersion freezing regime is not as pronounced as might be expected from the immersion freezing rates when comparing B53 and N12 (Fig. 5.6, 5.7). Also the numbers above the homogeneous freezing level are reduced, indicating less cloud droplets reaching the levels colder than $-36\,^{\circ}\mathrm{C}$. This aspect will be discussed in detail in the radiation section (6.2). Graupel behaves as expected from Fig. 5.6, with less particles below 9 km and more particles above the homogeneous freezing level. Hail numbers are reduced throughout the updraft, i.e., the larger rates at $z > 8$ km cannot compensate the smaller rates below (Fig. 5.6).

Although the number changes do not appear to be dramatic, they have important implications for the growth of large precipitating particles by riming and subsequent sedimentation properties. As a motivation for further discussions of microphysical aspects, the resulting precipitation fluxes are introduced next.

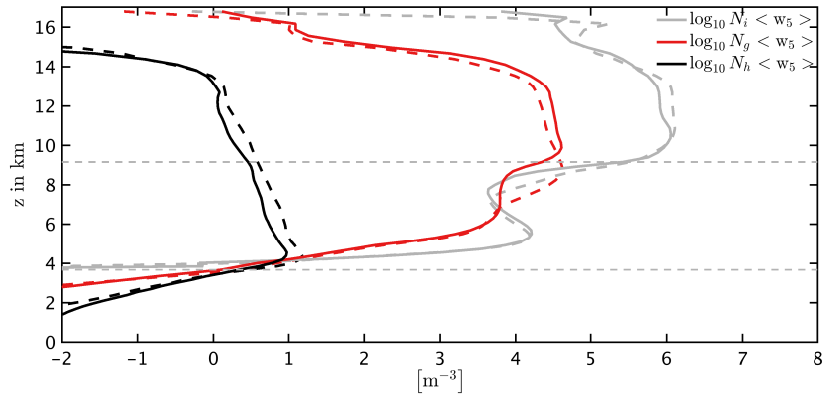


Fig. 5.9.: Number concentrations of cloud ice, graupel and hail as a comparison of the B53-based freezing (dashed lines) and N12-based freezing (full lines), with $N_{dust} = 10^5\,\mathrm{m}^{-3}$. Horizontal dashed lines indicate the levels of 0 °C and −36 °C.

Figure 5.10 shows domain-averaged sedimentation fluxes. The "effective" fluxes of rain ($R_\downarrow$), graupel ($G_\downarrow$) and hail ($H_\downarrow$) account only for those regions in which mass effectively sediments (Tab. A.1), while considering the vertical advection. Therefore, the flux of particle class $x$ is calculated as $(v_{qx} - w)\,Q_x$, with $v_{qx}$ being the sedimentation velocity of the first moment of $x$ (positive downwards).

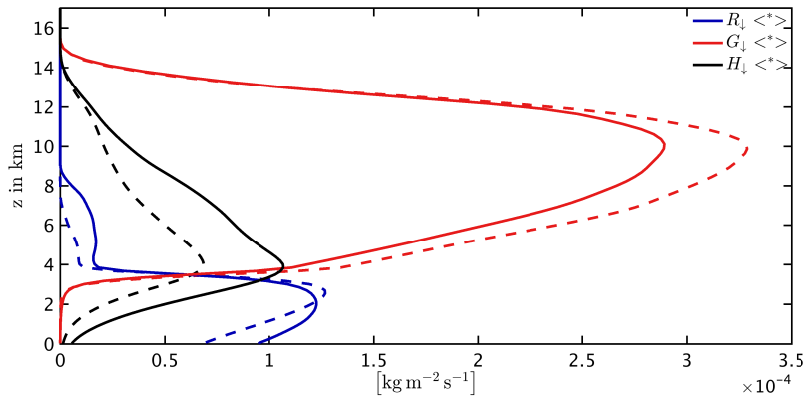


Fig. 5.10.: Effective sedimentation fluxes of cloud ice, snow, graupel, hail and rain as a comparison of the B53-based freezing (dashed lines) and N12-based freezing (full lines), with $N_{dust} = 10^5\,\mathrm{m}^{-3}$.

The rain flux (blue) can be divided into two distinct regimes which is the horizontally widespread area below 4 km corresponding to the melting regime, and rain at the edges of the convective core in regions of small positive and negative vertical velocities. At z > 4 km, it is evident that the N12 freezing leaves behind more rain mass (full line). Particularly in the sedimenting regime, this is also a result of the $v_{sed}$-dependent freezing rates. In the melting regime, there is a narrow band of smaller rain flux compared to B53 (dashed), corresponding to the smaller graupel flux arriving from aloft. Although the magnitude of the graupel flux is similar to the hail at 4 km, graupel particles melt efficiently, therefore their contribution to the rain formation is restricted to a narrow region. In contrast, the few but large hail

particles sediment very efficiently, enabling them to contribute to rain formation down to ground levels. Overall, the surface flux of rain is larger with N12 than with B53 (dashed), owing to the enhanced growth of hail within the convective core.

Generally, graupel and hail flux changes have opposite signs when the immersion freezing efficiency is modified. As shown in section 6.1, only with extremely efficient immersion freezing, graupel flux changes tend to have a reversed sign and act in the same direction as hail. With smaller immersion freezing rates (N12), the hail flux is significantly larger although it was shown that the hail number is smaller throughout the updraft, implying significantly larger mean particle masses. With the higher upper-level graupel number density and lower mass density as described below, graupel sedimentation efficiency is decreased. Snow hardly contributes to melting because it evaporates below the anvil, and the same applies for cloud ice (Fig. 4.3).

The largest relative flux changes are found for hail which is up to more than a factor of 5 larger near ground with N12. However, these differences can be strongly time-dependent with a tendency of decreased relative differences at later times (see also section 6.1.5). The microphysical interactions which determine the precipitation sensitivity to the efficiency of immersion freezing are discussed in detail in section 6.1. Therefore, we skip a more detailed discussion of the differences between B53- and N12-based freezing at this point, as the basic mechanisms are similar.

## 5.3. Summary

In this chapter, we compared the freezing rates and resulting microphysical properties which result from the IN-independent approach following Bigg (1953) and the mineral dust-based immersion freezing according to the dust properties of Niemand et al. (2012). The explicit aerosol dependence of rain drop immersion freezing was calculated based on the droplet microphysical history. By tracking the droplet collisions in the simulated cloud, it was found that in the regimes most relevant for immersion freezing, the majority of potential IN is contained in rain drops.

Technically, we concluded that rain PSD splitting is an improvement particularly for the freezing probability of large particles, and therefore precipitation formation. A detailed budgeting of $N_{coll,c/r}$ appears to be of secondary importance, but is included in our simulations.

With cloud-base mineral dust concentrations ranging from $10^4\,\mathrm{m}^{-3}$ to $10^6\,\mathrm{m}^{-3}$, the dust-based freezing rates are generally smaller than B53-based rates. This has important implications for the relative importances of homogeneous and heterogeneous freezing: While the efficient B53-based drop freezing depletes the majority of liquid mass below the homogeneous freezing regime, large amounts of rain-sized drops ($D > 80\,\mu\mathrm{m}$) can reach these levels when heterogeneous freezing is triggered by dust only. Generally, the largest contribution to the total number of freezing drops originates from drops smaller than $500\,\mu\mathrm{m}$ which are converted to cloud ice. Larger drops are converted to graupel and hail particles.

The smaller efficiency of liquid mass depletion resulting from the dust-based freezing has some implications for the formation of surface precipitation: With more liquid present, hail particles grow more efficiently by riming, while the growth of graupel particles is less efficient. Depending on the relative contributions of graupel and hail, the surface precipitation can be both increased or decreased. The importance of this antagonism will be further discussed in section 6.1.

The finding of many rain-sized drops up to the homogeneous freezing regime may be specific to very strong convection, as present in our simulations (see chapter 4 for a summary of cloud properties). In weaker convection and with inefficient immersion freezing, large drops may not be able to reach high altitudes because of gravitational settling on the one hand – for example, 500 µm-sized drops may fall with 2-3 $\mathrm{m\,s^{-1}}$, a drop of 1mm diameter would fall with approximately 5 $\mathrm{m\,s^{-1}}$, and the largest drops may reach nearly 10 $\mathrm{m\,s^{-1}}$ (Seifert et al., 2014, supplement Fig. 3). On the other hand, the probability of drop depletion by riming may be enhanced in weak updrafts, since the time to reach colder levels increases. Further discussions of these aspects, and implications for atmospheric IN concentrations, will be the subject of the overall conclusions of this work (section 7.2).

# 6. Cloud sensitivities to ice nuclei perturbations

In this chapter we analyze in detail the dependency of the microphysical states on mineral dust concentrations, derived from the "perturbed microphysics" (PM) approach (section 2.5). In this chapter, the perturbed dust concentrations $N_{dust,1/2}$ are defined as the relative deviations of $\pm 90\%$ of $N_{dust,0}$, resulting in a factor of 19 between the two perturbed microphysical states. The notation used here is summarized in section 2.5.3. $N_{dust,0}$ ranges from $10^4\,\mathrm{m}^{-3}$ to $10^8\,\mathrm{m}^{-3}$ with a stepping of a factor of 10.

For the interpretation of horizontally averaged vertical profiles (e.g., microphysical rates), we divide the cloud volume into two distinct regions, i.e., updraft regions ("lifting regimes", Tab. A.1) and regions with low positive or negative vertical velocities. The interactions occurring in the lifting regime can be interpreted as a trigger or determinant for the particle properties in the sedimentation regime. The latter is relevant for the surface precipitation formation by melting.

## 6.1. Precipitation

### 6.1.1. Sedimentation fluxes

Fig. 6.1 illustrates the mass fluxes in the sedimentation regimes of rain, graupel and hail. Unless otherwise stated, the vertical profiles are time-averaged between 00:20 and 02:00 hours in the following. As in section 5.2.2, the "effective" mass fluxes $R_\downarrow$, $G_\downarrow$, $H_\downarrow$ consider the grid-scale vertical transport, and disregard the lifting regions.

In panel (a.1), the surface precipitation decreases with increased dust concentrations. However, the differences are relatively small with low $N_{dust,0}$ concentrations. This behavior is also reflected in panels (a.2) and (a.3), where the absolute and relative surface flux changes are close to zero for the two lowest dust concentrations, $10^4\,\mathrm{m}^{-3}$ and $10^5\,\mathrm{m}^{-3}$. These two cases have positive flux changes within the whole melting region ($z < 4\,\mathrm{km}$), while the other cases with a surface flux reduction show positive changes in upper layers, and negative changes near the surface. This is the result of the interplay between melting graupel and hail as described in section 5.2.2. In particular, higher $N_{dust,0}$ simulations show a more dominant hail contribution in the lower melting regions (c.3) and a less dominant graupel contribution (b.3, $z > 4\,\mathrm{km}$).

The highest $N_{dust,0}$ results in the largest graupel fluxes (b.1) and smallest hail fluxes (c.1). This is consistent with the above comparison of B53 vs. N12 which basically illustrated the effects of different rain immersion freezing efficiencies. The relative changes are particularly large for the hail fluxes (c.3), resulting in a reduction of up to 55% due to increased mineral dust concentration by a factor of 19.

Next, graupel and hail properties are characterized with varying $N_{dust,0}$. In particular, it will be shown why graupel flux changes (absolute and relative) have a maximum in a specific range of $N_{dust,0}$, and why relative hail flux changes continue to grow with higher $N_{dust,0}$. In both cases, the efficiency of rain depletion in the convective updraft is crucial, triggered by the immersion freezing efficiency.

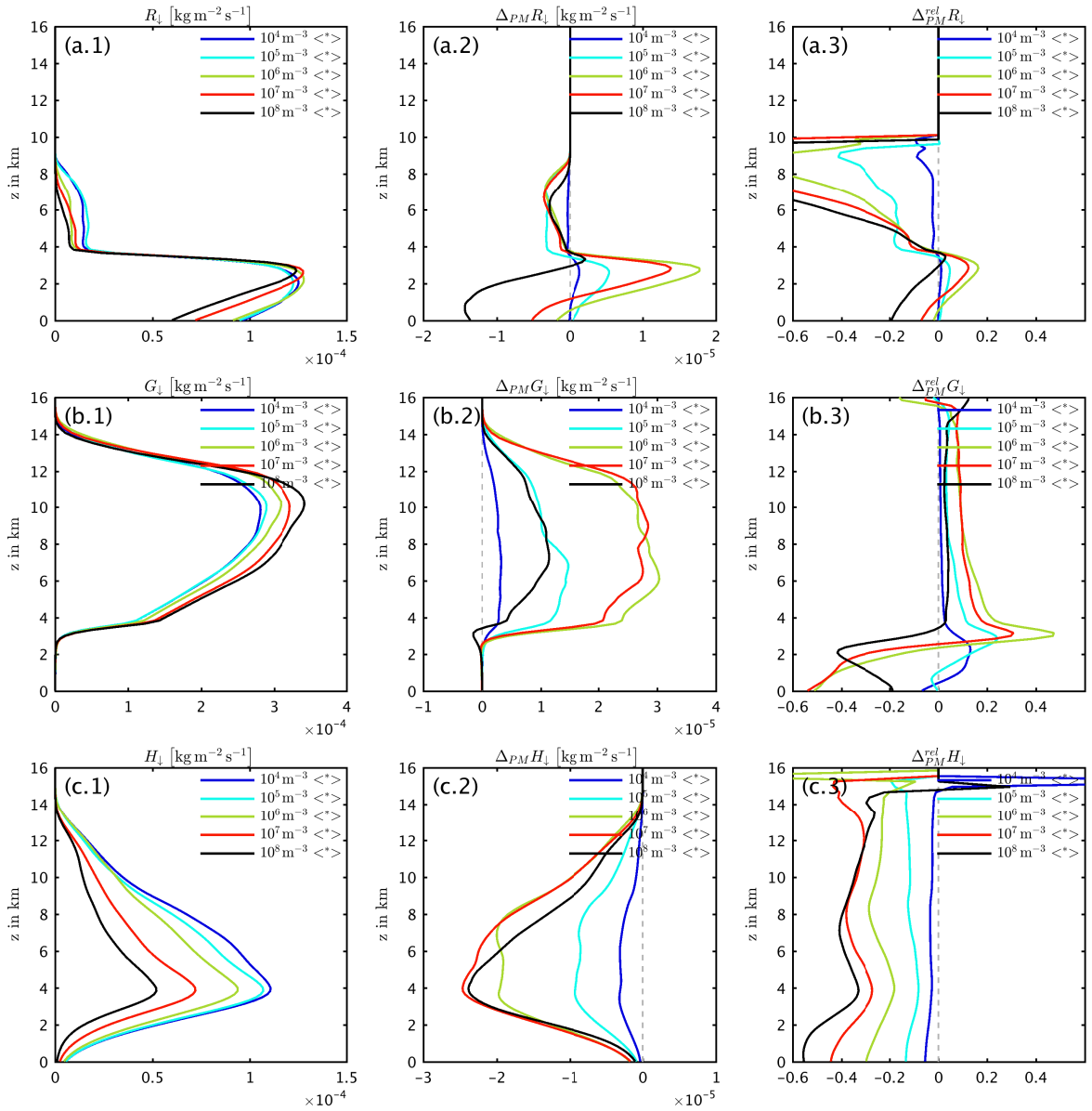


Fig. 6.1.: Sedimentation fluxes of rain (a.*), graupel (b.*) and hail (c.*). The vertical profiles show the base states (*.1), absolute changes (*.2) and relative changes (*.3) resulting from ice nuclei perturbations. Each color corresponds to mineral dust background concentrations ranging from $10^4\,\mathrm{m}^{-3}$ to $10^8\,\mathrm{m}^{-3}$.

### 6.1.2. Graupel properties

Figure 6.2 displays graupel mass and number concentrations averaged over lifting regimes, each line corresponding to a specific mineral dust background.

With $N_{dust,0}$ varying by 4 orders of magnitude, it may be surprising that the graupel masses are found within a factor of 2 at most (a.1). In Panel (a.2), $\Delta_{PM}Q_g$ becomes increasingly larger with increasing $N_{dust,0}$ in the three simulations with lowest $N_{dust,0}$. This is different among the three highest $N_{dust,0}$, where the maximum gain of mass is similar. It is related to the efficiency of rain mass depletion by

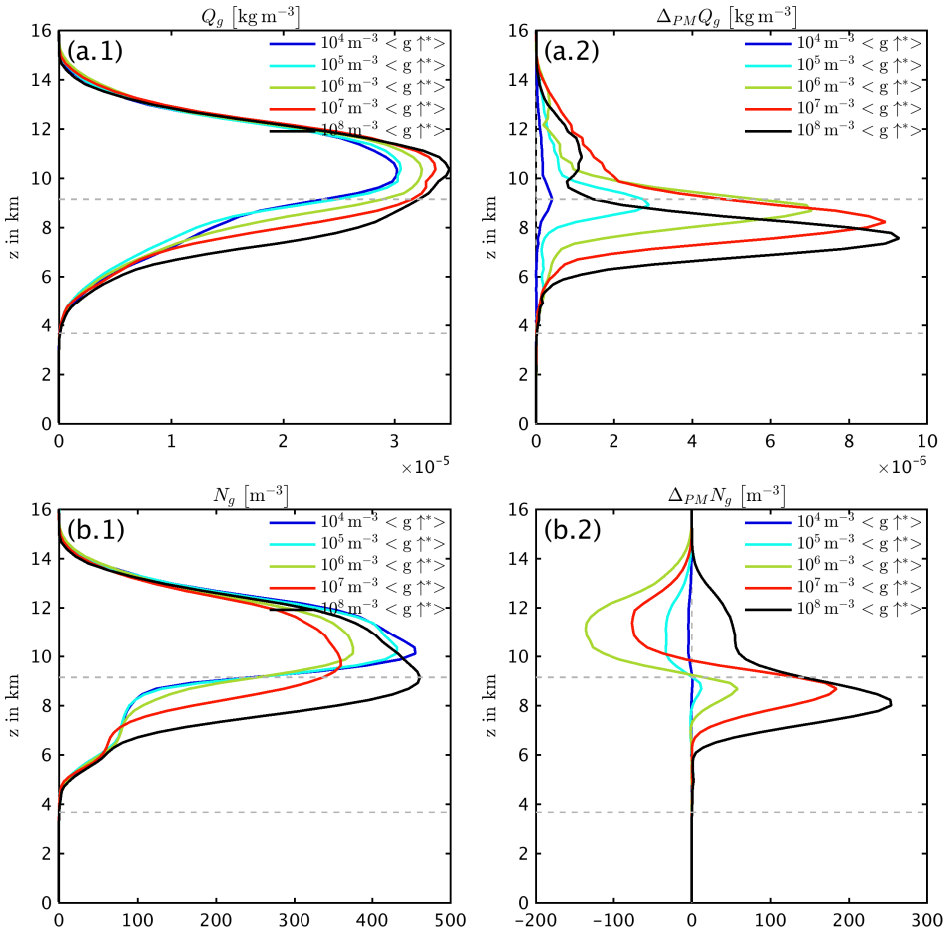


Fig. 6.2.: Graupel mass concentrations (a.*) and number concentrations (b.*), shown as vertical profiles of base states (*.1), and absolute changes (*.2) resulting from ice nuclei perturbations. Each color corresponds to mineral dust background concentrations ranging from $10^4\,\mathrm{m}^{-3}$ to $10^8\,\mathrm{m}^{-3}$. Horizontal dashed lines indicate the levels of 0 °C and −36 °C.

riming, as shown below. The mechanism of rain depletion becomes more important with high $N_{dust,0}$ when homogeneous freezing becomes less important relative to immersion freezing.

Graupel number perturbations are more complex than mass perturbations. The general tendency is an increase in lower levels and a decrease in upper levels (b.2). The upper-level reduction (z > 9 km) increases in magnitude with more $N_{dust,0}$ and favors enhanced sedimentation efficiencies due to larger mean masses. However, with $N_{dust,0}$ becoming larger than some threshold ($10^6 - 10^7\,\mathrm{m}^{-3}$), the reduction becomes smaller in magnitude ($10^7\,\mathrm{m}^{-3}$) and finally changes its sign ($10^8\,\mathrm{m}^{-3}$). Although mass changes in these levels are positive in all cases (Fig. 6.2), the more numerous particles in case of $N_{dust,0} = 10^8\,\mathrm{m}^{-3}$ counteract the mass change by reducing the mean mass (and fall velocity) which decreases the relative flux enhancement of graupel (b.3 in Fig. 6.1).

Overall, the largest graupel flux enhancement is found with $N_{dust,0} = 10^6\,\mathrm{m}^{-3}$ in these simulations, with increased mass and decreased number densities in upper levels. Mass gain in upper levels and the

concurrent number reduction in the perturbed states of $N_{dust,0} = 10^6\,\mathrm{m}^{-3}$ and $10^7\,\mathrm{m}^{-3}$ simulations is not independent of each other. The underlying mechanisms are shown in the following.

For the freezing rates we have already seen that more efficient freezing in lower levels is generally connected with smaller rates further above because of the enhanced rain mass depletion in lower levels. Similar dependencies exist for the gain of graupel mass by riming which has two main contributions. The largest rates originate from the growth of pre-existing graupel by collision with cloud and rain drops. The second important mechanism is graupel formation by collisions of cloud ice with rain drops. In the latter case, also the graupel number density increases in addition to mass. Figure 6.3 displays these two graupel mass sources.

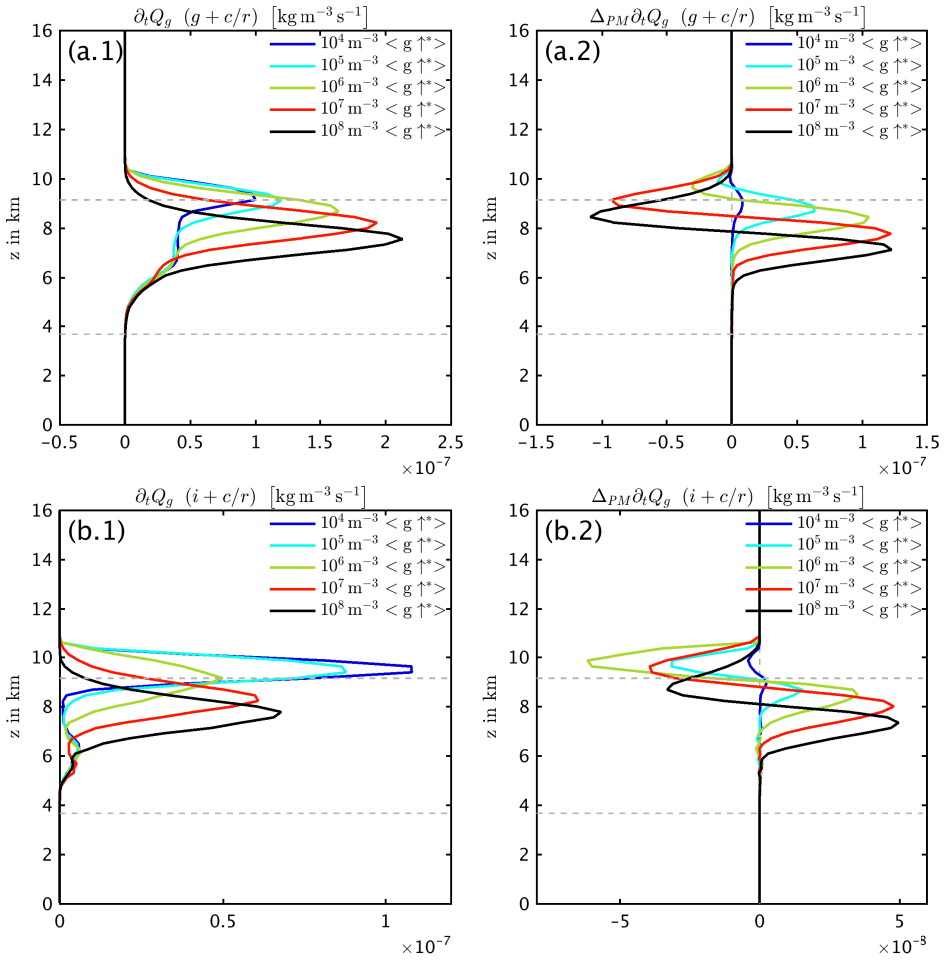


Fig. 6.3.: Riming rates of pre-existing graupel (a.*) and cloud ice (b.*). The vertical profiles show the base states (*.1) and absolute changes (*.2) resulting from ice nuclei perturbations. Each color corresponds to mineral dust background concentrations ranging from $10^4\,\mathrm{m}^{-3}$ to $10^8\,\mathrm{m}^{-3}$. Horizontal dashed lines indicate the levels of $0\,^\circ\mathrm{C}$ and $-36\,^\circ\mathrm{C}$.

Mass accumulation by riming of pre-existing graupel is most important (a.1). The maximum rates increase with more ice nuclei present, and the peak is shifted downwards in altitude. An important feature is the $N_{dust,0}$-dependence of the $\Delta_{PM}$-profiles (a.2). With low $N_{dust,0}$, there is only a small negative contribution in upper levels, i.e. the mass gain in lower levels is larger than the loss of mass aloft. This

is different with higher $N_{dust,0}$, i.e the lower-level gain stagnates while upper-level loss increases further. With $N_{dust,0} = 10^8\,\mathrm{m}^{-3}$, the overall $\Delta_{PM}\frac{\partial Q}{\partial t}$ by riming may be even negative which explains the smaller magnitude of $\Delta_{PM}Q_g$ with $N_{dust,0} = 10^8\,\mathrm{m}^{-3}$ compared to $10^7\,\mathrm{m}^{-3}$ (Fig. 6.2 a.2). The stagnating growth rates in lower levels – particularly in the $10^8\,\mathrm{m}^{-3}$ simulation – are much related to the limited amount of rain mass, i.e., the magnitude of $\Delta_{PM}Q_r$ becomes nearly es large as the base state rain mass (not shown). It may be asked whether the stagnation is a limitation of the model approach, induced by the relatively large dust perturbation of $N_{dust,0}\pm 90\%$. In section 6.1.7, we show that the general sensitivities are not influenced much by the exact definition of the IN perturbation, and there is no indication for an increasing divergence particularly with the largest $N_{dust,0}$.

The graupel formation by cloud ice riming (b.1/2) is of minor importance as a contributor to graupel mass changes. However, it modulates the number budget of graupel, and the dependence on $N_{dust,0}$ indicates a regime change (b.1) which may act as an explanation for the behavior of graupel number perturbations discussed above (Fig. 6.2 b.2). In the following, the connection of $\Delta_{PM}N_g$, rain and cloud ice properties will be discussed.

The prerequisite for graupel formation by cloud ice riming is the presence of large rain drops which is limited by the depletion mechanism in case of high $N_{dust,0}$. Thus, the condition for graupel formation by cloud ice riming being susceptible to ice nuclei perturbations is the overlap of large rain drop containing regions with the homogeneous freezing level where presence of cloud ice increases steeply. From $N_{dust,0} = 10^4\,\mathrm{m}^{-3}$ to $10^6\,\mathrm{m}^{-3}$, the peak of cloud ice riming becomes smaller, but becomes larger from $N_{dust,0} = 10^6\,\mathrm{m}^{-3}$ to $10^8\,\mathrm{m}^{-3}$ (panel b.1). This is reflected in $\Delta_{PM}$ of the rates, where low-$N_{dust,0}$ simulations have a larger loss in upper levels than is gained in lower levels, and high-$N_{dust,0}$ simulations have a larger gain in low levels. The turning point (i.e., regime change) is found between $N_{dust,0} = 10^6\,\mathrm{m}^{-3}$ and $10^7\,\mathrm{m}^{-3}$, respectively. This is consistent with the turning point of $\Delta_{PM}N_g$ (Fig. 6.2), beyond which the upper-level reduction of $N_g$ becomes smaller in magnitude with higher $N_{dust,0}$. Thus, beyond this turning point, the depletion of rain mass is effective enough to reduce the presence of large drops in the homogeneous freezing regime, thereby reducing the sensitivity of graupel formation in upper levels (b.2).

At the same time, in case of the highest $N_{dust,0}$, the heterogeneous ice formation as well as graupel formation become relatively strong in the "positive" regime. This means that the lower-level formation of graupel by either freezing or the riming of cloud ice (and corresponding positive number perturbations) becomes dominant compared to the upper-level effects. Therefore, with $N_{dust,0} = 10^8\,\mathrm{m}^{-3}$ in Fig. 6.2 b.2), we find larger graupel number concentration in the perturbed microphysical state in all levels.

Of course, graupel formation by cloud ice riming is also present below the homogeneous freezing level. There are also cloud ice particles from both immersion freezing and secondary production (Fig. 5.9) below 9 km, but with a considerably smaller number concentration than above 9 km. This explains the reversed trend of the peaking rates from $N_{dust,0} = 10^6\,\mathrm{m}^{-3}$ to $10^8\,\mathrm{m}^{-3}$ (b.1) because with $N_{dust,0} > 10^6\,\mathrm{m}^{-3}$, the lower-level ice number concentrations become sensitive to the dust perturbation. In contrast, the cloud ice concentrations in the heterogeneous freezing regime are dominated by ice multiplication with small $N_{dust,0}$ (Fig. 5.9).

### 6.1.3. Hail properties

Besides graupel, the second contributor to surface rain formation is the hail particle class. First, we focus on hail mass densities in hail lifting regimes depending on $N_{dust,0}$ (Fig. 6.4).

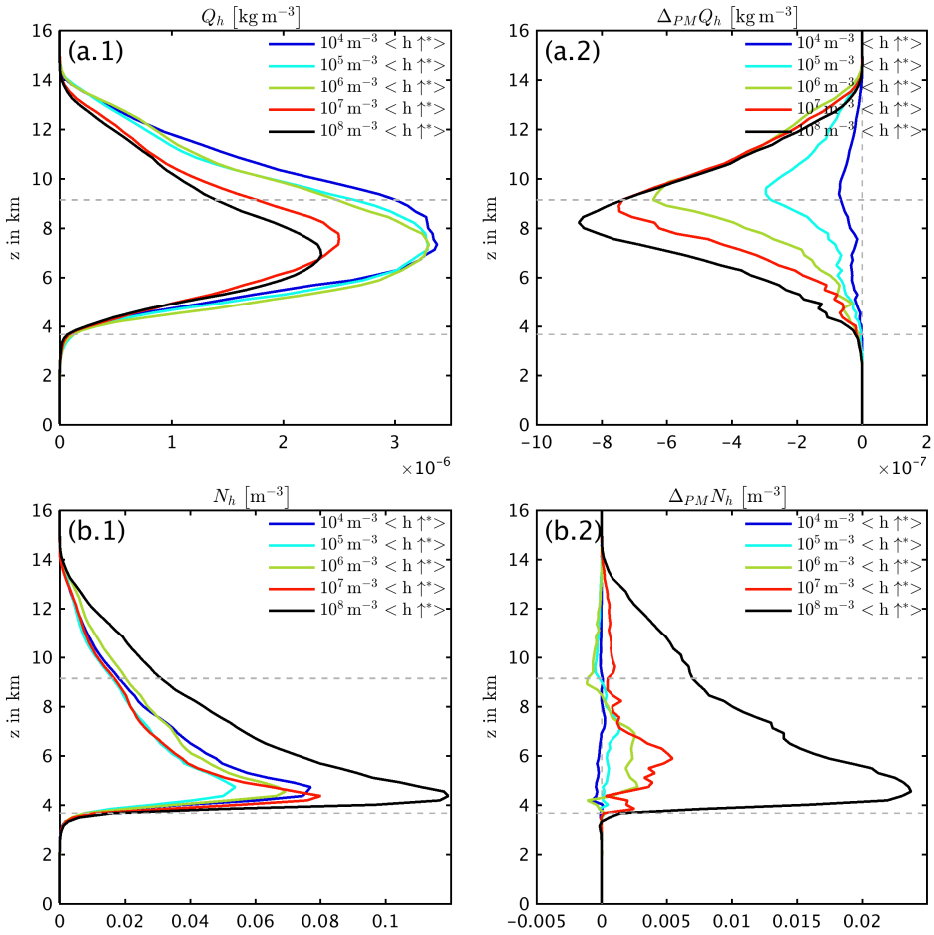


Fig. 6.4.: Hail mass concentrations (a.*) and number concentrations (b.*), shown as vertical profiles of base states (*.1), and absolute changes (*.2) resulting from ice nuclei perturbations. Each color corresponds to mineral dust background concentrations ranging from $10^4\,\mathrm{m}^{-3}$ to $10^8\,\mathrm{m}^{-3}$. Horizontal dashed lines indicate the levels of 0 °C and −36 °C.

Also here we see that the variation of $Q_h$ is relatively small (a.1) compared to the four orders of magnitude of $N_{dust,0}$. In contrast to graupel, we find a reduction of hail mass with more IN (a.2). The second aspect is that the reduction is larger with increasing $N_{dust,0}$, i.e., in the range of dust concentrations investigated here, $\Delta_{PM}Q_h$ has no turning point. Accordingly, the relative changes increase with increasing $N_{dust,0}$. Smaller upper-level hail mass densities favor decreased hail mean masses and fall velocities. The base state concentrations of hail do not have a clear tendency (b.1), except that with the largest mineral dust background, there are considerably more particles. Hail number perturbations (b.2) show similar structures as graupel number perturbations in some of the simulations. There is a tendency for increased lower-level concentrations ($N_{dust,0} = 10^5\,\mathrm{m}^{-3}$ to $10^8\,\mathrm{m}^{-3}$) and decreased upper-level concentrations ($N_{dust,0} = 10^4\,\mathrm{m}^{-3}$ to $10^6\,\mathrm{m}^{-3}$). Similar to graupel, the largest upper-level reduction ($\Delta_{PM}N_h < 0$)

is found with $N_{dust,0} = 10^6\,\mathrm{m}^{-3}$, and the reduction turns into an increase with $N_{dust,0}$ larger than $10^6\,\mathrm{m}^{-3}$. Thus, in the regime of $N_{dust,0} > 10^6\,\mathrm{m}^{-3}$, the positive $\Delta_{PM}N_h$ acts in the same direction as $\Delta_{PM}Q_h$ (i.e., towards smaller mean masses), which explains that the relative hail flux reduction continues to increase (Fig. 6.1 c.3). Since the hail downward mass flux is reduced also in cases with negative $\Delta_{PM}N_h$, we can conclude that overall the mass changes dominate the perturbed sedimentation flux, i.e., the negative upper-level values of $\Delta_{PM}N_h$ (b.2) are not large enough to enhance the downward flux by increasing the hail particle mean mass.

The underlying processes within the hail lifting regime are shown in Fig. 6.5. The dominant growth mechanism is the riming of pre-existing hail (a.1), while collection of smaller ice particles by hail makes minor contributions (not shown). For hail initiation, and therefore influence on number concentrations, there is the freezing of rain (section 5.2.1) on the one hand, and conversion of graupel particles by wet growth on the other hand (panels b.1/2). Their contribution to mass rates are rather small, but they are important for the interpretation of number changes.

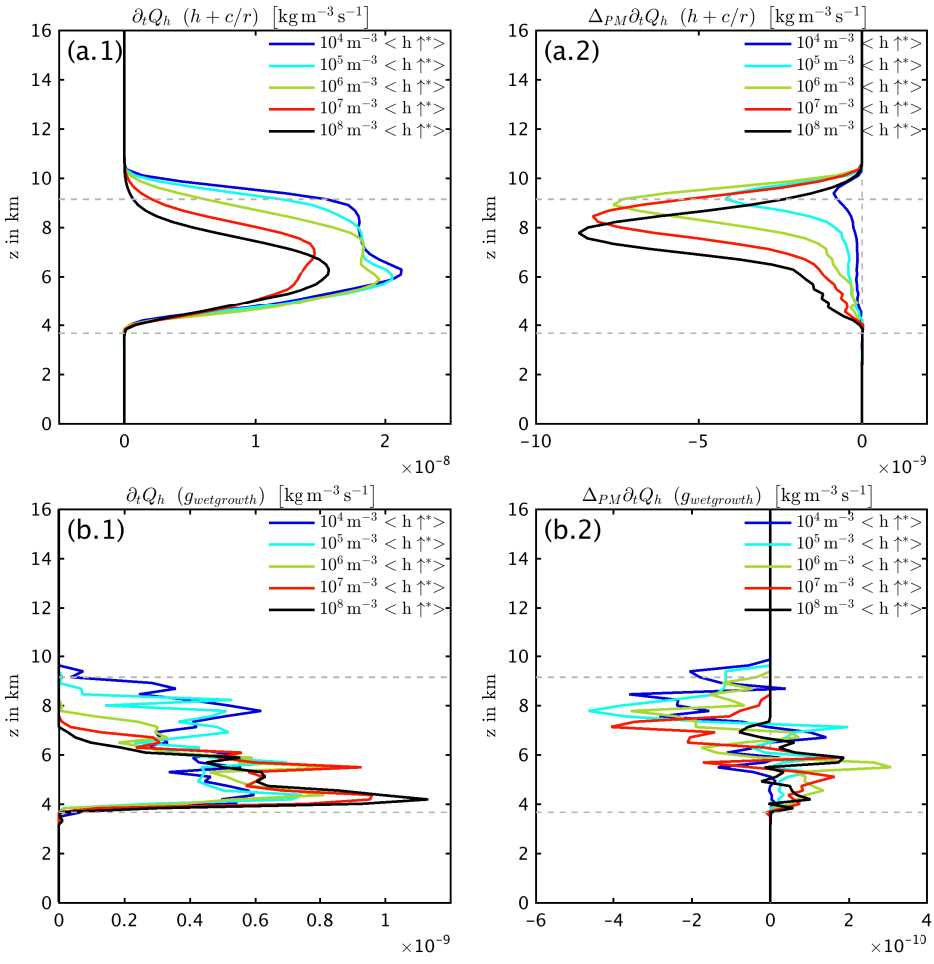


Fig. 6.5.: Mass change rates of hail due to riming of pre-existing hail (a) and wet conversion of graupel (b), shown as vertical profiles of base states (*.1) and absolute changes (*.2) resulting from ice nuclei perturbations. Each color corresponds to mineral dust background concentrations ranging from $10^4\,\mathrm{m}^{-3}$ to $10^8\,\mathrm{m}^{-3}$. Horizontal dashed lines indicate the levels of $0\,^\circ\mathrm{C}$ and $-36\,^\circ\mathrm{C}$.

Panels (a.1/2) show the riming rates as well as changes in the perturbed microphysical states. In contrast to the perturbed graupel riming rates, here we see a reduction in all levels. The relative reductions increase with higher $N_{dust,0}$, i.e., the depletion of liquid mass becomes more efficient. The time-averaged vertical profiles of graupel wet conversion (panels b.1/2) are noisy, i.e., these events occur "on occasion" in the 10 min-spaced snapshots of the model output. With increasing $N_{dust,0}$ and a downward-shifted maximum of graupel riming rates (Fig. 6.3), the peaks of wet conversion are shifted accordingly. In the perturbed microphysical states (b.2), there is a tendency of lower-level enhanced rates, and upper-level decreased rates with a larger magnitude. Therefore, the effect of rain depletion seems to be more dominant than a potential enhancement by larger graupel particles. An exception appears to be the case with largest $N_{dust,0}$, where the positive lower-level contribution is more pronounced than the negative part of the profile (b.2). This may explain the large positive $\Delta_{PM}N_h$ (Fig. 6.4) compared to the other simulations. Positive lower-level perturbations might be related to increased graupel presence as long as the rain depletion mechanism is not too dominant, as this process depends on heavy riming.

### 6.1.4. Graupel vs. hail growth

In a comparison of graupel and hail, we find that with more ice nuclei immersed in the droplets, the tendencies of graupel and hail growth changes are opposite (Fig. 6.1) although riming of pre-existing particles is the dominant mechanism for both particle types.

A possible explanation is that the most important factor for hail growth is the presence of liquid mass, and with more efficient rain depletion, hail riming is less efficient with more ice nuclei. Obviously, the lower-level increased hail formation by freezing (not shown) cannot balance this effect.

In case of graupel, riming growth in mid-levels increases in spite of the rain depletion mechanism, and a reduction of the graupel growth by riming is evident only in upper levels. An explanation may be found in an analysis of the particle fall velocities in their lifting regimes (negative downward, Fig. 6.6). In the perturbed microphysical states with more efficient immersion freezing, graupel fall velocities are increased on the order of 10% in lower levels ($z < 8$ km). This is different for hail, where the relative changes have minor magnitudes without a clear tendency (not shown).

### 6.1.5. Time dependence of rain flux sensitivities

The antagonism of graupel and hail in the melting layers is not constant in time, as shown in Fig. 6.7, where the scenario of $N_{dust,0} = 10^5\,\mathrm{m}^{-3}$ serves as an example. There is a tendency that with ongoing time, the graupel becomes more important relative to hail, i.e., reddish regions extend down to lower levels. In the following, an explanation for the mechanism behind the decreasing relative hail contribution with time is given.

In panel (a), the growing downward fluxes with time reflect the increasing horizontal extent of the convective cell. As the graupel begins to dominate the surface rain at 01:30 hours, the sign of flux change in the perturbed state turns from negative to positive (b,c). Therefore, the basic microphysical differences between earlier and later times will be analyzed in the following. Two distinct periods are considered, represented as time averages from 00:30 - 01:00 hours ("early stage"), and from 01:30 - 02:00 hours ("late stage"). Since the graupel properties are more robust with time (not shown), the change of hail properties is analyzed in the following. The sum of all microphysical hail mass change rates

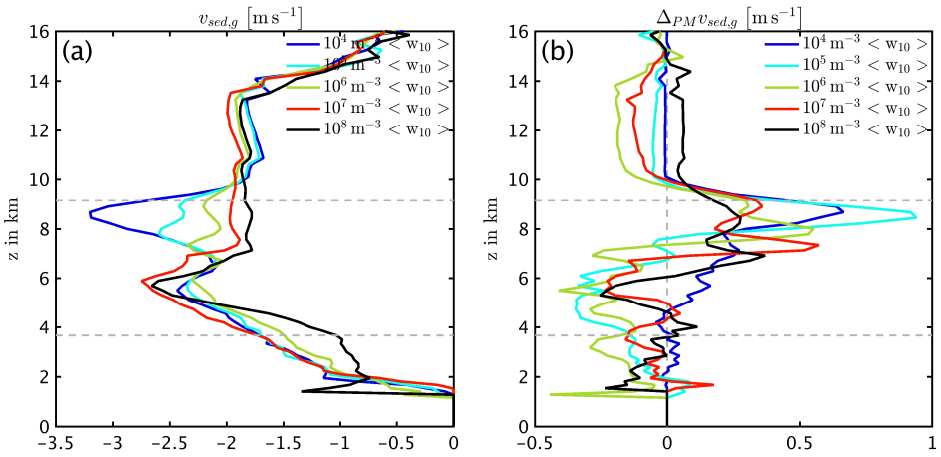


Fig. 6.6.: Graupel fall speeds representative of the 1st moment, shown as vertical profiles of base states (a) and absolute changes (b) resulting from ice nuclei perturbations. Each color corresponds to mineral dust background concentrations ranging from $10^4\,\mathrm{m}^{-3}$ to $10^8\,\mathrm{m}^{-3}$. Horizontal dashed lines indicate the levels of 0 °C and −36 °C.

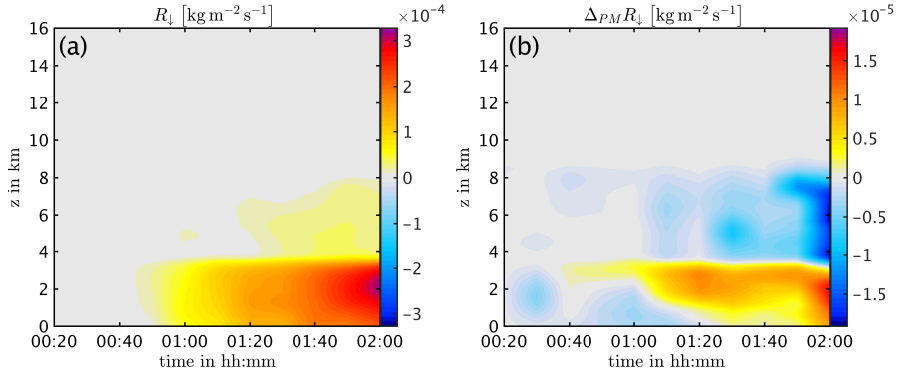


Fig. 6.7.: Sedimentation flux of rain, shown as the vertically resolved time series of the base state (a), absolute change (b) and relative change (c) resulting from ice nuclei perturbations. The mineral dust background concentration is $10^5\,\mathrm{m}^{-3}$.

(without sedimentation) and resulting hail mass profiles are analyzed for the early (panels a) and late period (panels b), with dashed lines corresponding to the lower IN concentration, and full lines to the higher concentration.

The largest differences between higher and lower IN concentrations are found in upper levels (z > 8 km), which is similar in both periods (panels a.1 and a.2; note the different scales). Although the absolute rate differences between the perturbed microphysical states (full vs. dashed lines) are similar in the two periods (a.1 vs. b.1), the relative difference is smaller in the late period. Furthermore, the peak growth rate is shifted downward with time, i.e., the largest hail growth occurs in regions which are hardly affected by the ice nuclei perturbation (z≈5 km, a.2). Thus, the upper level IN-induced changes make smaller contributions to the overall growth in the late period, which may explain the decrease of the relative hail

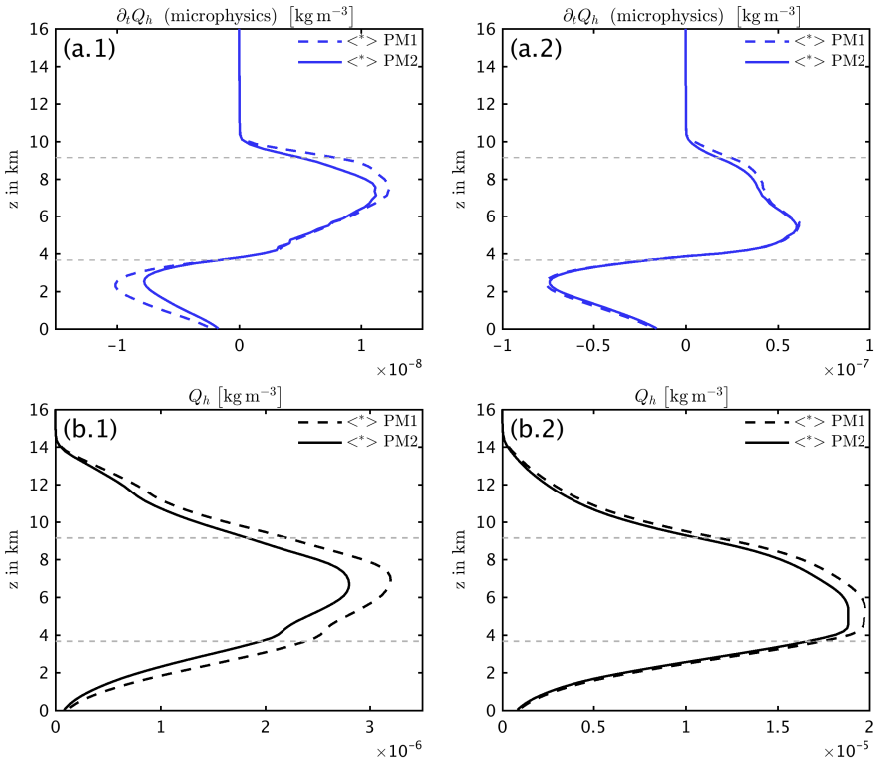


Fig. 6.8.: Hail microphysical mass change rates (a) and hail mass concentrations (b). Shown are the perturbed states (dashed: $N_{dust,0}$-90%; full lines: $N_{dust,0}$+90%) in the early period (*.1) and late period (*.2). The mineral dust background concentration is $10^5\,\mathrm{m}^{-3}$. Horizontal dashed lines indicate the levels of 0 °C and −36 °C.

flux change with time. The downward-shift of the hail growth peak coincides with the downward-shift of the hail mass (panels b.1/2). This, in turn, may be a result of the vertical profile of the sedimentation flux divergence, shown in Fig. 6.9. While from 8 km to 10 km the sedimentation flux divergence can balance the microphysical process rates to some extent, the convergence below 6 km contributes to the accumulation of mass. Accordingly, hail mass is redistributed from upper to lower levels with time, consistent with Fig. 6.8 (b.1/2).

### 6.1.6. Summary of graupel and hail sensitivities

The “optimal” graupel flux enhancement depends on two features, which is the gain of graupel mass in upper levels combined with a reduction of graupel number concentrations. The gain of mass is dominated by riming of pre-existing graupel by liquid drops, a mechanism which becomes increasingly inefficient with higher $N_{dust,0}$ due to rain depletion in lower levels. The height-dependent magnitude and sign of graupel number changes in the presence of more ice nuclei is likely caused by graupel formation by cloud ice riming, and therefore much related to the question whether large rain drops reach the regime of homogeneous freezing. Overall, the graupel flux enhancement is largest around the “turning point” of the cloud ice riming rates, i.e., in cases when immersion freezing is efficient enough that homogeneous freezing is not extremely dominant, but when immersion freezing is not too efficient to disable the in-

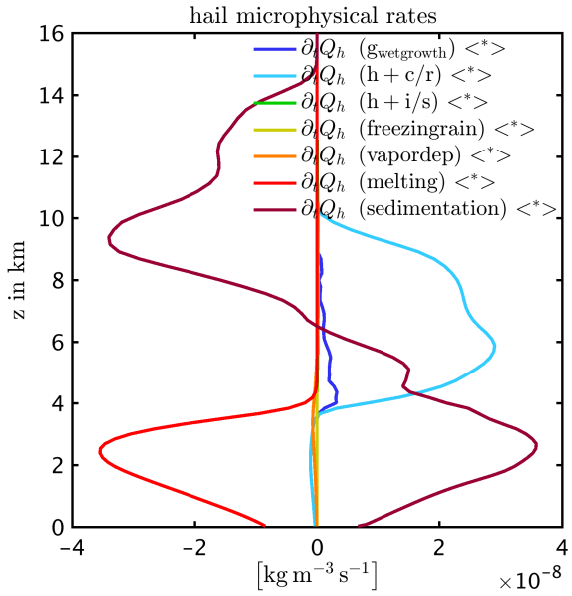


Fig. 6.9.: Hail microphysical mass change rates of the base state, calculated as domain averages, based on $N_{dust,0} = 10^5\,\text{m}^{-3}$.

teraction of large rain drops with homogeneously formed cloud ice. In section 6.2, it will be shown that this "turning point" is also relevant for anvil ice properties, and can be related to the relative contributions of heterogeneous and homogeneous droplet freezing to the mass budgets of cloud ice, with a 50/50 contribution found between $N_{dust,0} = 10^6\,\text{m}^{-3}$ and $10^7\,\text{m}^{-3}$.

Hail flux changes in perturbed IN scenarios show a more robust behavior. The magnitude of hail mass reduction in the convective core increases continuously with increasing $N_{dust,0}$. Number changes make small contributions to the perturbed hail fluxes, except for the case of highest $N_{dust,0}$. This may be attributed to the wet growth of graupel particles, contributing to significantly enhanced hail number concentrations. Similar to graupel, also $\Delta_{PM} N_h$ indicates the existence of a turning point in the same range of $N_{dust,0}$.

The antagonistic behavior of graupel and hail originates from the opposed sensitivity of riming growth. We find that the hail sensitivity is dominated by the amount of liquid mass available for riming, and with less rain mass in the presence of more IN, hail grows less efficiently. For graupel, we argued that the mean sedimentation velocity is increased in the perturbed state in the updraft regime, making the riming growth more efficient. In other words, the increased mid-level number concentration of graupel is more dominant than the effect of smaller rain mass available for riming, thus promoting enhanced accumulation of bulk graupel mass with more IN present.

The time dependence of hail flux changes was attributed to the downward-shift of hail mass peak with time. Therefore, the upper-level regions which are most sensitive to ice nuclei become less important to the overall hail growth, making the relative changes of hail precipitation less sensitive.

### 6.1.7. Precipitation sensitivities in different environments

This section gives an overview of surface precipitation changes depending on varying background mineral dust concentrations. Here we focus on the relative flux changes in the perturbed microphysical states. Negative values correspond to a reduction of surface precipitation in the presence of more ice nuclei. Panel (a) illustrates the results for surface rain and panel (b) those of surface hail. Graupel flux changes are implicitly contained in the rain flux because most of the graupel has melted before reaching the surface. Because graupel is also important for interpretation, the graupel flux changes at 4 km altitude are shown additionally in panel (c), corresponding to the flux directly before the melting level is reached.

Different from the figures of foregoing sections, an additional simulation with $N_{dust,0} = 10^9\,\mathrm{m}^{-3}$ is shown here. Although this may be far from dust concentrations which are typically found in the atmosphere, this simulation may be interpreted as a scenario with a high immersion freezing efficiency (e.g., given by biological or artificial seed particles, or a high abundance of volcanic ash particles as reported by Durant et al. (2008), regardless of the exact nature of the ice nucleating aerosols. Although the exact functional form of $n_s(T)$ depends on the aerosol particle type, exponential dependencies are commonly used also for aerosols other than desert dust (ref). Here, the focus is on microphysical responses to find out whether a turning point of the relative flux changes can also be found for hail, similar to graupel as described above.

The following scenarios are discussed in the following:

- Standard case
- Maritime CCN
- Convective environment
- Dust perturbation strength
- Microphysical assumptions of particle conversion
- Aerosol-independent freezing of rain drops (B53)

The “standard case” is based on the simulations which were discussed above in greater detail. Afterwards, the sensitivity of these results on the assumptions of CCN and cloud dynamical scenarios will be presented. Furthermore, the effect of assumptions made in the microphysical model will be highlighted.

#### Standard case

Here the wind shear and boundary layer humidity are specified as $25\,\mathrm{m\,s}^{-1}$ and $14\,\mathrm{g\,kg}^{-1}$ as intermediate values (u25q14, Tab. 4.2). Because of the time dependence shown in section 6.1.5, the results of every simulation consist of four data points. Red contains the time average over the whole period from 00:20 to 02:00 hours, while early stages are shown in grey (00:30 to 01:00 hours), mid periods in blue (01:00:01:30 hours), and mature states are shown in black (01:30 to 02:00 hours).

In panel (a), the overall trend is towards larger relative rain reductions with higher dust background concentrations. The most pronounced trend is found in the early stage with changes ranging from -5% ($N_{dust,0} = 10^4\,\mathrm{m}^{-3}$) to -28% ($N_{dust,0} = 10^8\,\mathrm{m}^{-3}$). The mature stage is more ambiguous, particularly with low $N_{dust,0}$, where small positive values appear and increase slightly between the cases of $10^4\,\mathrm{m}^{-3}$ and $10^5\,\mathrm{m}^{-3}$ dust particles. The mature period dominates the total mean value (red) which increases from close to zero to a small positive value and turns to larger negative values with dust concentrations from

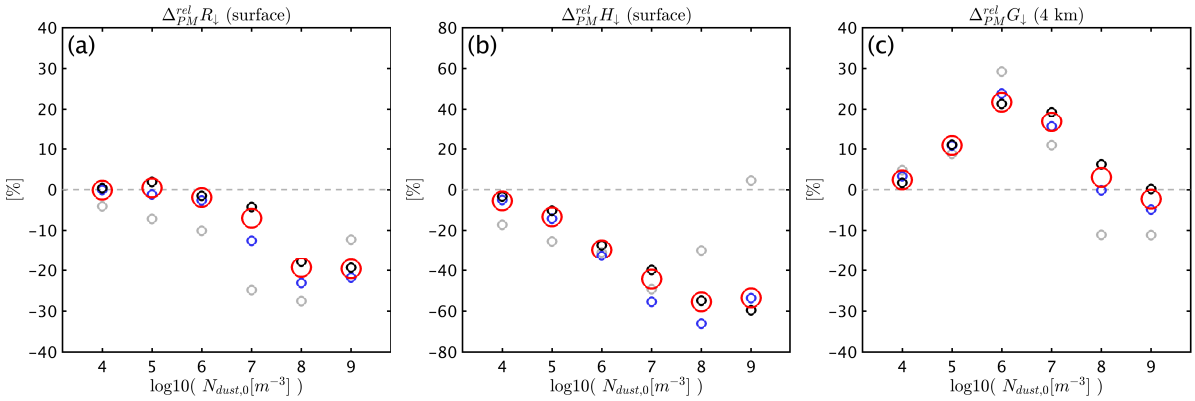


Fig. 6.10.: Relative flux changes of surface rain (a), surface hail (b) and graupel above the melting layer (c) for simulations with varying mineral dust background concentrations. Colors represent different periods, with red indicating 00:20 - 02:00 hours, gray 00:30 - 01:00 hours, blue 01:00 - 01:30, black 01:30 - 02:00 hours. The flux changes result from perturbations of $N_{dust,0} \pm 90\%$.

$10^6\,\mathrm{m}^{-3}$ to $10^8\,\mathrm{m}^{-3}$. The relative hail flux changes (b) are roughly twice as large as those of rain, and are negative in all cases except for the early stage in case of the highest immersion freezing activity. Here, the late period shows a clearer trend than the early period, ranging from -5% to -55%. For each period, a different turning point of the hail flux change can be identified. This is most pronounced in the early stage for which the largest relative hail flux reduction is found with $10^7\,\mathrm{m}^{-3}$, while the sensitivity is reduced quickly with higher $N_{dust,0}$ and may even turn positive, i.e., enhancement. Such a turning point is apparent also in later periods, but at higher $N_{dust,0}$. In contrast, the graupel flux enhancement above the melting layer (panel c) is largest at $N_{dust,0} = 10^6\,\mathrm{m}^{-3}$ and independent of time. With $N_{dust,0} = 10^9\,\mathrm{m}^{-3}$, graupel fluxes are suppressed rather than enhanced, as the tendencies described in section 6.1.2 continue with increasing dust content, owing to the combined effects of graupel riming growth and graupel initiation within the convective core.

Overall, the surface rain is hardly affected by dust perturbations with low $N_{dust,0}$ (i.e., dominant homogeneous freezing), and decreases with increasing ice nuclei content. Relative hail flux reductions are more pronounced with higher $N_{dust,0}$. The graupel enhancement is maximum with intermediate $N_{dust,0}$, when the relative contributions of heterogeneous and homogeneous to the overall droplet freezing are similar to each other (see also sections 6.1.2, 6.2.3).

### Maritime CCN

This section shows a set of simulations based on $100\,\mathrm{cm}^{-3}$ CCN background, representative for clean maritime environments Segal and Khain (2006). In Fig. 5.4 it was shown that the conversion processes from cloud to rain drops differ considerably. Here we show that the precipitation sensitivity in the two environments are very similar to each other in most of the cases. Circles indicate the continental CCN state as shown above (“standard case”, Fig. 6.10) for comparison, while triangles correspond to the maritime environment.

For the surface rain we see very similar results except for the mineral dust background of $10^7\,\mathrm{m}^{-3}$. In that case, the overall period is roughly 10% more sensitive in the maritime environment. In case of the

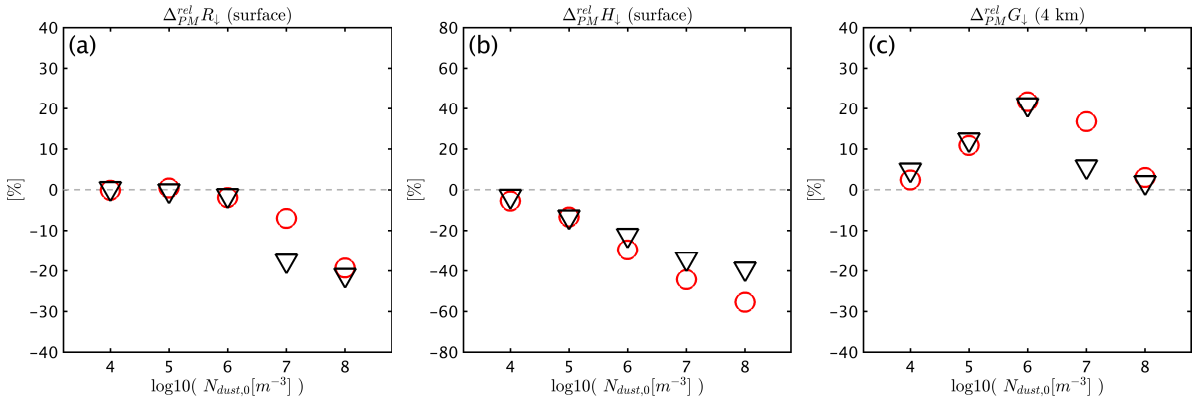


Fig. 6.11.: As Fig. 6.10, comparing the maritime CCN background (triangles) with the continental CCN background (circles corresponding to Fig. 6.10). Time-averaging includes the period from 00:20 - 02:00 hours.

surface hail flux, there is a trend of a larger divergence between the CCN environments as the immersion freezing activity increases. With highest $N_{dust,0}$, the maritime environment is roughly 20% less sensitive than the continental environment. Consistent with the rain sensitivities, graupel above the melting layer behaves significantly different only with $N_{dust,0} = 10^7\,\mathrm{m}^{-3}$. With the smaller graupel sensitivity in the maritime simulation, hail dominates the surface rain flux change, resulting in larger negative values in the specific case. This situation is shown in Fig. 6.12 which briefly introduces the sedimentation flux profiles as a comparison between continental (dashed) and maritime (full lines) environments.

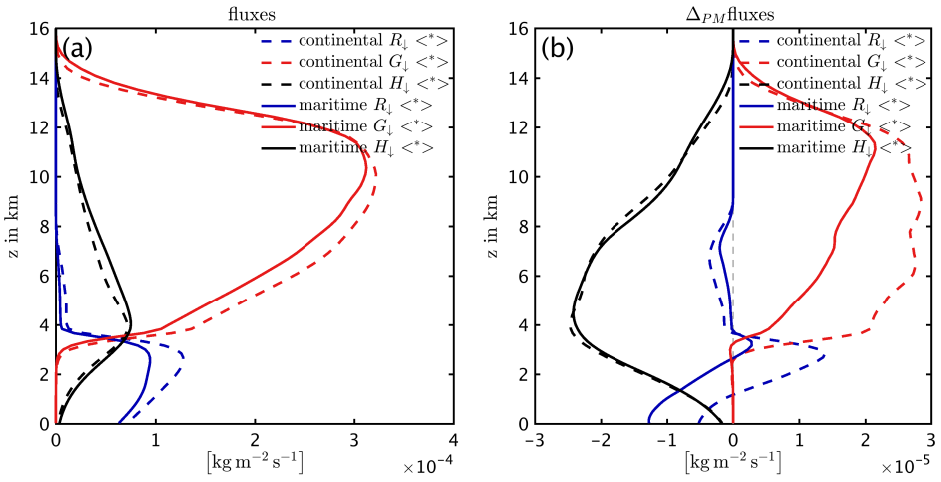


Fig. 6.12.: Effective precipitation fluxes of rain (blue), graupel (red) and hail (black), comparing the maritime environment (full lines) and continental environment (dashed lines). The vertical profiles show the base states (a) and absolute changes (b) resulting from ice nuclei perturbations, with $N_{dust,0} = 10^7\,\mathrm{m}^{-3}$.

Panel (a) shows that the precipitation fluxes are not very sensitive to the CCN environment in this case. Furthermore, the general expectation of enhanced rain formation with less CCN is not confirmed here because the rain formed in the convective updraft hardly contributes to the surface precipitation. Hail

sediments slightly more efficient, graupel is reduced to a larger extent and causes the surface rain flux to be reduced, relative to the continental environment (panel a). The sensitivity to immersion freezing is shown in panel (b). Here it appears that the absolute hail flux reduction with more IN of is very similar in both environments, while the sensitivity of graupel is reduced significantly in the maritime case. Thus, the resulting rain flux is dominated by the reduced hail flux which is offset by graupel only to a small extent in the uppermost melting levels.

### Convective environment

Here we summarize the sensitivity of surface precipitation changes in different atmospheric environments (section 4.2). We specify $N_{dust,0} = 10^7\,\mathrm{m}^{-3}$ which was shown to be more sensitive to IN perturbations compared to lower mineral dust backgrounds. The default simulation (u25q14) is indicated by circles. In contrast to the above figures, the simulation identifier is shown on the x-axis instead of $N_{dust,0}$.

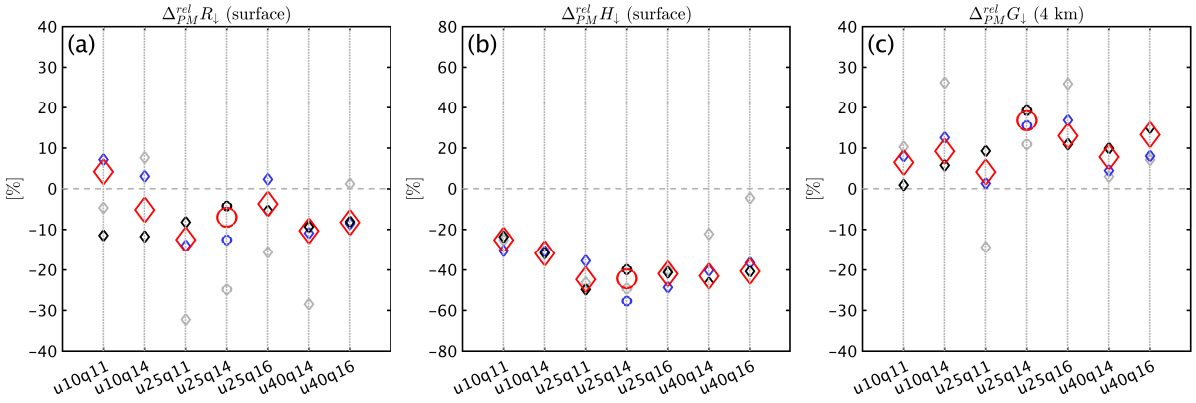


Fig. 6.13.: Relative flux changes of surface rain (a), surface hail (b) and graupel above the melting layer (c) for simulations in varying atmospheric environments, and $N_{dust,0} = 10^7\,\mathrm{m}^{-3}$. Colors represent different periods, with red indicating 00:20 - 02:00 hours, grey 00:30 - 01:00 hours, blue 01:00 - 01:30 hours, black 01:30 02:00 hours. The flux changes result from perturbations of $N_{dust,0}\pm 90\%$.

For the surface rain it is found that the time averages of the mature and total periods are relatively similar among the simulations, while the early stage (00:30 - 01:00 hours) is more variable in magnitude and sign. An exception is the case with weakest convection, u10q11, where the total mean value indicates enhanced surface rain.

The u10q11 simulation is further investigated with varying dust backgrounds, representative of generally weaker convection (see section 4.2). The resulting relative surface precipitation changes of u10q11 simulations are shown in Fig. 6.14, with circles indicating u25q14 simulations for comparison.

The low sensitivity with $N_{dust,0} = 10^4\,\mathrm{m}^{-3}$ is robust (panel a). With increasing $N_{dust,0}$, there is a strong tendency towards rain enhancement which peaks at $N_{dust,0} = 10^6\,\mathrm{m}^{-3}$, corresponding to the sensitivity of graupel. The peak at $10^6\,\mathrm{m}^{-3}$ in panel (a) indicates that the basic microphysical interactions which determine graupel flux changes are still robust in the environment of less intense convection. Only in the dissipating stage (black diamonds, t>01:30), the graupel flux enhancement disappears, making the rain flux change negative. Only with $N_{dust,0} = 10^8\,\mathrm{m}^{-3}$, the negative contribution of hail begins to dominate the surface rain. Hail flux sensitivities are generally lower in u10q11 simulations than in

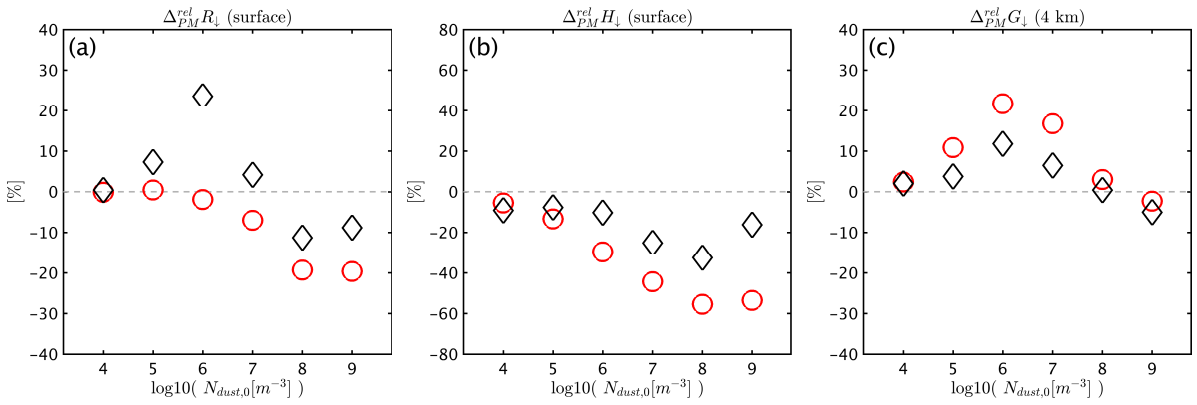


Fig. 6.14.: As Fig. 6.10, comparing weak convection (u10q11, diamonds) with the strong convective environment (u25q14, circles corresponding to Fig. 6.10). Time-averaging includes the period from 00:20 - 02:00 hours.

u25q14 simulations (panel b). Two outliers are found during the late period with $N_{dust,0} = 10^5\,\mathrm{m}^{-3}$ and $10^8\,\mathrm{m}^{-3}$ which can be attributed to the uncertain statistics of sporadically occurring "hail events" during the dissipating stage, as only four output snapshots are contained in the late period time average. For the case of u10q11 with $N_{dust,0} = 10^6\,\mathrm{m}^{-3}$ we saw a maximum in the surface rain enhancement. This situation is depicted in Fig. 6.15 which shows the vertical sedimentation flux profiles and their changes under perturbed microphysical conditions.

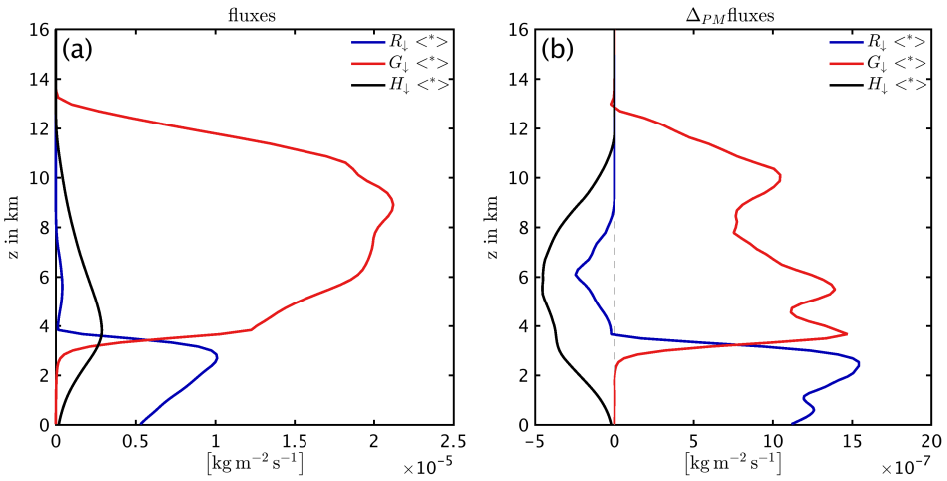


Fig. 6.15.: Effective precipitation fluxes of rain (blue), graupel (red) and hail (black). The vertical profiles show the base states (a) and absolute changes (b) resulting from ice nuclei perturbations, with $N_{dust,0} = 10^6\,\mathrm{m}^{-3}$.

As expected from the above results, the absolutely dominating contributor to rain formation is graupel, with a factor of 5 larger downward mass flux compared to hail on top of the melting level (panel a, z≈4 km).

### Dust perturbation strength

Our default IN perturbations in this chapter are defined as the relative deviations of ±90% of $N_{dust,0}$. In section 6.1.2 we speculated whether the magnitude of the perturbation might be a limiting factor to yield artificial sensitivities. Here we confirm the microphysical sensitivities when using a smaller perturbation of $N_{dust,0}$±10%. For the direct comparison between the perturbation strengths, a normalization with the relative change of dust concentrations, $rdN = \frac{N_2 - N_1}{N_0}$ is included. According to the definitions of perturbed concentrations, $rdN$ is independent of $N_{dust,0}$.

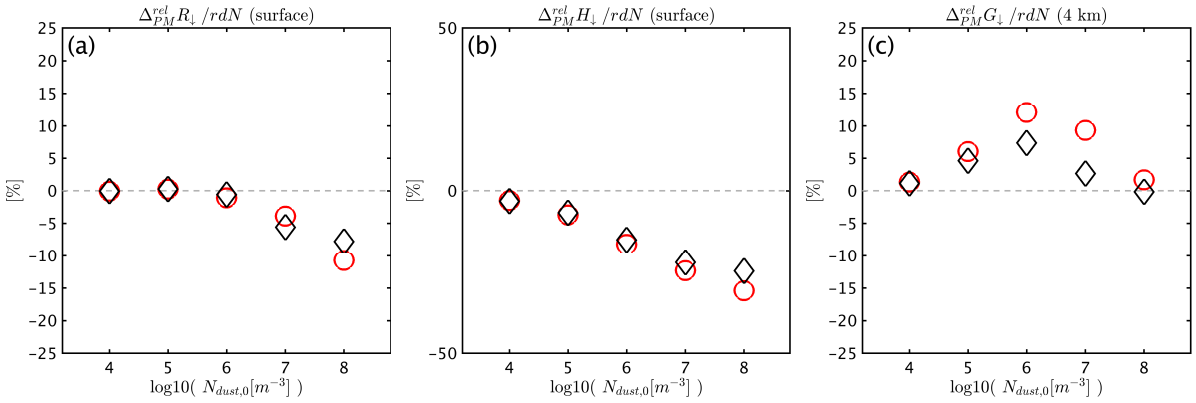


Fig. 6.16.: As Fig. 6.10, comparing smaller dust perturbations (±10%, diamonds) with the default perturbations (±90%, circles corresponding to Fig. 6.10). The results are normalized by the relative mineral dust perturbation. Time-averaging includes the period from 00:20 - 02:00 hours.

### Microphysical assumptions of particle conversion

This section is dedicated to microphysical assumptions rather than the atmospheric state. It is a common approach in cloud simulations to sub-divide the ensemble of cloud particles into various particle classes. For liquid drops this is straight-forward, based on the size distributions of cloud and rain drops. For ice particles, the partitioning is less obvious because the particles not only evolve in size, but depending on their microphysical history and the processes that have contributed to their growth, they have variable bulk densities and shapes. Therefore, two-moment schemes usually have classes for small/pristine "cloud ice", a snow-like category for the representation of aggregates, and denser graupel particles which have originated from riming. Less common is an additional high-density hail class, as simulated here. With more classes, the complex and case-dependent microphysical structure of deep convective clouds can be simulated in a greater detail and with a more realistic structure (e.g., Johnson et al., 2016). However, the categorizing in models is an artificial workaround to represent a continuum of particle properties found in nature, and with more categories present in the model, the conversion between the distinct classes becomes increasingly challenging.

It was shown that surface precipitation changes are very much dependent on the interplay of graupel and hail fluxes which are determined by riming growth to a large extent. Thus, we can expect a potential sensitivity to the exact treatment of riming. In this sensitivity test, the particle interactions between liquid drops and small ice, snow and graupel are of interest (c/r + i/s/g), which can result in graupel and/or hail

particles, with "and/or" being determined by user-defined options[1]. In the following, these are called type-2/3 simulations, the former representing the standard simulations of this work.

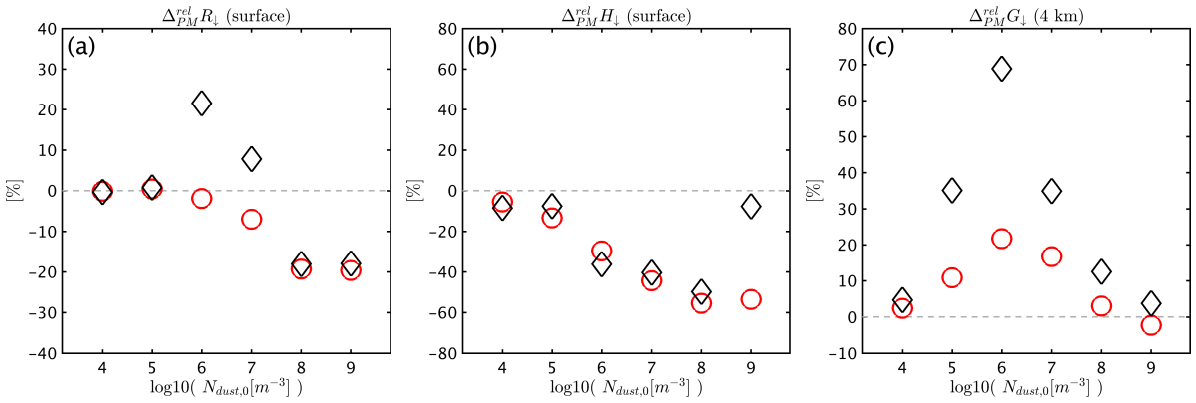


Fig. 6.17.: As Fig. 6.10, comparing type-3 simulations (diamonds) with the default setting (type-2; circles corresponding to Fig. 6.10). Time-averaging includes the period from 00:20 - 02:00 hours.

Figure 6.17 illustrates the changes of surface precipitation which originate from type-3 simulations, compared to type-2 simulations. Although the relative surface rain changes (panel a) are very similar with the lowest and highest $N_{dust,0}$ concentrations, we see that there are two cases ($10^6\,\mathrm{m}^{-3}$, $10^7\,\mathrm{m}^{-3}$) that deviate considerably from type-2-simulations, and have even opposite signs, indicating enhanced surface precipitation in the presence of more IN. The two $N_{dust,0}$ cases with the largest differences correspond to the turning point of the graupel sensitivity which was shown to be determined by the graupel formation by cloud ice riming in type-2 simulations (section 6.1.2). Here the relative sensitivity is enhanced by a factor of 2-3 around $N_{dust,0} = 10^6\,\mathrm{m}^{-3}$ (panel c). For the hail fluxes, the differences of relative surface flux changes are less pronounced, although single periods do have opposite signs, too (not shown). A general finding is that in type-3 simulations, hail properties are more similar to graupel than in type-2 simulations, with larger mass densities, smaller particle mean masses and a more efficient melting below 4 km altitude. This shift in the simulated particle properties attributes a higher relative contribution of graupel flux changes to the surface rain sensitivity, thus yielding a surface rain enhancement rather than a decrease with intermediate $N_{dust,0}$. Further discussion of graupel and hail properties is given in section B.1.

#### Aerosol-independent freezing of rain drops (B53)

A final comparison of B53- and N12-based cloud sensitivities is given for two environments, i.e., the standard case (u25q14, Fig. 6.18) and weak convective case (u10q11, Fig. 6.19).

Compared to N12-simulations, the surface rain change is more pronounced with B53-based rain freezing in most of the dust scenarios, while the magnitudes of both graupel and hail are smaller (Fig. 6.18).

[1] In the COSMO model, two modes are available when both graupel and hail are present. By choosing between "ice_typ=2" or "ice_typ=3", it is distinguished how rimed masses are distributed among graupel and hail. All above simulations were based on number 2, where riming of i/s/g may cause accumulation of graupel mass, but does not affect hail formation or growth. Hail is only affected with "ice_typ=3" – in this case, graupel mass and number may also be depleted due to conversion to hail (i.e., $g + r \rightarrow h$).

Furthermore, the graupel changes have opposite signs, i.e., in B53-based simulations, graupel and hail changes do not counteract each other.

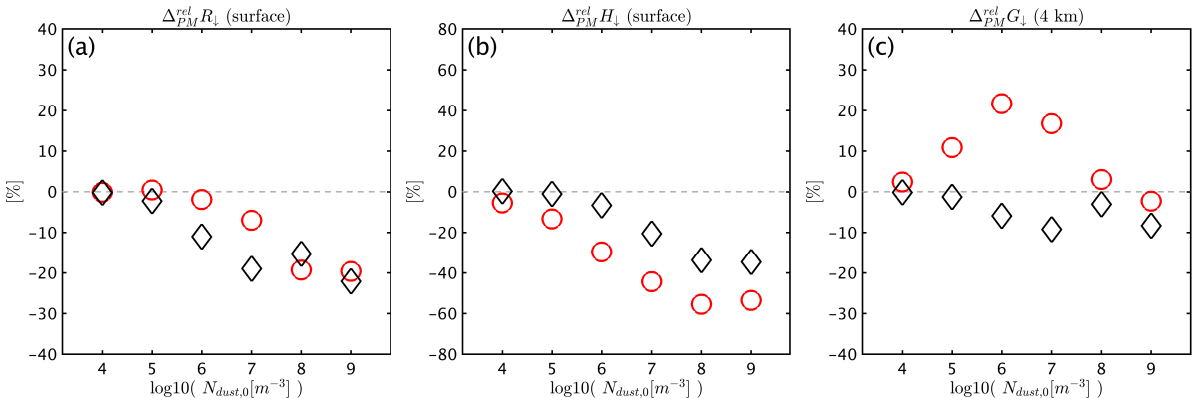


Fig. 6.18.: As Fig. 6.10, comparing the aerosol-independent B53 approach (diamonds) with the new implementation of N12 for freezing rain (circles corresponding to Fig. 6.10). Simulations are based on strong convection (u25q14). Time-averaging includes the period from 00:20 - 02:00 hours.

The opposite behavior of graupel may be regarded as one of the most important differences between B53- and N12-based rain freezing, in particular when graupel dominates the formation of surface rain. Figure 6.19 summarizes the u10q11 scenario, in which hail production is of minor importance. Accordingly, the simulated surface rain sensitivities yield opposite signs in most of the cases (panel a).

The reason for the opposite behavior of graupel is likely to originate from the perturbed freezing rates of large drops without explicit consideration of aerosols: With all IN attributed to the cloud droplets, secondary processes such as riming deplete more liquid mass in the perturbed scenario, thus yielding reduced freezing rates of large drops with more IN present (eq. 2.1).

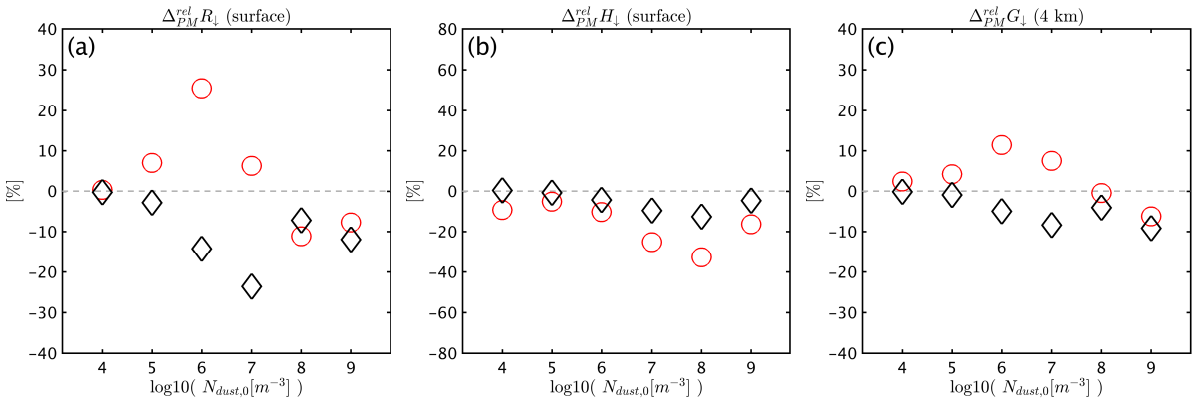


Fig. 6.19.: As Fig. 6.10, comparing the aerosol-independent B53 approach (diamonds) with the new implementation of N12 for freezing rain (circles corresponding to Fig. 6.10). Simulations are based on weak convection (u10q11). Time-averaging includes the period from 00:20 - 02:00 hours.

### 6.1.8. Summary of precipitation flux changes

In section 6.1.7, it was shown that in all cases the qualitative behavior of graupel and hail sedimentation flux changes upon ice nuclei perturbations are robust, with reduced hail fluxes and enhanced graupel fluxes in the presence of more ice nuclei. Only in case of extremely efficient immersion freezing which was represented by assuming more than $10^8\,\mathrm{m}^{-3}$ mineral dust, graupel fluxes tend to be reduced. This qualitative behavior is robust in cases of stronger and weaker convection, as well as in simulations with maritime CCN background. Even in case of different assumptions of graupel and hail production during riming, the qualitative flux changes of both graupel and hail is consistent.

However, the surface rain flux modifications show more variability, resulting from the antagonistic growth sensitivity of graupel and hail. By shifting the magnitudes and relative importances of hail reduction and graupel enhancement, the horizontal mean surface rain may be both enhanced or decreased. In spite of the partly strong time dependencies during the cell evolution, a general tendency towards larger rain reduction with higher mineral dust background concentrations is found in cases of strong convection. This is different in cases of weaker convection when graupel dominates the surface rain formation, and the most pronounced rain enhancements are found with intermediate immersion freezing efficiencies.

The model-specific treatment of particle conversion during riming has the potential of shifting the relative importances towards graupel, resulting in a simulated rain enhancement instead of reduction. It was also shown that without explicit aerosol dependence of freezing rain drops, the sign of graupel sensitivity to ice nuclei perturbations cannot be reproduced, thus resulting in rain reduction in all simulated cases. This may be misguiding particularly in weak convective cases, when graupel is more important for rain production than hail.

## 6.2. Radiation and anvil ice

In this section, the effects of aerosol-dependent ice formation on radiative fluxes are analyzed. We begin with horizontally and temporally averaged profiles of net fluxes of longwave and shortwave radiation (section 6.2.1). Next, cloud ice properties and mechanisms of anvil ice formation are discussed (sections 6.2.2, 6.2.3, 6.2.4), which will finally lead us to the budgets of cloud droplets (section 6.2.5). In section 6.2.7, the sensitivities of cloud albedo and longwave fluxes to ice nuclei perturbations will be summarized in different atmospheric environments and in a wide range of mineral dust background concentrations.

In contrast to the previous section, averaging areas are now defined columnwise for consistency with the calculation method of the radiative transfer calculations. All horizontal mean values will contain the "cloudy columns" from surface to the top of the simulated atmosphere. Condition for cloudy columns is a content of at least $10^{-7}\,\mathrm{kg\,m^{-3}}$ liquid or ice mass in at least one level ($< \mathrm{cld}_{||} >$, see Tab. A.1). The underlying surface albedo is defined as 0.3.

According to the model implementation in COSMO (Ritter and Geleyn, 1992), net incoming/ downward fluxes have positive signs (relevant for shortwave radiation), and net outgoing/ upward fluxes have negative signs (relevant for longwave radiation). Consistent with the notation of Ritter and Geleyn (1992), "solar" is used synonymously with shortwave fluxes, and "thermal" corresponds to longwave fluxes. Furthermore, "flux" corresponds to "net flux" in the following descriptions.

### 6.2.1. Radiative fluxes

Figure 6.20 shows the vertical profiles of solar and thermal fluxes and their changes in the perturbed microphysical states. Given the large horizontal extent of the convective outflow, most relevant for the mean radiative properties in the cloudy column is cloud ice. In contrast to cloud-free areas with top-of-atmosphere (TOA) net shortwave fluxes (FSW) as large as $800\,\mathrm{W\,m^{-2}}$, they are reduced to values below $550\,\mathrm{W\,m^{-2}}$ in the cloudy column (a.1) due to the reflection by the cloud, i.e., the effect of cloud albedo. Below cloud, FSW is on average smaller than $300\,\mathrm{W\,m^{-2}}$. The largest vertical gradients are found in the levels of the largest ice number and mass concentrations around 12 km, as indicated by the horizontal dashed lines (see section 6.21 for ice properties).

In the perturbed microphysical state, the net SW flux can be both enhanced and reduced (a.2/3, full lines). Thus, depending the perturbations of anvil ice mass and number concentrations, the cloud becomes optically thinner or thicker which varies under different conditions of $N_{dust,0}$.

In Fig. 6.20, the magnitude of FSW sensitivity to ice nuclei perturbations increases from $N_{dust,0} = 10^4\,\mathrm{m^{-3}}$ to $N_{dust,0} = 10^8\,\mathrm{m^{-3}}$ (+10%), and changes its sign with $N_{dust,0} > 10^8\,\mathrm{m^{-3}}$. Simulations with $N_{dust,0} < 10^7\,\mathrm{m^{-3}}$ behave slightly different than the rest. For example, in case of $N_{dust,0} = 10^6\,\mathrm{m^{-3}}$ we see that the net flux is larger at the surface, while at the same time the cloud albedo is enhanced, reducing the net flux at TOA (a.2/3). This means that in the perturbed microphysical state, the absorption of short wave radiation is decreased in cloud layers, but cloud albedo is slightly enhanced with $N_{dust,0} \leq 10^6\,\mathrm{m^{-3}}$. This behavior is most pronounced in regions close to the convective core where the cloud vertical extent is particularly large (not shown).

The net outgoing thermal fluxes (FLW) are smallest in magnitude at ground levels (b.1) as a result of the downward component of the atmospheric radiation. The dip in the magnitude of FLW within the anvil

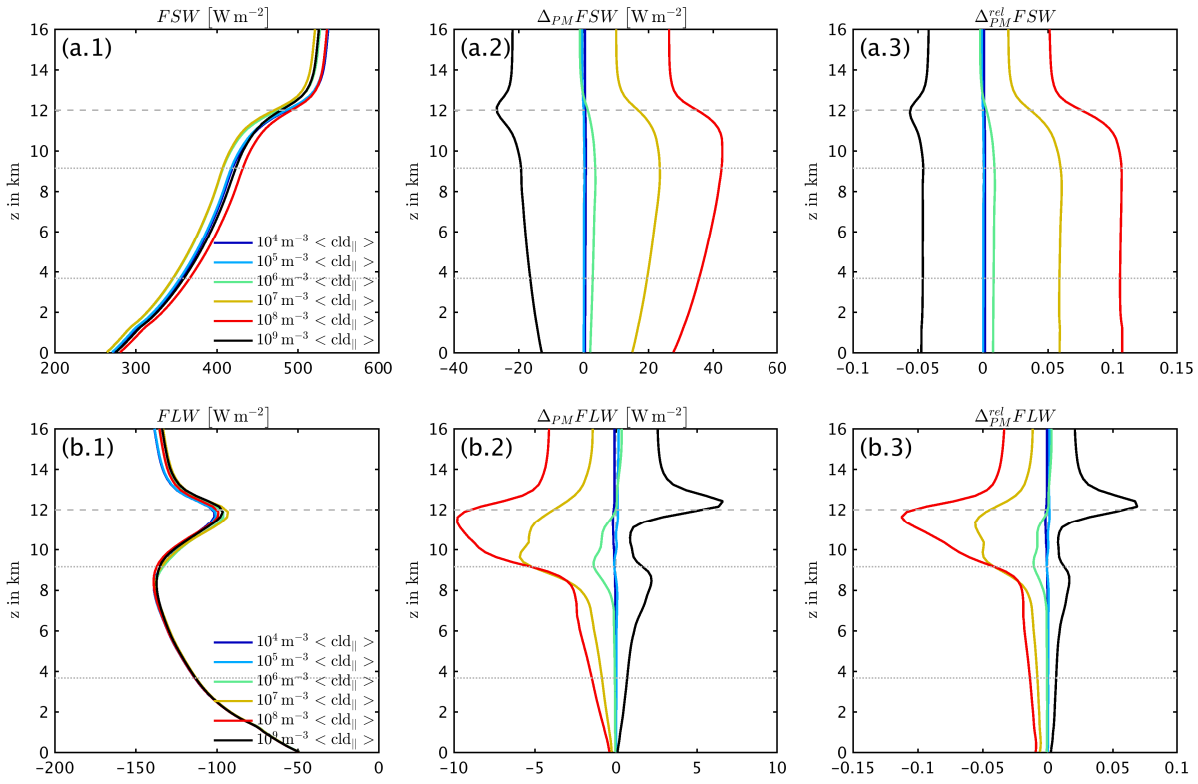


Fig. 6.20.: Shortwave (a.*) and longwave (b.*) radiative fluxes, shown as the vertical profiles of base states (*.1), absolute changes (*.2) and relative changes (*.3) resulting from ice nuclei perturbations. Each color corresponds to mineral dust background concentrations ranging from $10^4\,\mathrm{m}^{-3}$ to $10^9\,\mathrm{m}^{-3}$. Dotted horizontal lines indicate the levels of 0 °C and −36 °C, and dashed horizontal lines indicate the maximum of anvil ice concentrations.

(9 km to 14 km) results from the longwave emission of the anvil ice, as up- and downward contributions to FLW cancel out to some extent.

With more dust present in the perturbed microphysical states, the behavior of $\Delta_{PM}FLW$ (b.2/3) is similar to $\Delta_{PM}FSW$. Again, the turning point is found at $N_{dust,0} = 10^8\,\mathrm{m}^{-3}$, where the cloud becomes optically thinner in the longwave spectrum, most pronounced anvil levels. With a reduced anvil absorption and emission, more longwave radiation emitted from lower levels (both ground and water vapor below cloud) can pass through the anvil without being absorbed. An alternative interpretation can be a higher altitude of the effective emission height of the anvil ice, i.e., the colder anvil would emit less efficiently. However, no tendencies of shifted anvil altitudes are directly visible as shown section 6.21. Furthermore, the spatial structure of $\Delta_{PM}FLW$ indicates that the thinning of the outer anvil edges is the more important effect (not shown), favoring the hypothesis of smaller absorption.

TOA sensitivities are larger than below cloud. In part, this is related to the water vapor from levels below the anvil which contributes to the downward atmospheric radiation. This vapor contribution can either be independent of the perturbed cloud state (e.g., below the outer regions of the anvil), or contributes with a positive sign in regions of enhanced graupel evaporation below the anvil (not shown). In

contrast, levels above the anvil are subjected to the cloud ice radiative properties more directly, as there is hardly any vapor present which would tend to damp the sensitivity.

### 6.2.2. Cloud ice properties

In section 6.2.1, it was indicated that the radiative flux changes result from the interplay of perturbed cloud ice mass and number densities in anvil regions. In this section, the cloud ice properties will be discussed for the whole range of mineral dust concentrations. First, we focus on the intercomparison cloud ice effective radii, cloud ice mass, and cloud ice number concentrations. Subsequently, the underlying microphysical mechanisms are presented.

Figure 6.21 summarizes cloud ice effective radii, mass densities and number densities, represented by horizontal averages over the cloudy columns in simulations with $N_{dust,0}$ varying from $10^4\,\mathrm{m}^{-3}$ to $10^9\,\mathrm{m}^{-3}$. The definition of $R_{eff,i}$ follows Fu (1996); Fu et al. (1998), as implemented in the model. Note that in this analysis, the convective cores make only a minor contribution to the averaged vertical profiles, and the largest contribution originates from columns directly related to the wide-spread convective outflow as well as sedimentation regimes below.

$R_{eff,i}$ has a maximum at altitudes corresponding to the lower boundary of the anvil, below which the evaporation of ice crystals becomes dominant. Under conditions of increased $N_{dust,0}$, the overall trend is towards smaller crystals in all layers. This is also evident from the negative $\Delta_{PM}R_{eff,i}$ (a.2/3). The largest absolute changes at most altitudes are found with $N_{dust,0} = 10^7\,\mathrm{m}^{-3}$. At z=12 km where the maximum anvil ice content is found in the profiles of horizontal mean values, the simulation with $N_{dust,0} = 10^9\,\mathrm{m}^{-3}$ shows a strong decrease of radii compared to lower levels (a.2). On the relative scale, this is the simulation with the highest sensitivity around 12 km (a.3), which promotes the sudden change of radiative flux perturbations (Fig. 6.20).

Panel (b.1) shows the mass concentrations for varying $N_{dust,0}$. In anvil levels, there is a clear tendency of reduced cloud ice mass with increasing $N_{dust,0}$. These upper-level properties are determined within the convective core to a large extent, and will be analyzed further in section 6.2.3. In the perturbed microphysical states, the absolute upper-level ice mass reduction is largest with $N_{dust,0} = 10^7\,\mathrm{m}^{-3}$ (b.2). The absolute mass reductions peak around 12 km, corresponding to the base state profile peaks, while the relative reductions are relatively constant above 10 km (b.3). With the highest $N_{dust,0}$, the upper-level mass reduction is decreased compared to smaller $N_{dust,0}$ (b.2/3). The different tendencies in the evaporation regime (b.1) may be the result of less pronounced subsaturation with higher $N_{dust,0}$ due to the effect of graupel – however, these levels are of minor importance for the TOA radiative fluxes. Anvil ice numbers become larger in simulations with more active immersion freezing (c.1). In panels (c.2/3), the simulation with highest $N_{dust,0}$ deviates most from others, with both absolute and relative ice number enhancements being much larger.

Both positive $\Delta_{PM}N_i$ and negative $\Delta_{PM}Q_i$ support the tendency of smaller ice crystals within the anvil when more dust is present (a.1). In Fig. 6.20, the highest sensitivities towards optically thinner clouds were found with $N_{dust,0} = 10^8\,\mathrm{m}^{-3}$. Here, we find that this is the simulation with the largest relative ice mass reduction around 12 km (b.3), while at the same time the number changes in these levels are close to zero (c.3), i.e., the counteracting effect of more ice crystals is minimized in this specific range of $N_{dust,0}$.

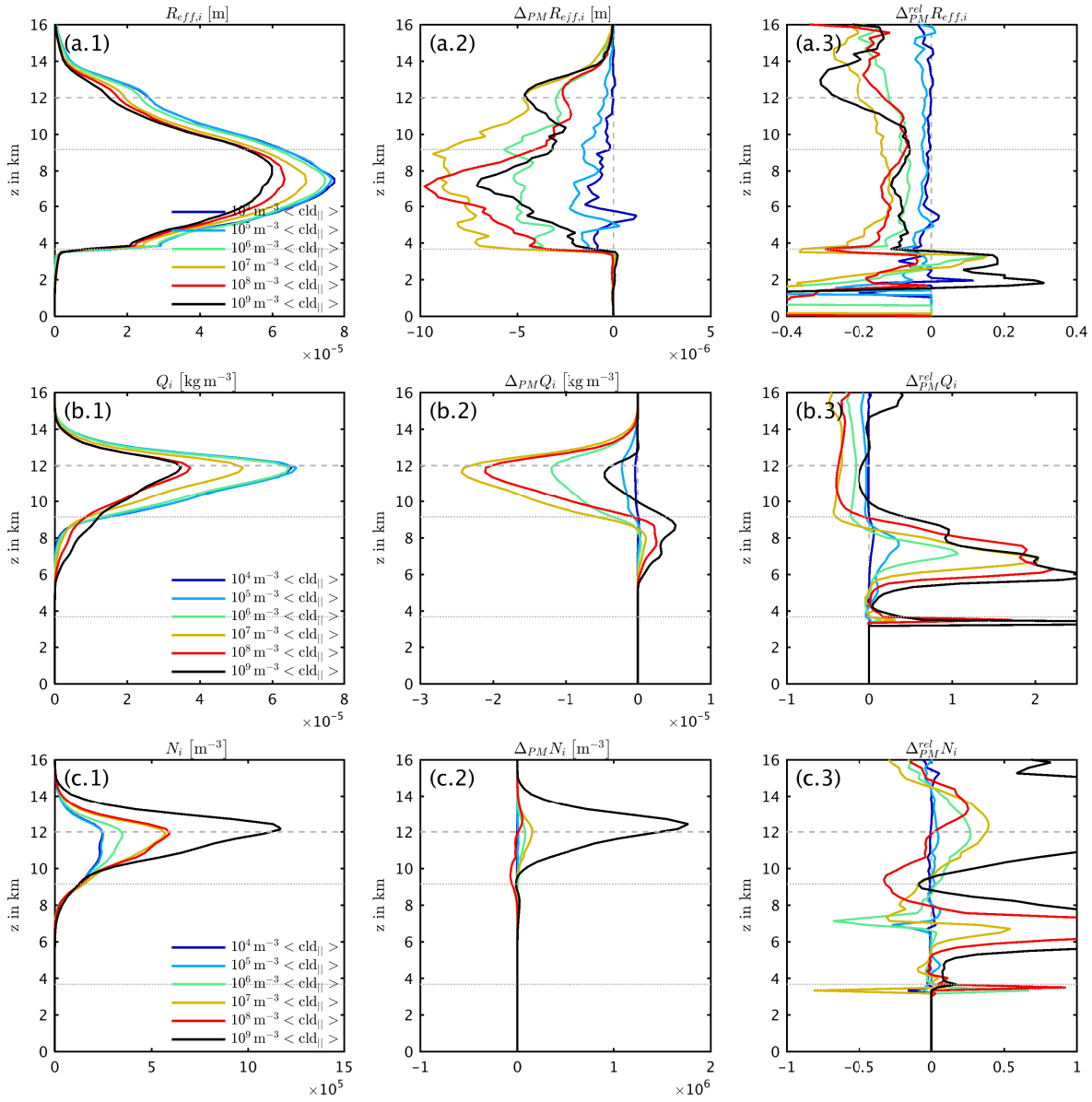


Fig. 6.21.: Cloud ice effective radii (a), mass densities (b) and number densities (c), shown as the vertical profiles of base states (*.1), absolute changes (*.2) and relative changes (*.3) resulting from ice nuclei perturbations. Each color corresponds to mineral dust background concentrations ranging from $10^4\,\mathrm{m}^{-3}$ to $10^9\,\mathrm{m}^{-3}$. Dotted horizontal lines indicate the levels of 0 °C and −36 °C, and dashed horizontal lines indicate the maximum of anvil ice concentrations.

This may be interpreted as a hint that the ice properties around 12 km altitude are most important for the modification of radiative fluxes, corresponding to level of highest mean ice water content.

### 6.2.3. Cloud ice mass budgets

Next, we focus on the determinants of anvil ice properties, i.e., the microphysical budget terms of mass and number concentrations. This will indicate the reasons for peaking ice mass changes in a certain range

of immersion freezing efficiency, and the reason for the particularly high anvil ice number sensitivity in case of the largest $N_{dust,0}$. Therefore, processes in the convective core are analyzed which determine the convective outflow properties. As a proxy for the "core", vertical velocities larger than $5\,\mathrm{m\,s^{-1}}$ are identified. Although technically, lifting regimes ($w > v_{qi}$, see Tab. A.1) of cloud ice could be calculated, such regions are also found in the outflow within grid-scale turbulent eddies and wave structures, thus yielding an ambiguous measure to distinguish between convective core and outflow.

First, the simulation of $N_{dust,0} = 10^5\,\mathrm{m^{-3}}$ will give an overview of the relative contributions of single processes (Fig. 6.22). Two main contributions to the cloud ice mass budget can be identified, which is the freezing of rain drops with diameters smaller than 500 µm, and the conversion of cloud ice into other cloud particle classes during the riming process (a). Immersion freezing of cloud droplets makes only a minor fraction, and homogeneous cloud droplet freezing is also small compared to rain freezing. Furthermore, ice growth by vapor deposition and cloud ice depletion by ice-ice collisions are present with relatively small magnitudes. In the perturbed microphysical state (b), the absolute changes are dominated by freezing rain and riming. The sum of these two perturbed rates is negative in the region of homogeneous freezing, which is a first hint for upper-level ice mass loss in presence of more ice nuclei.

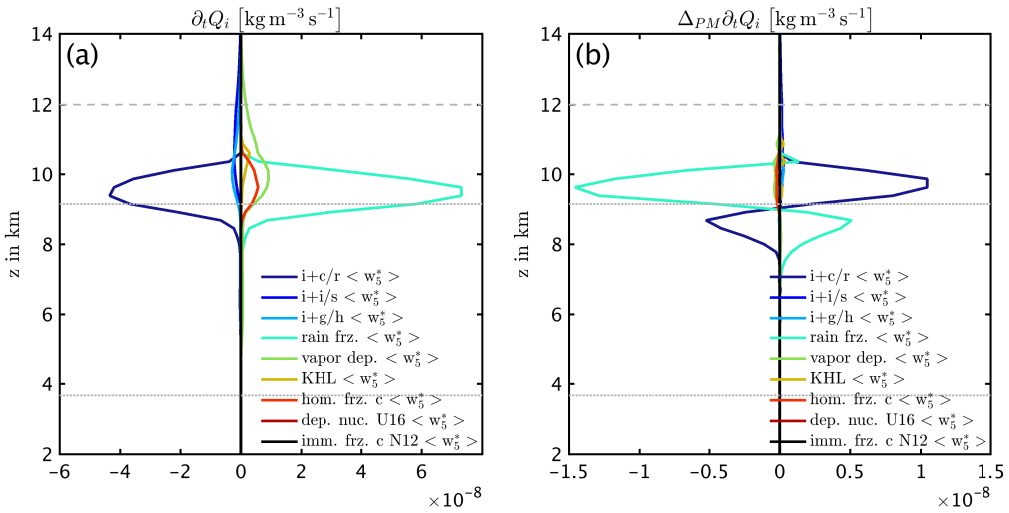


Fig. 6.22.: Microphysical budget contributions to cloud ice mass, shown as vertical profiles of base states (a) and absolute changes (b) resulting from ice nuclei perturbations, with $N_{dust,0} = 10^5\,\mathrm{m^{-3}}$. Dotted horizontal lines indicate the levels of 0 °C and −36 °C, and dashed horizontal lines indicate the maximum of anvil ice concentrations.

When $N_{dust,0}$ is larger than in the case shown here, the most important difference is the increasing contribution of vapor deposition, both absolute and for $\Delta_{PM}\frac{\partial Q_i}{\partial t}$ (not shown), while its magnitude is still small compared to freezing and riming rates. Therefore we focus on the latter two processes in the following (Fig. 6.23) in order to explain the upper-level mass loss with higher $N_{dust,0}$, as shown in Fig. 6.21. In the following, "freezing" denotes the sum of all drop freezing mechanisms of both cloud and rain drops which form cloud ice.

With small $N_{dust,0}$, nearly all cloud ice mass is formed in the homogeneous freezing region above 9 km (a.1). As long as homogeneous freezing is dominant, the peak is reduced in magnitude, but remains at a constant altitude. With increasing liquid mass depletion below z=9 km, a turning point is reached at

some "critical concentration" $N_{dust,0} = N_{crit}$. With $N_{dust,0} > N_{crit}$, the peak of the freezing rate is shifted to lower altitudes and increases in magnitude with further increase of $N_{dust,0}$. In the simulation with $N_{dust,0} = 10^7\,\mathrm{m}^{-3}$, the "step" at 9 km and the peak below indicate that $N_{dust,0} = 10^7\,\mathrm{m}^{-3}$ is slightly beyond $N_{crit}$. Panel (a.2) reflects the downward-shift of the freezing rates. With $N_{dust,0} < N_{crit}$, the absolute upper-level mass loss is more pronounced than the lower-level gain. The relative freezing rate changes (a.3) show that only with small $N_{dust,0}$, the freezing rates scale proportional to the dust perturbation. With high $N_{dust,0}$ and in cold levels, the relative rate enhancement is no longer equal to the relative dust increase because not every activated particle can contribute to the triggering of drop freezing ($\lambda_{IN} >> 1$).

The riming depletes ice mass in most cases (b.1), i.e., cloud ice is converted to larger ice particle classes on average. An exception is found with $N_{dust,0} = 10^9\,\mathrm{m}^{-3}$ when large rain is depleted before reaching the homogeneous freezing regime, and collisions of cloud ice with small remaining droplets accumulate cloud ice mass (black line around 9 km). The riming rates (b.1) are closely related the the freezing rates (a.1). In the perturbed microphysical state with more efficient rain freezing (b.2), cloud ice riming rates become larger in magnitude in lower levels, and smaller above (b.2). Thus, the gain of ice mass by freezing outweighs the loss of liquid mass by freezing. However, the upper-level mass "gain" (i.e., less efficient depletion by riming) is smaller than the loss by less efficient freezing (a.2, z > 9 km) in those simulations where homogeneous freezing makes significant contributions (all but $N_{dust,0} = 10^9\,\mathrm{m}^{-3}$).

Due to the inequality of positive and negative contributions by riming (b.2) and freezing (a.2) at altitudes above 9 km, the upper-level mass loss (Fig. 6.21 b.1/2) with more $N_{dust,0}$ is results mainly from the sum of these two mechanisms. This general behavior is plausible when we regard the freezing process as a trigger, and the riming to be the consequence – i.e., the consequence follows its trigger. This is further highlighted in panels (c) which illustrate the sum of all cloud ice budget terms related to drop freezing and riming. With more mineral dust present (c.2), the tendency can become both positive and negative in the heterogeneous freezing region, but is clearly negative in the homogeneous freezing regime. The most pronounced loss is found in simulations with $N_{dust,0}$ being close to the "turning point" around $10^7\,\mathrm{m}^{-3}$, $N_{crit}$, and thus when homogeneous and heterogeneous mass freezing rates make similar contributions. This can describe the peaking total ice mass sensitivity which was shown in Fig. 6.21 (b.2).

With $N_{dust,0} > N_{crit}$, other mechanisms than discussed here become increasingly important for the upper-level mass loss in the perturbed microphysical state. Particularly in case of $N_{dust,0} = 10^9\,\mathrm{m}^{-3}$, e.g., cloud ice mass consumption by collisions with other ice particles has higher magnitudes (not shown). Furthermore, the cirrus freezing parameterization (i.e., freezing of solution droplets) following Kärcher et al. (2006, KHL hereafter) contributes increasingly to ice mass in these cases. The role of KHL will be further discussed in the next section related to ice number concentrations. Sensitivity tests will show a potential of this parameterization to modulate the simulated sensitivities, but with a small magnitude compared to the overall radiative flux changes (section 6.2.7). Thus, we are confident that our conclusions are not challenged by the effect of this specific part of the model, originally designed for the appropriate simulation of cirrus formation in large-scale models rather than strong convection in cloud-resolving simulations.

### 6.2.4. Cloud ice number budgets

Here, we show the origins of anvil ice number concentrations and their dependence on the mineral dust background $N_{dust,0}$. There are three main contributions to upper-level ice numbers in the model,

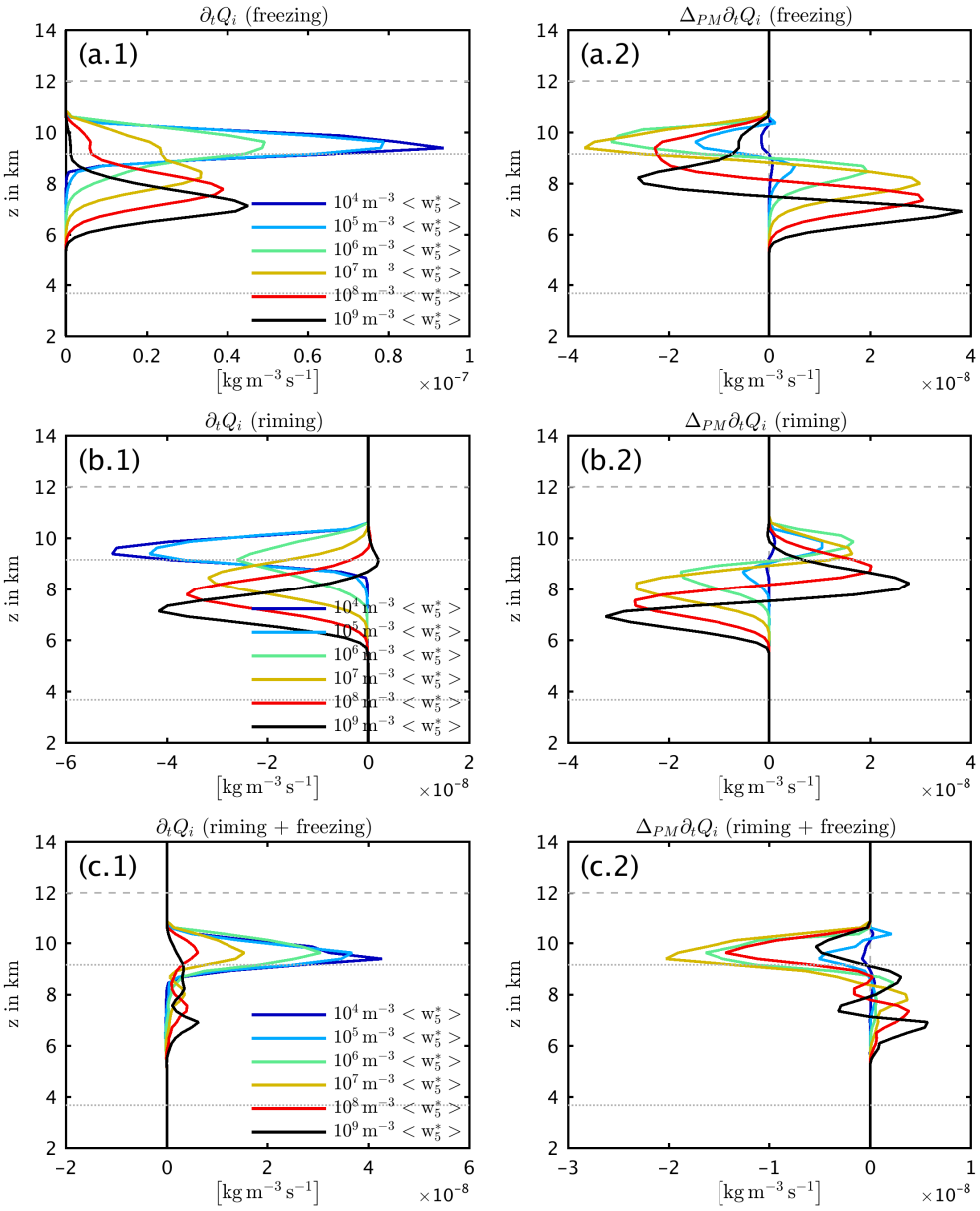


Fig. 6.23.: Cloud ice formation rates by freezing (a), depletion/growth by riming (b) and the sum of freezing and riming (c). The vertical profiles show the base states (*.1), absolute changes (*.2) and relative changes (*.3) resulting from ice nuclei perturbations. Each color corresponds to mineral dust background concentrations ranging from $10^4\,\mathrm{m}^{-3}$ to $10^9\,\mathrm{m}^{-3}$. Dotted horizontal lines indicate the levels of 0 °C and −36 °C, and dashed horizontal lines indicate the maximum of anvil ice concentrations.

depending on $N_{dust,0}$: Homogeneous freezing of cloud droplets, the KHL parameterization for freezing solution droplets and with highest $N_{dust,0}$, the deposition nucleation following Ullrich et al. (2016). An example of rate analysis is given in Fig. 6.24 for $N_{dust,0} = 10^5\,\mathrm{m}^{-3}$. In this case, we see that homogeneous freezing of cloud droplets makes the highest contribution, followed by KHL and rain drop freezing, while collisions of cloud ice with other particles reduce the number. Also in panel (b) which shows the differences in the perturbed microphysical state, we find the most dominant processes to be homogeneous

cloud droplet freezing and KHL, but an appropriate interpretation is not possible based on these data (noisy peaks in panel b). In contrast to previous sections where the process rates were analyzed based on the 10 minute-spaced model output, this temporal resolution is not enough to enable a meaningful interpretation of number process rates.

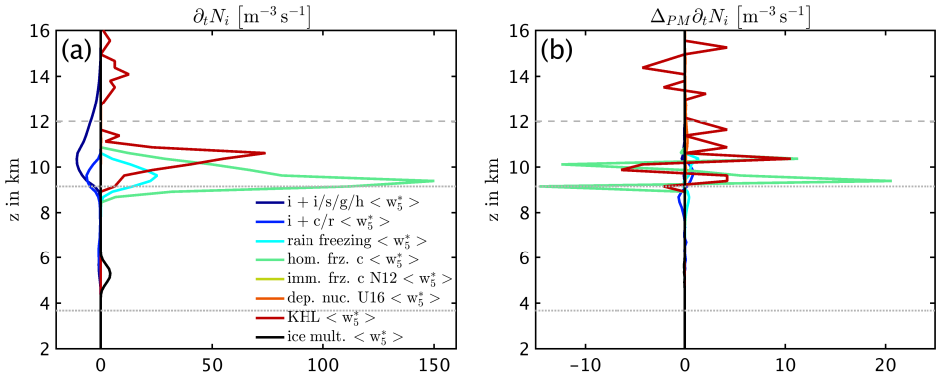


Fig. 6.24.: Microphysical budget contributions to cloud ice number density, shown as vertical profiles of base states (a) and absolute changes (b) resulting from ice nuclei perturbations, with $N_{dust,0} = 10^5\,\mathrm{m}^{-3}$. Dotted horizontal lines indicate the levels of 0 °C and −36 °C, and dashed horizontal lines indicate the maximum of anvil ice concentrations.

Instead of further interpreting rates, additional sensitivity simulations were carried out to understand the relative importances of the three dominant processes. For each one of the concentrations from $N_{dust,0} = 10^5\,\mathrm{m}^{-3}$ to $10^9\,\mathrm{m}^{-3}$, three different setups are compared (STD vs. KHLoff vs. FRZonly): The standard setup (STD) includes all mechanisms, corresponding to the simulations analyzed throughout this work. A further setup will excludes the KHL parameterization (KHLoff), and one setup yields the results when also deposition nucleation is switched off. In the latter case, the only primary ice formation mechanism is therefore given by heterogeneous and homogeneous droplet freezing (FRZonly).

In Fig. 6.21, the positive $\Delta_{PM}N_i$ above 9 km was similar for all $N_{dust,0}$ from $10^5\,\mathrm{m}^{-3}$ to $10^7\,\mathrm{m}^{-3}$. Thus, these three concentrations are grouped in Fig. 6.25 and analyzed in the following. We see that in panels (a), KHLoff (yellow) and FRZonly (black) yield very similar ice concentrations, thus we conclude that Ullrich et al. (2016) does not contribute to the anvil ice number concentrations significantly. The concentrations in STD simulations compared to KHLoff show an enhancement of the mean concentrations up to 50% at 12 km altitude (yellow vs. blue, c.3), indicating an increasing contribution by the KHL parameterization with increasing $N_{dust,0}$. Nevertheless, the dominant ice formation mechanism is given by homogeneous freezing. With perturbed ice nuclei, the general trends of $\Delta_{PM}N_i$, i.e., upper-level ice number enhancements (panels b) are robust in KHLoff and FRZonly simulations. Consistent with panels (a), the deposition nucleation is negligible for $N_{dust,0}$ from $10^5\,\mathrm{m}^{-3}$ to $10^6\,\mathrm{m}^{-3}$, while an increasing contribution to the sensitivity is given with $N_{dust,0} = 10^7\,\mathrm{m}^{-3}$ (b.3). In panels (b.2/3), the higher sensitivies in the STD simulation compared to KHLoff (blue vs. yellow) indicates that KHL tends to enhance the overall cloud sensitivity to perturbed ice nuclei concentrations. Note that with the horizontal averaging over the cloudy column, ice numbers within the core contribute only to a minor extent to the profiles shown here.

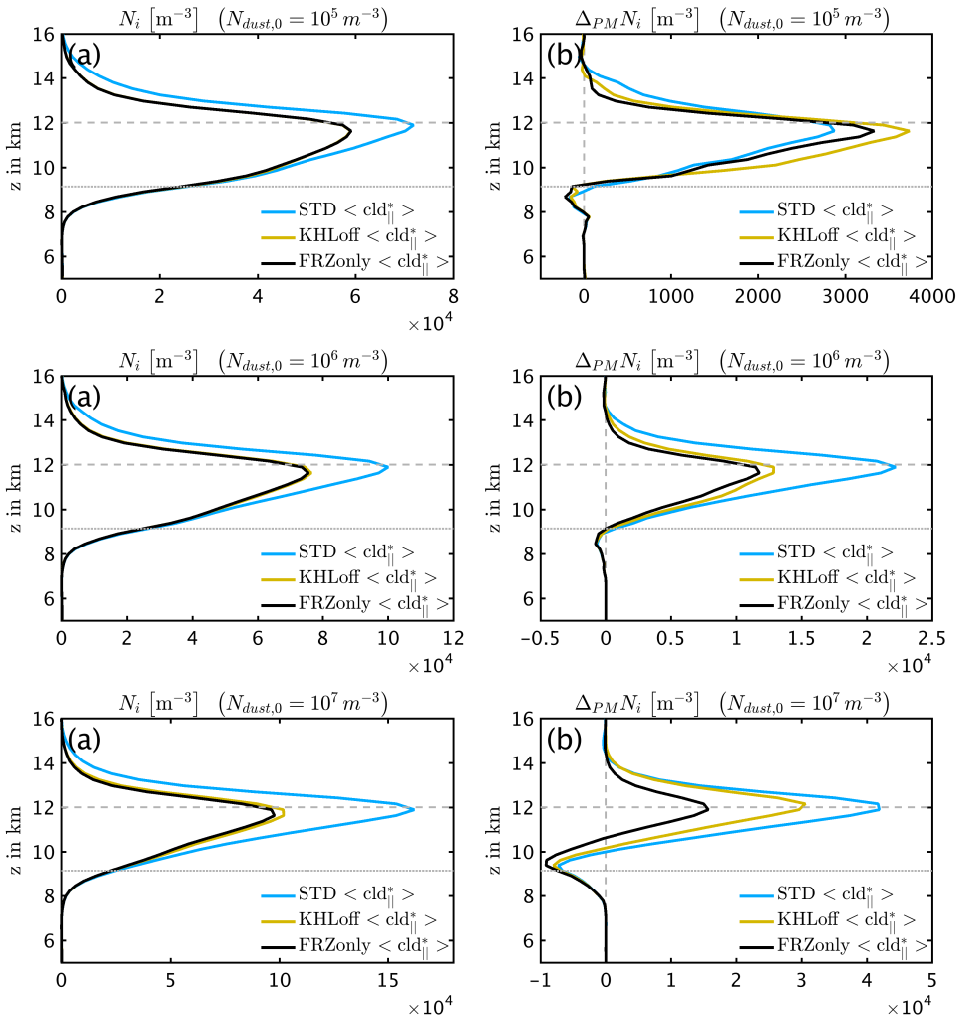


Fig. 6.25.: Cloud ice number densities in simulations with $N_{dust,0} = 10^5\,\mathrm{m}^{-3}$ (upper panels), $N_{dust,0} = 10^6\,\mathrm{m}^{-3}$(mid panels) and $N_{dust,0} = 10^7\,\mathrm{m}^{-3}$ (lower panels). Colors indicate the three sensitivity simulations STD (blue), KHLoff (yellow), FRZonly (black). The vertical profiles show the base states (a) and absolute changes (b) resulting from ice nuclei perturbations. Dotted horizontal lines indicate the levels of $-36\,^{\circ}$C, and dashed horizontal lines indicate the maximum of anvil ice concentrations.

The highest radiative flux sensitivities were found with $N_{dust,0} = 10^8\,\mathrm{m}^{-3}$ (Fig. 6.20), related to the small ice number perturbation at 12 km altitude ($\Delta_{PM} N_i \approx 0$). Here, we see that this result of the STD simulation (blue) arises from the counteracting effects of KHL and deposition nucleation (Fig. 6.26 b). In the FRZonly simulation (black), we now see that $\Delta_{PM} N_i$ becomes negative in all levels. Thus, less droplets freeze homogeneously with more ice nuclei present, which is different from lower $N_{dust,0}$.

With $N_{dust,0} = 10^9\,\mathrm{m}^{-3}$ (Fig. 6.27), the contribution of dust deposition nucleation is dominant. The horizontal average of anvil ice number is ten times as large when deposition nucleation is considered (panel a), while KHL is not important (a, yellow vs. blue). Note that in panel (a) the average ni is even slightly larger when KHL is disregarded, i.e., KHL may suppress some of the deposition nucleation by depletion of supersaturation. These relative importances are also reflected in $\Delta_{PM} N_i$, i.e., the large

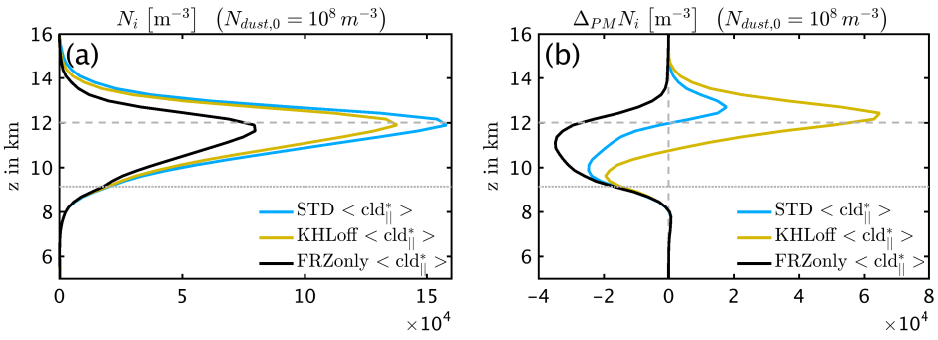


Fig. 6.26.: Cloud ice number densities in simulations with $N_{dust,0} = 10^8\,\mathrm{m}^{-3}$. Colors indicate the three sensitivity simulations STD (blue), KHLoff (yellow), FRZonly (black). The vertical profiles show the base states (a) and absolute changes (b) resulting from ice nuclei perturbations. Dotted horizontal lines indicate the levels of $-36\,^\circ$C, and dashed horizontal lines indicate the maximum of anvil ice concentrations.

positive ice number perturbation shown in Fig. 6.21 originates from deposition nucleation. If the latter is absent, $\Delta_{PM} N_i$ is negative due to less cloud droplet homogeneous freezing (black).

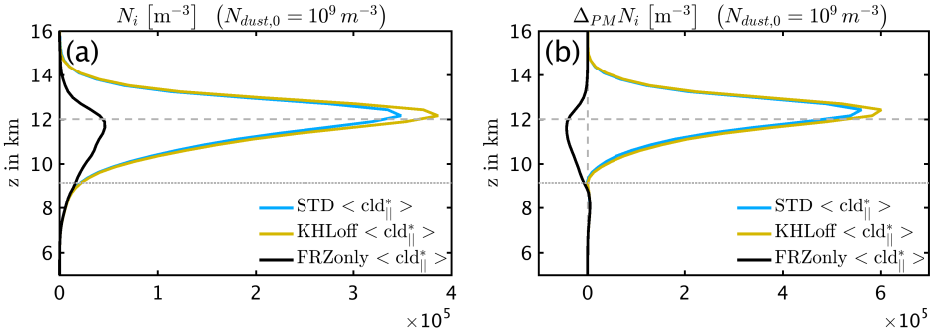


Fig. 6.27.: Cloud ice number densities in simulations with $N_{dust,0} = 10^9\,\mathrm{m}^{-3}$. Colors indicate the three sensitivity simulations STD (blue), KHLoff (yellow), FRZonly (black). The vertical profiles show the base states (a) and absolute changes (b) resulting from ice nuclei perturbations. Dotted horizontal lines indicate the levels of $-36\,^\circ$C, and dashed horizontal lines indicate the maximum of anvil ice concentrations.

### 6.2.5. Cloud droplet number budgets

With cloud droplets being an important component to determine anvil ice number concentrations by homogeneous freezing, the origin of upper-level cloud droplets may be of interest, and their enhanced presence in the perturbed microphysical state ($\Delta_{PM} N_c$>0) in particular. On the one hand, we might expect enhanced droplet depletion by riming in the presence of more ice nuclei. On the other hand, a less pronounced cloud droplet depletion by accretion on rain drops might counteract the riming effect, since with more IN present, less rain reaches upper levels. Figure 6.28 summarizes the rates of cloud droplet formation and depletion, given by groups of freezing (both heterogeneous and homogeneous), collisions (involving both liquid and ice), activation and evaporation. Because of the high temporal variability, these data are based on 1-minute-spaced model output. Furthermore, the rates of activation and evaporation

are pre-calculated as a three-dimensional running mean on model runtime, since often sparse but strong events occur in the model. In this calculation, each time step contributes to the pre-existing mean value of a specific location with a weight of 1%. The data are based on the simulation with $N_{dust,0} = 10^6\,\mathrm{m}^{-3}$ in a FRZonly setup (see section 6.2.4).

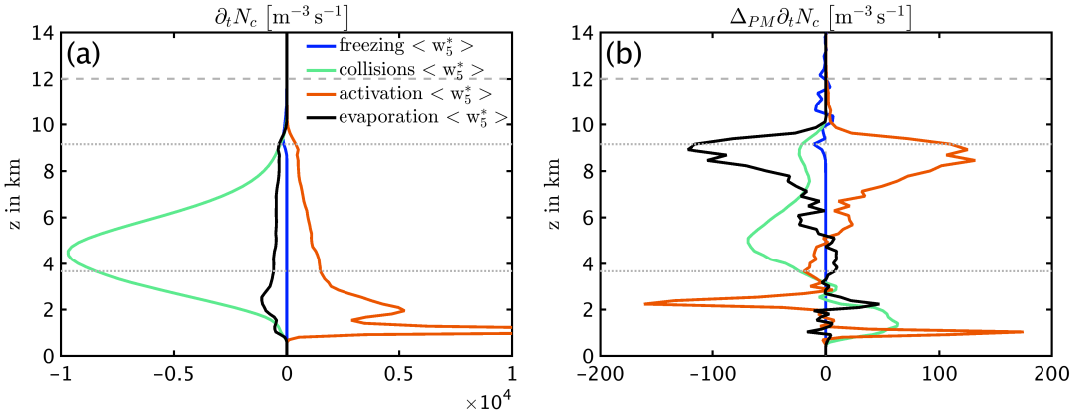


Fig. 6.28.: Microphysical budget contributions to cloud droplet number density, shown as the vertical profiles of base states (a) and absolute changes (b) resulting from ice nuclei perturbations, with $N_{dust,0} = 10^6\,\mathrm{m}^{-3}$. Dotted horizontal lines indicate the levels of 0 °C and −36 °C, and dashed horizontal lines indicate the maximum of anvil ice concentrations.

In the base state (a), collisions make the dominant contribution to droplet depletion. They are also non-negligible in the perturbed microphysical state at lower levels (z < 8 km), i.e., the depletion from 4 km to 7 km is more active than evaporation. However, two dominant processes relevant for the perturbed droplet numbers exist at altitudes above 7 km, given by CCN activation and evaporation, the latter being calculated implicitly due to saturation adjustment (see section 2.2). The very similar structures in time and space (not shown) might indicate that positively perturbed activation rates are counteracted by negatively perturbed evaporation rates to some extent, and vice versa. However, an important difference between the two contributions is the sequential order of the processes within the microphysical code: While activation occurs at the very beginning of the microphysical time step, saturation adjustment and corresponding evaporation is calculated in the very end of the microphysics. Thus, any newly activated droplets are immediately subject to other microphysical processes, and homogeneous freezing in particular. Therefore, the enhanced upper-level droplet activation (b, z > 8 km) has a direct influence on the resulting anvil ice numbers. For further discussion of upper-level droplet numbers, see section B.2.

With temperature and vertical velocities being identical in the perturbed microphysical states (i.e., equal to the base state by definition), we conclude that the enhancement of droplet numbers is likely to originate from the perturbations of water vapor concentrations which has the potential to influence both activation and evaporation of cloud droplets. Although the activation following Segal and Khain (2006) is independent of the magnitude of supersaturation, a pre-condition for activation is given by the grid-scale $RH_w$ being greater than 100% which is more likely to be met with $\Delta_{PM}Q_v$>0. Usually, we think of a more pronounced vapor depletion by cloud ice particles in the presence of enhanced ice nuclei concentrations. Here, we find that the vapor depletion by graupel particles is even more pronounced

than the effect of cloud ice. Figure 6.29 displays a comparison of vapor deposition rates for three $N_{dust,0}$ (blue,$10^5\,\mathrm{m}^{-3}$; yellow, $10^6\,\mathrm{m}^{-3}$; black, $10^7\,\mathrm{m}^{-3}$), averaged over the convective core regions.

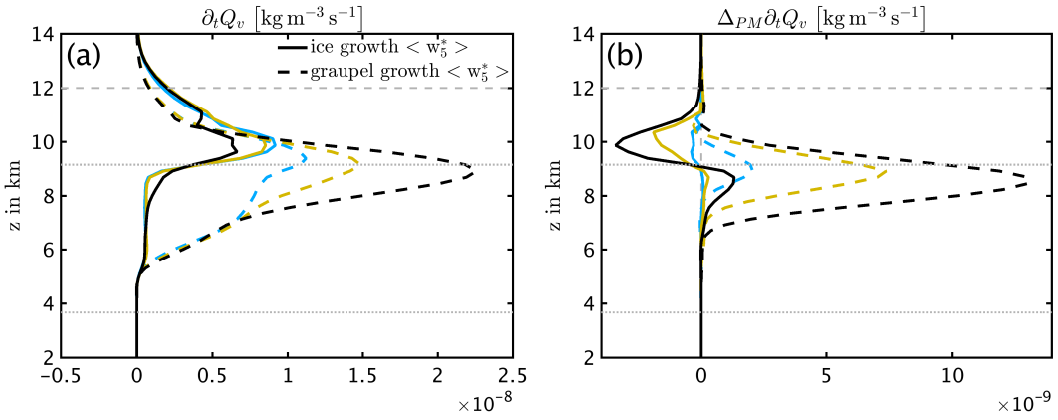


Fig. 6.29.: Mass growth rates of cloud ice (full lines) and graupel (dashed lines) in simulations with $N_{dust,0} = 10^5\,\mathrm{m}^{-3}$ (blue), $N_{dust,0} = 10^6\,\mathrm{m}^{-3}$ (yellow) and $N_{dust,0} = 10^7\,\mathrm{m}^{-3}$ (black). The vertical profiles show the base states (a) and absolute changes (b) resulting from ice nuclei perturbations. Dotted horizontal lines indicate the levels of 0 °C and −36 °C, and dashed horizontal lines indicate the maximum of anvil ice concentrations.

Panel (a) shows that the rates of graupel growth are larger than the growth of cloud ice by a factor of 2 to 3. In the perturbed state (b), both rates are increased below 9 km. An important difference between cloud ice and graupel is the reduced vapor depletion by cloud ice above 9 km in those regions where homogeneous freezing of cloud droplets becomes dominant.

In order to explain the higher abundance of cloud droplets (and anvil ice) in the presence of more ice nuclei based on the perturbed vapor concentration, an expected pre-condition would be the presence of more vapor which would either enable enhanced activation or less pronounced evaporation (Fig. 6.28). The positive growth rate perturbations of cloud ice and graupel ($\Delta_{PM}rate$>0) both tend to deplete more vapor, therefore we may hypothesize that the negative upper-level cloud ice contribution ($\Delta_{PM}rate$<0), z > 9 km) to the vapor budget may be the more important effect (i.e., the cloud ice depositional growth within the homogeneous freezing regime). On the other hand, the large contributions by graupel up to ≈10 km may question this hypothesis. Note that the averaging accounts only for updrafts, i.e., not the whole interactions of cloud particles and vapor are covered.

Finally, we want to separate the specific effects of perturbed vapor depositional growth of cloud ice and graupel particles. For this purpose, further sensitivity simulations were performed, where the mass growth rates by vapor deposition in the perturbed microphysical states were forced to be equal to the base state growth rates by vapor deposition, i.e., $\Delta_{PM}$ of the vapor deposition rate is equal to zero by definition.

In Fig. 6.30, full lines show the resulting number concentrations in standard simulations, dashed lines show the results with cloud ice vapor deposition being equal to the base state, and dotted lines show the results with graupel vapor deposition being equal to the base state. For simplicity, only updrafts are considered for averaging. Black lines indicate cloud droplet numbers, and blue lines cloud ice numbers. The qualitative behavior of the cases with dominant homogeneous freezing ($N_{dust,0} = 10^5\,\mathrm{m}^{-3}$ / $10^6\,\mathrm{m}^{-3}$

/ $10^7\,\mathrm{m}^{-3}$) is very similar, although with different magnitudes. Therefore, only the results of $N_{dust,0} = 10^6\,\mathrm{m}^{-3}$ are shown in Fig. 6.30.

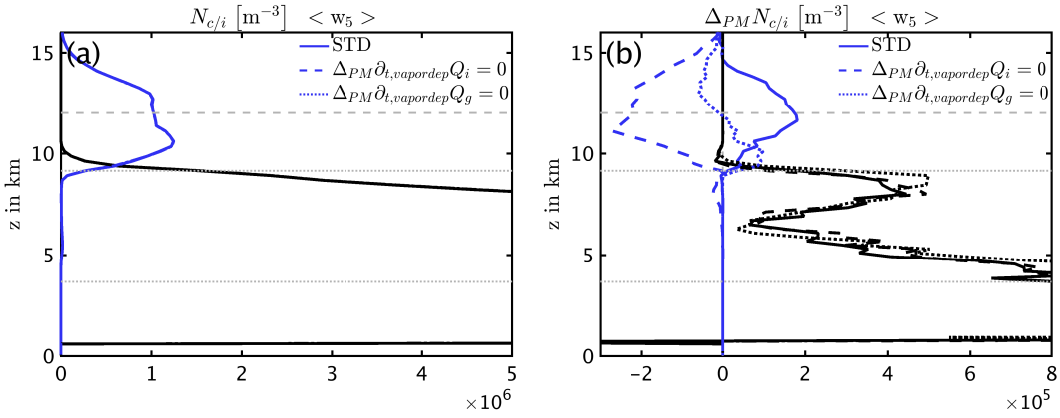


Fig. 6.30.: Cloud droplet (black) and cloud ice (blue) number densities in simulations with $N_{dust,0} = 10^6\,\mathrm{m}^{-3}$. Line styles indicate the standard simulation (full lines), cloud ice depositional growth being equal to the base state (dashed), and graupel depositional growth being equal to the base state (dotted). The vertical profiles show the base states (a) and absolute changes (b) resulting from ice nuclei perturbations. Dotted horizontal lines indicate the levels of 0 °C and −36 °C, and dashed horizontal lines indicate the maximum of anvil ice concentrations.

By suppressing the effect of a modified cloud ice growth on the water vapor concentration and subsequent droplet budgets, the sign of anvil ice number perturbation above the homogeneous freezing level turns negative ($\Delta_{PM}N_i$<0, dashed blue line in panel b), in contrast to the standard simulation. This means that within the homogeneous freezing regime where the dashed line and full line diverge sharply (z≈9 km), the influence of cloud ice vapor deposition on the cloud droplet number (and subsequent freezing) is the dominant mechanism to determine the sign of the anvil number concentration changes in the perturbed IN scenario. As proven by the dotted blue line, also depositional growth of graupel particles has some influence on the resulting anvil ice number, but to a smaller extent and with more ambiguity of the sign of $\Delta_{PM}N_i$.

Based on these simulations, we can conclude that the overall interplay between cloud ice vapor deposition, vapor concentration and droplet numbers within a very narrow regime of homogeneous droplet freezing determines the anvil ice number concentration changes in the perturbed microphysical states: With reduced initial homogeneous freezing rates (i.e., in the warmer regime of homogeneous freezing) of cloud droplets and subsequent smaller depositional growth of cloud ice, more cloud droplets are available for freezing in the narrow regime of coexistent cloud droplets and homogeneous freezing (i.e., in the colder regime of homogeneous freezing). Nevertheless, no direct conclusion is offered here about the relative contributions of parameterized activation vs. evaporation. Physically, the evaporation effect of droplets makes sense because larger droplets freeze homogeneously at higher temperatures (say, $T > -37\,^\circ$C) than smaller droplets (say, $T < -37\,^\circ$C). Consistent with the Wegener-Bergeron-Findeisen process (see chapter 1), the remaining smallest droplets will tend to evaporate in the presence of the larger frozen drops, thus being no longer available for freezing (Phillips et al., 2007).

Because of the narrow temperature regime, strong updrafts, and dependence of the processes discussed here on the simulated supersaturation, some uncertainty may be associated with the droplet depletion. However, the contribution of anvil ice numbers to the radiative flux perturbations is rather small compared to the effect of anvil ice mass, at least in the regime of dominant homogeneous freezing. Therefore, the overall radiative sensitivities are not expected to be affected significantly by WBF-related mechanisms during homogeneous droplet freezing.

### 6.2.6. Summary of anvil ice sensitivities

With $N_{dust,0} \leq 10^6\,\mathrm{m}^{-3}$, radiative fluxes are sensitive only to a minor extent. In the regime from $N_{dust,0} = 10^7\,\mathrm{m}^{-3}$ to $N_{dust,0} = 10^8\,\mathrm{m}^{-3}$, optically thinner clouds are found with more IN present, owing to reduced cloud ice mass contents. Only with deposition nucleation being dominant to determine anvil ice numbers ($N_{dust,0} = 10^9\,\mathrm{m}^{-3}$), the convective outflow is optically thicker in the perturbed microphysical state.

In section 6.2.3, it was shown that the maximum cloud ice mass reduction at $N_{dust,0} = N_{crit}$ is determined by the relative contributions of homogeneous and heterogeneous cloud ice mass formation rates ($N_{crit} \approx 10^7\ \mathrm{m}^{-3}$), promoting optically thinner anvils. Since the enhanced ice numbers tend to counteract this effect to some extent, the peaking radiative sensitivity is found at $N_{dust,0} = 10^8\,\mathrm{m}^{-3}$, where the number perturbations are less pronounced in this specific case.

For perturbed anvil ice number concentrations, cloud droplet homogeneous freezing is the determinant in most of the cases ($N_{dust,0} < 10^8\,\mathrm{m}^{-3}$). In turn, cloud droplet numbers in upper levels are highly sensitive to the perturbed vapor depositional growth of cloud ice within the homogeneous freezing regime. Some modulation is given by the cirrus parameterization according to KHL, while it may be questioned whether extremely strong updrafts in deep convection are within the scope of KHL, and ice formation in liquid-containing regions of the convective updraft should be considered by this part of the model, as this treatment corresponds to the assumption to find solution droplets which have not been activated as CCN. However, it will be shown that the general conclusions are hardly affected by this parameterization (section 6.2.7, Fig. 6.40). In cases of $N_{dust,0} \geq 10^7\,\mathrm{m}^{-3}$, deposition nucleation becomes increasingly important, and is dominant with $10^9\,\mathrm{m}^{-3}$. Thus, anvil ice number concentrations dominate the effect of perturbed radiative fluxes, promoting optically thicker clouds with more IN present.

### 6.2.7. Radiative sensitivities in different environments

After having clarified the basic mechanisms of radiative flux changes as a result of ice nuclei perturbations, the dependencies of radiative properties on a broad range of background mineral-dust concentrations – corresponding to varying immersion freezing efficiencies – is summarized in the following. We focus on the relative changes of the total atmospheric albedo and longwave net fluxes at the top of the atmosphere (TOA), while considering only model data of the cloudy column for the horizontal mean values. TOA albedo is calculated as $\alpha_{TOA} = 1 - \frac{FSW_{TOA}}{1368\,\mathrm{W\,m^{-2}}\,\mu_0}$, with $\mu_0$ being the cosine of zenith angle. While the sign of $\Delta_{PM}\alpha_{TOA}$ is opposite from $\Delta_{PM}FSW_{TOA}$, the magnitude and spatial structures are similar to the underlying fluxes (not shown). Time splitting is analogous to the precipitation section (6.1.7), with red data points containing the time average over the whole period (00:20 - 02:00 hours), while early stages are shown in grey (00:30 - 01:00 hours), mid periods in blue (01:00 - 01:30 hours), and late/mature stages are shown in black (01:30 - 02:00 hours). Negative values indicate optically thinner clouds in the presence of more ice nuclei, determined by the combined effect of cloud ice mass and number concentrations in the convective outflow (section 6.2.2).

The following scenarios are discussed in the following:

- Standard case
- Maritime CCN
- Convective environment
- Homogeneous freezing of haze droplets (KHL)
- Microphysical assumptions of particle conversion
- Aerosol-independent freezing of rain drops (B53)

#### Standard case

Figure 6.31 summarizes the radiative fluxes discussed in section 6.2.1, based on the standard environment (u25q14, $1700\,\mathrm{cm^{-3}}$ CCN background, section 4.2). The relative albedo changes (a) range from close to zero up to 8% in the late period of the simulation ($N_{dust,0} = 10^8\,\mathrm{m^{-3}}$). With $N_{dust,0} > 10^8\,\mathrm{m^{-3}}$, the sensitivity decreases sharply and turns to positive values. The time dependency indicated by the small circles' colors may indicate a slightly reduced effect of number changes at early stages (gray), and an increasing relative contribution at later times (blue, black). For example, the negative sign of the gray circle at $N_{dust,0} = 10^6\,\mathrm{m^{-3}}$ implies a dominant effect of $\Delta_{PM}Q_i$ rather than $\Delta_{PM}N_i$. Later, with $\Delta_{PM}N_i$ becoming dominant, the sign turns positive. This shift with time is also consistent with $N_{dust,0} = 10^9\,\mathrm{m^{-3}}$ where $\Delta_{PM}N_i$ was shown to be the cause of the change in sign – this effect is smaller in the beginning, and increases in the mature stage. The described time dependence is similar for both quantities, albedo and FLW.

#### Maritime CCN

In the maritime CCN environment ($100\,\mathrm{cm^{-3}}$ CCN background), the sensitivities in the medium range of $N_{dust,0}$ are larger than in the continental environment, for both albedo and longwave fluxes (Fig. 6.32). Thus, the turning point is reached at $N_{dust,0} = 10^7\,\mathrm{m^{-3}}$ instead of $10^8\,\mathrm{m^{-3}}$, with a higher magnitude.

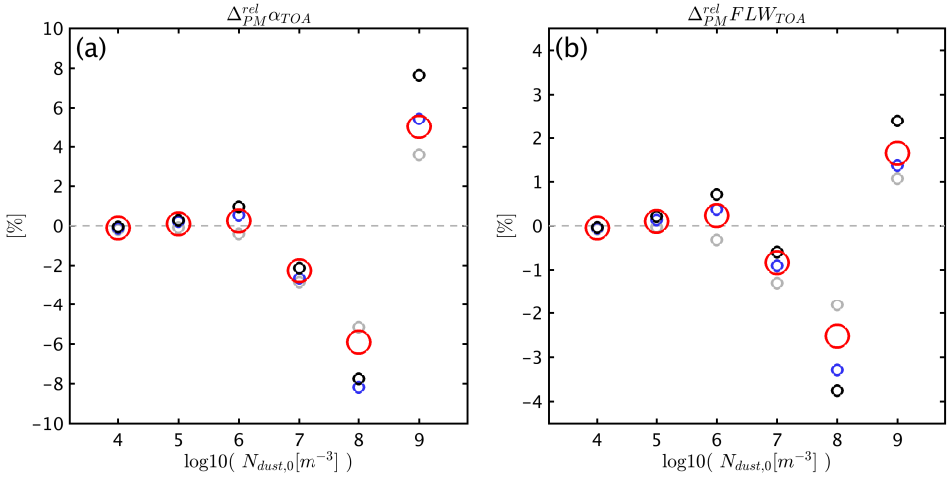


Fig. 6.31.: Relative changes of TOA albedo (a) and TOA FLW (b) for simulations with varying mineral dust background concentrations. Colors represent different periods, with red indicating 00:20 - 02:00 hours, grey 00:30 - 01:00 hours, blue 01:00 - 01:30 hours, black 01:30 - 02:00 hours. The flux changes result from perturbations of $N_{dust,0}\pm 90\%$.

Since a dust concentration of $10^8\,\mathrm{m}^{-3}$ corresponds to a dust fraction of 1 at cloud base, we disregard higher dust concentrations than that.

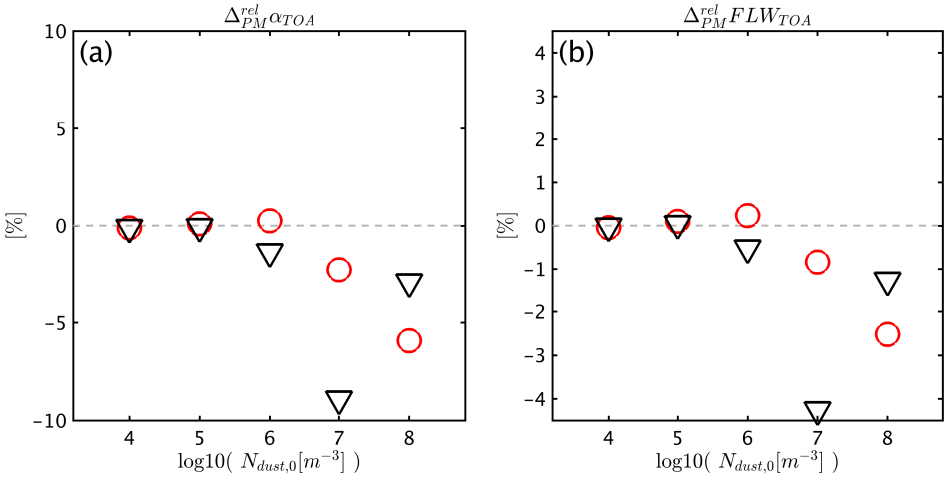


Fig. 6.32.: As Fig. 6.31, comparing the maritime CCN background (triangles) with the continental CCN background (circles corresponding to Fig. 6.31). Time-averaging includes the period from 00:20 - 02:00 hours.

Overall, the sensitivity of anvil cloud ice mass is higher in the maritime environment than in the continental simulations (not shown). This circumstance is also reflected in the microphysical budget terms, as indicated in Fig. 6.33 for a base concentration of $N_{dust,0} = 10^5\,\mathrm{m}^{-3}$. The overall contributions of single processes are still close to the continental case (a, dashed lines). The enhanced sensitivity is reflected in panel (b), where the cloud ice formation by heterogeneous freezing is roughly twice as large

(z < 9 km). As in the standard case, the upper-level mass loss (z > 9 km) due to reduced homogeneous freezing rates is much larger than the gain below 9 km.

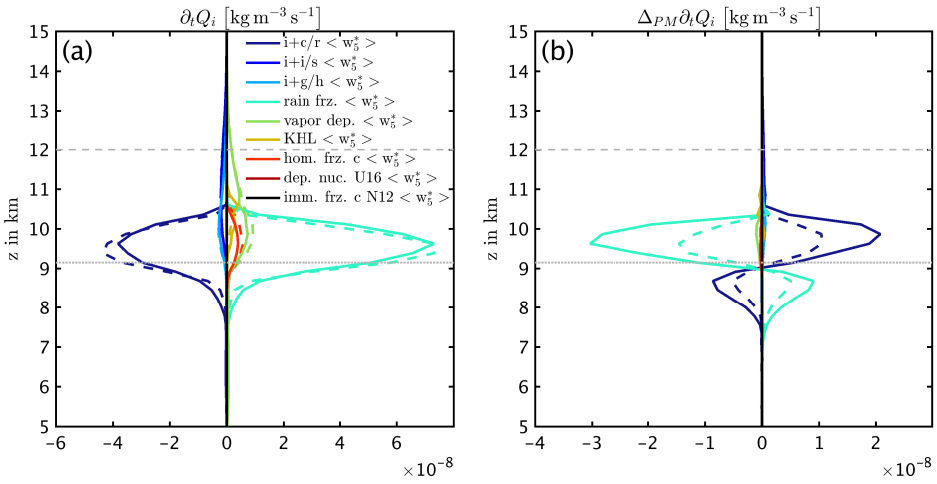


Fig. 6.33.: Cloud ice mass microphysical budgets of the maritime (full lines) and continental scenario (dashed lines) with $N_{dust,0} = 10^5\,\mathrm{m}^{-3}$. The vertical profiles show the base states (a) and absolute changes (b) resulting from ice nuclei perturbations. Dotted horizontal lines indicate the levels of 0 °C and −36 °C, and dashed horizontal lines indicate the maximum of anvil ice concentrations.

The enhanced sensitivity of cloud ice formation by immersion freezing (Fig. 6.33 b), z < 9 km) can be explained by the rain properties in the marine environment, as compared to the continental case. Fig. 6.34 illustrates the bulk rain mass (a), rain number concentration (b) as well as the bulk number of mineral dust particles contained in rain drops (c). The rain properties are consistent with the general expectation that with less CCN present at cloud base, less but larger cloud droplets are formed which are converted more efficiently to rain drops by collisional growth. Accordingly, both rain mass and number concentrations are increased (a/b, full lines). Above the −12 °C level in which mineral dust begins to trigger freezing (z > 5 km), these differences are compensated more or less quickly, depending on $N_{dust,0}$. With the more efficient conversion of cloud to rain drops, significantly more dust particles are found in the bulk rain mass with marine CCN concentrations (c, full lines), which finally explains the increased sensitivity of the immersion freezing rates to dust perturbations – and subsequent enhanced cloud ice mass loss by decreased homogeneous freezing.

The more efficient immersion freezing can also explain the turning point (Fig. 6.32), shifted to a lower $N_{dust,0}$ of $10^7\,\mathrm{m}^{-3}$. With more dust contained in rain drops compared to the continental scenario, the critical $N_{dust,0}$ which results in a dominant heterogeneous freezing is reached with smaller $N_{dust,0}$.

### Convective environment

For $N_{dust,0} = 10^7\,\mathrm{m}^{-3}$, varying convection-permitting environment in terms of wind shear and boundary layer humidity are summarized in Fig. 6.35. The most pronounced differences are found in the cases of u25q11 and u40q14 which are more sensitive than others. Analogous to the precipitation section (6.1.7), the two cases of u10q11 (weakest convection) and u25q11 are further analyzed for the whole range of dust concentrations in the following.

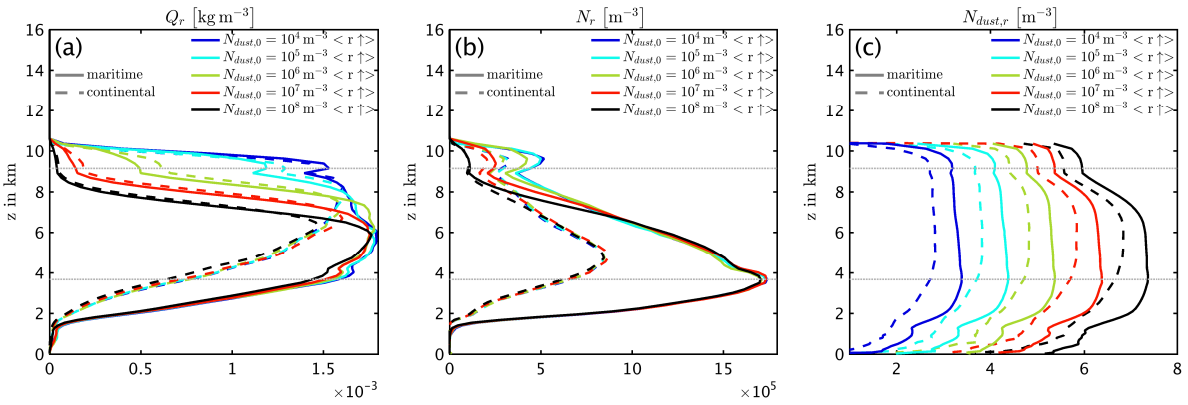


Fig. 6.34.: Rain mass (a), number concentrations (b) and mineral dust particles immersed in rain, as a comparison budgets of the maritime (full lines) and continental scenario (dashed lines). The vertical profiles are representative for the rain lifting regime. Each color corresponds to mineral dust background concentrations ranging from $10^4\,\mathrm{m}^{-3}$ to $10^8\,\mathrm{m}^{-3}$. Dotted horizontal lines indicate the levels of 0 °C and −36 °C.

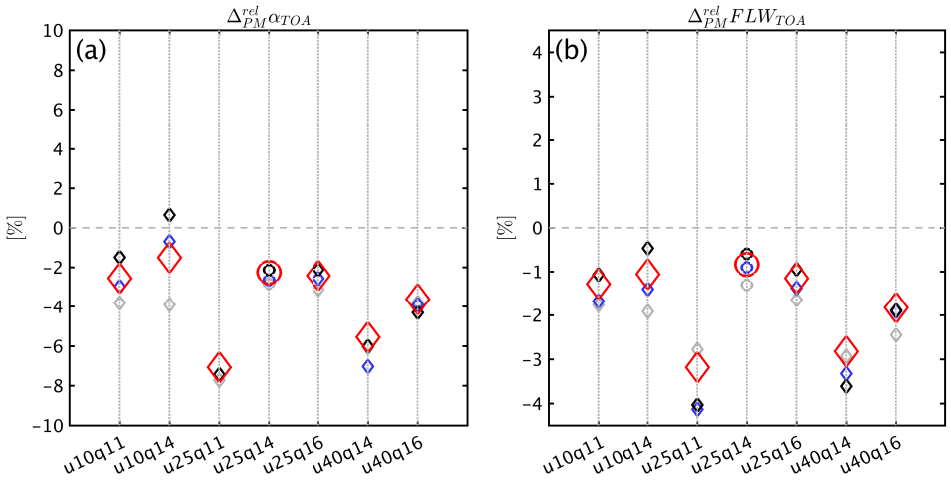


Fig. 6.35.: Relative changes of TOA albedo (a) and TOA FLW (b) for simulations in varying atmospheric environments, with $N_{dust,0} = 10^7\,\mathrm{m}^{-3}$. Colors represent different periods, with red indicating 00:20 - 02:00 hours, gray 00:30 - 01:00 hours, blue 01:00 - 01:30 hours, black 01:30 - 02:00 hours. The flux changes result from perturbations of $N_{dust,0}$±90%. The standard case (u25q14) is indicated by circles, corresponding to Fig. 6.31.

In the u10q11 environment (Fig. 6.36), the differences range within 1% (on the scale of the ordinate) compared to u25q14, except for $N_{dust,0} = 10^6\,\mathrm{m}^{-3}$. Although not shown explicitly in this case, the enhanced optical thickness may arise from an enhanced sensitivity of anvil ice number concentrations.

In the u25q11 environment (Fig. 6.37), we find a tendency towards increased sensitivities compared to the standard case (u25q14). The enhancement to be most pronounced in the range of $N_{dust,0}$ from $10^6\,\mathrm{m}^{-3}$ to $10^8\,\mathrm{m}^{-3}$. An exception is the sensitivity of albedo with $N_{dust,0} = 10^9\,\mathrm{m}^{-3}$, in which case the result is dominated by $\Delta_{PM}N_i$, originating from a more efficient deposition nucleation (section 6.2.4).

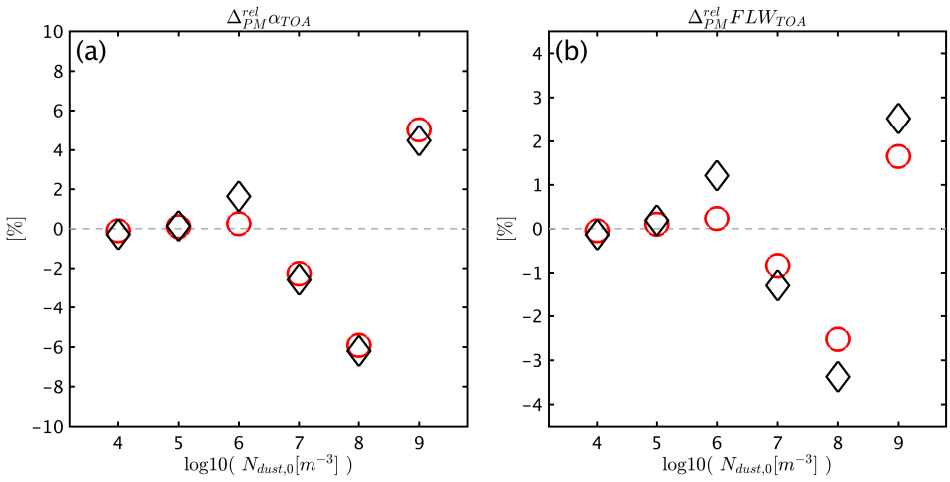


Fig. 6.36.: As Fig. 6.31, comparing weak convection (u10q11, diamonds) with the strong convective environment (u25q14, circles corresponding to Fig. 6.31). Time-averaging includes the period from 00:20 - 02:00 hours.

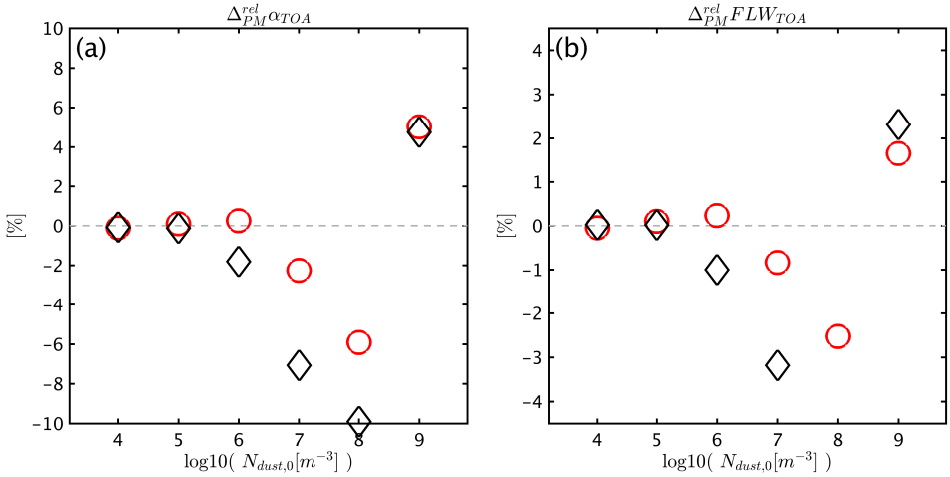


Fig. 6.37.: As Fig. 6.31, comparing intermediate convection (u25q11, diamonds) with the strong convective environment (u25q14, circles corresponding to Fig. 6.31). Time-averaging includes the period from 00:20 - 02:00 hours.

A brief analysis of cloud ice mass formation rates and rain properties will yield some hints at the origin of enhanced sensitivities. The analysis is shown for the $N_{dust,0} = 10^7\,\mathrm{m}^{-3}$ case. In Fig. 6.38, dashed lines indicate the standard case (u25q14), and full lines correspond to the case involving decreased boundary layer humidity (u25q11). With the decreased convective strength and horizontal cloud extent, the horizontal mean values are generally smaller with weaker convection. More importantly, we find a downward-shift of the most active heterogeneous freezing levels. The shift enhances the relative importance of immersion freezing compared to homogeneous freezing, and increases the depletion of liquid mass in lower levels.

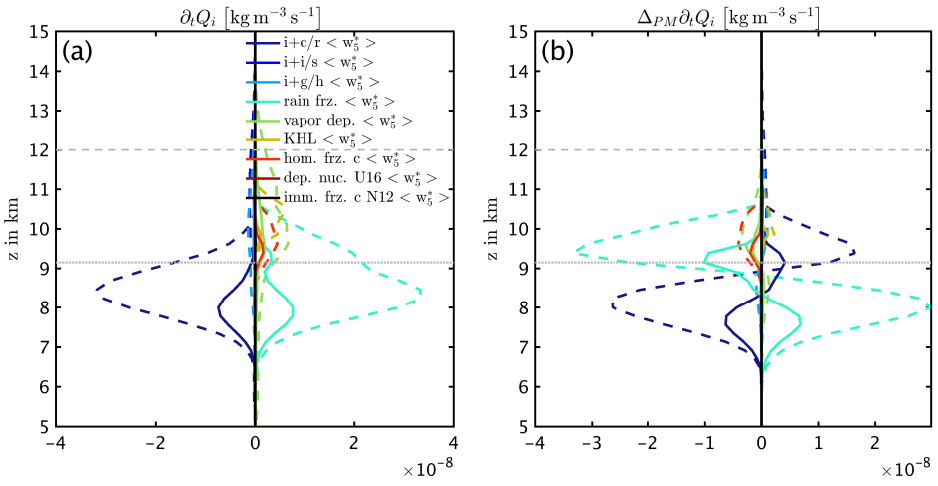


Fig. 6.38.: Cloud ice mass microphysical budgets of the weaker convection (full lines, u25q11) and standard scenario (dashed lines, u25q14) with $N_{dust,0} = 10^7\,\mathrm{m}^{-3}$. The vertical profiles show the base states (a) and absolute changes (b) resulting from ice nuclei perturbations. Dotted horizontal lines indicate the levels of 0 °C and −36 °C, and dashed horizontal lines indicate the maximum of anvil ice concentrations.

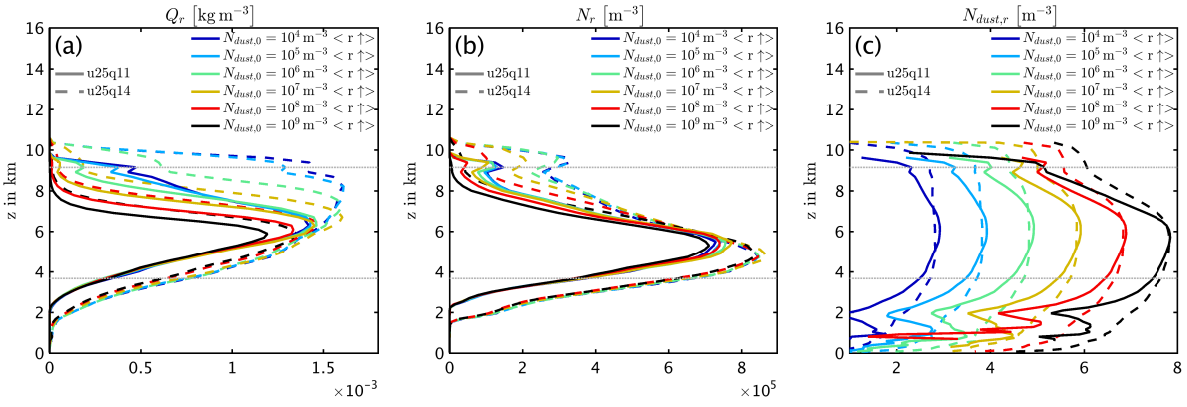


Fig. 6.39.: Rain mass (a), number concentrations (b) and mineral dust particles immersed in rain, as a comparison budgets of the weaker convection (full lines, u25q11) and standard scenario (dashed lines, u25q14). The vertical profiles are representative for the rain lifting regime. Each color corresponds to mineral dust background concentrations ranging from $10^4\,\mathrm{m}^{-3}$ to $10^9\,\mathrm{m}^{-3}$. Dotted horizontal lines indicate the levels of 0 °C and −36 °C.

In Fig. 6.39, the rain properties are representative for rain lifting regimes, and independent of the cloud horizontal extent. Although rain masses and number concentrations are smaller in case of the weaker convection (a/b, full lines), there are regions in the mid levels where the mineral dust concentrations immersed in rain are enhanced compared to the stronger convection (c). This results in a more efficient depletion of upper-level rain mass (a).

Evident from the simulation of weakest convection (u10q11, Fig. 6.36), a reduced convective strength does not necessarily result in increased particle accumulation in rain and thus enhanced sensitivity to dust perturbations. On the other hand, certain dynamical environments such as the u25q11 case shown

here, and the case of u40q14 (not shown), seem to promote the efficient conversion of cloud droplet-immersed particles to rain-immersed particles. In the simulation of u40q14 with $N_{dust,0} = 10^7\,\mathrm{m}^{-3}$ (Fig. 6.35), the increase of $N_{dust,r}$ is smaller in magnitude, but distributed over a broader range of levels (not shown). Accordingly, the immersion freezing efficiency is enhanced in all levels, rather than being shifted downwards.

### Homogeneous freezing of haze droplets (KHL)

In section 6.2.4, it was speculated how much the cirrus parameterization following Kärcher et al. (2006) influenced the sensitivity results. Since in some situations, this parameterizations contributes significantly to anvil ice formation within strong convective updrafts and even in the presence of liquid water, two types of sensitivity simulations were conducted in the range of $N_{dust,0}$ from $10^6\,\mathrm{m}^{-3}$ to $10^9\,\mathrm{m}^{-3}$. The first test involved the suppression of KHL-based ice formation in regions of water supersaturation to identify strong convective updrafts, indicated by "+" signs in Fig. 6.40. Since also in these simulations, nearly all of the KHL-based ice formation occurs in the convective updraft after the air parcels have passed the regime of homogeneous droplet freezing, a second test was intended to confirm the sensitivities in case of KHL being switched off ("x" signs).

Here we see that although some modulation of the standard case-based results is given by the KHL parameterization, the basic dependencies of radiative flux changes on $N_{dust,0}$ are quite robust. Although the sign of albedo change is ambiguous in the $N_{dust,0} = 10^6\,\mathrm{m}^{-3}$ scenario, the magnitude of changes is negligible with this concentration.

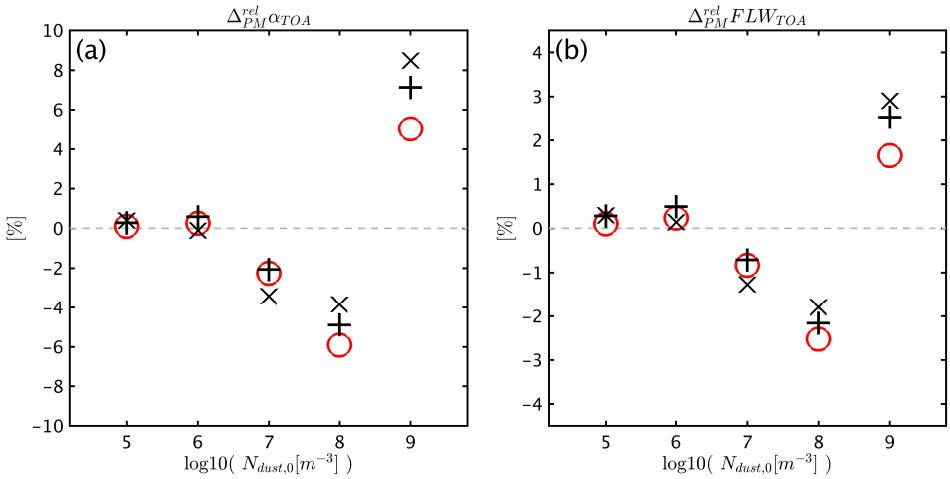


Fig. 6.40.: As Fig. 6.31, comparing the sensitivity simulations with KHL restricted to $RH_w$<100% (+), KHL switched off (x) and the standard simulation (circles, corresponding to Fig. 6.31). Time-averaging includes the period from 00:20 - 02:00 hours.

### Microphysical assumptions of particle conversion

In case of the precipitation sensitivity, it was shown that some assumptions made during the riming process can considerably alter the simulated change of surface rain. In terms of radiative flux changes

upon ice nuclei perturbations, no large differences are found (Fig. 6.41) because cloud ice properties are not influenced much by this specific treatment. In all simulations with $N_{dust,0} < 10^9$, trend towards slightly increased sensitivities is found, but small in magnitude. Although not shown here, this may be related to a modified re-distribution of water vapor due to the change of graupel properties. The latter were shown to influence the anvil ice number concentrations via depositional growth in section 6.2.4.

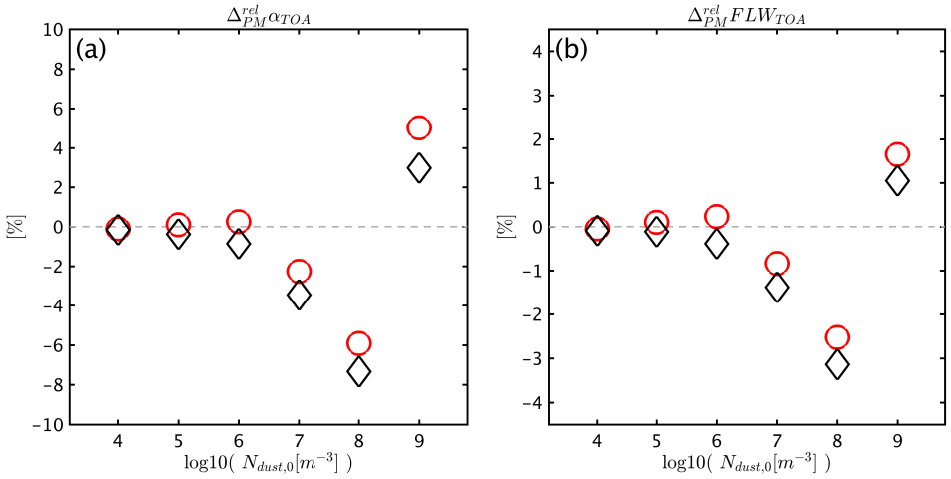


Fig. 6.41.: As Fig. 6.31, comparing "ice_typ=3" (diamonds) with the default choice "ice_typ=2" (circles corresponding to Fig. 6.31). Time-averaging includes the period from 00:20 - 02:00 hours.

### Aerosol-independent freezing of rain drops (B53)

Here we are interested in a comparison of simulated cloud sensitivities with and without aerosol-dependent freezing of rain drops. Cloud ice budgets are much dependent on the freezing of rain drops smaller than 500 µm, and cloud ice mass in particular.

Figure 6.42 summarizes both standard cases (u25q14, large symbols) and weak convective cases (u10q11, small symbols). Consistent with the findings shown above (Fig. 6.36), only minor differences between the two convective environments (i.e., stronger and weaker convection) are found. However, major differences do exist between simulations with B53- and N12-base freezing.

Figure 6.42 shows that with B53-based rain freezing (diamonds), the turning point is shifted downwards by two orders of magnitude of $N_{dust,0}$ ($10^6\,\mathrm{m}^{-3}$ vs. $10^8\,\mathrm{m}^{-3}$). The simulated sensitivities in a specific scenario can thus be very different in sign and magnitude. This tendency may be expected from the analysis of section 6.2.2 which showed that the specific $N_{dust,0}$ of the turning point is related to the relative importance of heterogeneous vs. homogeneous freezing. On the other hand, the underlying process changes are very different in the direct comparison of B53- and N12-based rain freezing (not shown). Two main differences can be identified: First, we usually find a less efficient heterogeneous freezing of in the presence of more ice nuclei. This counter-intuitive behavior arises from the B53-based parameterization which is only dependent on the rain mass content. With more cloud ice particles present, the enhanced rain mass depletion yields smaller freezing rates of rain. The second major difference is the generally higher importance of vapor depletion by ice depositional growth in lower levels of B53-based clouds. This is plausible because of the generally higher presence of ice particles.

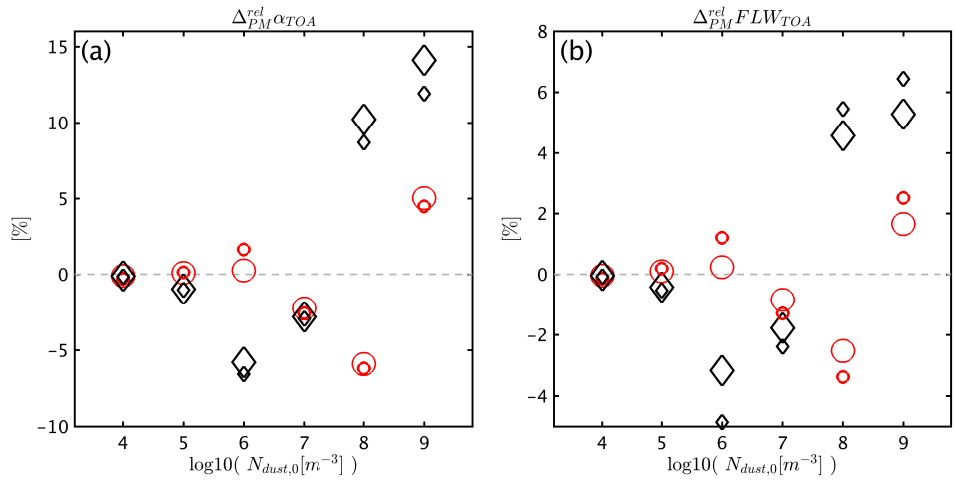


Fig. 6.42.: As Fig. 6.31, comparing the aerosol-independent B53 approach (diamonds) with the new implementation of N12 for freezing rain (circles corresponding to Fig. 6.31). Simulations are based on strong convection (large symbols, u25q14) and on weak convection (small symbols, u10q11). Time-averaging includes the period from 00:20 - 02:00 hours.

### 6.2.8. Summary of radiative flux changes

In this section, we showed the radiative flux sensitivities to ice nuclei perturbations, depending on the mineral dust background concentration and atmospheric environments. The relative changes of albedo as seen from TOA have magnitudes of approximately $\pm 6\%$ when averaged over the cloud-containing columns, and TOA longwave radiative fluxes are less sensitive, but show similar qualitative dependencies: Up to the dust concentration of $10^6\,\mathrm{m}^{-3}$, generally small sensitivities are found. With higher mineral dust backgrounds, the dominating properties of anvil ice mass yield a regime of cloud optical thinning upon IN perturbations. When surpassing a turning point (here, $N_{dust,0} = 10^8\,\mathrm{m}^{-3}$), optically thicker anvils result from the dominating ice number perturbations, ultimately caused by the contribution of deposition nucleation.

This behavior is similar in all cases which involve the dust-based freezing, with some modulation as follows: In maritime environments, we find enhanced sensitivities, caused by the increased efficiency of cloud-to-rain drop conversion and corresponding particle content within the rain drops. Also in some dynamically different environments, the conversion efficiency appears to be slightly enhanced. Microphysical assumptions in the model (except for the treatment of freezing) cause only minor modulations of the cloud radiative sensitivity which is in contrast to the simulation of precipitation.

Large differences are found in the comparison of B53- and N12-based freezing: Owing to the overall high drop freezing efficiency (B53), the turning point in the regime of negative cloud sensitivity (thinning) is shifted towards smaller concentrations of $N_{dust,0}$ by two orders of magnitude. Nevertheless, the qualitative behavior, i.e., positive sensitivity beyond the turning point, is similar with both versions of drop freezing. These similarities arise from the mechanisms which dominate the perturbations of anvil ice mass and number properties, i.e., homogeneous freezing in the “negative” regime, and deposition nucleation in the “positive” regime.

# 7. Conclusions

The interdependencies between aerosol particles, cloud microphysical mechanisms, cloud evolution and atmospheric circulation pose challenges to our understanding of the mechanisms involved in, and the final outcome of aerosol perturbations which act to modulate precipitation and radiation.

In this work, we have analyzed the effects of mineral dust particles in clouds, focussing on their role as ice nuclei (IN) in the mixed-phase and convective outflow regimes. A new approach to parameterize the aerosol-dependent freezing probability of rain-sized drops has been derived (section 2.3). By making use of the "perturbed microphysics" implementation (section 2.5), we have distinguished between the microphysical interactions, and the tendencies of cloud-dynamical responses to either enhance or suppress the microphysical tendencies.

## 7.1. Summary

In accordance with the research questions put forward in section 1.4, the summary of this work is as follows:

In chapter 3 we have shown that with the coupling between cloud properties, radiation and boundary layer dynamics, the microphysical sensitivity of cloud glaciation to IN perturbations is enhanced in magnitude by approximately 50%. However, the cloud-dynamical enhancement decays in a quasi-equilibrium state of the simulation.

In the simulations of deep convective clouds, our new implementation of aerosol-dependent rain drop freezing (section 2.3) has major effects on the simulated liquid water content in the convective core, on precipitation formation, and on the simulated sensitivities to IN perturbations. To our knowledge, this is the first implementation in bulk microphysical models to explicitly account for the conversion of cloud-immersed particles to rain-immersed particles in order to consider the rain drop microphysical history for the calculation of freezing probabilities. With average atmospheric mineral dust concentrations, we find generally smaller freezing efficiencies of large drops when comparing the dust-dependent implementation with the widely-used parameterization based on Bigg (1953, section 5.3).

Surface rain formation is dominated by melting of graupel and hail. Graupel and hail growth by riming often tend to counteract each other in perturbed IN scenarios, thus making the change of surface rain case-specific (section 6.1): In graupel-dominated clouds associated with weak convection, surface rain is enhanced, with a maximum sensitivity found at intermediate mineral dust background concentrations. In hail-dominated clouds, corresponding to supercells, surface rain and hail precipitation is reduced, owing to the less efficient growth of hail with more IN present.

Radiative flux changes as a result of IN perturbations have been characterized by two distinct regimes (section 6.2): With intermediate mineral dust concentrations and dominant homogeneous freezing, the reduced cloud ice mass concentrations in the convective outflow yield optically thinner anvils. In our sce-

narios with relatively high dust concentrations and dominant deposition nucleation on mineral dust, IN perturbations yield optically thicker clouds as a result of more numerous and smaller anvil ice particles.

In our cases of deep convection, cloud droplet freezing properties appear to be of minor importance compared to rain-sized drops, owing to the efficient conversion of cloud droplet-immersed IN to rain-immersed IN. In other types of clouds – e.g., with colder cloud bases – more emphasis might be put on the perturbed freezing of cloud droplets, i.e., when the formation of large drops by drop-drop collisions is less pronounced.

The comparison of maritime and continental CCN scenarios showed that precipitation sensitivities were affected to a relatively small extent, while more significant differences were found for radiation. Apparently, the different sensitivities of precipitation and radiation to the CCN environment originate from the indirect pathway of precipitation formation via riming, while the anvil radiative properties are more directly related to the cloud ice particles initiated by freezing.

## 7.2. Discussion

An general indicator for regime changes – when scanning through a variety of mineral dust background concentrations, i.e., IN abundance – appears to be the role of homogeneous freezing. In particular, a critical point ($N_{crit}$) may be defined such that with $N_{dust} < N_{crit}$, homogeneous freezing is dominant, and with $N_{dust} > N_{crit}$, the depletion of liquid water is controlled at warmer temperatures, and is therefore linked to the IN perturbation more directly. Whether the considered dust concentration is below or above $N_{crit}$ will thus modulate the dominance of prevalent mixed-phase mechanisms. Here we show that for the radiative flux sensitivity, $N_{crit}$ is characterized by the mass rates of freezing rain to determine the sensitivity of cloud ice mass in the convective outflow (section 6.2.2). Similar dependencies were found for perturbed concentrations of precipitating particles, thus modulating the sedimentation efficiency (section 6.1.2).

Most of the phenomena analyzed in this work could be explained by analysis of processes within the mixed-phase updraft regime, implying that collection mechanisms in ice-only regimes and further processing of condensate during sedimentation appear to be of secondary importance for the cloud sensitivities to ice nuclei perturbations. With this finding, it may be interesting whether the tendencies found here can be reproduced when using parcel models. Although these models are limited to distinct updraft trajectories by design, they enable the use of extremely detailed microphysical schemes which is particularly gainful for the representation of aerosol processing (section 2.3.6). Since in-situ characterizations of strong convection may be hardly feasible, the use of models with a maximum detail of process representation may be a way to validate less-detailed model simulations based on a process analysis. Such comparisons may be particularly critical to enhance our understanding of the mechanisms involved in aerosol perturbations – CCN or IN – whose primary effect is to modify the cloud particle size distributions not only during initiation of the smallest cloud constituents, but also during the depletion of the largest drops by freezing (Khain, 2009). Still, three-dimensional setups will be indispensable particularly for precipitation, since – from a cloud-integrated point of view – surface precipitation is the small difference between two large values aloft, that is, growth of condensate and loss by evaporation and sublimation (Khain, 2009).

**Mineral dust as dominant IN species?**

In our simulations with mineral dust-dependent immersion freezing of rain drops, we find that large numbers of rain-sized drops survive the immersion freezing regime and finally freeze homogeneously. This seems reasonable when rain drops are more numerous than a limited concentration of dust particles. With the small efficiency of drop depletion, we speculate whether in strong convection it may be common to find large drops at temperatures below $-30\,^{\circ}\mathrm{C}$, or whether we miss important mechanisms in the model, such as additional types of IN (Knopf et al., 2014). If we consider large drops in such regimes rather unlikely, we may conclude that mineral dust cannot be the dominant particle species for immersion freezing in the coldest portion of the mixed-phase regime – assuming that the microphysical interactions other than freezing are represented appropriately in the model.

The number of rain-sized drops which are able to reach the homogeneous freezing regime also depends on factors other than IN concentrations: The efficiency of rain drop formation is determined by the initial cloud droplet size distribution and therefore CCN concentrations, and the time to reach the colder levels results from both cloud-base temperature and convective strength. Although the time for rain drop formation is longer in weaker updrafts, the chance for drop depletion by riming increases, thus promoting the glaciation of the mixed-phase regime. The clouds simulated in this work range from strong single cells to very strong supercell convection with relatively warm cloud bases. Thus, the microphysical behavior of weaker convective clouds should be the subject of future efforts in order to enable a validation of modeled upper-level liquid water content with available measurements, which may help to constrain the role of upper-level immersion freezing of mineral dust and other aerosol particles.

Rosenfeld and Woodley (2000) observed high liquid water contents in deep convective clouds down to $-37.5\,^{\circ}\mathrm{C}$, although the majority of droplets was smaller than $20\,\mu\mathrm{m}$ in diameter. This situation was reproduced successfully in the model simulations of Khain et al. (2001), suggesting three conditions to find high amounts of supercooled liquid water: High concentrations of CCN yield numerous but small cloud droplets, making the conversion to rain inefficient, and the efficiencies of droplet freezing small. Furthermore, the formation of relatively small graupel resulted in inefficient riming, promoting a dominant homogeneous droplet freezing in upper levels. In contrast, a more efficient glaciation was found with maritime CCN concentrations, yielding rain-sized drops by collision-coalescence, higher freezing probabilities, and larger graupel particles supported the faster glaciation by riming. Furthermore, Khain et al. (2001) note that the consideration of turbulence may influence the simulated riming rates significantly. They conclude that often models are unable to reproduce the persistence of highly supercooled liquid because of overestimated rates of rain drop formation and associated high freezing probabilities of large drops. In our implementation, whether or not the formation of rain-sized drops is overestimated may be of secondary importance in terms of freezing efficiency: Although freezing still depends on the autoconversion efficiency and drop sizes (e.g., as shown in the comparison of continental and maritime regimes in section 6.2.7), the main factor to determine the freezing probability is given by the fraction of mineral dust particles compared to the CCN at cloud base (section 2.3.2).

The lack of in-situ measurements to prove the existence of large drops at cold temperatures may arise from the difficult or even dangerous conditions for aircrafts to take measurements in strong convection, owing to both turbulence and icing. Furthermore, the characterization of maritime environments may not be representative for continental deep convection (Khain et al., 2001).

Based on our comparison of dust-dependent freezing and the more efficient ice formation according to Bigg (1953), it is also unclear whether the widely-used standard approach for droplet freezing in models tends to overestimate cloud glaciation considerably under average atmospheric conditions. Here we suggest that a) the freezing rates of rain drops should not be completely independent of the drop effective cooling rate, otherwise even continuously-warming drops are allowed to freeze (section 2.3.1), and b) the representativeness of the rain water collected by Barklie and Gokhale (1959) – yielding the parameters for the Bigg-based formulation – should be confirmed by future field studies. This may lead to enhanced skills of models without explicit consideration of aerosol properties to predict the properties of mixed-phase clouds.

## 7.3. Outlook

### Coupling of microphysics and dynamics in deep convection

While for the Arctic stratocumulus cloud type a well-defined effect of the cloud-dynamical contribution to the overall sensitivity is illustrated in chapter 3, similar analyses remain to be done for the case of deep convection: Figure 7.1 gives an impression of the perturbed vertical velocities, resulting from an ensemble of 18 IN-perturbed simulations, generated by varying fluctuations in the initial fields of temperature and vertical velocity (section 2.5.4).

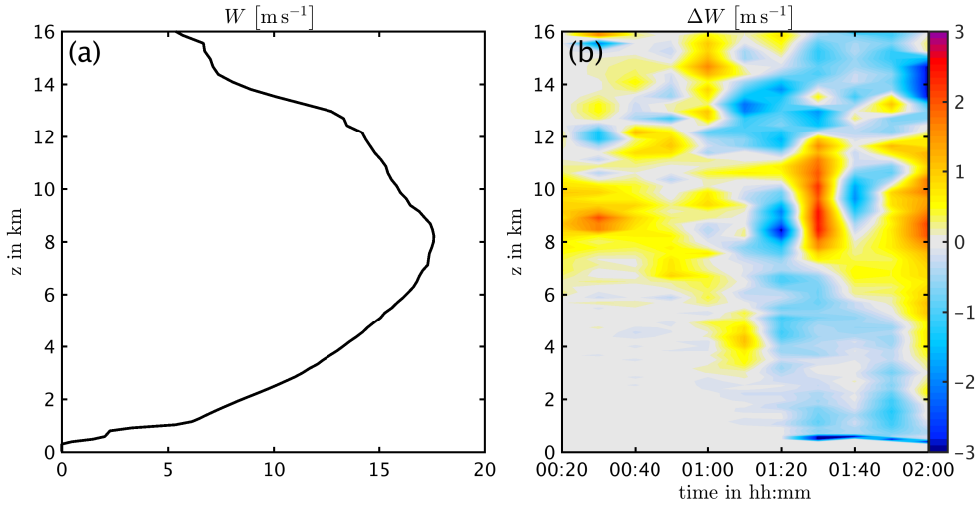


Fig. 7.1.: Ensemble mean vertical velocities, shown as profiles of the base state (a), and the time-resolved velocity perturbation as a result of increased immersion freezing efficiency (b, $N_{dust,0} \pm 90\%$). The scenario involves a base concentration of $10^7\,\mathrm{m}^{-3}$ mineral dust particles which is in a range of the highest sensitivities (chapter 6). Averaging is performed over the regimes of updrafts stronger than $5\,\mathrm{m\,s}^{-1}$, and from 00:20h to 02:00 hours in time in panel (a).

Panel (a) shows the base state mean vertical velocity which is maximum around the homogeneous freezing regime. In panel (b), the time-resolved vertical profiles of vertical velocity perturbations illustrate an ambiguous behavior. Although there is a tendency of increased buoyancy around the homogeneous freezing levels (z≈9 km), the primary expectation of stronger updrafts with more IN present is not confirmed in all regions of the cloud and at all times. At this point, we can speculate about the origin

of the weakened convective strength, such as increased condensate mass which would tend to decrease updraft velocities, or the effects of entrainment. In addition to the vertical dynamics as such, also the modulation of precipitation and radiation should be continued to be quantified. To date, preliminary analyses indicate a tendency of enhanced precipitation sensitivities by cloud-dynamical feedbacks, but further ensemble simulations will be beneficial.

#### Microphysical buffering in cloud systems

In the course of this project, mesoscale simulations over Germany were carried by Paul Platzer (Platzer, 2015). The "perturbed microphysics" approach was used to show the applicability in real-case mesoscale simulations, and to quantify the effects of ice nuclei perturbations in a frontal system (Barthlott and Hoose, 2015). Fig. 7.2 illustrates the changes of the vertically integrated cloud water content as a result of IN perturbations, where we see distinct patterns of both positive and negative deviations from the microphysical base state. For precipitation, we can speculate about antagonistic effects similar to section 6.1: The rain which is created within the melting regime may be dominated by either of the three precipitating ice types – snow, graupel, hail – and depending on the dominating type of rain formation and microphysical regime, is increased or decreased in a perturbed-IN scenario. The spatial organization in Fig. 7.2 may indicate the existence of distinct microphysical regimes.

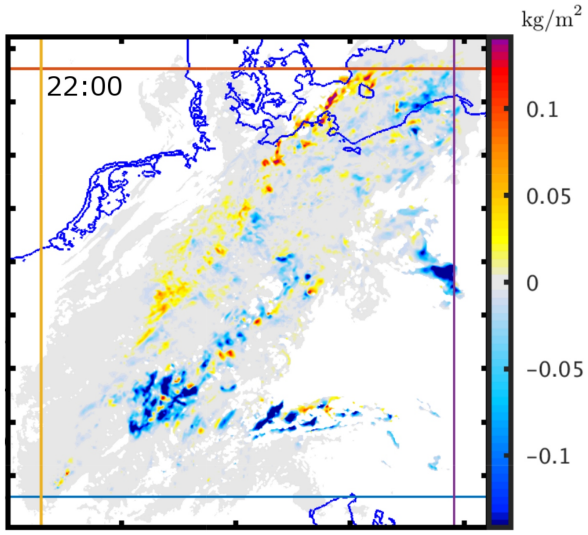


Fig. 7.2.: Liquid water path perturbations ($\Delta_{PM}LWP$) in a frontal cloud system over Germany on April 26 2013, resulting from increased ice nucleation activity of mineral dust. Courtesy of Paul Platzer.

Such behavior is consistent with the results of Seifert et al. (2012) who find that on a spatial and temporal average, aerosol perturbations have minor effects on the surface precipitation, concluding that the interaction of microphysics with cloud-dynamics is necessary for the interpretation of cloud fields as a buffered system. Here we have presented an appropriate tool to investigate aerosol perturbations on larger scales while explicitly suppressing the feedback on dynamics. This may be an interesting opportunity to see whether the behavior of surface precipitation can be explained by the sole effect of "microphysical buffering", or whether the buffering which involves the atmospheric circulation is necessary to make surface precipitation relatively insensitive to aerosol perturbations on the scale of cloud systems.

# A. List of symbols

## A.1. Averaging

Tab. A.1.: Averaging methods used in this work. $Q_c$ and $Q_i$ are the cloud droplet and cloud ice mass densities. $v_{qx}$ is the sedimentation velocity of the first moment of particle class x (positive downward), and w is the grid-scale vertical velocity.

| symbol | description |
|---|---|
| $<$ cld $>$ | "cloudy" regions, where $(Q_c + Q_i) > 10^{-7}\,\mathrm{kg\,m^{-3}}$ |
| $<$ w$_5$ $>$ | convective regions with updrafts stronger than $5\,\mathrm{m\,s^{-1}}$ |
| $<$ x $\uparrow>$ | regions in which the mass of hydrometeor class x is effectively lifted ("lifting regime of x"), i.e., where $v_{qx} < w$ |
| $<$ x $\downarrow>$ | regions in which the mass of hydrometeor class x is effectively sediments ("sedimentation regime of x"), i.e., where $v_{qx} > w$ |
| $<$ cld$_{\|\|}$ $>$ | columwise averaging over cloud-containing areas, where $(Q_c + Q_i) > 10^{-7}\,\mathrm{kg\,m^{-3}}$ in at least one level of the column |
| $<^*>$ | domain-wide mean value, including zeros |
| $<$ ...$_\#$ $>$ | averaging perpendicular to the paper plane, yielding two-dimensional spatial distributions |
| $<$ ... $>$ | regions which do not fulfill the conditions within brackets do not contribute to horizontal mean values, e.g., $<$ cld $>$ is representative for in-cloud conditions |
| $<$ ...$^*$ $>$ | regions which do not fulfill the conditions within brackets contribute with zeros to horizontal mean values, i.e., the values are not representative for the cloud regions, but may yield a better comparison depending on the subject of interest (e.g., comparison of domain-wide sedimentation fluxes or particle formation rates) |

## A.2. Acronyms

| Acronym | Description |
|---|---|
| AMPC | Arctic mixed-phase clouds |
| B53 | Bigg (1953) |
| c, r, i, s, g, h | hydrometeor classes: cloud droplets, rain drops, cloud ice, snow, graupel, hail |
| CCN | cloud condensation nuclei |
| COSMO | Consortium for Small-scale Modeling |
| DM | "driving microphysics" |
| IN | ice nuclei |
| ISDAC | Indirect and Semi-Direct Aerosol Campaign |
| KHL | Kärcher et al. (2006) |
| MCS | mesoscale convective system |
| N12 | Niemand et al. (2012) |
| PM | "perturbed microphysics" |
| PM1 | perturbed microphysical state with reduced IN content relative to $N_{dust,0}$ |
| PM2 | perturbed microphysical state with increased IN content relative to $N_{dust,0}$ |
| PSD | particle size distribution |
| SB06 | Seifert and Beheng (2006) |
| SK06 | Segal and Khain (2006) |
| WBF | Wegener-Bergeron-Findeisen |
| WK82 | Weisman and Klemp (1982) |

## A.3. Letters

| Symbol | Unit | Description |
|---|---|---|
| $a$ | different | parameterization constants |
| $a_{N12}$ | $\mathrm{K}^{-1}$ | parameter according to Niemand et al. (2012) |
| $A$ | $\mathrm{kg}^{-(\nu+1)}\mathrm{m}^{-3}$ | coefficient of the generalized Gamma-distribution |
| $b$ | different | parameterization constants |
| $b_{N12}$ | 1 | parameter according to Niemand et al. (2012) |
| $B$ | $\mathrm{kg}^{-\mu}$ | exponent of the generalized Gamma-distribution |
| $c$ | K | parameterization constant |
| $c_{u/v}$ | $\mathrm{s}^{-1}$ | nudging coefficient for horizontal wind components |
| $d$ | $\mathrm{K}^{-1}$ | parameterization constant |
| $D$ | m | diameter of aerosol particles and hydrometeor species |
| $D_{coll,r}$ | m | diameter corresponding to the mean mass of rain-collected droplets |
| $e$ | different | parameterization constant; cloud-dynamical "enhancement" factor |
| $f(x)$ | $\mathrm{m}^{-3}\,\mathrm{kg}^{-1}$ | number density function with respect to particle mass |
| $f_{dust,cb}$ | 1 | cloud-base fraction of mineral dust relative to total CCN |
| $f_{dust,loc}$ | 1 | local fraction of mineral dust relative to total CCN |
| $FSW$ | $\mathrm{W\,m}^{-2}$ | net shortwave radiative flux (positive downward) |
| $FLW$ | $\mathrm{W\,m}^{-2}$ | net longwave radiative flux (positive downward) |
| $G_{\downarrow}$ | $\mathrm{kg\,m}^{-2}\,\mathrm{s}^{-1}$ | downward effective mass flux of graupel, corrected for vertical advection |
| $H_{\downarrow}$ | $\mathrm{kg\,m}^{-2}\,\mathrm{s}^{-1}$ | downward effective mass flux of hail, corrected for vertical advection |
| $n_s(T)$ | $\mathrm{m}^{-2}$ | ice nucleation active surface site density |
| $LWP$ | $\mathrm{kg\,m}^{-2}$ | liquid water path |
| $n_{dust}(D)$ | $\mathrm{m}^{-4}$ | number density function of dust particles (Paukert and Hoose, 2014a) |
| $n_{dust,r}(D)$ | $\mathrm{m}^{-4}$ | lognormal size distribution of dust particles immersed in rain drops |
| $n_r$ | $\mathrm{m}^{-3}$ | number density of rain drops in a finite interval of $f(x)$ |
| $N_{act}$ | $\mathrm{m}^{-3}$ | number density of activated CCN |
| $N_{CCN}$ | $\mathrm{m}^{-3}$ | number density of CCN |
| $N_{coll,c/r}$ | $\mathrm{m}^{-3}$ | number density of collected CCN by cloud droplets/ rain drops |
| $N_{crit}$ | $\mathrm{m}^{-3}$ | number density of mineral dust IN associated with similar freezing contributions of immersion freezing and homogeneous freezing |
| $N_{dust(,c/r)}$ | $\mathrm{m}^{-3}$ | number density of mineral dust particles available as IN (immersed in cloud droplets/ rain drops) |
| $N_{dust,0}$ | $\mathrm{m}^{-3}$ | base concentration in "perturbed microphysics" simulations |
| $N_{ice,r}$ | $\mathrm{m}^{-3}$ | number density of ice particles (i/g/h) formed by freezing rain |
| $N_{IN,r}$ | $\mathrm{m}^{-3}$ | number density of activated ice nuclei in the bulk mass of rain |
| $N_x$ | $\mathrm{m}^{-3}$ | number density of particle class $x \in \{c,r,i,s,g,h\}$ |
| $P(X)$ | 1 | probability mass function of a discrete random variable $X$ |
| $q_r$ | $\mathrm{kg\,m}^{-3}$ | mass density of rain drops in a finite interval of $f(x)$ |
| $Q_x$ | $\mathrm{kg\,m}^{-3}$ | mass density of particle class $x \in \{c,r,i,s,g,h\}$ |
| $Q_{PM1/2}$ | different | quantity in the perturbed microphysical state ($N_{dust,0} \pm x\%$) |
| $r_{CCN}$ | $\mathrm{kg}^{-1}$ | CCN number concentration per droplet liquid mass |
| $R_{eff,i}$ | m | cloud ice effective radius according to Fu (1996) |
| $R_{\downarrow}$ | $\mathrm{kg\,m}^{-2}\,\mathrm{s}^{-1}$ | downward effective mass flux of rain, corrected for vertical advection |

| Symbol | Unit | Description |
|---|---|---|
| $RH_i$ | % | relative humidity with respect to ice |
| $RH_w$ | % | relative humidity with respect to liquid water |
| $s_i$ | 1 | saturation ratio with respect to ice ($\frac{RH_i}{100\%} - 1$) |
| $S$ | different | sensitivity (change of a quantity in a perturbed state) |
| $S_{dust,r}$ | $\mathrm{m^2\,m^{-3}}$ | total surface area of rain-immersed dust particles per volume of air |
| $\overline{S}_{dust,r}$ | $\mathrm{m^2\,m^{-3}}$ | mean surface area of rain-immersed dust particles per volume of air |
| $t$ | s | time |
| $T$ | K | temperature |
| $T_c$ | °C | temperature |
| $v_{qx}$ | $\mathrm{m\,s^{-1}}$ | sedimentation velocity of the first moment of particle class x (positive downward) |
| $v_{sed}$ | $\mathrm{m\,s^{-1}}$ | single particle sedimentation velocity (positive downwards) |
| $w$ | $\mathrm{m\,s^{-1}}$ | vertical velocity |
| $W$ | 1 | weight |
| $x$ | kg | cloud particle mass |
| $x_{coll,r}$ | kg | mean drop mass ($= Q_r/N_{coll,r}$) |
| $x_{liq,dust}$ | kg | mean drop mass ($= Q_r/N_{dust,r}$) |
| $x_{ubd}$ | kg | upper boundary of mass x for integration over $f(x)$ |
| $z$ | m | vertical coordinate |
| $z_0$ | m | altitude below which the mineral dust concentration is constant |
| $z_e$ | m | exponential decay scale height |

## A.4. Greek letters

| Symbol | Unit | Description |
|---|---|---|
| $\alpha_{TOA}$ | 1 | shortwave atmospheric albedo as seen from the top of the atmosphere |
| $\Delta_{PM}Q$ | different | difference of a quantity $Q$ between perturbed microphysical states |
| $\Delta^{rel}_{PM}Q$ | 1 | relative difference of a quantity $Q$ between perturbed microphysical states |
| $\gamma$ | 1 | lower incomplete gamma function |
| $\Gamma$ | 1 | complete gamma function |
| $\lambda_c$ | 1 | mean collected CCN per cloud droplet |
| $\lambda_r$ | 1 | mean collected CCN per rain drop |
| $\lambda_{IN}$ | 1 | mean activated IN per rain drop |
| $\mu_0$ | 1 | cosine of the sun zenith angle |
| $\mu$ | 1 | exponent of the generalized Gamma-distribution |
| $\nu$ | 1 | exponent of the generalized Gamma-distribution |
| $\rho_w$ | $\mathrm{kg\,m^{-3}}$ | density of liquid water |

# B. Appendix - uncertainty considerations

In spite of the relations found in our simulations, a range of uncertainties must be considered. First, we return to graupel and hail properties as a result of conversion assumptions (section B.1). Furthermore, the influence of CCN activation scheme on upper-level cloud droplet and anvil ice properties is illustrated in section B.2.

## B.1. Particle conversion

In section 6.1.7 it was shown that the assumptions of particle interactions can shift the relative contribution of graupel and hail fluxes considerably (Fig. 6.17). These differences deserve some more attention, and are analyzed in the following.

We begin with a comparison of the vertical profiles of horizontally and temporally averaged downward fluxes of rain, graupel and hail, as well as their changes in the presence of more ice nuclei (Fig. B.1). Full lines correspond to type-3 simulations[1], dashed lines are the same type-2 fluxes as shown in Fig. 6.20. Each color corresponds to a specific mineral dust background concentration $N_{dust,0}$. Absolute surface rain fluxes (a.1) and the variance with different IN backgrounds are similar with both specifications of ice_typ (dashed vs. full lines). However, with type 3 there are larger fluxes at top of the melting region which originate from the larger hail amounts (c.1). The faster vertical decay of rain – i.e., evaporation – is also the result of the hail properties. Although its fluxes are roughly twice as large with type 3, the hail particles melt faster, and only a minor fraction reaches the ground levels, therefore the melting contribution to rain formation is missing in the lower levels. Another effect may be the smaller rain drop sizes as a result of smaller hail particles. Overall, the hail properties become more similar to graupel, with more but smaller particles, more total mass and larger fluxes (see below). Graupel has smaller fluxes in type-3 simulations. This shifts the relative importances of graupel and hail, resulting in the positive signs of surface rain changes with $N_{dust,0} = 10^6\,\mathrm{m}^{-3}$ and $10^7\,\mathrm{m}^{-3}$ (a.2; yellow/red). In these cases, $\Delta_{PM}$ of the graupel flux is largest in terms of absolute as well as relative changes with more IN (panels b.2/3), while the relative changes of hail fluxes are quite similar between type-2 and -3 results (c.3).

In summary, it is positive that the sign of all graupel and hail flux changes with varying ice nuclei is robust in all simulations and with both assumptions for graupel and hail formation during riming. However, since the two particle classes influence the liquid rain in opposite ways, the relative importance of graupel and hail flux changes is crucial to the resulting rain. Particularly in type-3 simulations the relative graupel contribution is fostered in a certain range of mineral dust background ($10^6\,\mathrm{m}^{-3}$ / $10^7\,\mathrm{m}^{-3}$),

[1] In the COSMO model, two modes are available when both graupel and hail are present. By choosing between "ice_typ=2" or "ice_typ=3", it is distinguished how rimed masses are distributed among graupel and hail. All above simulations were based on number 2, where riming of i/s/g may cause accumulation of graupel mass, but does not affect hail formation or growth. Hail is only affected with "ice_typ=3" – in this case, graupel mass and number may also be depleted due to conversion to hail (i.e., $g + r \rightarrow h$).

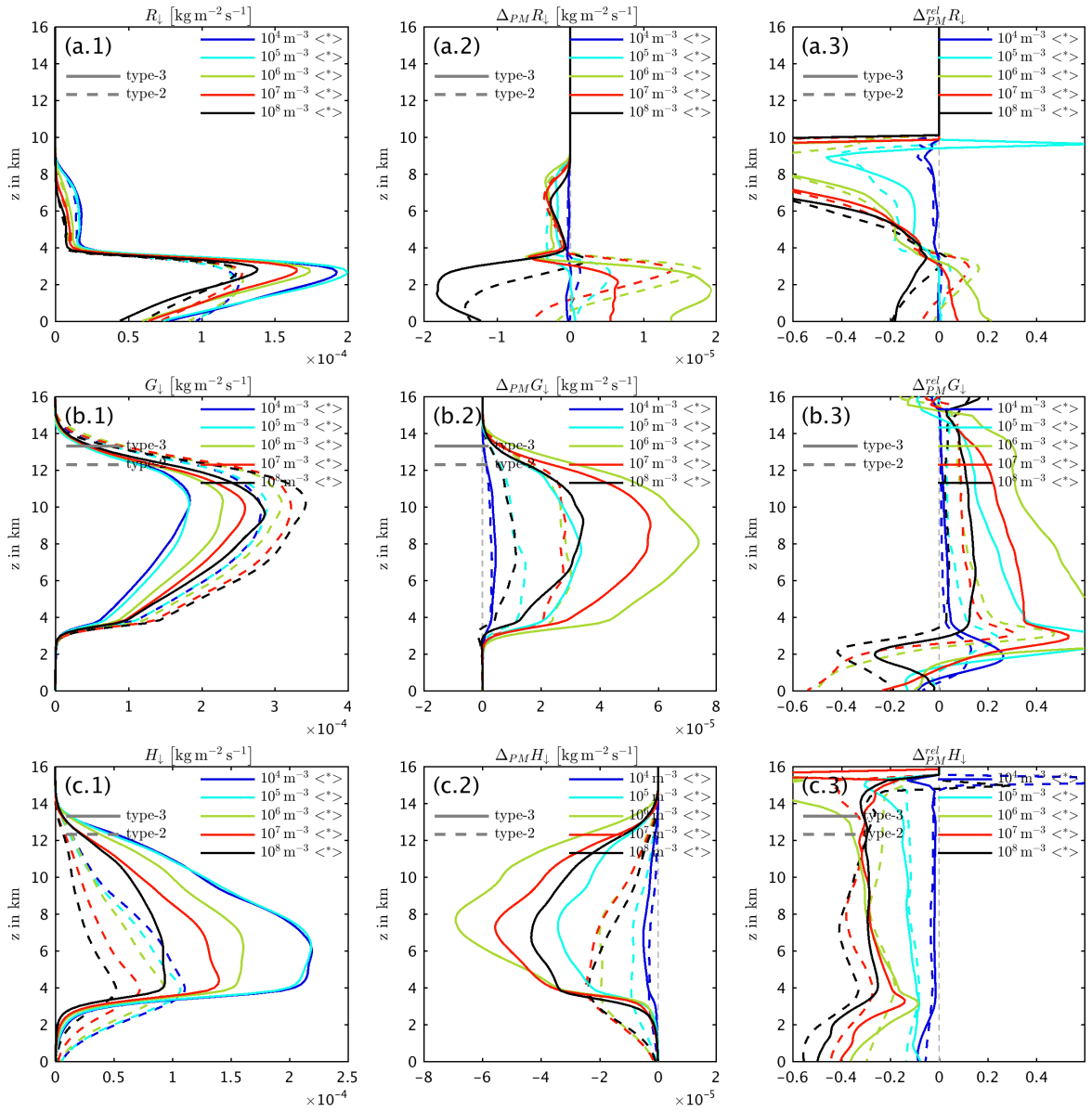


Fig. B.1.: Sedimentation fluxes of rain (a), graupel (b) and hail (c), as a comparison of type-2 simulations (dashed lines) and type-3 simulations (full lines). The vertical profiles show the base states (*.1), absolute changes (*.2) and relative changes (*.3) resulting from ice nuclei perturbations. Each color corresponds to mineral dust background concentrations ranging from $10^4\,\mathrm{m}^{-3}$ to $10^8\,\mathrm{m}^{-3}$.

which originates from a maximum in the positive $\Delta_{PM}Q_g$ and a minimum in the negative $\Delta_{PM}N_g$, with the same underlying mechanisms as presented for type-2 simulations (section 6.1.2).

A short description of graupel and hail properties in type-3 simulations is provided in the following. As indicated above, the vertical profiles of of $\Delta_{PM}Q_g$, $\Delta_{PM}N_g$ and the dependencies on $N_{dust,0}$ are very similar between type-2 and type-3 simulations. Without a detailed discussion, the only noteworthy detail in Fig. B.2 seems to be that the upper-level $\Delta_{PM}N_g$ becomes positive with $N_{dust,0} = 10^7\,\mathrm{m}^{-3}$ (red),

which happened only at $10^8\,\mathrm{m}^{-3}$ in the type-2 results. This makes the flux enhancement of the $10^6\,\mathrm{m}^{-3}$ simulation (yellow) more outstanding in contrast to type-2.

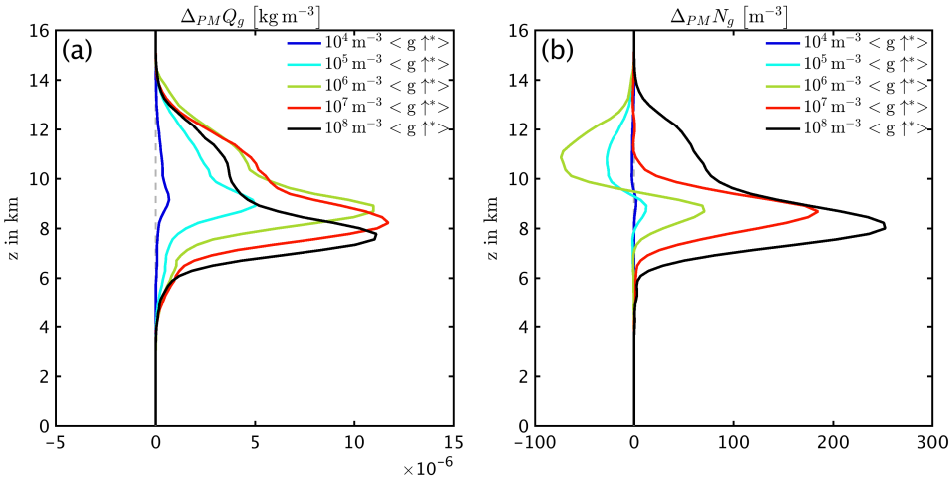


Fig. B.2.: Absolute changes of (a) mass concentrations and (b) number concentrations of graupel in type-3 simulations, resulting from ice nuclei perturbations. Each color corresponds to mineral dust background concentrations ranging from $10^4\,\mathrm{m}^{-3}$ to $10^8\,\mathrm{m}^{-3}$.

The same is shown for hail mass and number densities in the five $N_{dust,0}$ simulations with type-3 riming, averaged over hail lifting regimes. Since the hail properties are different to type-2 results in a more fundamental way, also the base states of $Q_h$ and $N_h$ will be shown in addition to their changes in perturbed microphysical states (Fig. B.3).

Compared to type-2, we see an increase of the base state hail mass by a factor of five. The generally decreasing mass with more $N_{dust,0}$ (a.1) is consistent with previous results, although the dependence of $\Delta_{PM}Q_h$ on $N_{dust,0}$ is different (a.2). Instead of a continuously larger reduction, we find a turning point in simulation of $10^6\,\mathrm{m}^{-3}$ (yellow), and a slightly decreased magnitude of $\Delta_{PM}Q_h$ with larger $N_{dust,0}$. Type-3 number densities are increased by a factor of 10 to 100, compared to type-2 (b.1). A clear separation is found between the base states of $N_{dust,0}$ from $10^4\,\mathrm{m}^{-3}$ to $10^6\,\mathrm{m}^{-3}$, and $10^7\,\mathrm{m}^{-3}$ to $10^8\,\mathrm{m}^{-3}$. In the cases of low immersion freezing activity, there is a mechanism that initiates large amounts of new hail particles above 8 km. This mechanism is absent with $N_{dust,0} = 10^7\,\mathrm{m}^{-3}$ and $10^8\,\mathrm{m}^{-3}$, i.e., the depletion of rain plays a crucial role for the separation of these distinct aerosol regimes. This grouping of high and low dust background simulations is not found in the perturbed microphysical states of $N_h$. In contrast to type-2 $\Delta_{PM}N_h$, there is a medium-$N_{dust,0}$ simulation with a maximum sensitivity ($10^6\,\mathrm{m}^{-3}$, yellow). Another basic difference is the negative sign in all levels and all simulations which tends to increase the mean hail mass with more ice nuclei, therefore counteracting the hail flux reduction arising from the negative $\Delta_{PM}Q_h$.

Here we showed the potential sensitivity of simulated precipitation to the assumptions of hail formation during riming processes. Further modifiers of simulated supercell precipitation were documented by, e.g., Gilmore et al. (2004), who find a difference up to a factor of 4 in the accumulated surface precipitation, resulting from the choice of particle-specific properties such as graupel size distribution parameters and bulk densities. This illustrates the particular limitations of bulk microphysical schemes, owing to

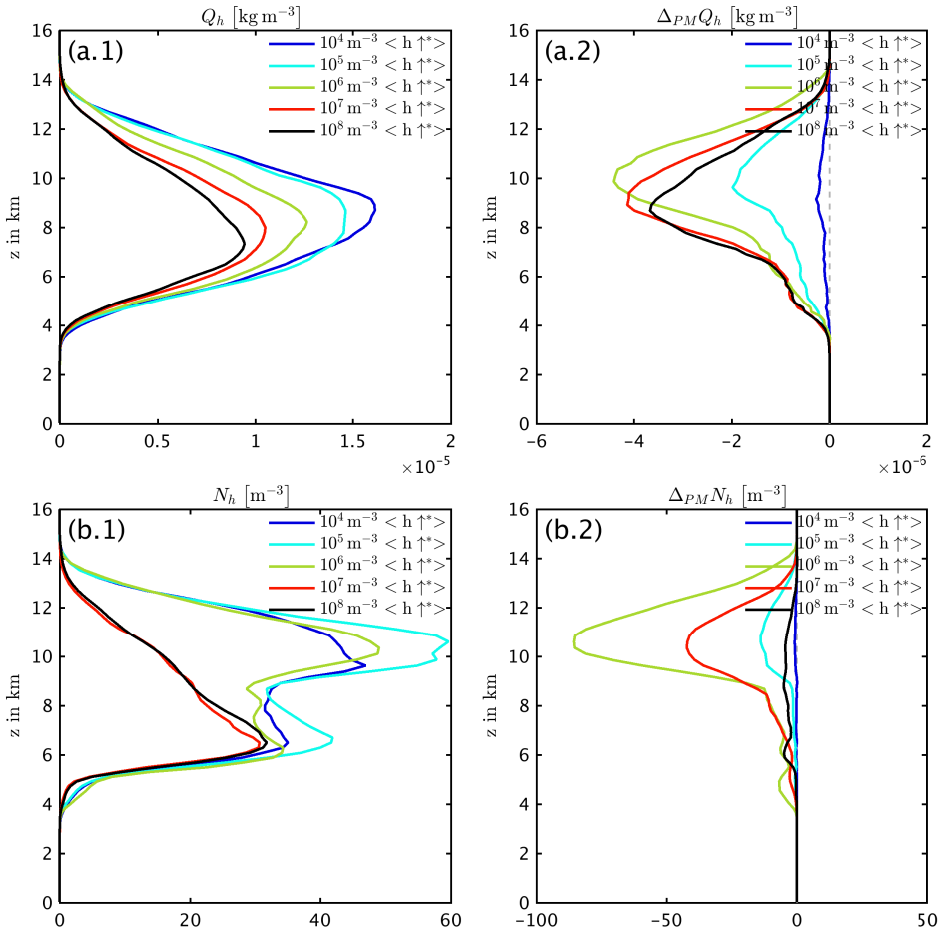


Fig. B.3.: Mass (a) and number (b) concentrations of hail in type-3 simulations, shown as vertical profiles of base states (*.1) and absolute changes (*.2) resulting from ice nuclei perturbations. Each color corresponds to mineral dust background concentrations ranging from $10^4\,\mathrm{m}^{-3}$ to $10^8\,\mathrm{m}^{-3}$.

the necessity of a-priori assumptions of particle size distributions and other parameters. Recent developments with consideration of the particle microphysical histories may reduce some ambiguities, e.g., by tracking the histories of riming which yield estimates of case-specific particle properties (Morrison and Milbrandt, 2015).

Only recently, the parameterizations for the fall velocities of non-spherical particles were revised for the scheme used here (Seifert et al., 2014). In our case, this may be particularly relevant for the simulated collisional growth of graupel and hail, and the resulting precipitation formation. Furthermore, when considering the precipitation at ground levels, it can be beneficial to account for the liquid mass fractions of melting snow, graupel and hail particles (e.g., Frick et al., 2013). Related to liquid fractions, further improvements may also be the explicit representation of wet growth of large hydrometeors (Phillips et al., 2014).

## B.2. Droplet activation

This section documents the model behavior when applying different approaches for cloud droplet activation. Although this is not the focus of this study, it is important to understand the underlying mechanisms in the model, and may be important for the reproduction of any results. In particular, the ice number concentrations in the convective outflow (section 6.2.2) are highly influenced by the different approaches as a result of cloud droplet homogeneous freezing. The resulting concentrations of cloud droplets and cloud ice are summarized in Fig. B.4. In the COSMO model, we can choose between the Twomey approach as presented by SB06, and the lookup tables according to (Segal and Khain, 2006, SK06 hereafter). The Twomey approach calculates the number of activated CCN as a function of grid-scale supersaturation, while the SK06 method accounts for the grid-scale vertical velocity and aerosol properties. A basic difference between the two schemes is the vertical distribution of aerosol concentrations, which by default is uniform for Twomey-based activation, and has an exponential decay rate on the scale of 2000 m for SK06-based activation.

A further choice concerns in-cloud droplet activation. For a parcel of air that becomes supersaturated with respect to water during ascent, the activation of aerosols as CCN occurs in a relatively narrow range within tens of meters at cloud base (e.g., Khain et al., 2000), followed by a rapid depletion of excess water vapor by condensational droplet growth. Therefore the supersaturation to enable further activation of the remaining interstitial aerosol is usually low above the cloud base. Although it is argued that upon reduction of cloud droplet numbers by collision-coalescence and riming the supersaturation may increase high enough to enable in-cloud activation (Pinsky and Khain, 2002), this feature is hard to resolve in a conventional bulk microphysical scheme as used here. Instead of explicit prediction of the supersaturation depending on the condensational growth of droplets, the common approach is to rely on saturation adjustment in the presence of cloud droplets. In the implementation used here, at the end of each model time step the supersaturation is forced to be zero, with excess water vapor being converted to cloud water. For this reason, in our model setup we assume that any simulated in-cloud activation is an artifact rather than physically-based. It is suppressed by choosing a model option which requires a sub-saturated level below the level in which activation may occur.

Another potential issue of cloud droplet activation results from the budgeting of aerosol concentrations: Consideration of previously activated aerosol particles is particularly important in case that in-cloud droplet formation is allowed. The standard model approach is to parameterize the number of activated CCN, and to add the difference between parameterized and existing droplet number to the model grid box, implying that all existing cloud droplets are representative for the number of previously activated aerosol. This tends to overestimate the activation rates. In this case of deep convection, the cloud droplet number concentration is reduced by up to two orders of magnitude within the updraft due to the collection by rain drops and ice particles. In this work, the sum of $N_{coll,c}$ and $N_{coll,r}$ – intended to represent all CCN incorporated in cloud and rain drops (section 2.3.3) – is used to represent activated CCN. As this is available as a by-product of the extended treatment of rain freezing, we do not need an additional tracer.

Figure B.4 illustrates the cloud droplet and ice number concentrations as simulated by three different model setups. The profiles are representative for the updraft regions with vertical velocities larger than $5\,\mathrm{m\,s^{-1}}$.

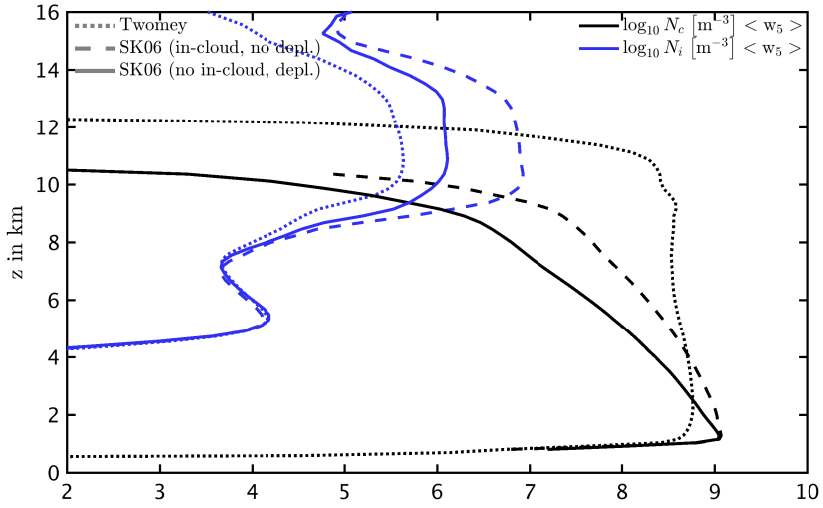


Fig. B.4.: Number concentrations of cloud droplets (black) and cloud ice (blue), as simulated by three model setups: Twomey (dashed lines), SK06 with in-cloud activation (thin full lines) and without in-cloud activation including CCN depletion (thick full lines). Note that the droplets extending to higher than 11 km in the Twomey-based simulation originate from a defective parameterization of homogeneous freezing in earlier model versions.

The black dashed line shows the Twomey approach including in-cloud activation. It appears that $N_c$ is hardly reduced within the updraft, with more than $10^8\,\mathrm{m}^{-3}$ droplets reaching the homogeneous freezing level. Since all the droplets freeze upon further lifting, a default approach is to hard-limit the ice number to a reasonable maximum of $5 \times 10^5\,\mathrm{m}^{-3}$. In general, such a limit may be a reasonable limit to avoid excessive and ice production, but tends to suppress the sensitivities in this study. Therefore the hard-limit was deactivated, and alternative activation schemes were tested. The full lines represent the number concentrations resulting from the SK06 method with and without in-cloud activation. In the latter case, the mean value of $N_i$ ($< \mathrm{w}_5 >$) regions results in $10^6\,\mathrm{m}^{-3}$ (dark blue, thick line). Note that the cloud ice number in the convective outflow is further diluted, and fits well the original hard limit (section 6.2.2), while being physically based and not suppressing sensitivities to aerosols artificially. The resulting anvil ice numbers fit reasonably to recently published data of in-situ measurements of convective outflows (Luebke et al., 2016).

# C. Bibliography


Altaratz, O., I. Koren, L. Remer and E. Hirsch (2014). Review: Cloud invigoration by aerosols – coupling between microphysics and dynamics. *Atmos. Res. 140-141*, 38–60.

Baldauf, M., A. Seifert, J. Förstner, D. Majewski, M. Raschendorfer and T. Reinhardt (2011). Operational convective-scale numerical weather prediction with the COSMO model: Description and sensitivities. *Mon. Weather Rev. 139*, 3887–3905.

Barahona, D. and A. Nenes (2011). Dynamical states of low temperature cirrus. *Atmos. Chem. Phys. 11*, 3757–3771.

Barklie, R. H. D. and N. R. Gokhale (1959). The freezing of supercooled water drops. *Scientific Report, Stormy Weather Group, McGill University, Montreal* , MW–30, 43–64.

Barthlott, C. and C. Hoose (2015). Spatial and temporal variability of clouds and precipitation over Germany: multiscale simulations across the "gray zone". *Atmos. Chem. Phys. 15*, 12361–12384.

Bauer, P., A. Thorpe and G. Brunet (2015). The quiet revolution of numerical weather prediction. *Nature 525*, 47–55.

Beard, K. V. and H. T. Ochs (1995). Collisions between small precipitation drops. Part II: Formulas for coalescence, temporary coalescence, and satellites. *J. Atmos. Sci. 52*, 3977–3996.

Beheng, K. D. (1981). Stochastic riming of plate-like and columnar ice crystals. *Pure Appl. Geophys. 119*, 820–830.

Beheng, K. D. and F. Herbert (1986). Mathematical studies on the aerosol concentration in drops changing due to particle scavenging and redistribution by coagulation. *Meteorol. Atmos. Phys. 35*, 212–219.

Bigg, E. K. (1953). The formation of atmospheric ice crystals by the freezing of droplets. *Q. J. Roy. Meteor. Soc. 79*, 510–519.

Blahak, U. (2008). Towards a better representation of high density ice particles in a state-of-the-art two-moment bulk microphysical scheme. 15th International Conf. on Clouds and Precipitation, July 7-11, 2008, Cancun, Mexico.

Boose, Y., Z. A. Kanji, M. Kohn, B. Sierau, A. Zipori, I. Crawford, G. Lloyd, N. Bukowiecki, E. Herrmann, P. Kupiszewski, M. Steinbacher and U. Lohmann (2016). Ice nucleating particle measurements at 241 K during winter months at 3580 m MSL in the Swiss Alps. *J. Atmos. Sci. 73*, 2203–2228.

Bott, A. (1989). A positive definite advection scheme obtained by nonlinear renormalization of the advective fluxes. *Mon. Weather Rev. 117*, 1006–1016.

Boucher, O., D. Randall, P. Artaxo, C. Bretherton, G. Feingold, P. Forster, V.-M. Kerminen, Y. Kondo, H. Liao, U. Lohmann, P. Rasch, S. Satheesh, S. Sherwood, B. Stevens and X. Zhang (2013). *Clouds and Aerosols. In: Climate Change 2013: The Physical Science Basis. Contribution of Working Group I to the Fifth Assessment Report of the Intergovernmental Panel on Climate Change [Stocker, T.F., D. Qin, G.-K. Plattner, M. Tignor, S.K. Allen, J. Boschung, A. Nauels, Y. Xia, V. Bex and P.M. Midgley (eds.)].* Cambridge University Press, Cambridge, United Kingdom and New York, NY, USA.

Braham, R. R. (1964). What is the role of ice in summer rain-showers? *J. Atmos. Sci. 21*, 640–645.

Chosson, F., P. A. Vaillancourt, J. A. Milbrandt, M. K. Yau and A. Zadra (2014). Adapting two-moment microphysics schemes across model resolutions: Subgrid cloud and precipitation fraction and microphysical sub-time step. *J. Atmos. Sci. 71*, 2635–2653.

Cohard, J.-M. and J.-P. Pinty (2000). A comprehensive two-moment warm microphysical bulk scheme. I: Description and tests *126*, 1815–1842.

Cotton, R. J. and P. R. Field (2002). Ice nucleation characteristics of an isolated wave cloud. *Q. J. Roy. Meteor. Soc. 128*, 2417–2437.

Cotton, W. R., G. J. Tripoli, R. M. Rauber and E. A. Mulvihill (1986). Numerical simulation of the effects of varying ice crystal nucleation rates and aggregation processes on orographic snowfall. *J. Clim. Appl. Meteorol. 25*, 1658–1680.

Curry, J. A., W. B. Rossow, D. Randall and J. L. Schramm (1996). Overview of Arctic cloud and radiation characteristics. *J. Clim. 9*, 1731–1764.

Cziczo, D. J., K. D. Froyd, C. Hoose, E. J. Jensen, M. Diao, M. A. Zondlo, J. B. Smith, C. H. Twohy and D. M. Murphy (2013). Clarifying the dominant sources and mechanisms of cirrus cloud formation. *Science 340*, 1320–1324.

Dagan, G., I. Koren and O. Altaratz (2015). Competition between core and periphery-based processes in warm convective clouds – from invigoration to suppression. *Atmos. Chem. Phys. 15*, 2749–2760.

de Boer, G., T. Hashino and G. J. Tripoli (2010). Ice nucleation through immersion freezing in mixed-phase stratiform clouds: Theory and numerical simulations. *Atmos. Res. 96*, 315–324.

Diehl, K. and S. K. Mitra (2015). New particle-dependent parameterizations of heterogeneous freezing processes: sensitivity studies of convective clouds with an air parcel model. *Atmos. Chem. Phys. 15*, 12741–12763.

Durant, A. J., R. A. Shaw, W. I. Rose, Y. Mi and G. G. J. Ernst (2008). Ice nucleation and overseeding of ice in volcanic clouds. *J. Geophys. Res. Atmos. 113*, D09206.

Fan, J., S. Ghan, M. Ovchinnikov, X. Liu, P. J. Rasch and A. Korolev (2011). Representation of Arctic mixed-phase clouds and the Wegener-Bergeron-Findeisen process in climate models: Perspectives from a cloud-resolving study. *J. Geophys. Res. 116*, D00T07.

Fan, J., T. Yuan, J. M. Comstock, S. Ghan, A. Khain, L. R. Leung, Z. Li, V. J. Martins and M. Ovchinnikov (2009). Dominant role by vertical wind shear in regulating aerosol effects on deep convective clouds. *J. Geophys. Res. Atmos. 114*, D22206.

Frick, C., A. Seifert and H. Wernli (2013). A bulk parametrization of melting snowflakes with explicit liquid water fraction for the COSMO model. *Geosci. Model Dev. 6*, 1925–1939.

Fu, Q. (1996). An accurate parameterization of the solar radiative properties of cirrus clouds for climate models. *J. Clim. 9*, 2058–2082.

Fu, Q., P. Yang and W. B. Sun (1998). An accurate parameterization of the infrared radiative properties of cirrus clouds for climate models. *J. Clim. 11*, 2223–2237.

Garrett, T. J., L. Avey, P. I. Palmer, A. Stohl, J. A. Neuman, C. A. Brock, T. B. Ryerson and J. S. Holloway (2006). Quantifying wet scavenging processes in aircraft observations of nitric acid and cloud condensation nuclei. *J. Geophys. Res. Atmos. 111*, D23S51.

Garrett, T. J. and C. Zhao (2006). Increased Arctic cloud longwave emissivity associated with pollution from mid-latitudes. *Nature 440*, 787–789.

Gilmore, M. S., J. M. Straka and E. N. Rasmussen (2004). Precipitation uncertainty due to variations in precipitation particle parameters within a simple microphysics scheme. *Mon. Weather Rev. 132*, 2610–2627.

Grabowski, W. W. (2014). Extracting microphysical impacts in large-eddy simulations of shallow convection. *J. Atmos. Sci. 71*, 4493–4499.

Grabowski, W. W. (2015). Untangling microphysical impacts on deep convection applying a novel modeling methodology. *J. Atmos. Sci. 72*, 2446–2464.

Grabowski, W. W. and D. Jarecka (2015). Modeling condensation in shallow nonprecipitating convection. *J. Atmos. Sci. 72*, 4661–4679.

Grabowski, W. W. and J. C. Petch (2009). Deep convective clouds. In: Heintzenberg, J. and R. J. Charlson (eds.), *Clouds in the Perturbed Climate System: Their Relationship to Energy Balance, Atmospheric Dynamics, and Precipitation.* Struengmann Forum Report, Massachusetts Institute of Technology, Cambridge.

Hallett, J. and S. C. Mossop (1974). Production of secondary ice particles during the riming process. *Nature 249*, 26-28.

Hande, L. B., C. Engler, C. Hoose and I. Tegen (2015). Seasonal variability of Saharan desert dust and ice nucleating particles over Europe. *Atmos. Chem. Phys. 15*, 4389–4397.

Hansen, J. E. and L. D. Travis (1974). Light scattering in planetary atmospheres. *Space Science Reviews 16*, 527–610.

Hartmann, S., S. Augustin, T. Clauss, H. Wex, T. Šantl Temkiv, J. Voigtländer, D. Niedermeier and F. Stratmann (2013). Immersion freezing of ice nucleation active protein complexes. *Atmos. Chem. Phys. 13*, 5751–5766.

Herzog, H.-J., U. Schubert, G. Vogel, A. Fiedler and R. Kirchner (2002a). LLM - the high-resolving nonhydrostatic simulation model in the DWD - project LITFASS Part I: modeling technique and simulation method. Tech. Report No. 4, Consortium for Small-Scale Modelling, Offenbach am Main, Germany.

Herzog, H.-J., G. Vogel and U. Schubert (2002b). LLM - a nonhydrostatic model applied to high-resolving simulations of turbulent fluxes over heterogeneous terrain. *Theor. Appl. Climatol. 73*, 67-86.

Hoffmann, N., D. Duft, A. Kiselev and T. Leisner (2013). Contact freezing efficiency of mineral dust aerosols studied in an electrodynamic balance: quantitative size and temperature dependence for illite particles. *Faraday Discuss. 165*, 383–390.

Hohenegger, C., D. Lüthi and C. Schär (2006). Predictability mysteries in cloud-resolving models. *Mon. Weather Rev. 134*, 2095–2107.

Hong, S.-Y. and J. Dudhia (2012). Next-generation numerical weather prediction: Bridging parameterization, explicit clouds, and large eddies. *Bull. Am. Meteor. Soc. 93*, ES6–ES9.

Hoose, C. and O. Möhler (2012). Heterogeneous ice nucleation on atmospheric aerosols: a review of results from laboratory experiments. *Atmos. Chem. Phys. 12*, 9817–9854.

Houze, R. A. (1993). *Cloud Dynamics*. Academic Press, San Diego, California, USA.

Hu, Y. X. and K. Stamnes (1993). An accurate parameterization of the radiative properties of water clouds suitable for use in climate models. *J. Clim. 6*, 728–742.

Järvinen, E., M. Schnaiter, G. Mioche, O. Jourdan, V. N. Shcherbakov, A. Costa, A. Afchine, M. Krämer, F. Heidelberg, T. Jurkat, C. Voigt, H. Schlager, L. Nichman, M. Gallagher, E. Hirst, C. Schmitt, A. Bansemer, A. Heymsfield, P. Lawson, U. Tricoli, K. Pfeilsticker, P. Vochezer, O. Möhler and T. Leisner (2016). Quasi-spherical ice in convective clouds. *J. Atmos. Sci.* doi: 10.1175/JAS-D-15-0365.1 (in press).

Jeffery, C. A. and P. H. Austin (1997). Homogeneous nucleation of supercooled water: Results from a new equation of state. *J. Geophys. Res. Atmos. 102*, 25269–25279.

Johnson, J. S., Z. Cui, L. A. Lee, J. P. Gosling, A. M. Blyth and K. S. Carslaw (2015). Evaluating uncertainty in convective cloud microphysics using statistical emulation. *J. Adv. Model. Earth Syst. 7*, 162–187.

Johnson, M., Y. Jung, D. T. Dawson II and M. Xue (2016). Comparison of simulated polarimetric signatures in idealized supercell storms using two-moment bulk microphysics schemes in WRF. *Mon. Weather Rev. 144*, 971–996.

Kärcher, B., J. Hendricks and U. Lohmann (2006). Physically based parameterization of cirrus cloud formation for use in global atmospheric models. *J. Geophys. Res. Atmos. 111*, D01205.

Khain, A., M. Ovtchinnikov, M. Pinsky, A. Pokrovsky and H. Krugliak (2000). Notes on the state-of-the-art numerical modeling of cloud microphysics. *Atmos. Res. 55*, 159–224.

Khain, A., D. Rosenfeld and A. Pokrovsky (2005). Aerosol impact on the dynamics and microphysics of deep convective clouds. *Q. J. Roy. Meteor. Soc. 131*, 2639–2663.

Khain, A. P. (2009). Notes on state-of-the-art investigations of aerosol effects on precipitation: a critical review. *Environ. Res. Lett. 4*, 015004.

Khain, A. P., K. D. Beheng, A. Heymsfield, A. Korolev, S. O. Krichak, Z. Levin, M. Pinsky, V. Phillips, T. Prabhakaran, A. Teller, S. C. van den Heever and J.-I. Yano (2015). Representation of microphysical processes in cloud-resolving models: Spectral (bin) microphysics versus bulk parameterization. *Rev. Geophys. 53*, 247–322.

Khain, A. P., D. Rosenfeld and A. Pokrovsky (2001). Simulating convective clouds with sustained supercooled liquid water down to -37.5 °C using a spectral microphysics model. *Geophys. Res. Lett. 28*, 3887–3890.

Klaus, D., K. Dethloff, W. Dorn, A. Rinke and D. L. Wu (2016). New insight of Arctic cloud parameterization from regional climate model simulations, satellite-based, and drifting station data. *Geophys. Res. Lett. 43*, 5450–5459.

Klein, H., S. Nickovic, W. Haunold, U. Bundke, B. Nillius, M. Ebert, S. Weinbruch, L. Schuetz, Z. Levin, L. A. Barrie and H. Bingemer (2010). Saharan dust and ice nuclei over Central Europe. *Atmos. Chem. Phys. 10*, 10211–10221.

Klein, S. A., R. B. McCoy, H. Morrison, A. S. Ackerman, A. Avramov, G. de Boer, M. Chen, J. N. S. Cole, A. D. Del Genio, M. Falk, M. J. Foster, A. Fridlind, J.-C. Golaz, T. Hashino, J. Y. Harrington, C. Hoose, M. F. Khairoutdinov, V. E. Larson, X. Liu, Y. Luo, G. M. McFarquhar, S. Menon, R. A. J. Neggers, S. Park, M. R. Poellot, J. M. Schmidt, I. Sednev, B. J. Shipway, M. D. Shupe, D. A. Spangenberg, Y. C. Sud, D. D. Turner, D. E. Veron, K. von Salzen, G. K. Walker, Z. Wang, A. B. Wolf, S. Xie, X.-M. Xu, F. Yang and G. Zhang (2009). Intercomparison of model simulations of mixed-phase clouds observed during the ARM Mixed-Phase Arctic Cloud Experiment. I: Single-layer cloud. *Q. J. Roy. Meteor. Soc. 135*, 979–1002.

Knopf, D. A., P. A. Alpert, B. Wang, R. E. O'Brien, S. T. Kelly, A. Laskin, M. K. Gilles and R. C. Moffet (2014). Microspectroscopic imaging and characterization of individually identified ice nucleating particles from a case field study. *J. Geophys. Res. Atmos. 119*, 10,365–10,381.

Koenig, L. R. (1963). The glaciating behavior of small cumulonimbus clouds. *J. Atmos. Sci. 20*, 29–47.

Koop, T., B. Luo, A. Tsias and T. Peter (2000). Water activity as the determinant for homogeneous ice nucleation in aqueous solutions. *Nature 406*, 611–614.

Korolev, A. (2007). Limitations of the Wegener-Bergeron-Findeisen mechanism in the evolution of mixed-phase clouds. *J. Atmos. Sci. 64*, 3372–3375.

Korolev, A. and G. Isaac (2003). Phase transformation of mixed-phase clouds. *Q. J. Roy. Meteor. Soc. 129*, 19–38.

Korolev, A., A. Khain, M. Pinsky and J. French (2015). Theoretical study of mixing in liquid clouds – part 1: Classical concept. *Atmos. Chem. Phys. Discussions 15*, 30211–30267.

Korolev, A. V. and I. P. Mazin (2003). Supersaturation of water vapor in clouds. *J. Atmos. Sci. 60*, 2957–2974.

Krämer, M., C. Rolf, A. Luebke, A. Afchine, N. Spelten, A. Costa, J. Meyer, M. Zöger, J. Smith, R. L. Herman, B. Buchholz, V. Ebert, D. Baumgardner, S. Borrmann, M. Klingebiel and L. Avallone (2016). A microphysics guide to cirrus clouds – Part 1: Cirrus types. *Atmos. Chem. Phys. 16*, 3463–3483.

Kristjánsson, J. E. (2002). Studies of the aerosol indirect effect from sulfate and black carbon aerosols. *J. Geophys. Res. Atmos. 107*, 4246.

Ladino Moreno, L. A., O. Stetzer and U. Lohmann (2013). Contact freezing: a review of experimental studies. *Atmos. Chem. Phys. 13*, 9745–9769.

Lamb, D. and J. Verlinde (2011). *Physics and Chemistry of Clouds*. Cambridge University Press.

Lin, Y.-L., R. D. Farley and H. D. Orville (1983). Bulk parameterization of the snow field in a cloud model. *J. Clim. Appl. Meteorol. 22*, 1065–1092.

Lohmann, U. and J. Feichter (2005). Global indirect aerosol effects: a review. *Atmos. Chem. Phys. 5*, 715–737.

Lorenz, E. N. (1963). Deterministic nonperiodic flow. *J. Atmos. Sci. 20*, 130–141.

Low, T. B. and R. List (1982). Collision, coalescence and breakup of raindrops. Part I: Experimentally established coalescence efficiencies and fragment size distributions in breakup. *J. Atmos. Sci. 39*, 1591–1606.

Luebke, A. E., A. Afchine, A. Costa, J.-U. Grooß, J. Meyer, C. Rolf, N. Spelten, L. M. Avallone, D. Baumgardner and M. Krämer (2016). The origin of midlatitude ice clouds and the resulting influence on their microphysical properties *16*, 5793–5809.

Mason, R. H., M. Si, C. Chou, V. E. Irish, R. Dickie, P. Elizondo, R. Wong, M. Brintnell, M. Elsasser, W. M. Lassar, K. M. Pierce, W. R. Leaitch, A. M. MacDonald, A. Platt, D. Toom-Sauntry, R. Sarda-Estève, C. L. Schiller, K. J. Suski, T. C. J. Hill, J. P. D. Abbatt, J. A. Huffman, P. J. DeMott and A. K. Bertram (2016). Size-resolved measurements of ice-nucleating particles at six locations in North America and one in Europe. *Atmos. Chem. Phys. 16*, 1637–1651.

McFarquhar, G. M., S. Ghan, J. Verlinde, A. Korolev, J. W. Strapp, B. Schmid, J. M. Tomlinson, M. Wolde, S. D. Brooks, D. Cziczo, M. K. Dubey, J. Fan, C. Flynn, I. Gultepe, J. Hubbe, M. K. Gilles, A. Laskin, P. Lawson, W. R. Leaitch, P. Liu, X. Liu, D. Lubin, C. Mazzoleni, A.-M. Macdonald, R. C. Moffet, H. Morrison, M. Ovchinnikov, M. D. Shupe, D. D. Turner, S. Xie, A. Zelenyuk, K. Bae, M. Freer and A. Glen (2011). Indirect and Semi-direct Aerosol Campaign. *Bull. Am. Meteor. Soc. 92*, 183–201.

Morrison, H., G. de Boer, G. Feingold, J. Harrington, M. D. Shupe and K. Sulia (2012). Resilience of persistent Arctic mixed-phase clouds. *Nature Geosci. 5*, 11–17.

Morrison, H., R. B. McCoy, S. A. Klein, S. Xie, Y. Luo, A. Avramov, M. Chen, J. N. S. Cole, M. Falk, M. J. Foster, A. D. Del Genio, J. Y. Harrington, C. Hoose, M. F. Khairoutdinov, V. E. Larson, X. Liu, G. M. McFarquhar, M. R. Poellot, K. von Salzen, B. J. Shipway, M. D. Shupe, Y. C. Sud, D. D. Turner, D. E. Veron, G. K. Walker, Z. Wang, A. B. Wolf, K.-M. Xu, F. Yang and G. Zhang (2009).

Intercomparison of model simulations of mixed-phase clouds observed during the ARM Mixed-Phase Arctic Cloud Experiment. II: Multilayer cloud. *Q. J. Roy. Meteor. Soc. 135*, 1003–1019.

Morrison, H. and J. Milbrandt (2011). Comparison of two-moment bulk microphysics schemes in idealized supercell thunderstorm simulations. *Mon. Weather Rev. 139*, 1103–1130.

Morrison, H. and J. A. Milbrandt (2015). Parameterization of cloud microphysics based on the prediction of bulk ice particle properties. Part I: Scheme description and idealized tests. *J. Atmos. Sci. 72*, 287–311.

Niemand, M., O. Möhler, B. Vogel, H. Vogel, C. Hoose, P. Connolly, H. Klein, H. Bingemer, P. DeMott, J. Skrotzki and T. Leisner (2012). A particle-surface-area-based parameterization of immersion freezing on desert dust particles. *J. Atmos. Sci. 69*, 3077–3092.

Noppel, H., U. Blahak, A. Seifert and K. D. Beheng (2010). Simulations of a hailstorm and the impact of CCN using an advanced two-moment cloud microphysical scheme. *Atmos. Res. 96*, 286–301.

Ovchinnikov, M., A. S. Ackerman, A. Avramov, A. Cheng, J. Fan, A. M. Fridlind, S. Ghan, J. Harrington, C. Hoose, A. Korolev, G. M. McFarquhar, H. Morrison, M. Paukert, J. Savre, B. J. Shipway, M. D. Shupe, A. Solomon and K. Sulia (2014). Intercomparison of large-eddy simulations of Arctic mixed-phase clouds: Importance of ice size distribution assumptions. *J. Adv. Model. Earth Syst. 6*, 223–248.

Ovchinnikov, M., A. Korolev and J. Fan (2011). Effects of ice number concentration on dynamics of a shallow mixed-phase stratiform cloud. *J. Geophys. Res. 116*, D00T06.

Paukert, M. and C. Hoose (2014a). Modeling immersion freezing with aerosol-dependent prognostic ice nuclei in Arctic mixed-phase clouds. *J. Geophys. Res. Atmos. 119*, 9073–9092.

Paukert, M. and C. Hoose (2014b). Quantification of cloud susceptibilities to ice nuclei. 14th Conf. on Cloud Physics, July 7-11, 2014, Boston, Mass., USA.

Petters, M. D. and S. M. Kreidenweis (2007). A single parameter representation of hygroscopic growth and cloud condensation nucleus activity. *Atmos. Chem. Phys. 7*, 1961–1971.

Phillips, V. T. J., A. M. Blyth, P. R. A. Brown, T. W. Choularton and J. Latham (2001). The glaciation of a cumulus cloud over New Mexico. *Q. J. Roy. Meteor. Soc. 127*, 1513–1534.

Phillips, V. T. J., P. J. DeMott and C. Andronache (2008). An empirical parameterization of heterogeneous ice nucleation for multiple chemical species of aerosol. *J. Atmos. Sci. 65*, 9.

Phillips, V. T. J., L. J. Donner and S. T. Garner (2007). Nucleation processes in deep convection simulated by a cloud-system-resolving model with double-moment bulk microphysics. *J. Atmos. Sci. 64*, 738–761.

Phillips, V. T. J., A. Khain, N. Benmoshe and E. Ilotoviz (2014). Theory of time-dependent freezing. Part I: Description of scheme for wet growth of hail. *J. Atmos. Sci. 71*, 4527–4557.

Pinsky, M., A. Khain and A. Korolev (2014). Analytical investigation of glaciation time in mixed-phase adiabatic cloud volumes. *J. Atmos. Sci. 71*, 4143–4157.

Pinsky, M., A. Khain and M. Shapiro (2001). Collision efficiency of drops in a wide range of reynolds numbers: Effects of pressure on spectrum evolution. *J. Atmos. Sci. 58*, 742–764.

Pinsky, M. B. and A. P. Khain (2002). Effects of in-cloud nucleation and turbulence on droplet spectrum formation in cumulus clouds. *Q. J. Roy. Meteor. Soc. 128*, 501–533.

Platzer, P. (2015). *Perturbed microphysics due to ice nuclei*. Internship report, Karlsruhe Institute of Technology.

Politovich, M. (2015). *AVIATION METEOROLOGY | Aircraft Icing*. Encyclopedia of Atmospheric Sciences, 160-165. Academic Press, Oxford, 2nd ed.

Pruppacher, H. R. and J. D. Klett (1997). *Microphysics of Clouds and Precipitation*. Atmospheric and Oceanographic Sciences Library. Kluwer Academic Publishers, Dordrecht, The Netherlands, 2nd ed.

Raschendorfer, M. (2001). The new turbulence parameterization of LM. Newsletter No. 1, Consortium for Small-Scale Modelling, Offenbach am Main, Germany.

Ritter, B. and J.-F. Geleyn (1992). A comprehensive radiation scheme for numerical weather prediction models with potential applications in climate simulations. *Mon. Weather Rev. 120*, 303–325.

Rokicki, M. L. and K. C. Young (1978). The initiation of precipitation in updrafts. *J. Appl. Meteorol. 17*, 745–754.

Rosenfeld, D., U. Lohmann, G. B. Raga, C. D. O'Dowd, M. Kulmala, S. Fuzzi, A. Reissell and M. O. Andreae (2008). Flood or drought: How do aerosols affect precipitation? *Science 321*, 1309–1313.

Rosenfeld, D. and W. L. Woodley (2000). Deep convective clouds with sustained supercooled liquid water down to -37.5 °C. *Nature 405*, 440–442.

Segal, Y. and A. Khain (2006). Dependence of droplet concentration on aerosol conditions in different cloud types: Application to droplet concentration parameterization of aerosol conditions. *J. Geophys. Res. Atmos. 111*, D15204.

Seifert (2002). *Parametrisierung wolkenmikrophysikalischer Prozesse und Simulation konvektiver Mischwolken*. Ph.D. dissertation, faculty of physics at University of Karlsruhe (TH).

Seifert, A. (2008). On the parameterization of evaporation of raindrops as simulated by a one-dimensional rainshaft model. *J. Atmos. Sci. 65*, 3608–3619.

Seifert, A. and K. D. Beheng (2001). A double-moment parameterization for simulating autoconversion, accretion and selfcollection. *Atmos. Res. 59-60*, 265–281.

Seifert, A. and K. D. Beheng (2006). A two-moment cloud microphysics parameterization for mixed-phase clouds. Part 1: Model description. *Meteorology and Atmospheric Physics 92*, 45–66.

Seifert, A., U. Blahak and R. Buhr (2014). On the analytic approximation of bulk collision rates of non-spherical hydrometeors. *Geosci. Model Dev. 7*, 463–478.

Seifert, A., C. Köhler and K. D. Beheng (2012). Aerosol-cloud-precipitation effects over Germany as simulated by a convective-scale numerical weather prediction model. *Atmos. Chem. Phys. 12*, 709–725.

Seifert, P., A. Ansmann, I. Mattis, U. Wandinger, M. Tesche, R. Engelmann, D. Müller, C. Pérez and K. Haustein (2010). Saharan dust and heterogeneous ice formation: Eleven years of cloud observations at a central European EARLINET site. *J. Geophys. Res. Atmos. 115*, D20201.

Shupe, M. D. and J. M. Intrieri (2004). Cloud radiative forcing of the Arctic surface: The influence of cloud properties, surface albedo, and solar zenith angle. *J. Clim. 17*, 616–628.

Siebesma, A. P., C. S. Bretherton, A. Brown, A. Chlond, J. Cuxart, P. G. Duynkerke, H. Jiang, M. Khairoutdinov, D. Lewellen, C.-H. Moeng, E. Sanchez, B. Stevens and D. E. Stevens (2003). A large eddy simulation intercomparison study of shallow cumulus convection. *J. Atmos. Sci. 60*, 1201–1219.

Simmel, M., K. Diehl and S. Wurzler (2005). Numerical simulation of the microphysics of an orographic cloud: Comparison with measurements and sensitivity studies. *Atmos. Environ. 39*, 4365–4373.

Simmel, M., T. Trautmann and G. Tetzlaff (2002). Numerical solution of the stochastic collection equation – comparison of the Linear Discrete Method with other methods. *Atmos. Res. 61*, 135–148.

Simpson, J. E. (1997). *Gravity Currents in the Environment and the Laboratory*. Cambridge University Press, 244 pp.

Smagorinsky, J. (1963). General circulation experiments with the primitive equations: I. The basic experiment. *Mon. Weather Rev. 91*, 99-164.

Solomon, A., M. D. Shupe, P. O. G. Persson and H. Morrison (2011). Moisture and dynamical interactions maintaining decoupled Arctic mixed-phase stratocumulus in the presence of a humidity inversion. *Atmos. Chem. Phys. 11*, 10127–10148.

Stephens, G. L. (1978). Radiation profiles in extended water clouds. I: Theory. *J. Atmos. Sci. 35*, 2111–2122.

Taylor, J. W., T. W. Choularton, A. M. Blyth, Z. Liu, K. N. Bower, J. Crosier, M. W. Gallagher, P. I. Williams, J. R. Dorsey, M. J. Flynn, L. J. Bennett, Y. Huang, J. French, A. Korolev and P. R. A. Brown (2016). Observations of cloud microphysics and ice formation during COPE. *Atmos. Chem. Phys. 16*, 799–826.

Thompson, G., R. T. Bruintjes, B. G. Brown and F. Hage (1997). Intercomparison of in-flight icing algorithms. Part I: WISP94 real-time icing prediction and evaluation program. *J. Atmos. Sci. 12*, 878–889.

Twomey, S. (1977). The influence of pollution on the shortwave albedo of clouds. *J. Atmos. Sci. 34*, 1149–1152.

Ullrich, R., C. Hoose, O. Möhler, M. Niemand, R. Wagner, K. Höhler, N. Hiranuma, H. Saathoff and T. Leisner (2016). A new ice nucleation active site parameterization for desert dust and soot. *manuscript submitted for publication* .

Vali, G. (1971). Quantitative evaluation of experimental results on the heterogeneous freezing nucleation of supercooled liquids. *J. Atmos. Sci. 28*, 402–409.

Vali, G. (1994). Freezing rate due to heterogeneous nucleation. *J. Atmos. Sci. 51*, 1843–1856.

Vali, G. (2014). Interpretation of freezing nucleation experiments: singular and stochastic; sites and surfaces. *Atmos. Chem. Phys. 14*, 5271–5294.

Vali, G. and E. J. Stansbury (1966). Time-dependent characteristics of the heterogeneous nucleation of ice. *Can. J. Phys. 44*, 477–502.

van den Heever, S. C., G. G. Carrió, W. R. Cotton, P. J. DeMott and A. J. Prenni (2006). Impacts of nucleating aerosol on Florida storms. Part I: Mesoscale simulations. *J. Atmos. Sci. 63*, 1752–1775.

Vogel, B., H. Vogel, D. Bäumer, M. Bangert, K. Lundgren, R. Rinke and T. Stanelle (2009). The comprehensive model system COSMO-ART – radiative impact of aerosol on the state of the atmosphere on the regional scale. *Atmos. Chem. Phys. 9*, 8661–8680.

Wagner, R., A. Kiselev, O. Möhler, H. Saathoff and I. Steinke (2016). Pre-activation of ice-nucleating particles by the pore condensation and freezing mechanism. *Atmos. Chem. Phys. 16*, 2025–2042.

Warren, S. G., R. M. Eastman and C. J. Hahn (2007). A survey of changes in cloud cover and cloud types over land from surface observations, 1971-96. *J. Clim. 20*, 717–738.

Weisman, M. L. and J. B. Klemp (1982). The dependence of numerically simulated convective storms on vertical wind shear and buoyancy. *Mon. Weather Rev. 110*, 504–520.

Welti, A., F. Lüönd, Z. A. Kanji, O. Stetzer and U. Lohmann (2012). Time dependence of immersion freezing: an experimental study on size selected kaolinite particles. *Atmos. Chem. Phys. 12*.

Wisner, C., H. D. Orville and C. Myers (1972). A numerical model of a hail-bearing cloud. *J. Atmos. Sci. 29*, 1160–1181.

Yang, F., M. Ovchinnikov and R. A. Shaw (2013). Minimalist model of ice microphysics in mixed-phase stratiform clouds. *Geophys. Res. Lett. 40*, 3756–3760.

Yi, B., P. Yang, B. A. Baum, T. L'Ecuyer, L. Oreopoulos, E. J. Mlawer, A. J. Heymsfield and K.-N. Liou (2013). Influence of ice particle surface roughening on the global cloud radiative effect. *J. Atmos. Sci. 70*, 2794–2807.

# Acknowledgments

My honest gratitude is due to Corinna Hoose for accompanying my scientific way for more than five years, for giving me the opportunity to carry out this work, for stimulating new ideas, and for enabling me to conduct research in a self-reliant manner while being supportive whenever needed.

The contribution of Martin Simmel to the contents of this work is much appreciated, and the endurance to go trough a number of iterations of SPECS model simulations in particular, as well as the help with the interpretation of results.

Paul Platzer has contributed to this work during his internship at KIT. The efforts to validate early versions of the model code, and the fruitful discussions of final results gave valuable insights in the perturbed mesoscale simulations, which may be the basis of further research. Some of the data needed for this subproject were provided by Christian Barthlott.

Bernhard Vogel, Max Bangert, Heike Vogel as well as Tobias Schad are acknowledged for providing the basis of the model and for helpful discussions. Technical and scientific discussions with Axel Seifert, Uli Blahak and Franziska Glaßmeier are much appreciated. I am also grateful to Greg Thompson, Wojtek Grabowski and Hugh Morrison for discussions and for sharing unpublished information.

During the past years, the IMK-AAF team has played a crucial role in providing a friendly atmosphere and giving insight into exciting lab work which has been a particular profit for me, “the modeler”.

Significant amounts of computing resources have been provided by the Steinbuch Centre for Computing (SCC), Karlsruhe. This work has been funded by the Helmholtz Association through the Climate Initiative REKLIM and the President’s Initiative and Networking Fund.